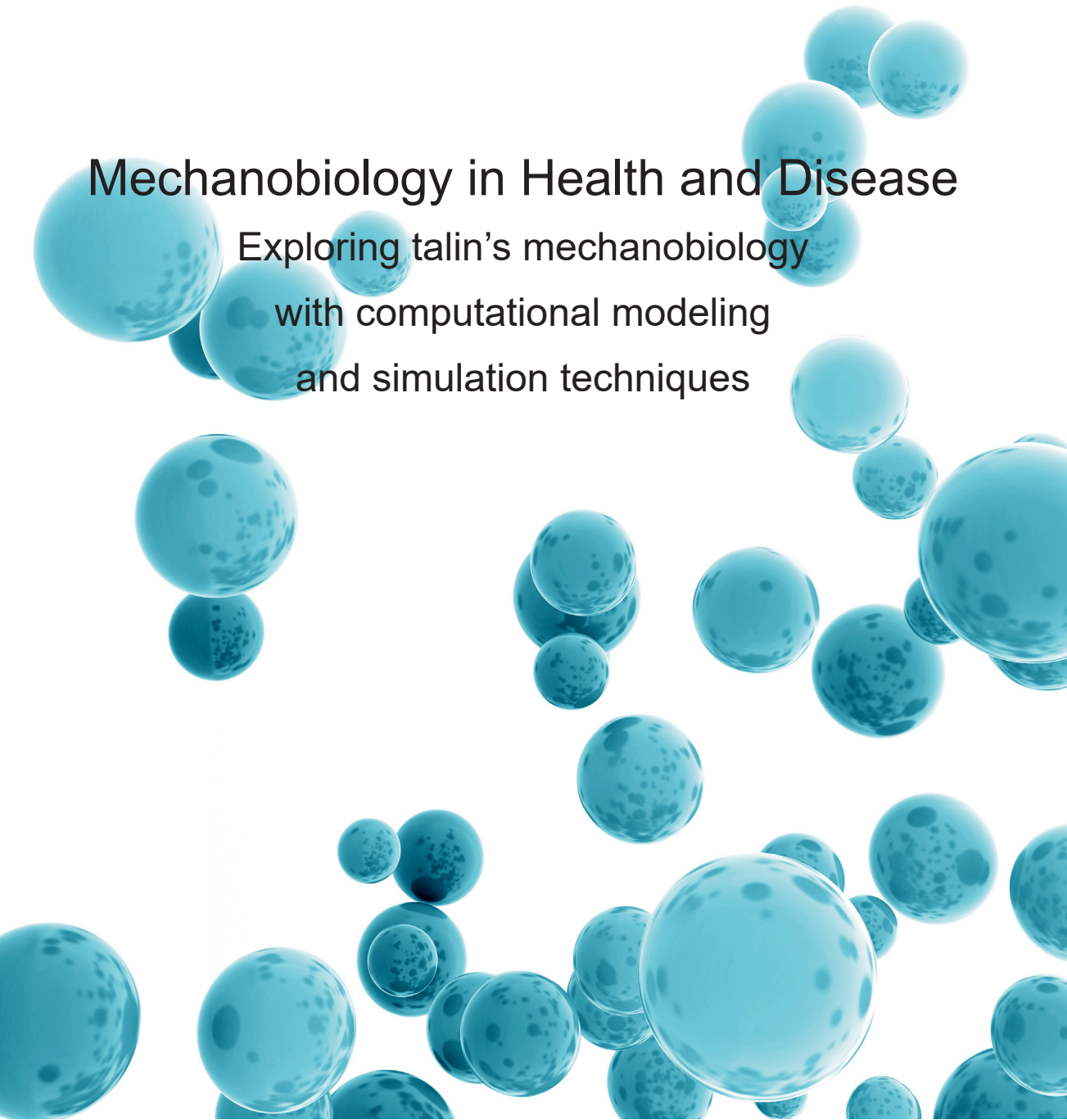


MAGDALÉNA von ESSEN

# Mechanobiology in Health and Disease

Exploring talin's mechanobiology  
with computational modeling  
and simulation techniques





MAGDALÉNA von ESSEN

## Mechanobiology in Health and Disease

Exploring talin's mechanobiology  
with computational modeling  
and simulation techniques



ACADEMIC DISSERTATION

To be presented, with the permission of  
the Faculty Council of the Faculty of Medicine and Life Sciences  
of the University of Tampere,  
for public discussion in the Jarmo Visakorpi auditorium  
of the Arvo building, Arvo Ylpön katu 34, Tampere,  
on 16 November 2018, at 12 o'clock.

UNIVERSITY OF TAMPERE

MAGDALÉNA von ESSEN

Mechanobiology in Health and Disease

Exploring talin's mechanobiology  
with computational modeling  
and simulation techniques

*Acta Universitatis Tamperensis 2423*  
*Tampere University Press*  
*Tampere 2018*



UNIVERSITY  
OF TAMPERE

ACADEMIC DISSERTATION

University of Tampere, Faculty of Medicine and Life Sciences  
Finland  
Imperial College London, Department of Bioengineering  
United Kingdom

*Supervised by*

Associate Professor Vesa P. Hytönen  
University of Tampere  
Finland

*Reviewed by*

Docent Tiina Salminen  
Åbo Akademi  
Finland  
PhD André H. Juffer  
University of Oulu  
Finland

The originality of this thesis has been checked using the Turnitin OriginalityCheck service in accordance with the quality management system of the University of Tampere.

Copyright ©2018 Tampere University Press and the author

Cover design by  
Mikko Reinikka

Acta Universitatis Tamperensis 2423  
ISBN 978-952-03-0863-6 (print)  
ISSN-L 1455-1616  
ISSN 1455-1616

Acta Electronica Universitatis Tamperensis 1933  
ISBN 978-952-03-0864-3 (pdf)  
ISSN 1456-954X  
<http://tampub.uta.fi>

Suomen Yliopistopaino Oy – Juvenes Print  
Tampere 2018



*This PhD thesis is dedicated to My Family, Mathias and Vera.*

*Thank you both for making my life anything but boring, full of surprises,*

*interesting challenges, humor and laughter.*

# ACKNOWLEDGEMENTS

I would like to express my deep gratitude to Associate Professor Vesa Hytönen, my research supervisor, for his patient guidance and never-ending optimism, enthusiastic encouragement and useful critiques of this research work. His enormous area of expertise has broadened my view on mechanobiology in general, as well as on experimental design, data analysis and visualization.

I would also like to thank M.Sc. Rolle Rahikainen for brainstorming on talin mutagenesis and successful collaboration on the talin R3 destabilization. His hard work in the cell experiments and overall attitude indeed made this multidisciplinary research possible. I am thankful for a fruitful collaboration with Professor Armando del Rio Hernandez and M.Sc. William Haining from the Department of Bioengineering, Imperial College London. Our pleasant two year collaboration provided interesting multidisciplinary insights into mechanobiology and methodology applications. I would like to extend my thanks to M.Sc. Sampo Kukkurainen for his introduction to the wonders of computational protein modelling and simulation techniques, as well as to Dr. Vasyly Mykuliak for his advice in computational methodology, assistance and enormous work he has done to study intermediate states in protein unfolding patterns. I wish to thank Professor Terho Lehtimäki, Professor Niku Oksala, Dr. Emma Raitoharju and Dr. Ilkka Seppälä for their achievements in cardiovascular research and for providing me with an interesting opportunity of investigating talin disease connection in atherosclerosis.

My grateful thanks are also extended to M.Sc. Latifeh Azizi for her continuous hard work on the talin rod mechanobiology, her endless optimism and warm presence. My warmest thoughts will always be in the FinnMedi 1 building, 4<sup>th</sup> floor office shared with Dr. Juha Määttä, who encouraged me along the way.

During the years I had the pleasure to meet and collaborate with number of talented researchers in the Protein Dynamics group and I would like to thank every one of them for creating an inspiring and motivating environment full of work drive as well as humor.

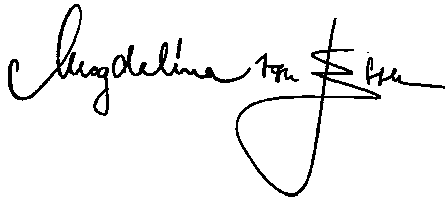
I am grateful to my thesis committee members Professor Katriina Aalto-Setälä, Professor Matti Nykter and Dr. Teemu Ihalainen for their support and

encouragement while steering my research towards completion. I thank them all for sharing their expertise and valuable advice. I thank my reviewers Adjunct Professor Tiina Salminen and Dr. André Juffer for their valuable comments and constructive feedback to improve this work.

I wish to thank the University of Tampere for their financial support via TGPBB graduate school. And I would like to acknowledge CSC Center for Scientific Computing, Finland, for computational resources and technical support.

At last but not least I wish to express my deepest gratitude to my husband Mathias and daughter Vera, my family and family-in-law for their patients, optimism, support and encouragement during my studies and research.

Oxford, July 2018

A handwritten signature in black ink, reading "Angelina von Steiner". The signature is written in a cursive style with a large, prominent loop at the end of the last name.



# ABSTRACT

All living organisms are continuously exposed to mechanical forces that are exerted on them by their surroundings. The ability of organisms, and more importantly, the ability of individual cells to receive mechanical signals and respond to the stimuli, is fundamental to life. Mechanosensing is present in all cell and tissue types from differentiating to highly differentiated units. Thanks to the variety of roles and cellular components it is not surprising that a vast variety of diverse diseases has been and is continuously being recognized as diseases of mechanotransduction.

The need to define disease symptoms, to discover their causes, to cure illnesses or to increase the quality of life has accumulated significant amount of knowledge and led to discoveries and inventions in various scientific fields. The intensive research is constantly providing enormous amount of multidisciplinary information. In this thesis, I target the subcellular and protein structures that are implicated in mechanotransduction and their known connection to a disease. I provide a comprehensive overview of the known cellular and structural data, disease connection, interactions and mechanotransduction pathway associations.

Further in the work, I focus on the mechanosensitivity of talin protein together with other  $\alpha$ -helical proteins, in particular vinculin and  $\alpha$ -catenin. The disease association of talin and vinculin expression is investigated in atherosclerosis and plaque formation with microarray analysis (MA) and qRT-PCR low-density array. All the analyzed talin and vinculin genes are significantly and consistently downregulated in atherosclerotic plaques compared to healthy control. The differences in expression levels between stable and unstable plaques are found statistically insignificant. Nonetheless, a negative tendency in the protein expression in unstable plaques is observed. This investigation shows for the first time the involvement of talin and vinculin in atherosclerosis. It suggests that impaired tissue mechanostability affects the tissue remodeling and healing capabilities leading to development of unstable plaques.

Despite the abundance of  $\alpha$ -helical folds among the proteome and their undeniable relevance in health and disease, the fundamental principles of their behavior under mechanical load are poorly understood. Furthermore, it is still not fully known how cells sense and interpret mechanical forces and how they drive

their mechanical response. In the following, talin mechanosensitivity is investigated in a multidisciplinary research combining computational molecular dynamics (MD) and steered molecular dynamics (SMD) simulation with single-molecule atomic force microscopy (smAFM) and cellular experiments supported by biochemical analysis.

Utilizing computationally designed mutations we show that destabilization of the talin rod R3 subdomain decreases cellular traction force generation. Decreased force traction modifies the dynamics of talin and vinculin in focal adhesions and results in a formation of talin-rich yet unstable adhesions. We also report a link between talin mechanostability and cell migration rate. Finally, talin destabilization leads to involvement of different integrin subtypes and sensing of extracellular matrix (ECM) proteins. Experiments with truncated forms of talin confirm the mechanosensory role of the talin R3 subdomain. This study provides clear evidence of how talin rod subdomain unfolding acts as a key regulator in focal adhesion and in the adhesion formation. Additionally, this research confirms the central role of talin rod in cellular processes such as cell migration and substrate sensing.

Secondly, we show that the entire talin rod can be unfolded by mechanical force. Such unfolding occurs under a physiological range of forces between 10 and 40 pN. We also demonstrate, through a combination of smAFM and SMD, that the different subdomains within the talin rod display a specific hierarchy of mechanostability. These results provide a mechanism by which different force conditions within the cell control gradual unfolding of the talin rod, modify talin interactions, and result in a finely tuned cellular response to applied forces.

Finally, we investigate unfolding of talin and  $\alpha$ -catenin proteins. SMD simulations reveal that talin and  $\alpha$ -catenin  $\alpha$ -helical subdomains unfold through a stable 3-helix conformation. Even though the talin 5-helix subdomains are mechanically stable folds, a second stable conformation representing the 3-helix state is detected in force induced unfolding. Also mechanically weaker 4-helix subdomains unfold into a mechanically stable 3-helix state. Specifically designed mutants, utilizing disulfide clamps to protect the stable state, support the intermediate model in both computational and experimental setups. The unfolding intermediate was recognized in talin and  $\alpha$ -catenin subdomains, yet the biological significance of this stable state remains unclear. Better understanding of similar fundamental principles of mechanical unfolding mechanisms could be a major step towards comprehensive mechanoregulation models in health and in disease.

# TIIVISTELMÄ

Kaikki elävät organismit vastaanottavat mekaanisia viestejä ympäristöstään. Kyky vastaanottaa mekaanisia signaaleja ja erityisesti yksittäisten solujen kyky reagoida mekaanisiin viesteihin ovat keskeisen tärkeitä elintoiminnoille. Mekaanisten viestien vastaanottamista tapahtuu kaikissa solu- ja kudostyypeissä aina erilaistuvista soluista jo pitkälle erilaistuneisiin soluihin. Ei siten yllätä, että yhä useampia mekanoviestintään liittyviä solujen rakenneosasia on liitetty erilaisiin sairauksiin.

Tarve ymmärtää sairauksia ja niiden alkuperää, hoitaa niitä ja ylipäänsä parantaa elämänlaatua on johtanut laajamittaiseen tiedon hankkimiseen ja uusien keksintöjen syntymiseen useilla eri tieteenaloilla. Nykyaikainen monitieteinen tutkimus tuottaa valtavan määrän informaatiota. Tämä väitöskirja keskittyy solun rakenteiden tarkasteluun mekanoviestinnän näkökulmasta. Pyrin tarkastelemaan mekanoviestinnän ja sairauksien yhteyksiä kokonaisvaltaisen lähestymistavan avulla, jossa huomioidaan solun rakenne, proteiinien tunnetut rakenteet, proteiinien jo tunnetut yhteydet sairauksiin, molekyylien keskinäiset vuorovaikutukset ja mekanotransduktion mahdollistavat, useista molekyyleistä koostuvat rakenteelliset kokonaisuudet.

Tarkastelen yksityiskohtaisemmin taliini-proteiinin rakenteen säätelyä mekaanisten viestien toimesta. Laajennan tarkastelua  $\alpha$ -helikaalisten proteiinien toimintaan, tarkastellen erityisesti vinkuliinin ja  $\alpha$ -kateniinin rakennetta. Taliinin ja vinkuliinin yhteyttä ateroskleroosiin tutkittiin vertailemalla proteiinien ekspressiotasoa sairaissa ja terveissä verisuonissa käyttäen microarray-tekniikkaa ja kvantitatiivista reaaliaikaista PCR-tekniikkaa. Taliini- ja vinkuliinigeenien havaittiin olevan vähemmän ekspressoituja ateroskelroottisissa plakeissa verrattuna terveisiin verrokkikudoksiin. Vertailimme myös stabiilien ja epästabiilien plakkien ekspressiotasoa, joissa havaittiin heikko negatiivinen korrelaatio taliini- ja vinkuliiniekspression ja plakin vakavuuden välillä, joka ei kuitenkaan tilastollisessa testauksessa tuottanut selkeää eroa. Tulokset viittaavat siihen, että alentunut kudoksen mekaaninen kestävyys heikentää kudosaaurioiden korjautumista ja repeytymien paranemista, johtaen epästabiilien ateroskelroottisten plakkien syntymiseen. Tämä tutkimus on ensimmäinen, joka osoittaa taliinin ja vinkuliinin tärkeän roolin ateroskeleroosin kehittämisessä.

Huolimatta siitä, että  $\alpha$ -helikaaliset proteiinit ovat yleisiä proteomissa ja ne epäilemättä ovat hyvin merkityksellisiä terveyden ylläpitämisessä ja sairauksien synnyssä, niiden rakenteellinen käyttäytyminen mekaanisen rasituksen alla tunnetaan huonosti. Tämän lisäksi on huomioitavaa, ettei sitä, miten solut tunnistavat mekaanisia signaaleja ja kuinka mekaaniset signaalit vaikuttavat solujen toimintaan tunneta hyvin. Tämän vuoksi tässä työssä tarkasteltiin taliini-proteiinin käyttäytymistä mekaanisen rasituksen alaisena. Käytimme monitieteistä lähestymistapaa, jossa yhdistettiin laskennallinen molekyyliidynamiikka (MD) ja suunnattu (engl. steered) molekyyliidynamiikka (SMD) kokeelliseen yhden molekyylin atomivoimamikroskopiitekniikkaan (smAFM) ja solujen avulla tehtäviin kokeisiin sekä biokemiallisiin analyyseihin.

Käyttämällä laskennallisen biologian avulla suunniteltuja mutaatioita, näytimme, että taliinin rod-domeenin aladomeenin R3 heikentäminen vähentää solun supistumiskykyä. Taliinin ja vinkuliinin havaittiin kertyvän fokaaliadheesioiksi kutsuttuihin solun hienorakenteisiin niin, että niiden sitoutuminen oli dynamisempaa ja lopputuloksena oli taliinirikkaita, mutta epävakaita adheesiorakenteita. Havaitimme myös yhteyden taliinin kestävyuden ja solun migraationopeuden välillä. Lisäksi huomasimme, että taliinin heikentäminen vaikuttaa siihen, että miten solu käyttää eri integriinityyppejä. Lyhennetyillä taliinin muodoilla tehdyt kokeet tukevat R3 aladomeenin mekanosensorista roolia. Kokonaisuutena tämä tutkimus osoitti, että taliinin rod-domeenin aladomeenin laskostumisen avautuminen on keskeinen solu-sidekudos adheesioiden rakentumisen säätelijä. Saimme myös lisää vahvistusta taliinin merkityksestä solun migraatiossa ja ympäristön tunnistamisessa.

Väitöskirjan osatyö Haining ym. osoitti, kuinka koko taliinin rod-domeeni on mahdollisesti mekaanisten signaalien kontrolloima. Havaitimme, että aladomeenin avautuminen tapahtuu jo 10-40 pN voiman ansiosta, joka on samaa luokkaa kuin mitä yksittäisiin proteiineihin kohdistuva voima on elävissä soluissa. Kokeet smAFM:n avulla yhdistettyinä SMD-simulaatioihin osoittivat, että taliiniin rod-domeenin aladomeenin mekanostabiilisuus vaihtelee. Näiden tulosten perusteella voidaan esittää mekanismi, jossa taliinin rod-domeeni toimii solussa mekanosensorina, ja välittää aladomeenin purkautumisen avulla eteenpäin signaaleja, joiden avulla solu voi reagoida ympäristönsä olosuhteisiin.

Väitöskirjan viimeisessä osatyössä tarkasteltiin taliinin ja  $\alpha$ -kateniinin käyttäytymistä mekaanisen rasituksen alla. SMD-simulaatiot osoittivat, että nämä proteiinit purkautuvat stabiilin 3-heliksiä käsittävän välimuodon kautta. Vaikka taliinin 5-heliksi aladomeenit ovat mekaanisesti kestäviä, on mahdollista, että

kolmen heliksin välimuoto syntyy aladomeenin aukipurkautumisen ansiosta. Heikompia 4-heliksi aladomeenien havaittiin purkautuvan helposti 3-heliksi-tilaan, mikä on niiden mekaanisesti vahvin olomuoto. Simulaatiotulokset varmistettiin kokeellisesti suunnittelemalla disulfididoksia, jotka estävät 3-heliksi-tilan purkautumisen. Näiden aukipurkautumisen välimuototilojen biologisen merkityksen tarkempi selvittäminen vaatii jatkotutkimuksia. Proteiinien mekaanisen aukilaskostumisen parempi ymmärtäminen on askel kohti kokonaisvaltaista mekanosignaaloinnin ymmärtämistä, mikä auttaa sekä solun normaalin toiminnan hahmottamisessa että sairauksien mekanismien selvittämisessä ja niiden hoitojen kehittämisessä.



# TABLE OF CONTENTS

1	Introduction .....	21
1.1	Scope of the work.....	22
2	Review of the Literature.....	23
2.1	Mechanosensitivity .....	23
2.2	Mechanotransduction.....	23
2.2.1	Mechanotransduction as a vital cellular function.....	24
2.2.2	Physical forces triggering mechanotransduction .....	25
2.2.3	Conversion of mechanical stimuli into chemical pathways .....	26
2.3	Mechanostability .....	26
2.3.1	Mechanostability of singular protein domains .....	26
2.3.2	Mechanostability of multi-domain systems .....	27
2.3.3	Orientation of the pulling force.....	28
2.3.4	Catch bonds .....	28
2.4	Mechanoactivation.....	29
2.5	Components in mechanotransduction .....	29
2.5.1	Extracellular structures.....	30
2.5.2	Cell membrane receptors .....	30
2.5.2.1	Non-integrin receptors in cell-ECM .....	30
2.5.2.2	Integrin receptors and focal adhesions .....	31
2.5.2.3	Dystroglycan-Sarcoglycan complexes .....	32
2.5.2.4	Cadherin receptors and desmosomes .....	32
2.5.2.5	Cadherin receptors and adherens junctions .....	33
2.5.2.6	Tight junctions .....	33
2.5.2.7	Other membrane structures and receptors .....	34
2.5.3	Cytoskeleton.....	34
2.5.3.1	Light filaments .....	35
2.5.3.2	Intermediate filaments .....	36
2.5.3.3	Microtubules.....	36
2.5.3.4	Membrane skeleton .....	36
2.5.4	Nucleus .....	37
2.5.5	Muscle fiber.....	37
2.6	Talin - focal adhesion adaptor protein .....	40

2.6.1	Structure and interactions .....	40
2.6.2	Functions in focal adhesion and focal adhesion maturation.....	42
2.6.3	Mechanosensitive properties of talin .....	43
2.7	Diseases of mechanotransduction: known villains and suspects .....	43
2.7.1	Cardiovascular diseases .....	44
2.7.2	Skeletal muscle disorders.....	45
2.7.3	Diseases of bone and cartilage .....	45
2.7.4	Cancer.....	46
2.7.5	Other diseases .....	46
2.7.6	Talin and disease.....	46
2.8	Mechanobiology and disease in graphical overview.....	48
3	Aims of the study .....	53
4	Materials and methods.....	54
4.1	Mechanobiology overview and graphical representation .....	54
4.2	Mechanical unfolding of proteins and investigation methods .....	54
4.2.1	Computational molecular dynamics methods (II, III, IV) .....	55
4.2.1.1	System and parameters .....	55
4.2.1.2	Classical molecular dynamics (MD).....	56
4.2.1.3	Steered molecular dynamics methods (SMD).....	57
4.2.2	Computational vs. experimental methods.....	58
4.3	Molecular and trajectory visualization (II, III, IV) .....	59
4.4	Mutation design and mutagenesis (II) .....	59
4.5	Methods of talin and vinculin expression in atherosclerotic plaque (I) .....	60
4.6	Biochemical analysis of talin R3 destabilized mutants (II).....	61
4.7	Cell experiments in analysis of talin R3 destabilized mutants (II) .....	61
4.8	Single molecule Atomic Force Microscopy (smAFM) in talin mechanical unfolding (III, IV).....	62
5	Results .....	63
5.1	Mechanobiology and disease summary (unpubl.).....	63
5.1.1	Levels of mechanotransduction effect.....	64
5.1.2	Causatives of mechanotransduction diseases .....	64
5.2	Talin and disease (I).....	65
5.3	Talin mutagenesis (II).....	68

5.4	Talin destabilization in SMD (II) .....	69
5.5	Talin destabilization in SMD simulation, biochemical analysis and <i>in vivo</i> (II).....	72
5.6	Talin rod and mechanosensitivity (III).....	73
5.7	Talin unfolds over a range of forces (III) .....	74
5.8	Unfolding of single talin rod bundles in SMD (III).....	75
5.9	3-helix intermediate in 5-helix subdomains (IV) .....	78
5.10	3-helix intermediate in 4-helix subdomains (IV) .....	80
5.11	3-helix intermediate in talin tandem subdomains (IV) .....	80
5.12	3-helix intermediate in constant force SMD .....	81
5.13	3-helix intermediate in smAFM.....	83
6	Discussion .....	84
6.1	Mechanotransduction components in disease .....	84
6.2	Talin and vinculin expression in atherosclerosis .....	85
6.3	Challenges of mechanotransduction disease research .....	87
6.4	Talin destabilization in computational and cell investigation.....	88
6.5	Talin as a fine mechanosensor.....	90
6.6	Fundamental principles of protein unfolding .....	91
6.7	Model of talin mechanobiology.....	94
6.8	Computational methods: advantages and limitations .....	99
7	Conclusions .....	101
8	References .....	103
9	Original publications.....	116

# LIST OF ABBREVIATIONS

A (ALA)	alanine
aa	amino acid
ABP	actin binding protein
ABS	actin binding site
AFM	atomic force microscopy
AJ	adherens junctions
BCAM	basal cell adhesion molecule
C (CYS)	cysteine
C-Src	protein tyrosine kinase
CH	calponin homology
COSMIC	Catalogue Of Somatic Mutations In Cancer
DCM	dilated cardiomyopathy
DD	dimerization domain
DES	desmosome
DGC	dystroglycan complex
DLC1	deleted in cancer 1
DNA	deoxyribonucleic acid
ECM	extracellular matter
EPCAM	epithelial cell adhesion molecule
FA	focal adhesion
FAK	focal adhesion kinase
FRAP	fluorescence recovery after photobleaching
fs	femtosecond
FX	focal complex
G (GLY)	glycine
GJ	gap junctions
GROMACS	gromingen machine for chemical simulation
HCM	hypertrophic cardiomyopathy
IBS	integrin binding site
ICAM	intracellular adhesion molecule

ICM	intracellular matter
IF	intermediate filament
Ig	immunoglobulin
Ig CAM	immunoglobulin superfamily of cell adhesion molecule
K	Kelvin
KANK	KN motif and ankyrin repeat domain-containing protein 1
KCl	calcium chloride
kJ	kilojoule
L (LEU)	leucine
LITA	left internal thoracic artery
MA	microarray analysis
MD	molecular dynamics
MEF	mouse embryonic fibroblast
MT	microtubules
MΦ	macrophage
NA	nascent adhesions
NCAM	neural cell adhesion molecule
NCBI	National Center for Biotechnology Information
nm	nanometer
ns	nanosecond
OMIM	Online Mendelian Inheritance in Men
PECAM	platelet endothelial cell adhesion molecule
pN	piconewton
ps	picosecond
Q (GLN)	glutamine
qRT-PCR	quantitative reverse transcription polymerase chain reaction
RCSB PDB	Protein Data Bank
RIAM	Rap1-GTP-interacting adaptor molecule
RMSD	root mean square deviation
S (SER)	serine
SEC	size exclusion chromatography
SGC	sarcoglycan complex
SLS	static-light scattering intensity
smAFM	single-molecule atomic force microscopy
SMD	steered molecular dynamics
T (THR)	threonine

TJ	tight junctions
TLN1	talín-1 gene
TLN2	talín-2 gene
TM	transmembrane
TVS	Tampere Vascular Study
V (VAL)	valine
VBS	vinculin binding site
VCAM	vascular cell adhesion molecule
VCL	vinculin gene
VMD	visual molecular dynamics
WASP	Wiscot-Aldrich syndrome protein
WT	wild-type

# LIST OF ORIGINAL PUBLICATIONS

This thesis is based in the original publications listed below. These publications are referred in the text by Roman numerals.

- I            **von Essen M\***, Rahikainen R\*, Oksala N, Raitoharju E, Seppälä I, Mennander AA, Sioris T, Kholová I, Klopp NN, Illig T, Karhunen PJ, Kähönen M, Lehtimäki T and Hytönen VP. Talin and vinculin are downregulated in atherosclerotic plaque; Tampere Vascular Study. *Atherosclerosis* 255 (2016): 43-53. doi:[10.1016/j.atherosclerosis.2016.10.031](https://doi.org/10.1016/j.atherosclerosis.2016.10.031)
- II            Rahikainen R\*, **von Essen M\***, Schäfer M, Qi LS, Azizi L, Kelly C, Ihalainen TO, Wehrle-Haller B, Bastmeyer M, Huang C and Hytönen VP. Mechanical stability of talin rod controls cell migration and substrate sensing. *Scientific Reports* (2017). doi:[10.1038/s41598-017-03335-2](https://doi.org/10.1038/s41598-017-03335-2)
- III           Haining AWM, **von Essen M**, Attwood SJ, Hytönen VP and Del Río Hernández A. All Subdomains of the Talin Rod Are Mechanically Vulnerable and May Contribute To Cellular Mechanosensing. *ACS Nano* (2016). doi:[10.1021/acsnano.6b01658](https://doi.org/10.1021/acsnano.6b01658)
- IV           Mykuliak V\*, Haining AWM\*, **von Essen M\***, Del Río Hernández A and Hytönen VP. Mechanical unfolding reveals stable 3-helix intermediates in talin and  $\alpha$ -catenin. *PLOS Computational Biology* 14(4): e1006126. <https://doi.org/10.1371/journal.pcbi.1006126> .

\* = equal contribution

# RESPONSIBILITIES OF MAGDALÉNA VON ESSEN IN THE ARTICLES COMPRISING THIS THESIS

- Article I: I contributed to the data analysis and preparation of figures. I was responsible for the writing of the original manuscript. The shared first author in this manuscript, Rolle Rahikainen, contributed to the histology, image analysis and manuscript writing.
- Article II: I was responsible for the design of mutations destabilizing the talin R3 domain and computational investigation of the effect of the mutations. The panel of tested mutants was designed together with Rolle Rahikainen. I contributed to the writing of the manuscript and preparation of the figures.
- Article III: I was responsible for the computational biology section of this work. I contributed to the writing of the manuscript.
- Article IV: I was mainly responsible for the formulation of the hypothesis and for the planning of the practical implementation in experiments. I contributed to the writing of the manuscript and interpretation of the results.

# 1 INTRODUCTION

All living organisms are continuously exposed to mechanical forces exerted on them by their surroundings. The ability of organisms, and more importantly, the ability of individual cells to receive mechanical signals and respond to the stimuli, is fundamental to life. The mechanical forces within biological systems are manifold and occur in many forms such as compression, stretch or shear.

The mechanical force caused by the gravity and weight on the bone structure is the most notorious example of the mechanical compression. It is well known, that the amount of mechanical stress exerted on the human bones modulates the structure of the trabecular sponge of large bones. The osteocytes of the spongy bone are found in a lattice-like network of matrix spikes. This matrix may appear to be a random network, but each spike forms along lines of stress to provide strength to the bone<sup>1</sup>. Any change in the mechanical stimuli reorganizes this network and leads to compromised ability to withstand the applied stress. For example, lack of mechanical stimuli has been recognized to increase bone resorption and possibly decrease bone formation leading to loss of bone mass and bone fragility. In particular, astronauts exposed to low gravity environment for prolonged periods of time lose up to 5% of bone mass each month when in space<sup>2</sup>. External mechanical force exposure as a result of exercise was also found beneficial in acceleration of bone formation and healing after fracture<sup>3</sup> or surgery<sup>4</sup>.

Another obvious example of mechanical force acting within living organism is the shear stress of the blood suspension and the hydrostatic pressure of the blood fluid on vessel walls. The shear of the cells and other blood components inside the vessels is an example of the constant, repeating pulsing exposure of cells and tissues to mechanical impulses from the outside environment<sup>5</sup>. The magnitude of the mechanical impulse affected by the blood pressure and modified by viscoelastic properties of the blood fluid may change the ability of the inner vessel lining to withstand the shear stress. This may mitigate the healing processes in the inner vessel injury and progress the corrosion of the blood vessels. Such impacts are especially important at the vessel branch points where slow tissue recovery may lead to a plaque formation and progress of vascular diseases<sup>6,7</sup>.

Also the working of a muscle cell in skeletal, heart and smooth muscle is an example of mechanical stretch and compression, as well as an example of force generation by the cells' actin-myosin complex<sup>8</sup>. Furthermore, the transduction of mechanical impulses and mechanosensing is an essential principle in hearing, skin sensitivity or touch<sup>9,10</sup>.

Overall, mechanosensing and response to the stimuli is vital to cellular development and differentiation. Moreover, mechanotransduction is crucial for the maintenance of homeostasis. When disturbed it may lead to the development of pathological conditions. The mechanical signals are detected by specialized cell surface receptors or stress-sensitive ion-channels and propagated into the cell to be converted into biochemical signaling cascades. These biochemical pathways regulate vital processes like migration, proliferation or differentiation in health and disease<sup>8,11,12,13</sup>.

## 1.1 Scope of the work

This work focuses on the mechanosensitive protein, talin, located at the intracellular side of the cell membrane<sup>14,15</sup>. It facilitates the connection between the extracellular matter (ECM) through the actin cytoskeleton and the cell's nucleus<sup>16</sup>. Talin is a mechanosensor and mechanotransducer protein, which changes its conformation depending on the acting mechanical force<sup>17</sup>. Despite intensive research of talin mechanobiology, the fundamental principles of its mechanosensitivity and mechanoregulation, and its involvement in disease remain unclear.

In addition, the work provides a mechanobiology overview of current knowledge in the field combining the cellular mechanotransduction pathways, protein structural information and interactions, and the connection to disease development.

## 2 REVIEW OF THE LITERATURE

In the following text, the current knowledge of mechanotransduction and mechanoregulation in health and disease is reviewed. First, terminology and fundamental characteristics in mechanobiology are introduced, followed by the description of cellular components in mechanotransduction. Finally, a review of disease associated mechanosensitive proteins and linked diseases are provided.

Mechanobiology is specified as a study of mechanisms and processes by which mechanical forces motivate molecular response and regulate cell shape and function. The major focus of mechanobiology lies on how physical forces contribute to development, cell differentiation, physiology and disease. The major challenge in the field is the investigation and interpretation of mechanotransduction; i.e. the mechanism by which cells sense and respond to mechanical signals<sup>18</sup>.

### 2.1 Mechanosensitivity

Mechanosensitivity is a term expressing a specific response to mechanical stimulation. It may be described as a change of protein conformation for example as a result of acting mechanical force leading to a change of protein-ligand binding<sup>17</sup>. Mechanosensitivity is common to a wide variety of cells in many different organisms. Importantly, mechanical stress can modulate physiological processes at the molecular, cellular, as well as systemic level.

### 2.2 Mechanotransduction

Mechanotransduction is the mechanism by which cells sense and respond to mechanical stimuli. In other words, mechanotransduction refers to the ability to sense the mechanical stimuli and to translate the signal into chemical cues and biological processes. These processes then lead to a certain cell response. On the

whole, mechanotransduction investigates the activities of individual molecules in isolation, and within living cells, tissues, organs and whole organisms<sup>19</sup>.

There are several subcellular structures and protein complexes within cells that possess mechanotransduction properties. For instance, mechanosensitive ion-channels react to lateral stretching leading to an alteration in the ion permeability<sup>20</sup>. Also G protein-coupled receptors probably undergo activation in the lipid membrane by mechanical forces<sup>21</sup>. Recently, great attention has been given to mechanotransduction at the cell-cell and cell-ECM adhesions. For example, focal adhesions (FA)<sup>11</sup>, cadherin complexes<sup>22</sup>, dystroglycan-sarcoglycan complexes (DGC-SGC)<sup>23</sup>, gap and tight junctions (GJ and TJ)<sup>24</sup> and many other subcellular cytoskeletal and nuclear structures play important roles in the mechanotransduction. The general components of mechanotransduction are visualized below in **Figure 1**.

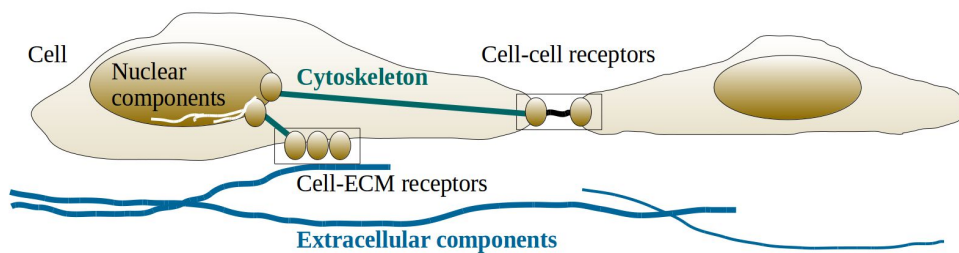


**Figure 1. Components in mechanotransduction.** Mechanical impulses are transferred from the extracellular space through the membrane receptors and cytoskeleton towards the nucleus. In the nucleus, mechanical forces affecting the skeletal structures may impact the DNA packing and protein expression.

## 2.2.1 Mechanotransduction as a vital cellular function

Mechanical forces, their sensation and transduction as well as the cellular response to those impulses are vital for the cell's survival, differentiation, development and vitality. The molecular and subcellular systems involved in the mechanosensing and mechanotransduction control and affect also the motility and the surface adhesion, the ability to proliferate and drive the cells' fitness. It has been mentioned, that mechanotransduction and mechanosensitivity is fundamental to life. We may also mention that certain complexes may possess several fundamental roles. Moreover, certain vital process may be ensured by a number of subcellular structures. And

finally, some protein complexes are abundant among organisms and tissue types, whereas other subcellular structures are highly specific to a particular cell type.

For example, FA complexes are vital for the development and differentiation starting at the gastrulation stages of embryogenesis<sup>12,25</sup>. FAs are also important for the cell adhesion to substrates and for the cell's locomotion<sup>26</sup>. Even a small change in the mechanosensitivity of one particular mechanosensor may lead in complete misinterpretation of the cell's surroundings leading to early cell death<sup>26</sup>.

While numerous molecules and subcellular structures have been shown to mediate force sensation and mechanical conversion to biological response, the mechanisms of how the whole cell interprets such molecular scale information and how it orchestrates a physiologically relevant response in the complexity of our whole bodies remains unclear<sup>19</sup>.

## 2.2.2 Physical forces triggering mechanotransduction

All the living cells are constantly exposed to mechanical forces with fundamental roles in the biological systems. The cell types, their tissue environment and functions may vary greatly. Therefore the scale of force magnitudes the cells withstand or require for normal function may also differ dramatically. The normal physical forces range from pure entropic elasticity regime (elastin) and few piconewtons (pN) (spectrin or talin), to over 300 pN typical for certain immunoglobulin domains and as high as 500 pN measured for Ig-like  $\beta$ -sheet fold of scaffoldins<sup>27,28,29,30,31,32</sup>.

For example physical forces acting on integrin molecule in the FA complexes are on the low range of few pN<sup>33</sup>. Integrin binding protein, talin, unfolds under the force range from 5 to 40 pN, depending on the subdomain<sup>29</sup>. On the other hand, the titin Ig modules I27 and I28 unfold under high force regime of 150 and 300 pN in atomic force microscopy (AFM) experiments, respectively<sup>34</sup>. Yet, filamin Ig domains 20 and 21 unfold with force between 15 and 37 pN measured by optical tweezers. However, the force needed for filamin activation and ligand binding is as low as 5 pN<sup>28</sup>. Titin kinase mechanosensitive domain unfolds between 30 to 50 pN depending on the experimental temperature<sup>35</sup>. It should be noted that the unfolding force magnitudes are pulling rate dependent. Therefore comparisons of absolute forces between methodologies should be assessed cautiously.

### 2.2.3 Conversion of mechanical stimuli into chemical pathways

Physical forces are involved in the regulation of many physiological processes such as vascular remodeling, maturation of bone<sup>1</sup> and cartilage<sup>36</sup>, or development of the heart<sup>37</sup>. In order to steer the complex developmental processes, the acting mechanical forces need to be interpreted by the cells; i.e. the mechanical stimuli need to be translated into chemical cues and pathways.

For example, it has been reported that compressive stress restricts the intercellular space surrounding epithelial cells and changes ligand availability as a result of the alteration of the cellular space. This in detail triggers cellular signaling via autocrine binding of epidermal growth factor ligands to the epidermal growth factor receptor<sup>38</sup>. Another example of stimuli conversion is the mechanical stretch activation of protein tyrosine kinase (c-Src). The mechanical stretch of the cytoskeleton increases binding of c-Src to the actin filament-associated protein. It was shown, that the cytoskeletal structure not only transmits physical forces intracellularly but can also convert them into biochemical reactions for signaling via specific binding sites and protein-protein interactions<sup>39</sup>.

## 2.3 Mechanostability

Mechanosensitivity and mechanotransduction processes are at the molecular level governed by mechanically active proteins. These mechanosensors undergo conformational change in response to acting mechanical force. Such conformational change modulates the protein function and the protein properties. Because of many diverse protein functions and environments they are exposed to, these mechanosensors show enormous ability to withstand a wide range of mechanical forces, i.e. mechanostability.

### 2.3.1 Mechanostability of singular protein domains

The mechanostability is usually assigned to the architecture of the protein and its secondary structure. Mechanostability is directly proportional to the number of hydrogen bonds of the contacting amino acids at the domain fastening ends<sup>32,40</sup>. It has been shown, experimentally and in simulation that the  $\beta$ -sheet sandwich fold is more stable as compared to the  $\alpha$ -helical fold. The largest mechanical stability has been assigned to Ig-like domains of cohesin I modules of scaffoldin proteins. The

great mechanostability is attributed to two shear mechanical clamps in tandem<sup>32</sup>. Also, cohesin  $\beta$ -sheets are longer compared to the Ig domain  $\beta$ -sheets in titin, suggesting the sheet length and number of hydrogen bonds contributes to the resulting unfolding force magnitude. The mechanostability of the cohesin I module is as high as 480 pN, compared to titin I32 at 298 pN and titin I27 domain at 210 pN<sup>32,41</sup>. Visualization of  $\alpha$ -helical and  $\beta$ -sheet secondary structures with different mechanostability is available in **Figure 2**.

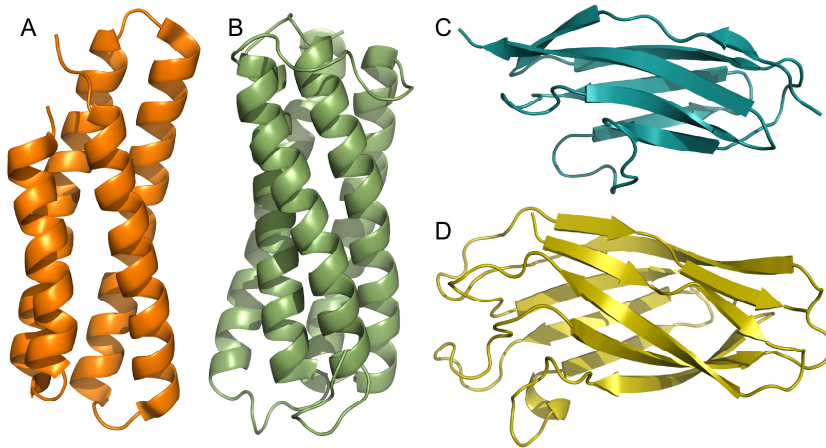


**Figure 2. Mechanostability and protein secondary structure.**  $\alpha$ -helix structure of talin rod 4-helix R3 subdomain (A) and a 5-helix R9 subdomain (B) show difference in mechanical stability due to number of helices and presence of hydrophobic core in R9.  $\beta$ -sheet fold of titin (C) and scaffoldin show difference in mechanical stability due to length of interacting  $\beta$ -sheets. Protein Data Bank (PDB) ids: A) 2L7A, B) 2KBB, C) 1TIU, D) 1OH<sup>42</sup>.

Also other mechanisms have been shown to contribute to the mechanical stability of proteins. For example, hydrophobic core detected in talin rod domains or in the fibronectin fold of tenascin increase the resistance to mechanical stretching<sup>43</sup>. Helix-rich proteins show decreasing mechanical stability depending on the helix content<sup>44</sup>. Also tertiary- and quaternary-structure-based elasticities (see paragraph 2.3.2) contribute to the final protein mechanosensitivity.

### 2.3.2 Mechanostability of multi-domain systems

The secondary protein structure is the main characteristics dictating the mechanical stability of mechanosensors. Furthermore, multi-domain mechanisms may modulate the protein stability under mechanical load.

Tertiary-structure-based elasticity of ankyrin is one example of such additional stability modulation. Here, the ankyrin amphipathic  $\alpha$ -helices form a super-helical spiral acting as a spring<sup>45</sup>. Quaternary-structure-based elasticity, described as stabilization by dimerization or oligomerization of protein structures has also been identified<sup>46</sup>. The additional mechanostability is usually gained from inter-domain contacts where several domains form essential stable bonds contributing to the protein mechanostability<sup>40</sup>. In detail, Sikora et al. identified these inter-domain contacts as tensile clamps, tensile clamps from a backbone knot-loop, shear between  $\alpha$ -helices, and an intra-domain shear between  $\beta$ -sheets stabilized by another domain<sup>40</sup>.

### 2.3.3 Orientation of the pulling force

The orientation of the pulling force may also have an impact on the resulting protein unfolding force. The works by Toofanny et al. and West et al. have shown that the pulling direction is highly influential to the force magnitude, unfolding time or affecting the unfolding trajectory itself, with modulation in the formation of unfolding intermediates<sup>47,48</sup>.

Also, the orientation of the pulling force in respect to the domain affects the unfolding mechanisms. Usually the unzipping mechanism shows lower force magnitude compared to shearing force<sup>31,40</sup>.

### 2.3.4 Catch bonds

The mechanical stability of protein structures may also be increased by a special type of noncovalent interactions known as catch bonds. These interactions become counterintuitively stronger under mechanical load, they dissociate slowly compared to normal noncovalent bonds and increase the mechanostability of the protein structure. A strong evidence of such bond has been described in mechanosensitive bacterial flagellar motor enabling the swimming motion of motile bacteria. In more detail, higher mechanical load exerted by viscous environment was found to increase the function of the protein motor suggesting that the protein mechanical stability was increased with increased stimuli<sup>49</sup>.

## 2.4 Mechanoactivation

The mechanical force acting on a mechanically susceptible protein leads to its stretching, and often to a change in its function or activity. Evidence from *in vivo* studies suggests that tension on fibronectin triggers domain unfolding and exposes cryptic binding sites. This allows ligand binding essential in the ECM assembly<sup>50</sup>. Similar activation mechanism has been recognized for the FA protein, talin. Talin, especially its mechanosensitive rod, undergoes force-induced conformational change leading to vinculin binding. The vinculin binding consequently stabilizes and strengthens the focal complexes into FAs<sup>17,51</sup>.

Another interesting example is the oxidation of vascular cell adhesion molecule (VCAM), which might affect the mechanical properties of the protein<sup>52</sup>. The modulation of the oxidation/reduction potential at the cell surface may alter the response of the cell to applied force. Alternatively, applied force could modulate the response of the protein to a variable oxidation potential. Such knowledge makes VCAM an interesting target in the atherosclerosis studies and the works focusing on the impact of fluid shear and blood pressure on the vascular injury.

## 2.5 Components in mechanotransduction

In the previous paragraphs, the complexity of the mechanotransduction mechanism is sketched. The great variety of mechanical force types and magnitudes needs to be sensed, transferred and interpreted by cells to produce an appropriate response. This requires corresponding complexity of mechanosensitive complexes and proteins. In the following, these are described in the terms of the force sensing and transduction from the extracellular space or between cells, through the cellular membrane and cytoskeletal structures towards the nucleus. It is also important to note, that some of these complexes and protein structures are abundant among cells, whereas others are highly tissue specific, posing yet another challenge in the understanding of the mechanotransduction principles.

Based on the cellular location and function in mechanocommunication, these complexes and proteins may be further classified into following groups: the structures of the extracellular space, complexes providing for the cell-ECM communication, complexes of the cell-cell interaction, stress-bearing proteins of the cytoskeleton, and the mechanosensitive structures of the nuclear membrane and the nucleus.

## 2.5.1 Extracellular structures

Mechanosensing is a continuous process in living cells and tissues including the assessment of the mechanics of the ECM. ECM is a three-dimensional scaffold and is often assessed through membrane bound integrin adhesions. The ECM, a fundamental matrix for the tissues homeostasis, is formed and maintained by the cells of the appropriate tissue. It is also remodeled and adapted during development and repaired as a response to injury or disease<sup>53</sup>. Vice versa, the character of the ECM is affecting the cell motility, differentiation, growth and even survival or death<sup>54,55</sup>.

Approximately 300 proteins have been identified to compose the extracellular space<sup>55</sup>; including 43 collagen units, 36 proteoglycans and approx. 200 glycoproteins. These are usually insoluble large proteins consisting of repeating structural units and accompanied by ECM-binding growth factors and other ECM-associated proteins.

Collagens provide for strength in all forms of ECMs including tendons, bones and cartilage, they are found in capsules around organs or in basement membranes<sup>56,57</sup>. Proteoglycans, such as perlecan, are spread among the collagen fibrils and provide for space-filling<sup>58</sup>. Finally, glycoproteins provide for interactions allowing ECM assembly, promoting cell adhesion and cell signaling (laminins<sup>57</sup>, fibronectins<sup>59</sup>, tenascins<sup>60</sup>, netrin<sup>61</sup>, von Willebrand factor, fibrinogen, fibrillins<sup>62</sup>, etc.).

## 2.5.2 Cell membrane receptors

The mechanosensing process of force detection, transfer and interpretation continues through cellular membranes towards the cells' cytoskeleton. Force sensitive membrane-bound receptors are crucial structures and complexes in this step of mechanotransduction responsible for the cell-ECM force sensing and cell-cell communication.

### 2.5.2.1 Non-integrin receptors in cell-ECM

There are two main groups of the cell-ECM receptors; nonintegrin receptors and integrins. Nonintegrin receptors contain the proteoglycan receptors (syndecan<sup>63</sup>, CD44 and trombospondin), and other receptor types such as CD36, and laminin

binding proteins<sup>64</sup>. It was shown, that for example CD44-ankyrin binding is involved in lymphocyte adhesion<sup>65</sup>.

### 2.5.2.2 Integrin receptors and focal adhesions

Focal adhesions (FAs) comprise of membrane bound integrins represented by a large group of glycoprotein family proteins (**Figure 3**). Integrins bind mainly to ECM fibronectin, laminin, or collagen<sup>66</sup>. Some integrins also play important roles in heterotypic cell-cell adhesion<sup>67</sup>. Such interaction can be found in leukocyte attraction through the integrin-Ig receptor adhesion (ICAM, VCAM).

The whole integrin mediated adhesion starts with the formation of nascent adhesions, which develop to focal complexes (FXs). FXs attract other scaffolding components and adaptor proteins together with accumulation of integrin clusters, which progresses to the formation of mature FAs. FAs comprise a wide variety of cytoskeletal, signaling and membrane-associated adaptor proteins, such as talin, vinculin, focal adhesion kinase (FAK), KANK or RIAM<sup>11,54,66,68</sup>.

#### Focal adhesion – Integrin-mediated

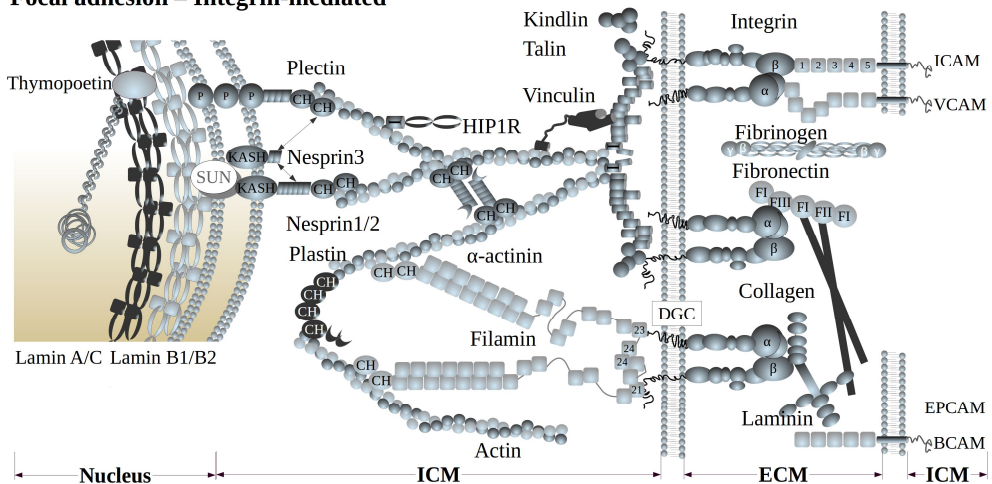


**Figure 3. Integrin receptors and focal adhesion (FA).** Integrin mediated cell-ECM and heterotypic cell-cell adhesion interconnecting the ECM to the cell's nucleus.

### 2.5.2.3 Dystroglycan-Sarcoglycan complexes

FAs are very complex structures that may attract additional membrane structures depending on the ECM. Highly abundant dystroglycan-sarcoglycan complexes (DGC-SGC) are present in mature FAs and directly bind ECM laminin or agrin to cytoskeletal dystrophin, utrophin or  $\alpha$ -actinin<sup>23</sup> (**Figure 4**). In addition, sarcospan, dystrobrevins and syntrophin compose the dystrophin-associated protein complex ensuring the membrane stability and force transduction<sup>69</sup>.

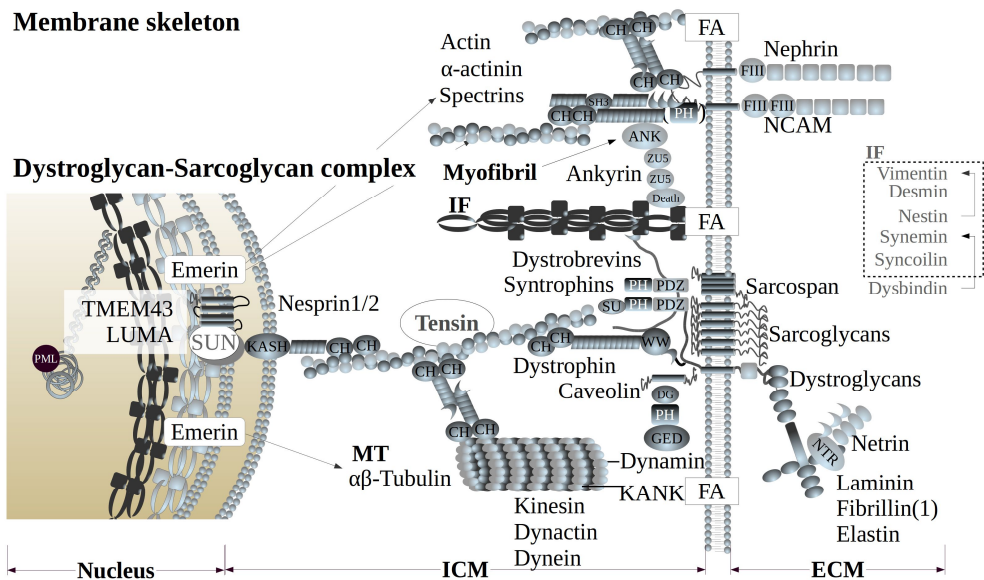


**Figure 4. Dystroglycan-Sarcoglycan complex (DGC-SGC) and membrane skeleton components.** Complex interlinks between cellular components creating a mechanical connection between ECM to the cell's nucleus.

### 2.5.2.4 Cadherin receptors and desmosomes

Desmosomes (DES) are adhesive intercellular junctions responsible for the intracellular communication through a connection of intermediate filament networks between cells (**Figure 5**). DESs are formed by desmosomal cadherins (desmogleins and desmocollins)<sup>70</sup>, armadillo proteins (plakoglobin and plakophilins) and plakins (desmoplakins, plectins and cell envelope proteins)<sup>71</sup>.

## Gap and Tight Junctions

### Desmosome

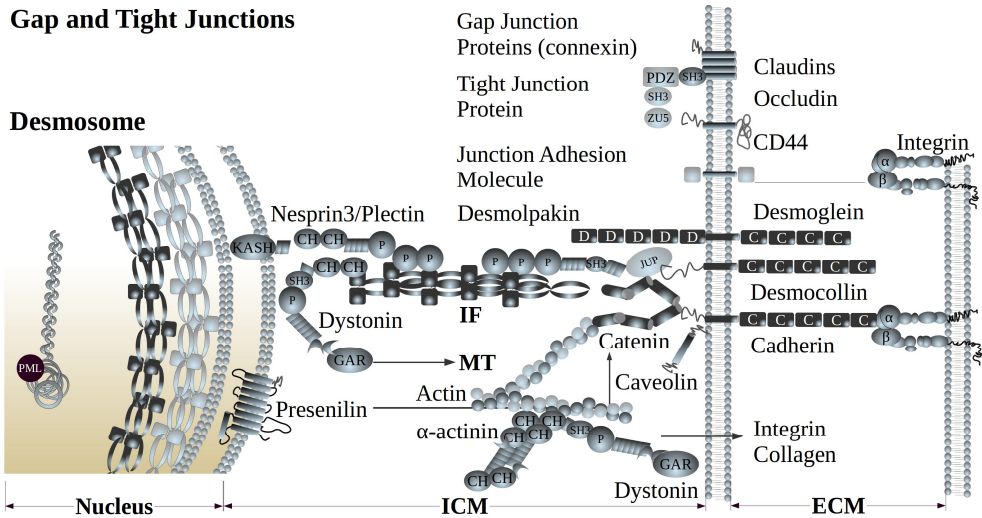


**Figure 5. Cadherin receptors in desmosomes (DES), gap (GJ) and tight junctions (TJ) in cellular adhesion.** Complex interactions of cellular components interlinking ECM and cells with the nucleus and cytoskeletal components.

### 2.5.2.5 Cadherin receptors and adherens junctions

Adherens junctions (AJ) are cadherin-catenin complexes centrally involved in cell-cell contacts (**Figure 5**). Various cadherins are important for myocyte-fibroblast and fibroblast-endothelial cell communication<sup>22</sup>. Classical cadherins (E-cadherin) form dimers and clusters, which provide intercellular interaction through their extracellular domains and intracellular actin binding<sup>67</sup>. Classical cadherins also directly bind cytoplasmic proteins of the catenin family, which locally organizes the actin cytoskeleton. The AJ assembly further leads to organization of tight junctions<sup>72</sup>.

### 2.5.2.6 Tight junctions

Tight junctions (TJ) form the continuous intercellular barrier between epithelial cells. Over 40 proteins have been identified to comprise the TJ; for example the proteins of the claudin family (occludin and tricellulin) (**Figure 5**). Among these, transmembrane claudins are the most critical for the tissue separation and moving of the solute through epithelium. In addition, cytoskeletal connectors (ZO proteins) interlink the AJ and TJ to the actin cytoskeleton<sup>24,72</sup>.

### 2.5.2.7 Other membrane structures and receptors

Gap junctions (GJ) are important for the cell-cell communication in cardiac cells through connexins (**Figure 5**). GJ allow for passive non-specific diffusion of molecules smaller than 1000 Da through the gap junction channel<sup>73</sup>.

G-protein-coupled receptors compose of seven transmembrane (TM)  $\alpha$ -helices forming a channel between ECM and intracellular space. The receptor activation involves extracellular ligand binding leading to a conformational change in the TM core. This causes a conformational change in the ligand intracellular interface and activated or deactivated ligand binding intracellularly<sup>74</sup>.

Immunoglobulin superfamily of cell adhesion molecules (Ig CAMs) have also been implicated in aspects of signal mechanotransduction<sup>66,67</sup>. Ig CAMs comprise a diverse group of adhesive receptors involved in the axon guidance and establishment of neural connections (NCAM, netrin). Also platelet endothelial cell adhesion molecules (PECAMs), vascular cell adhesion proteins (VCAMs) and intercellular adhesion molecules (ICAMs) are included in the Ig CAM receptor group<sup>66</sup>.

Selectins L-, E- and P-selectin are lectin-like adhesion receptors mediating heterotypic cell-cell interactions. P-selectins are, for example, found in endothelium and blood cells crucial in the leukocyte adhesion during inflammation<sup>66</sup>. Finally, ankyrin complexes link various TM proteins, such as CD44, to actin cytoskeleton mainly through the interaction with spectrin (i.e. fodrin)<sup>65</sup>.

## 2.5.3 Cytoskeleton

The cytoskeleton is a network of filaments and tubules in the cell's cytoplasm (**Figure 3 - Figure 5**). The cytoskeleton supports cells' shape, organizes its organelles and participates in the molecule transport. The cellular cytoskeleton has also crucial roles in the transfer of mechanical signals towards the cell's nucleus and conversion of the mechanical signal to biochemical signaling cascades. The cytoskeleton consists of three types of filaments; the light filaments (microfilaments), the intermediate filaments, and the microtubules<sup>77</sup>.

While each type of the cytoskeletal network has its own constituents and characteristics, the three networks rely upon one another. A growing number of proteins called cytolinkers has been identified interconnecting the cytoskeleton and binding it to transmembrane components<sup>78,79</sup>. For example, the plakin proteins such as plectin contain domains that bind to microfilaments (via calponin

homology domain), intermediate filaments (via plakin repeats) and microtubules (via Gas2-related domain)<sup>80</sup>. By crosslinking the cytoskeletal network and connecting it to the junctional complexes, plakins play vital roles in the cellular development and the maintenance of tissue homeostasis<sup>80</sup>. Dystrophin, sharing functionally similar domains to cytolinkers, links the cytoskeletal components to the dystroglycan complex<sup>81</sup>.

### 2.5.3.1 Light filaments

The light filaments (microfilaments, actin filaments) consist mainly of actin protein. In detail, there are two actin forms, i.e. the monomeric G-actin, and the filamentous F-actin<sup>82</sup>. The final superstructure is formed by two actin strands twisting into a spiral of the filament approx. 7 nm thick.

Light filaments transport molecules to organelles, aid cell motility and adhesion to surfaces. They are also vital in embryonic morphogenesis, immune surveillance and angiogenesis, as well as tissue remodeling and regeneration. These microfilaments mediate the formation of filopodia, stress fibers and FAs. The actin filaments are a part of the muscle cells and together with myosin chains form the contractile apparatus of the muscle unit<sup>77,83</sup>.

The dynamic transitions of the actin filaments are regulated by a variety of signaling, scaffolding and actin-binding proteins (ABPs). For example, the stress activated Rho-family GTPases regulate the actin-cytoskeleton dynamics and assembly<sup>84</sup>. ABPs, such as cofilin-, WASP, gelsolin- or calponin-homology proteins are essential for actin filament turnover<sup>83</sup>. In addition, formins mediate the formation of unbranched actin filaments among the nucleation and elongation roles<sup>85</sup>.

Spectrins, including spectrin, dystrophin and  $\alpha$ -actinin, are the most important actin crosslinking proteins<sup>86</sup> functioning as molecular scaffolds. These molecular scaffolds often connect the actin network to the membrane proteins ankyrin, laminin or dystroglycan<sup>23,65,75,86</sup>.

There are also other proteins linking the actin cytoskeleton to the membrane ensuring the tight spatial and temporal coordination between the membrane and the light filaments. These proteins represent a rather diverse group, however they are united with the presence of the membrane binding BAR domain<sup>83</sup>. The BAR domain consists of a dimer of two helical bundles with a positively charged membrane binding interface<sup>87</sup>. There are three groups of the BAR proteins with slightly different conformation of the dimer domain (N-BAR, I-BAR, F-BAR) all

of which are responsible for maintenance and formation of the membrane curvature through the membrane-BAR-actin or BAR-BAR interaction<sup>83</sup>.

### 2.5.3.2 Intermediate filaments

The intermediate filaments (IF) with diameter 8-12 nm are formed by a variety of cytoplasmic proteins, such as vimentin, desmin, nestin, synemin, syncoilin, dysbindin or keratin. In addition, lamins are found in the nucleus where they support the nuclear envelope<sup>88</sup>. The main function of the IF is the maintenance of the cell's shape and to provide structural support<sup>77</sup>. Furthermore, in conjunction with cell-cell junctions, the IF system generates transcellular network of both high rigidity and flexibility connecting individual cells into tissues. In comparison with the light filaments and microtubules, IFs often form mixed dimers with proteins from the same assembly group<sup>88</sup>.

### 2.5.3.3 Microtubules

The microtubules (MT) are stiff hollow tubes (23 nm) formed by  $\alpha$ - and  $\beta$ -tubulin subunits tightly bound by noncovalent bonds. The MTs form flagella, cilia and, most importantly, the centrosome. The centrosome is the center of MTs important for the formation of the mitotic spindle during cell division. MTs are also crucial in the molecule and nutrient transportation within the cell, and the position and organization of organelles<sup>77,78</sup>.

### 2.5.3.4 Membrane skeleton

Spectrin-based membrane skeleton was first identified at the inner site of the erythrocyte membrane, however it is considered nearly ubiquitous<sup>75</sup>. Spectrin tetramers form filamentous network, which is cross-linking membrane receptors (ankyrin and protein 4.1) with actin filaments (**Figure 4**). The main function of such membrane skeleton is the support of the cell shape, adhesion and maintenance of the membrane integrity, elasticity and stability<sup>76</sup>.

## 2.5.4 Nucleus

One of the two types of the IF systems is located at the inner site of the nuclear membrane<sup>88</sup>. The nuclear IF system composes of lamins, which together with a number of nuclear transmembrane and chromatin binding proteins constitute the nuclear lamina. The lamina is engaged in the organization of the heterochromatin and provides a platform for the assembly of various nuclear protein complexes<sup>89</sup>. These include emerin, the lamina-associated proteins laminB and laminA/C, and even the signaling molecules that interact with transcription factors.

In addition, the lamina connects through the SUN domain to microtubules, light and intermediate filaments through the nesprin proteins<sup>90,91</sup>. Both of the cytoskeleton and the nuclear lamina contribute significantly to the dynamics and structural integrity of individual cells and cells within tissues.

## 2.5.5 Muscle fiber

The muscle is composed of a heterogeneous collection of muscle fibers, which allow for remarkable plasticity and a variety of functions of the muscle fiber. The habitual level of contractile activity (endurance exercise training), loading state (resistance exercise training), the macronutrient supply or the environmental impacts are an example of the very diverse stimuli and conditions the muscle fiber can withstand<sup>92</sup>. Furthermore, the muscle is a dynamic system, which may adapt to an altering demand by a change in the fiber composition<sup>93</sup>. The muscle fibers are formed by sarcomeres as the individual structural and functional muscle units within the muscle cell; i.e. myocyte (**Figure 6**). Within each sarcomere, the myofibrillar proteins form the thick filament (6 myosin polypeptide chains) and the thin filament (actin with regulatory proteins troponin and tropomyosin)<sup>94</sup>. The interactions between these two filaments allow for the muscle contractions.

## Muscle Fiber Mechanobiology

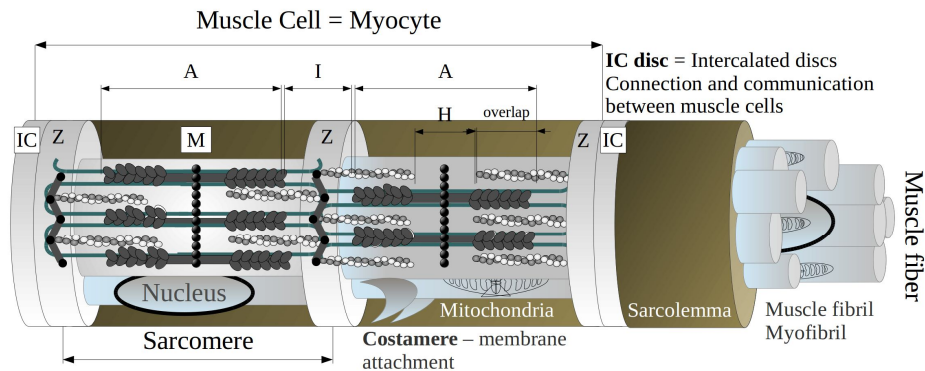


**Figure 6. Schematics of the muscle fiber components and compartments.** **A-band:** covers the myosin thick filament area within the sarcomere, **I-band:** covers the space between sarcomeres without the thick filament area, **IC-discs:** intercalated discs providing connection and communication between muscle cells, **H-line:** central part of costamere including the M-line and excluding the thin actin filaments, **M-band:** center line of costamere formed by myomesin, **Z-disc:** interconnecting sarcomeres inside muscle cell, formed by  $\alpha$ -actinin band and a complex of a variety of other proteins, **overlap:** the overlap of the acto-myosin complex is reduced during the sarcomere extension, **Sarcomere:** basic muscle cell contractile unit, a myocyte may contain two or more sarcomeres, **Sarcolemma:** muscle cell membrane, **Costamere:** protein complexes forming the attachments and adhesions to the muscle membrane. Actin: *white-gray spiral*, myosin: *dark gray domains*, titin: *green line*,  $\alpha$ -actinin: *zig-zag structure* in the Z-line.

The muscle fiber is further organized based on its histological character into specific bands; the M-band serves as a hub for protein signaling and protein turnover, the I-band and Z-disc contain the stretch-sensitive structures. Individual sarcomeres are stabilized by elastic titin filaments, which overlap at the Z-disc and M-band. Titin and its overlaps form a continuous elastic filament within the muscle fiber<sup>95</sup>.

Costameres are the muscle membrane associated protein complexes, which are transducing the mechanical forces between the nucleus and ECM of the basal lamina<sup>96</sup>. Costameres are interconnected by dystrophins, spectrins and other associated proteins at the muscle membrane to the ECM collagen, fibronectin or laminin. Also vinculin, sarcoglycan, desmin and other proteins have been found important for the costamere function in the sarcomere assembly<sup>95</sup>. The protein composition of the muscle fiber and myocyte is available in **Figure 7**.

# Muscle Cell Mechanobiology

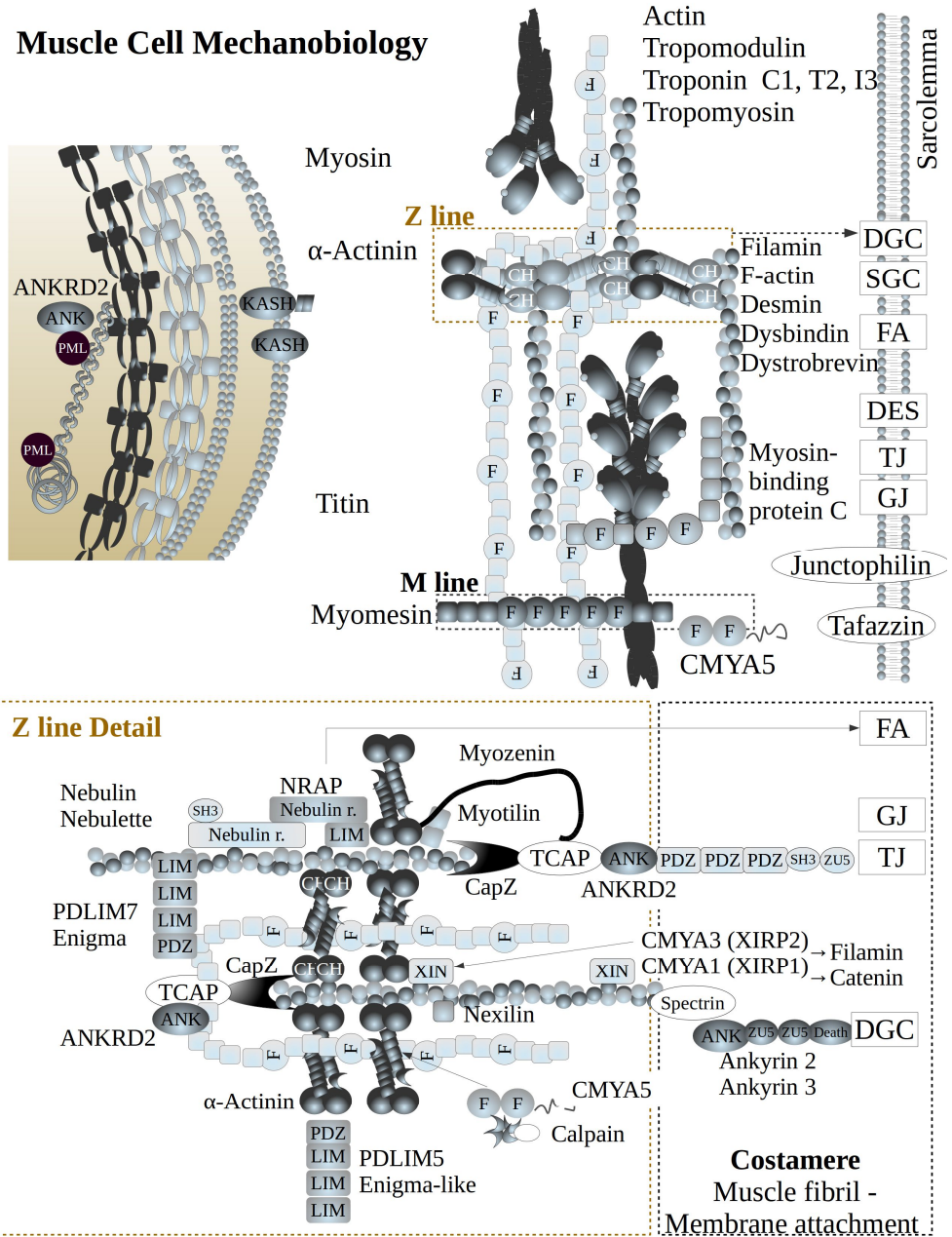
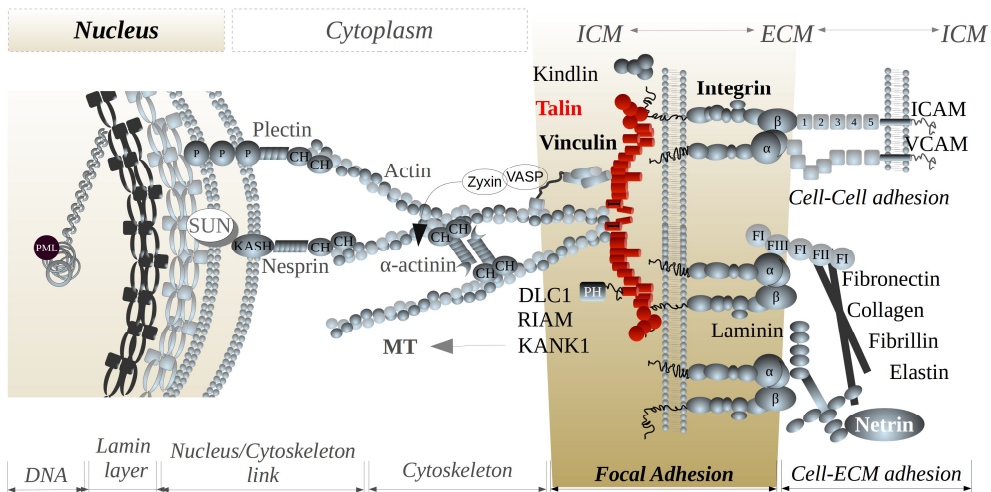


Figure 7. Muscle cell mechanobiology and protein composition of the muscle components.

## 2.6 Talin - focal adhesion adaptor protein

Talin is a large membrane-associated cytoplasmic protein (2541 aa, 270 kDa) highly concentrated at the FAs at cell-ECM and cell-cell contacts (**Figure 8**). Talin occupies a central role in the integrin-mediated adhesion guiding cell's proliferation and locomotion, its fitness and apoptosis. In more detail, talin binds to membrane-bound integrin receptors and to actin cytoskeleton and provides physical link between the ECM and intracellular compartments. Talin exists in two paralogs; talin-1 and talin-2. Talin-1 is ubiquitously expressed in tissues<sup>97</sup> while talin-2 is expressed mainly in the brain, skeletal tissue and in the mature heart<sup>98</sup>. During embryogenesis both talin forms are highly expressed in cardiomyocytes, however, talin-2 becomes the main isoform in the mature heart<sup>99</sup>.



**Figure 8. Talin subcellular location.** Talin (in red) is located at the cytoplasmic side of the cell membrane, concentrating at the focal adhesion (FA) complexes. Talin interacts with membrane bound integrins and connects the ECM-FAs to the actin cytoskeleton network.

### 2.6.1 Structure and interactions

Talin consists of two main domains; a globular N-terminal head domain and a flexible, extended C-terminal rod domain interconnected with an unstructured linker (**Figure 9**).

The head domain is formed by four subdomains (F0, F1, F2 and F3). The head domain structure lacking the F1-loop has been assessed as an atypical FERM

fold<sup>100</sup>. However, talin head in this form is biologically inactive. The main function of the talin head is the activation and interaction with the membrane integrin receptors<sup>101</sup>, focal adhesion kinase<sup>102</sup>, phospholipids<sup>103</sup>, transmembrane layilin<sup>104</sup> or Tiam1<sup>105</sup>. Talin and its adaptors impact the activation of the integrin receptor and guide the ECM and cell adhesion through the inside-out signaling<sup>106</sup>.

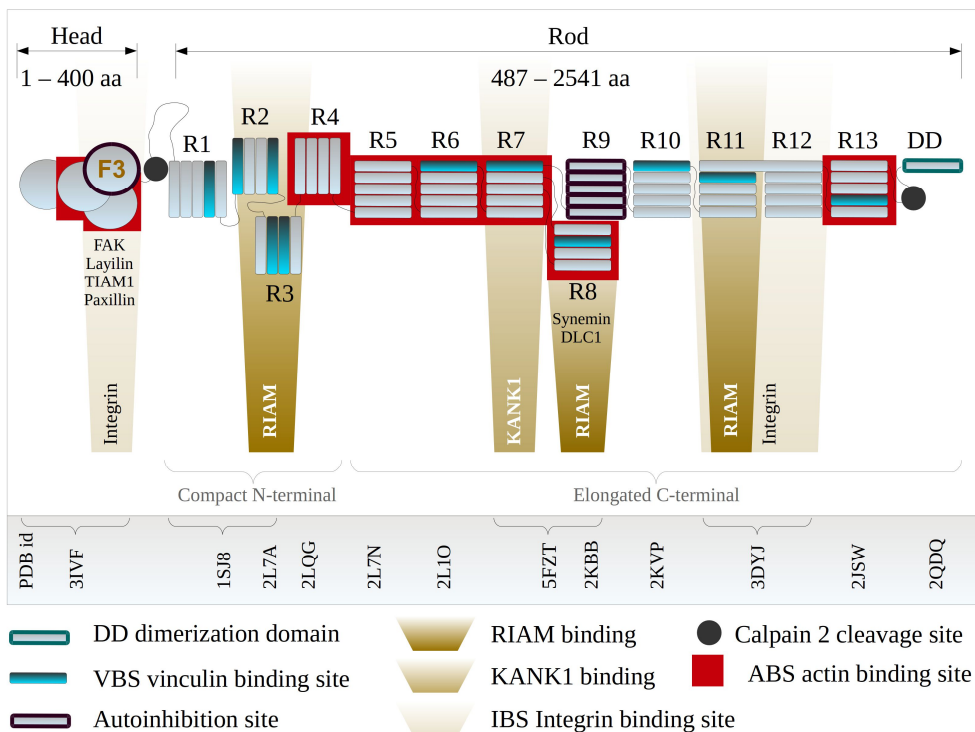


**Figure 9. Talin protein structure, domain quaternary organization and protein-protein interactions.** The N-terminal head domain of approx. 400 amino acids (aa) is connected by flexible linker (approx. 90 aa) to the mechanosensitive rod domain (approx. 2000 aa) and dimerization domain (DD). The rod domain contains 13 subdomains consisting of 4- and 5-  $\alpha$ -helix bundles in two distinct regions; the compact N-terminal rod (R1-R3) responsible for the initial mechanosensitivity, and the elongated C-terminal mainly carrying the mechanotransduction roles. There are two calpain2 cleavage sites (*black dots*) located between the head and rod domain; and between the C-terminal actin binding site (ABS) (*red squares*) in R13 and DD. Other ABSs are located in the F1 and F2 subdomain of the talin head and in R4-R8 central region of the talin rod. Among the rod domains, up to 11 vinculin binding sites (VBS) (*cyan rectangles*) can be found. Also other adaptors and protein ligands interacting with the whole talin are mentioned by text and indicated by yellow “spotlights”. The structure PDB ids representing for the appropriate protein part are denoted below the figure.

The C-terminal rod domain consists of 13 subdomains, formed by 4-5  $\alpha$ -helices<sup>107</sup> (denoted R1-R13) and a single  $\alpha$ -helix dimerization domain<sup>15</sup> (denoted DD). One of the principal interactions of the talin rod is with cytoskeletal actin filaments through the actin binding site (ABS) located in R13 with the presence of DD during the early adhesion formation<sup>108</sup>. Two other ABSs have been recognized in the F1-F2 subdomains of the talin head and in R4-R8 central region of the talin rod<sup>109,110</sup>. All three ABSs within the talin rod show distinct spatial and temporal localization within the cell adhesions and may assume different roles in the adhesion development and maturation<sup>108</sup>. This interaction with the light filaments is providing for the structural link and role of integrin-talin-actin complex. In addition, talin rod contains a variety of binding sites regulating its own activity (autoinhibition R9-F3)<sup>111</sup>, and binding sites for other structural and signaling proteins. Particularly, there are up to 11 vinculin binding sites (VBSs) buried within the subdomains among the talin rod<sup>112</sup>. Also binding sites for RIAM<sup>113</sup> and DLC1<sup>114</sup>, KANK1 (facilitating the connection to microtubules<sup>115</sup>), and IF protein synemin binding sites<sup>116</sup> are located in the talin rod. Finally, a secondary integrin binding site has been recognized at the C-terminal end of the talin rod<sup>117</sup>.

## 2.6.2 Functions in focal adhesion and focal adhesion maturation

The cell proliferation and migration is a dynamic process driven by continuous formation, maturation and turnover of FA sites<sup>11,118,119</sup>. Several types of cell matrix adhesions have been recognized; mainly based on the protein composition, size, shape and rigidity. The formation of the FA is initiated by talin activation, which is considered a key step in the stabilization of the integrin activated open form. The release of the talin auto-inhibited state into an active conformation involves the presence of kindlin, the opening of the talin's head-tail closed conformation and the binding to vinculin and actin<sup>120</sup>.

Consequently, integrins recruit focal adhesion kinase and talin to form **nascent adhesions** (NAs)<sup>119</sup>. NAs are small and highly transient early adhesive structures<sup>121</sup> located within the lamellipodium and prone to fast turnover. After early stages of maturation, NAs may develop into **focal complexes** (FXs) at the border of lamellipodium. FXs are also prone to fast disassembly, however they may grow and elongate into **focal adhesions** (FAs). FAs evolve slowly over time<sup>122</sup>, they form large adhesive plaques and involve clustered integrin and additional scaffolding

proteins such as vinculin. Vinculin serves as a FA reinforcing protein crosslinking talin with the actin filament<sup>123</sup>.

### 2.6.3 Mechanosensitive properties of talin

Talin binding to membrane integrin and cytoskeletal actin forms a physical and mechanical link between the ECM and cytosol. It has been long suspected that talin is a mechanosensitive protein changing its conformation and function in accordance with acting mechanical force. The fact that talin length varies in cells from 60 nm to 350-400 nm supports the hypothesis of protein unfolding and elongation as a result of applied mechanical force<sup>124</sup>. Great attention in this context has been given to the interaction of talin with another scaffolding protein, vinculin. The vinculin binding sites are buried inside the talin rod domain bundles and a conformational change is required prior to vinculin binding<sup>125</sup>. Indeed, mechanical force has been shown to induce such conformational change in computational simulation<sup>17,126</sup> and experimentally<sup>51</sup>.

How exactly these conformational changes are induced, controlled and reversed *in vivo* remain however unclear. A variety of protein interactions associated with the talin rod also suggests that the force-induced conformational changes may control a wider variety of talin's functions. To date, it has been suspected that the N-terminal compact end of the rod (R1-R3) is mainly responsible for the mechanosensitive functions of the whole talin rod whereas the remaining domains in the elongated C-terminal (R4-R13) account for the mechanotransduction roles<sup>113</sup>.

## 2.7 Diseases of mechanotransduction: known villains and suspects

Mechanobiology is vital for all living cells, including prokaryotes and eukaryotes, all cell and tissue types from differentiating to highly differentiated units. For instance, mechanical sensing plays crucial roles in adhesion onto cells in processes such as bacterial and viral adhesion prior to infection. Mechanotransduction is also crucial for the immune response of the organism by facilitating the adhesion of lymphocytes onto the infected cells. Hence, it is not surprising that a vast variety of

diverse diseases has been and is continuously being recognized as diseases of mechanotransduction.

### 2.7.1 Cardiovascular diseases

The cells and tissues of the heart and vasculature are constantly exposed to mechanical forces generated by the heart muscle and the circulating blood suspension. The cardiovascular diseases can be divided into three groups; the diseases of the heart, the diseases of the vascular system and the diseases affecting the blood cells.

The diseases of the heart account for various functional and morphological malfunctions of the heart muscle, for example cardiomyopathies, long QT syndrome or left ventricular noncompaction. Among these, common cardiomyopathies are well studied in different populations. In particular, hypertrophic cardiomyopathy (HCM) is an inherited heart disease where a part of the ventricular muscle wall becomes thickened and decreases the heart pumping efficiency. It is associated with arrhythmia and sudden cardiac death<sup>127</sup>. Number of mutations in the sarcomeric proteins has been recognized as a cause of HCM. For example mutations in  $\beta$ -cardiac myosin<sup>127</sup>, cardiac actin<sup>128</sup> and titin<sup>129</sup>, myosin protein binding C<sup>130</sup>, nexilin<sup>131</sup>, tropomyosin<sup>130</sup> or mutations in the troponin protein family<sup>132,133</sup> have been identified. Majority of the proteins mentioned as causatives for HCM have also been identified as causatives of dilated cardiomyopathy (DCM). DCM is the most common cardiomyopathy where the heart muscle becomes weakened and enlarged with reduced pumping efficiency. Among those proteins already mentioned,  $\alpha$ -actinin<sup>134</sup>, desmin<sup>135</sup>, vinculin<sup>136</sup>, and many other mechanosensitive proteins of the sarcomere and their mutations have been reported<sup>137,138</sup>.

A cerebrovascular disorder (Moyamoya) and multisystemic smooth muscle disorder caused by a mutation in  $\alpha$ -actinin 2<sup>139</sup>, or atherosclerosis affected by an alteration in kindlin family expression<sup>140</sup> are examples of vascular diseases of mechanotransduction.

Finally, there are diseases affecting the blood cells and other blood components. Elliptocytosis, spherocytosis or pyropoikilocytosis are severe diseases caused by mutations in erythrocytic spectrins<sup>141,142,143</sup>. These mutations cause a change in the red blood cell shape, its mechanostability and its ability to pass through vascular walls. In addition, the failure of platelet aggregation (integrin  $\beta$ 3)<sup>144</sup> and bleeding

disorder ( $\alpha$ -actinin1)<sup>145</sup> are yet another example of the blood-associated mechanotransduction disease.

## 2.7.2 Skeletal muscle disorders

Myopathies are the diseases of the skeletal muscle fiber resulting in the muscular weakness. The inherited diseases include types of muscular dystrophies, nemaline, mitochondrial or inflammatory myopathies, types of involuntary muscle contractions known as dystonia, and other disorders<sup>146</sup>.

Intensively studied muscular dystrophy diseases are often progressive and manifest by muscle weakness causing difficulties with basic motorics as well as with breathing and swallowing<sup>147</sup>. Many proteins of the mechanotransduction complexes contain mutations responsible for the development of different muscular dystrophies. In particular, mutations in dystrophin<sup>148</sup> and the proteins in the DGC-SGC<sup>149,150</sup> pathway with desmin<sup>151</sup> and caveolin3<sup>152</sup> are common disease causatives. Furthermore, the nuclear envelope mechanotransduction complexes, nesprin1-2<sup>153</sup> and laminA/C<sup>154</sup>, also play important roles in the dystrophy inheritance and development.

## 2.7.3 Diseases of bone and cartilage

The diseases of bone and cartilage are often severe conditions causing body malformations in combination with cognitive disabilities, heart problems and deafness. These diseases often lead to death in neonatal age. Several protein mutations in laminA/C<sup>155</sup> or fibrillin<sup>156</sup> have been identified in the bone and cartilage diseases.

In addition, filamin mutations cause atelosteogenesis. This is a lethal chondrodysplasia characterized by underdevelopment of long bones, spine and occasionally complete lack of ossification of single hand bones. Also boomerang dysplasia, a disorder characterized by unusual shape of long bones, or Larsen syndrome with typical joint dislocation, short stature, craniofacial dysmorphism<sup>157,158</sup> are caused by mutations in filamins. Furthermore, Baraitser-Winter syndrome manifesting with short stature, microcephaly and affected skull development combined with retina disorders and deafness is caused by mutations in cytoskeletal actin<sup>159,160</sup>. Extracellular collagen protein family is important in bone and cartilage development. Together with plastin mutations, collagen mutations

cause osteoporosis. These mutations are recognized to decrease bone density and increase bone fragility<sup>161,162</sup>.

## 2.7.4 Cancer

Even though genetic screening has been the main area in the cancer research, the way how cells sense their environment and how they adhere or proliferate has recently been recognized vital in the metastasis formation and cancer progression<sup>163</sup>. Nuclear lamins, collagen and ECM mechanical properties such as stiffness and elasticity drive the proliferation ability of cells<sup>164,165</sup>. The adhesion and locomotion of cells may be affected by alteration in talin expression, discussed in detail in 2.7.6. Furthermore, mutations in cadherin1 increase susceptibility to gastric<sup>166</sup>, breast<sup>167</sup>, endometrial and ovarian cancer<sup>168</sup>.

## 2.7.5 Other diseases

Cardiovascular diseases, myopathies, diseases of bone and cartilage or cancers are diseases directly connected with affected cellular or tissue mechanobiology. However, also other pathological conditions are directly or indirectly caused by mutations in the mechanotransduction components. For example, skin fragility, dermatosis and blistering are conditions caused by mutations or altered expression in number of mechanotransduction components, among others kindlin, plectin, integrin, laminin, or collagen<sup>169,170</sup>. Furthermore, mutations in integrin alpha-3 are associated with disrupted basement-membrane structures and compromise functions in kidney or lung<sup>171</sup>. Moreover, mutations in presenilin-1 cause dementia<sup>172</sup> and mutations in nesprin-1 are associated with degradation of cerebellum<sup>173</sup>.

## 2.7.6 Talin and disease

Both talin isoforms, talin-1 and talin-2, possess overlapping functions. It has been shown that both talins can take over each other's functions and compensate for an alteration in expression or gene knockdown in skeletal muscle. However, a double knockdown of talin-1 and talin-2 simultaneously is perinatal lethal in mice<sup>174</sup>. To date, the exact functional compensation principles remain unclear<sup>14</sup>.

Even though talin-1 has not been directly linked to any human disease<sup>175</sup>, it is vital for cellular differentiation and development<sup>12</sup>. Recently, a missense mutation in talin-2 head domain S339L was identified as a causative of fifth finger camptodactyly<sup>176</sup>. Camptodactyly is a digit deformity characterized by a permanent contracture of one or both fifth fingers. More severe types of type III may involve deformities also of other fingers of both upper extremities with variety of additional symptoms. Interestingly, type II camptodactyly manifests only in preadolescence at 7-11 years of age<sup>176</sup>.

In addition, talin-1 was found crucial for cell differentiation in gastrulation stage of embryonic development in mice, whereas talin-2 knockout causes only mild muscular dystrophies<sup>25</sup>. Conditional knockdown of talin-1 in the endothelial cells affects the angiogenesis and endothelial cell spreading causing embryonic lethality in mice<sup>12</sup>. In zebrafish, talin-1 partial deletion in the F2-F3 head domains cause a disruption in the cardiac Z-disc stability leading to cardiac dysfunction and vascular disorders<sup>177</sup>. Talin-1 expression is normally reduced in adult cardiac cells, yet increased talin expression was detected in hypertrophic myocardium and failing heart<sup>99</sup>. It was also shown that the loss of talin-1 compromised the differentiation of noncirculating B-cells in the spleen. Furthermore, the talin-1 null spleen located B-lymphocytes could not enter lymph nodes or return to the bone marrow<sup>178</sup>.

Recent cancer research has been intensively reporting on the alteration of talin-1 and talin-2 expression levels in different types of carcinomas and their metastasis. For example, talin-1 involvement was identified in the process of the carcinogenesis, infiltration and metastasis formation in the hepatocellular carcinomas. The talin-1 expression level in the liver tumor tissue was significantly lower compared to the healthy liver<sup>179</sup>. In addition, the concentration of cytoplasmic talin-1 was significantly increased in the prostate cancer metastasis compared to the primary prostate tumors<sup>180</sup>. In metastatic breast cancer, talin-1 was required to assist invasion<sup>181</sup>. Talin-1 was also upregulated in ovarian carcinoma<sup>182</sup> and in brain tumors<sup>183</sup>. Finally, in the nasopharyngeal carcinoma, expression of talin-1 was increased in distant metastasis and associated with poor survival prognosis<sup>184</sup>. Somatic mutation information related to cancer is also available in public database COSMIC where number of missense mutations in TLN1 and TLN2 genes have been reported. However, direct link of missense mutation to cancer and mechanisms of action await investigation<sup>185</sup>.

Talin may also be indirectly involved in diseases through defective integrin signaling. Decreased talin expression was found in bleeding disorders causing low platelet aggregation affecting the thrombus formation<sup>186</sup>. Moreover, talin was

required for the integrin activation in hematopoietic cells and the loss of talin lead to leukocyte adhesion deficiency<sup>187</sup>.

## 2.8 Mechanobiology and disease in graphical overview

Even though the effects of mechanical forces on living organisms have been observed and known for decades, the extend of the mechanobiology field especially on molecular and protein level is still under scrupulous investigation. In order to appreciate the complexity of the cellular response to mechanical stimuli, to understand the roles in disease development and to map common protein structural features, an overview of the available knowledge was prepared. **Figure 10** introduces the used secondary structure code to represent the known structurally homologous domains. **Figure 11** sketches the mechanobiology and disease connection at the FAs and the connected pathways. **Figure 12** illustrates the dystroglycan-sarcoglycan adhesions and describes the membrane skeleton. **Figure 13** concentrates on the cell mechanobiology at gap and tight junctions and at the desmosome. And finally, **Figure 14** introduces the myocyte mechanobiology in the muscle fiber.

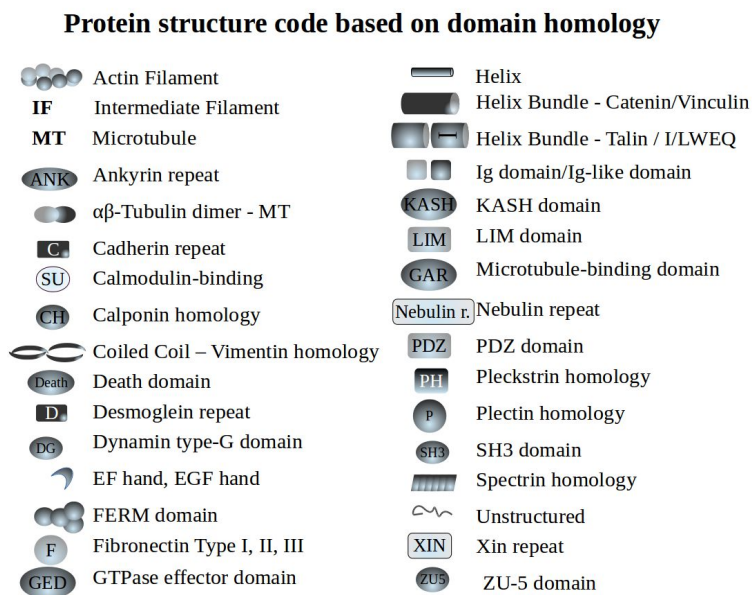


**Figure 10. Protein structure code.** A guide to the protein structural homology representation in mechanotransduction pathways as used throughout the graphical overview.

## Focal adhesion – Integrin-mediated

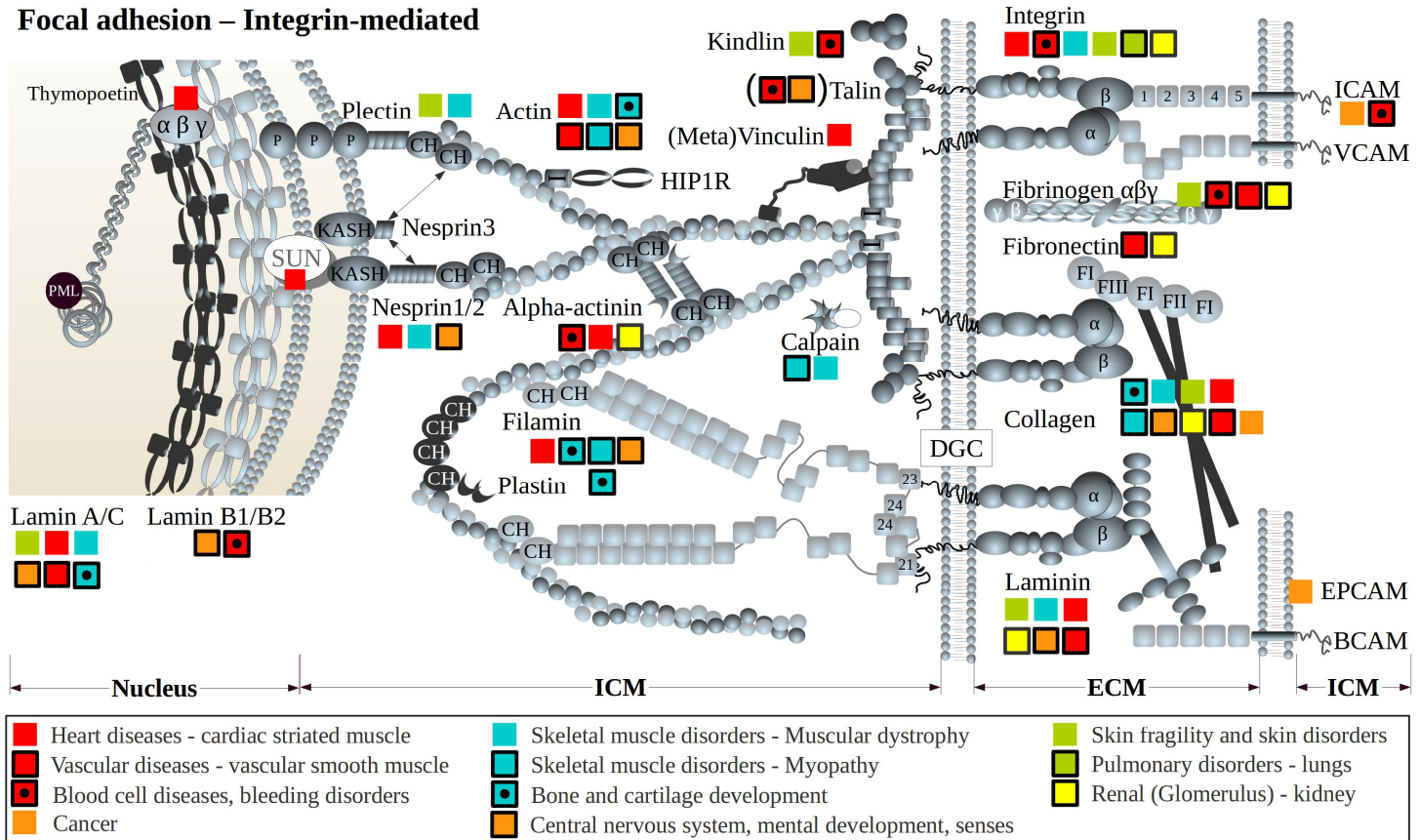


**Figure 11. Overview of mechanobiology and disease at focal adhesions (FAs).** Mechanotransduction components connecting the ECM, through FAs and cytoskeleton to nucleus with known secondary structure information and disease association<sup>42,97,175,188</sup>.

## Membrane skeleton

## Dystroglycan-Sarcoglycan complex

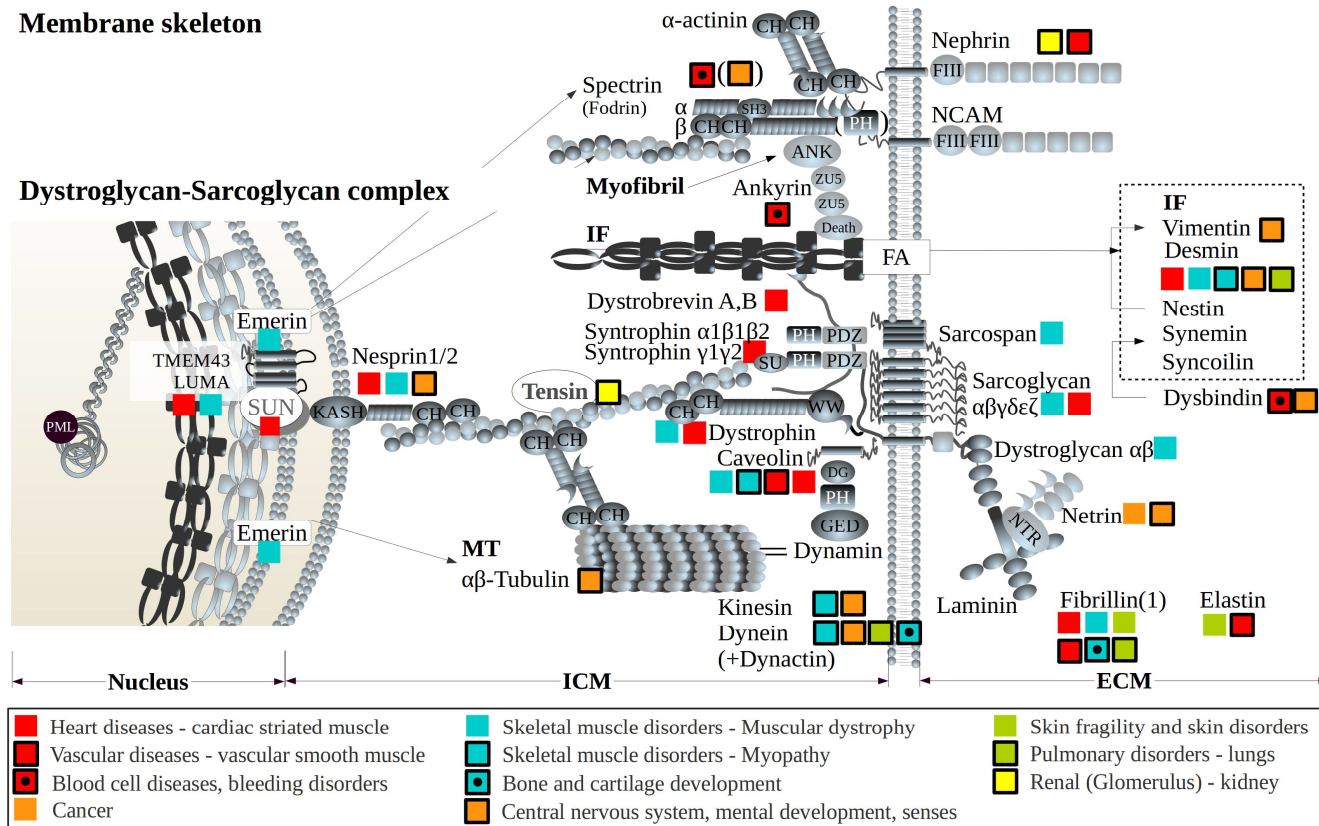


**Figure 12. Overview of mechanobiology and disease at the Dystroglycan-Sarcoglycan (DGC-SGC) complex and the membrane skeleton.** Mechanotransduction components connecting the ECM, through DGC-SGC and cytoskeleton to nucleus with known secondary structure information and disease association<sup>42,97,175,188</sup>.

## Gap and Tight Junctions

## Desmosome

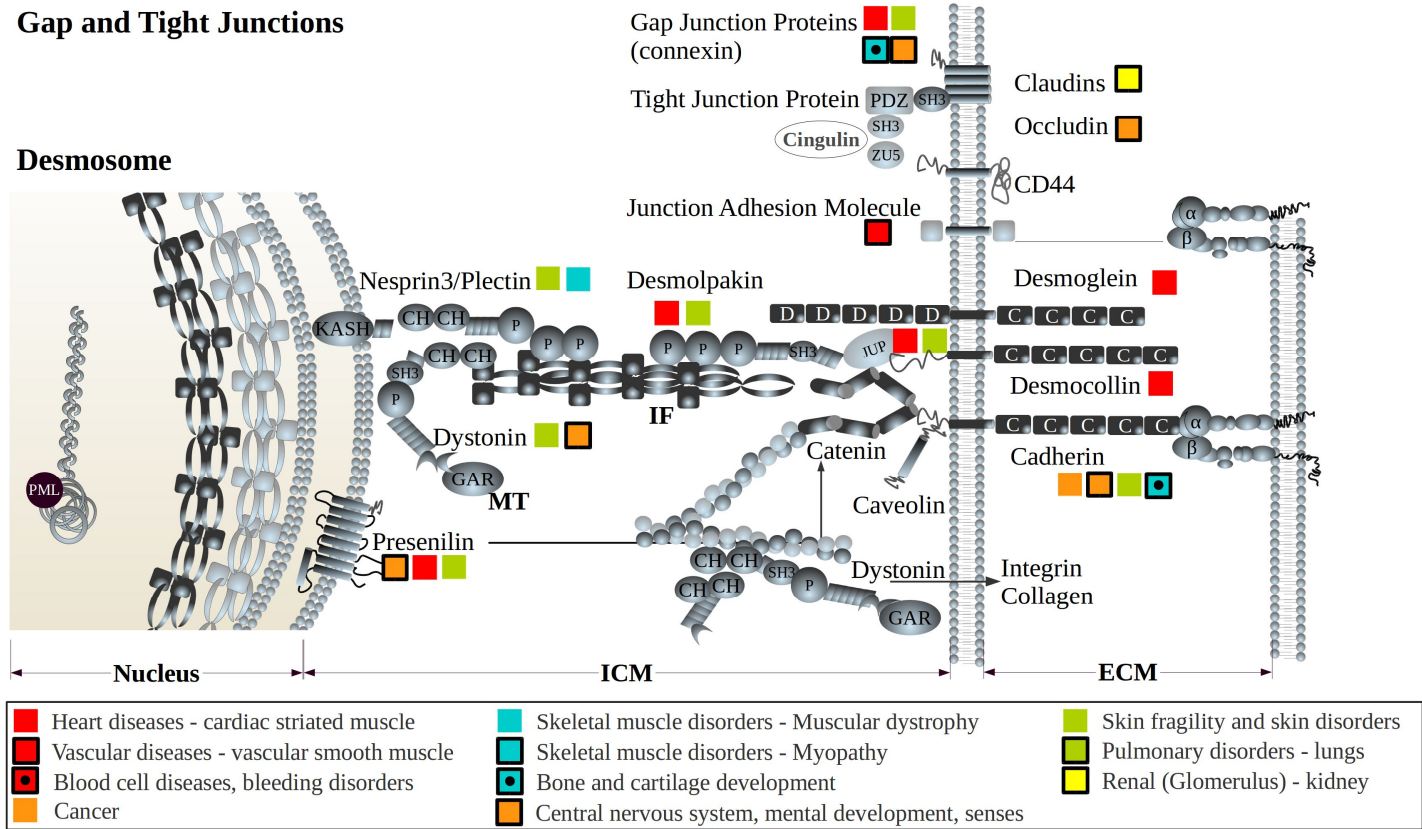


**Figure 13. Overview of mechanobiology and disease at the Gap (GJ) and Tight junctions (TJ) and the Desmosome (DES).** Mechanotransduction components connecting the ECM, through GJ, TJ, DES and cytoskeleton to nucleus with known secondary structure information and disease association<sup>42,97,175,188</sup>.

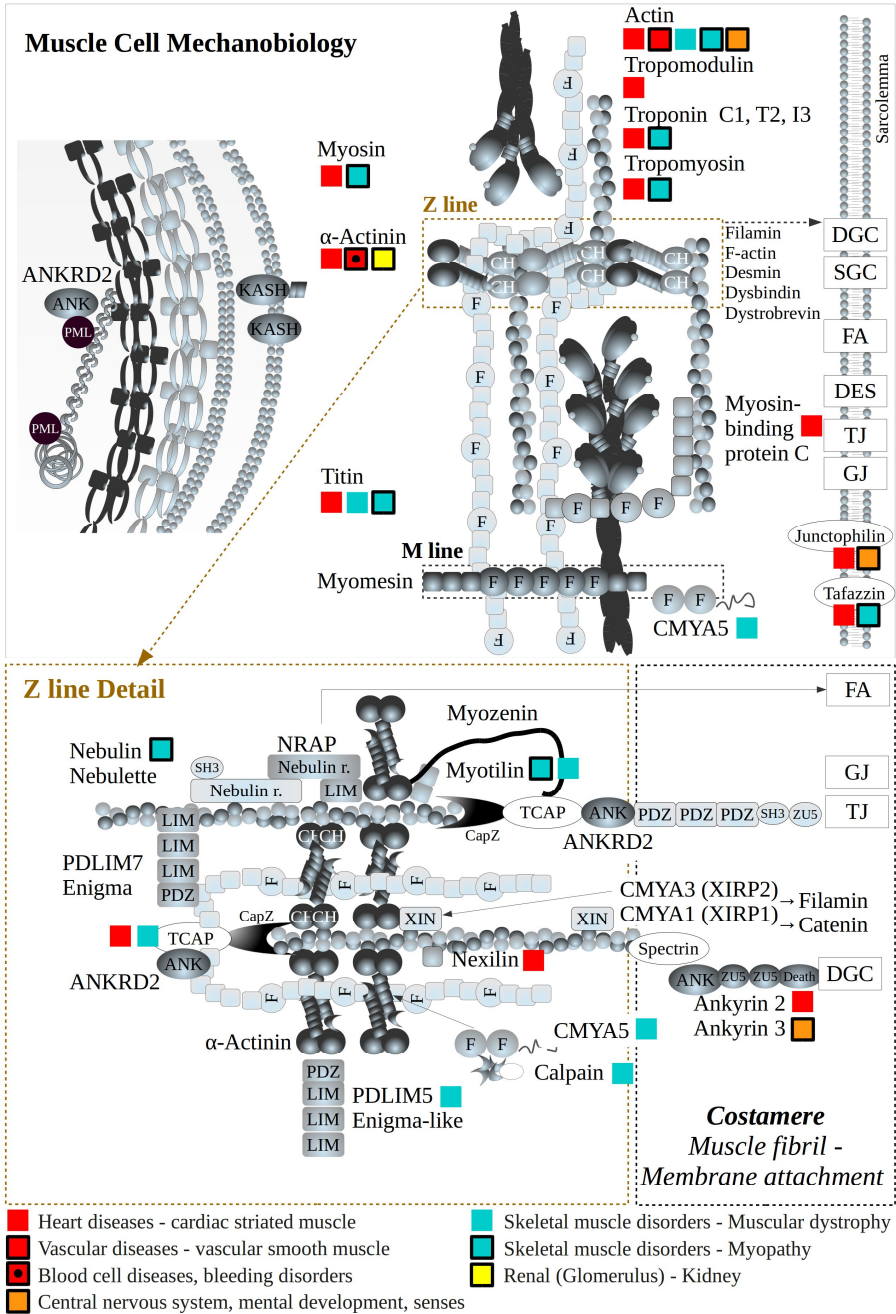


**Figure 14. Overview of mechanobiology and disease in the muscle cell components.** Mechanotransduction components connecting the ECM, through membrane complexes and cytoskeleton to nucleus with known secondary structure information and disease association<sup>42,97,175,188</sup>.

### 3 AIMS OF THE STUDY

The general target of the thesis was to link genetics to pathological development in mechanotransduction disease through the examination of mechanobiological principles on molecular and atomistic level. The focus of the study was the investigation of the mechanical behavior of talin protein by computational protein dynamics methods. In more detail, the aims of this work were as follows:

- I To investigate talin involvement in disease. We analyzed the changes in talin and vinculin expression levels in connection to atherosclerosis development. The aim was to study if altered expression of central mechanosensory proteins would cause disease susceptibility and/or disease development.
- II To investigate the link between the talin mechanobiology and cell response and to investigate the effects of talin destabilization by mutagenesis.
- III To investigate the fundamental principles of talin mechanotransduction. Here the focus was on the mechanical sensitivity of the talin rod  $\alpha$ -helical bundles and their response to mechanical force.
- IV To investigate the fundamental principles of  $\alpha$ -helical protein unfolding, its possible intermediate states and their importance in protein function.

## 4 MATERIALS AND METHODS

In this chapter, the *in silico* methods utilized in this thesis are described and compared to other existing methods implemented in the protein unfolding investigations. Publications accompanying this thesis are combining multidisciplinary methods in the mechanobiology and protein unfolding research. The author of the thesis was, however, responsible for the computational protein unfolding simulation, which is introduced in detail below. Multidisciplinary methodology applied outside the computational approach is briefly described in separate paragraphs based on the publications at the end of this chapter.

### 4.1 Mechanobiology overview and graphical representation

In the graphical overviews presented in the review of this thesis in **Figure 3 - Figure 14**, the investigation of mechanobiology on the protein level available in public databases and literature can be found. NCBI<sup>189</sup>, UniProt<sup>97</sup> and Ensembl<sup>188</sup> were investigated for the protein cellular location, tissue specific expression, disease association, structural homology and genome information. Protein structure and its availability were assessed in RCSB PDB Protein Data Bank (PDB)<sup>42</sup>, and the disease association was reexamined in Online Mendelian Inheritance in Men (OMIM)<sup>175</sup> database. Simple drawing tool of LibreOffice package was used to organize the data and visualize the figures.

### 4.2 Mechanical unfolding of proteins and investigation methods

Proteins respond to the mechanical impulses by a change in their conformation. Such change can be described as protein unfolding and elongation, or disintegration of domains. Several tools and methods have been developed to study the unfolding force magnitudes, binding activation by conformational changes, and fundamental principles of the force induced protein unfolding. In particular, atomic force microscopy (AFM)<sup>43</sup>, magnetic<sup>51</sup> or optical tweezers<sup>29</sup> are frequently

utilized experimental methods. Cell *in vitro* experiments with migration analysis or force traction microscopy further allow for the observation of the protein stability on the cell level. Recently, even elevated pressure conditions were used in the protein unfolding experiments causing talin R3 domain disintegration<sup>190</sup> under pressure of 2000 bar. *Ex vivo* unfolding force analysis, however, does not ensure realistic determination of true unfolding force magnitude under physiological conditions. To allow such insight in physiological setup, Grashoff et al. developed intracellular tension biosensor modules allowing precise force investigations *in vivo* at sensitivity as low as 3-5 pN<sup>191</sup>.

#### 4.2.1 Computational molecular dynamics methods (II, III, IV)

During the protein activation under mechanical force, involved conformational changes happen on atom scale level. These changes are therefore challenging to observe and track *in vivo* and *in vitro*. Despite existing limitations, computational *in silico* methods provide an atomic and molecular insight into these processes and activation events. On many occasions computational methods, classical molecular dynamics (MD) and steered molecular dynamics (SMD) have proven rather accurate and even predictive. Therefore these methods are often utilized to link experiments and theory<sup>192</sup>.

In the presented work, GROMACS (ver.4.6.7 (II, III), ver.2016.1 (IV)) simulation tool was utilized for all classical MD and SMD simulation using Sisu supercomputer at CSC, Finland. In principle, MD and SMD simulations solve the Newton's equation of motion for a system of interacting atoms in a given coordinate entity in small steps over a period of simulation time<sup>193</sup>.

##### 4.2.1.1 System and parameters

The simulation systems considered in this thesis were prepared starting from appropriate protein structure available in public databases<sup>42</sup>. For single domain simulation we have utilized PDB structures with corrections to reflect true talin protein sequence or exact sequences used in experimental setup.

Starting coordinates of multi-domain fragments demanded manual domain reorganization. Even though all talin rod subdomain structures have been solved, the quaternary structure remains largely unknown with the exception of R7-R8 and R11-R12 double domains. We used appropriate single PDB structures, organized

them based on talin sequence and oriented them in PyMol software ver.1.4.1. to produce one chain multi-domain talin rod fragment. We aimed to reproduce the current model of the rod domain organization. Needless to say, these fragments are hypothetical. Following the first adjustments based on talin sequence, the coordinates of all atoms excluding hydrogens were placed in a rectangular box with periodic boundary conditions, solvated with explicit water and 0.15 M KCl neutral solution.

CHARMM27 force field was utilized in all systems comprising this thesis. The force field algorithm is a mathematical model used for the approximation of the atomic-level forces acting on the simulated system. The accuracy of the force field usually dictates and determines the usefulness of the simulation results<sup>194</sup>. CHARMM27 is an updated CHARMM22 with CMAP correction. The latest force field version was used despite it has been shown to overstabilize the formation of helical structures<sup>194</sup>.

All simulations were performed in NPT canonical ensemble<sup>195</sup> with 2 fs time step. A combination of Berendsen<sup>196</sup> or v-rescale<sup>197</sup> thermostat algorithm was applied for the solution and protein separately at 310 K, and Berendsen barostat was set for solution and protein separately to 1 bar and compressibility to  $4.5 \times 10^{-5}$  bar. Each system was minimized to 100,000 steps with steepest descent algorithm.

#### 4.2.1.2 Classical molecular dynamics (MD)

Classical MD setup was used for system equilibration performed for duration of 1 ns (III) or 10 ns (II, IV). The equilibration progress was followed on backbone RMSD (Root Mean Square Deviation). Also the observation of the system and protein stability and for protein consequent refolding (II) after force release was followed under classical MD parameter setup. All classical MD simulations were performed under isotropic conditions. A selection of used parameters and simulation algorithms used in classical MD and in pulling simulations are available in **Table 1**.

**Table 1.** Selection of setting and parameters of equilibration, classical MD and pulling SMD simulations as implemented in GROMACS ver. 4.6.7 (II, III) and GROMCS ver.2016.1 (IV).

	Publication II, III	Publication IV
integrator	md	md
constraint_algorithm	lincs	lincs
constraints	h-bonds	h-bonds
lincs_iter	1	1
lincs_order	4	4
ns_type	grid	grid
nstlist	5	10
cutoff-scheme	-	verlet
vdwtype	switch	cut-off
vdw-modifier	-	potential-switch
rvdw_switch	1	1
rvdw	1.2	1.2
rcoulomb	1.4	1.2
rlist	1.4	1.2
coulombtype	PME	PME
pme_order	4	4
fourierspacing	0.12	0.12
ewald_rtol	-	1.00E-005

#### 4.2.1.3 Steered molecular dynamics methods (SMD)

All pulling simulations were performed under semi-isotropic conditions where the pressure control was abolished in the z-direction of the simulation box; i.e. in the direction of the pulling force. In the umbrella pulling algorithm, the spring constant was set to 1000 kJ/mol nm<sup>2</sup>. The pulling force was applied to the C $\alpha$  of the first and last amino acid residue at the N- and C-terminal ends of the fragment, respectively (III, IV). The pulling vector between the N- and C- points was oriented in parallel to z-axis of the simulation box, i.e. the pulling direction of the box.

In publication II, the N- and C- terminal helices (R3H1 and R3H4) identified by four C $\alpha$  atoms each, were pulled apart to disintegrate the R3 domain. Constant force pulling protocol was used at magnitude of 150 pN. In publication III end-to-end pulling with constant velocity at 0.1 and 2 nm/ns was implemented. And in publication IV, constant velocity pulling at a rate of 2 nm/ns and constant force pulling regime with force magnitude in range of 160 – 300 pN was used.

In the publication III, the force of the spring was calculated according to the equation [1]:

$$F = k_{\text{spring}} (x_{\text{ideal } t} + x_0 - x_t) \quad [1]$$

where  $k_{\text{spring}}$  is the spring constant,  $x_{\text{ideal } t}$  is the ideal elongation with velocity at time point without any resisting forces,  $x_0$  is the initial pulling vector length at time 0ns corresponding to the folded domain dimensions, and  $x_t$  is the pulling vector length at the time point. In publication (IV) the force causing the unfolding was extracted during the simulation trajectory production every 100 ps. This was specified in the pulling parameter file (\*.mdp) as a separate output file (nstfout=5000).

## 4.2.2 Computational vs. experimental methods

The unfolding force of a mechanosensitive protein depends largely on its structure as was mentioned in paragraph 2.3. However, the measured unfolding force magnitude may vary also depending on the applied research method. In general, the unfolding forces are unfolding speed dependent, i.e. the force magnitude is affected by the pulling rate<sup>198</sup>. Since different methods are limited to different pulling rates, the measured force magnitude is affected by the choice of the applied method.

**Table 2** provides a comparison of unfolding forces and speeds reported for titin Ig domains as the most studied protein domains in the field. As can be observed, the computational SMD methods report dramatically higher unfolding forces. This is a result of the insufficient computational efficiency demanding large simulation time step, simulation activation within nanoseconds and hence higher pulling speeds compared to experimental methods (smAFM, optical or magnetic tweezers).

Similar difference in the unfolding force magnitude has been recognized over a range of different proteins and secondary structure folds<sup>199</sup>. For  $\alpha$ -helical structure of talin R1-R3(partial), the unfolding with magnetic tweezers and consequent vinculin binding appeared at 12 pN<sup>51</sup> while in SMD the minimal constant force regime leading to protein unfolding for the identical fragment was 200 pN<sup>17</sup>.

The unfolding force has also been shown to be temperature dependent. For example, titin kinase mechanosensitive domain was unfolded in a force magnitude range of 30 to 50 pN depending on the experimental temperature<sup>35</sup>.

Finally, the force application point and the orientation of the pulling vector in respect to the orientation of the unfolding domain may affect the unfolding force magnitude as well as the unfolding dynamics. For instance, the force applied to the N- and C- terminus causes complete unfolding of the domain whereas pulling whole helices rather result to domain disintegration<sup>17</sup>.

**Table 2.** Comparison of unfolding forces and speeds of titin Ig domains by experimental and computational methods. For more information on other protein folds and domains see<sup>199</sup>.

Titin domain	Experimental (smAFM)		Computational (SMD)		References
	$F_{\max}$ [pN]	$v_{\text{pulling}}$ [nm/s]	$F_{\max}$ [pN]	$v_{\text{pulling}}$ [nm/s]	
I1 <sub>I27</sub>	127	600			200
I4	171 (+/-26)				41
I5	155 (+/-33)				41
I4-I11	150-200 (+/-30)				41
I27	204 (+/-30)	0.2-1.5	2479	1.00E+011	41,201,202,203
			2040	5.00E+010	201,202
I28	257 (+/-27)		2554	1.00E+011	41,201,202,203
			2082	5.00E+010	201,202
I27-I28	211-306	1			203
I27-I30	230				204
I27-I34	150-330 (+/-20)	1			41
I27-I34	231 (+/-6)	0.5			205
I32	298 (+/-24)				41
I34	281				41

### 4.3 Molecular and trajectory visualization (II, III, IV)

Resulting trajectories were analyzed with VMD ver. 1.9.1. An average sliding window method was applied to minimize fluctuation and eliminate noise in the force presentation caused by low time step and sampling setting for data collection.

### 4.4 Mutation design and mutagenesis (II)

Multiple sequence alignment (Clustal Omega) and conservation analysis were performed in order to identify candidates for mutation design (III) based on

principles reviewed in Kumar and Li<sup>202</sup> and proposed by Yao et al.<sup>206</sup>. The alignments were visualized and analyzed with Jalview. PyMOL, Molecular graphics system, ver. 1.4.1 was used for visualization, target residue identification and following mutagenesis.

## 4.5 Methods of talin and vinculin expression in atherosclerotic plaque (I)

Vascular samples analyzed for the talin and vinculin gene expression were collected during open vascular procedures between 2005 and 2015. These arterial samples including the femoral, carotid and abdominal aortic regions are included in the Tampere Vascular Study (TVS) collection. The whole blood and monocyte fractions were collected during 2008.

The expression levels of arterial and whole blood samples were analyzed with Illumina HumanHT-12 v3 Expression BeadChip. Microarray experiments were performed by Sentrix Human-6 Expression BeadChip. Microarray data were log<sub>2</sub> transformed in R software after the background subtraction in Illumina GenomeStudio. Statistical analyses were performed with R version 2.15.0. Statistical significance in the expression level difference was assessed with nonparametric Wilcoxon signed-rank test and the log-transformed data. Significance was assessed after Bonferroni correction for multiple testing at  $p < 0.05/42$  to 0.001. Difference in expression was considered significant when  $p < 0.05$ . Validation of the results was performed by low-density qRT-PCR-array.

Correlation between sample subgroups and their marker profiles were investigated with hierarchical clustering and Spearman correlation analysis. Heatmap.2 function and gplots R library were used for the analysis with Pearson dissimilarity and average linkage for the hierarchical clustering analysis.

The talin and vinculin isoforms expression, tissue localization in plaque and healthy left internal thoracic artery (LITA) control as well as the tissue morphology was further investigated with confocal immunofluorescence study of frozen and paraffin-embedded samples. These methods are in greater detail described in Article I.

## 4.6 Biochemical analysis of talin R3 destabilized mutants (II)

DNA fragments corresponding to the talin-1 residues 795-911 were subcloned into a modified pHis vector in order to create an N-terminally His6-tagged construct. The His6-tag was separated from the talin fragment by an 11 amino acid residue linker. The modified R3 talin subdomain was expressed in *E. coli*, purified using affinity chromatography and dialyzed, followed by electrophoretic analysis.

Size exclusion chromatography (SEC) with liquid chromatography was used to analyze the solubility and size of the talin WT and mutated R3 forms, static light-scattering intensity (SLS) and mass spectrometry were used to determine the size and molecular weight of the talin R3 forms. CD spectroscopy performed with Chirascan instrument was used to determine the secondary structure content, thermal stability and folding of the wild-type and mutated talin R3 forms. These methods are described in detail in Article II.

## 4.7 Cell experiments in analysis of talin R3 destabilized mutants (II)

Wild-type MEF cell line and TLN1-/-TLN2-/- MEF cell line were utilized in the experiment. C-terminal EGFP- or m-Cherry tags were used in the full length mouse talin-1. Destabilizing mutations were created with overlapping mutagenesis primers and silent restriction sites. Truncated talin forms were created by subcloning mouse talin-1 fragments (aa 1-913 and 2296-2541) into a modified plasmid backbone. All of the created constructs were authenticated by DNA sequencing.

All cells were imaged after immunostaining and fixing with fixed parameters to allow quantitative image analysis and comparison between all the samples. Fluorescence recovery after photobleaching (FRAP) analysis for talin and vinculin were performed on circular regions with 2  $\mu\text{m}$  diameter on exactly one region per cell. FRAP experiments were used to study the dynamics of the FAs, where photobleaching was done with 488 nm argon laser at high intensity. Traction forces for talin-1 WT and destabilized mutants were analyzed on gels with 0.2  $\mu\text{m}$  beads conjugated with fibronectin followed over 12 hours and analyzed with confocal microscope. Migration analysis was performed on polystyrene well plates coated with fibronectin and imaged over 12 hours at 120 second intervals. These methods are in detail described in Article II.

## 4.8 Single molecule Atomic Force Microscopy (smAFM) in talin mechanical unfolding (III, IV)

The talin constructs together with I27 flanking were synthesized and cloned into pFN18a and expressed in *E. coli*. Glass cover slips were functionalized with chloroalkane ligand to HaloTag. In the AFM experiments, a commercial AFS-1 from Luigs & Neumann, GmbH was utilized. The cantilevers used were gold-coated OBL-10 levers from Bruker. The spring constants varied between 4 and 10 pN/nm. The cantilever was pressed onto the surface with a force of approx. 300 pN to bind the cantilever to the polyprotein. Force extension experiments were conducted at 400 nm/s retraction rate. The peaks of the unfolding force were identified by adjustable smoothing with a moving box average with a local maxima search. Unadjusted distance from the HaloTag to the force peak was also measured. These methods utilized by our collaborators are in detail described in Article III and IV.

# 5 RESULTS

In the following chapter the results of the thesis are presented based on the original articles (I-IV) and unpublished investigations (unpubl.). The results summary is organized based on the topics introduced in the literature review reflecting the state of the mechanobiology and talin protein research in health and disease.

## 5.1 Mechanobiology and disease summary (unpubl.)

Pathologies and diseases have always driven human investigations in biology and medicine. The need to define symptoms, to discover causes, to cure illnesses or to increase the quality of life has led to a vast amount of knowledge and invention in various scientific fields. The progress of genetics research, diagnostic methods, biotechnology, bioinformatics and computational tools accumulate continuously new information in biology in healthy and pathological development. Such multidisciplinary input, however, results in extensive and incomprehensive collection of information.

Here I targeted the subcellular and protein structures implicated in mechanotransduction and their known connection to a disease. I aimed to provide a comprehensive overview of the known cellular and structural data, disease connection, interactions and mechanotransduction pathway association. The resulting graphical representation illustrated in **Figure 11 - Figure 14** show that numerous subcellular and protein structures involved in the force sensing and propagation are associated with or linked to diverse diseases of the heart, skeletal muscle or bone and to developmental issues starting at the gastrulation stages of the embryonic development. With the variety of cellular functions depending on the mechanotransduction systems, it is not surprising that abnormal regulation or functioning of these inter- and intracellular components is often causing disease development<sup>13,207,208</sup>. The detailed overview presented also the need for general description and classification of the mechanotransduction diseases as a concern of the cause.

### 5.1.1 Levels of mechanotransduction effect

To assess any abnormality in the mechanotransduction pathway as a cause of pathological development, the abnormal observation has to be analyzed from the view of the affected level. In other words, for any disease causative we may be able to describe the change of the protein conformation, its connected effect on the cell's behavior and the ability to form tissues. Ideally, all the levels should be known to address the abnormality with a suitable medical solution:

1. **protein level** - effect on the protein mechanostability and its ability to withstand mechanical force and undergo conformational changes, interpretation of force magnitudes and translation to chemical cues
2. **subcellular level** - affecting organelles and the intracellular communication, affecting the DNA packing and protein expression
3. **cellular level** - affecting the locomotion and stiffness, cells vitality, survival and susceptibility to injury, differentiation or proliferation, homotypic and heterotypic cell-cell adhesion, cell-ECM adhesion and communication
4. **tissue level** - affecting the intercellular communication and tissue formation, remodeling, recovery, maintaining tissue homeostasis and integrity, maintaining intercellular gaps and important barriers
5. **organ level** - leading to affected organ morphology and physiology (skin, lungs, heart or bone and cartilage) leading to pathological development

### 5.1.2 Causatives of mechanotransduction diseases

The causatives of mechanotransduction diseases may be identified on several different levels. For instance we could identify the disease cause by its origin as: **A) molecular and genetic causes** including changes in the protein expression and cellular concentration (including causes such as mutation in promotor regions or epigenetics), or by functional mutation in the mechanosensor protein; or **B) physical origins** including for example the life-style and environment, hemodynamics, etc.

By the type of direct or indirect effect, the disease causatives may be described as: **A) primary** meaning a single or multiple mutations in the mechanosensitive protein affecting directly its mechanosensitivity and force propagation; and

**B) secondary** including alteration or mutation in another cellular component affecting the expression level of mechanosensor in question.

Finally, the effect of single protein missense mutation may cause alteration in mechanosensitive behavior in multiple ways. These mutation effects may be described as follows:

1. mutation located in the ligand binding site affecting the upstream or downstream mechanobiology, i.e. the modification of the force interpretation and translation of the mechanical stimuli into chemical cues
2. mutation in the ligand binding site affecting the ability of target protein to correctly localize within the cell compartments
3. mutation affecting the mechanosensitivity of the protein leading to changes in the protein folding and its mechanical stability
4. mutation affecting the mechanical stability of the target protein causing alteration in quaternary domain organization, modifying domain-domain interactions of the mechanosensor leading to a change in force sensing and translation of the mechanical force into chemical signal

It is also important to note that some of the disease causes may manifest immediately and show clear disease symptoms. On the other hand, there are diseases which remain asymptomatic for decades and manifest only under certain conditions.

## 5.2 Talin and disease (I)

Talin protein is a key constituent of FAs, which play an important role in the tissue remodeling, and in the maintenance of tissue integrity and homeostasis. Even though a single functional mutation in talin-1 protein has not been associated or linked to any pathological condition, changes particularly in talin-1 expression levels in disease have been recognized<sup>99,180</sup>. In such light, talin and vinculin as the major constituents of FAs, and the contribution of altered expression levels were investigated in development or increase of susceptibility to atherosclerosis (I). The mechanobiology of the atherosclerotic plaque formation and the potential role of FAs is introduced in **Figure 15**.

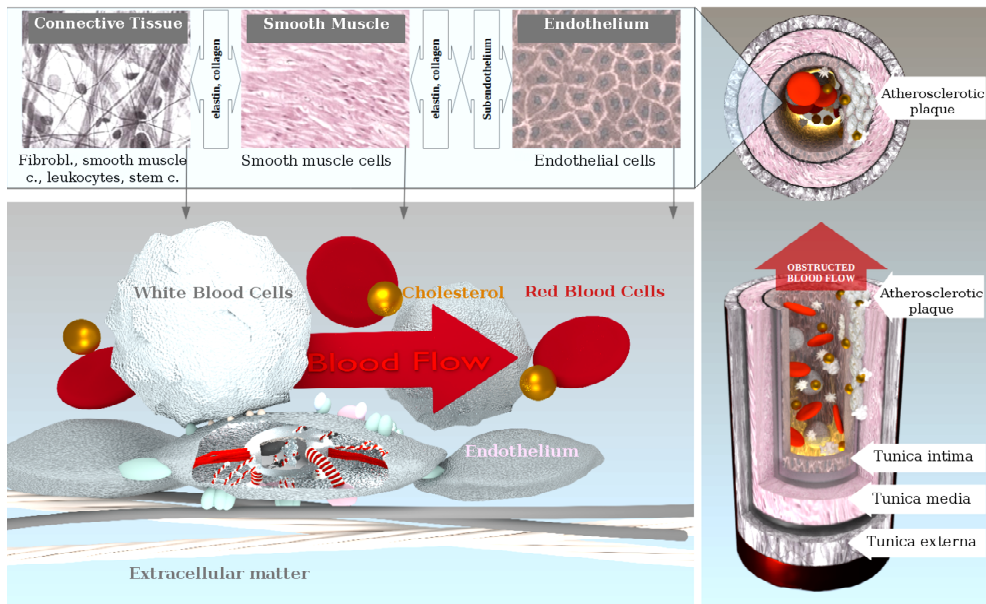


**Figure 15. The artery with atherosclerotic plaque and the development of atherosclerosis from organ to cell level mechanobiology.** The deposition of macrophages in the vessel wall results in obstructed blood flow in the vessel lumen increasing the shear of the blood suspension on the inner vessel lining (Tunica intima). The modified mechanical stimulus impacts the remodeling capabilities of the endothelium and progresses the corrosion of the vessel wall leading to inflammation in the endothelium and smooth muscle and formation of the atherosclerotic plaque.

In this work, microarray analysis and qRT-PCR low-density array were implemented to analyze talin-1, talin-2, meta-vinculin and vinculin gene expression in circulating blood and arterial plaque. It was shown that talin-1, talin-2, meta-vinculin and vinculin genes were significantly and consistently downregulated in plaques of the carotid, abdominal aortic and femoral regions compared to left internal thoracic artery (LITA) control (Article I, Fig.1E-H, Supplementary Table 2). An exemplary comparison of expression in plaque and control is shown for talin-1 and vinculin in **Figure 16**. Among the different arterial bed samples, the expression in carotid arterial samples exhibited greater reduction in the expression compared to femoral arterial beds (Article I, Fig.2, Supplementary Table 2). At the same time, the expression of neither of the investigated genes was affected in circulating monocytes or in the whole blood (Article 1, Supplementary Table 1A).

The expression profiles of the investigated genes were further analyzed as a function of disease progression (Article I, Fig.1A-D). Even though the differences in expression levels between stable and unstable plaques were not statistically

significant, we observed further negative tendency in the expression of talin-1, talin-2 and meta-vinculin in the unstable atherosclerotic plaques.

Confocal tissue imaging revealed high expression of talin-1 in LITA endothelium (Article I, Fig.3A). A gradient of talin-1 expression was observed in plaque with reduction close to the vessel lumen, i.e. talin-1 staining was not observed in the atherosclerotic endothelium while increasing expression was detected towards tunica media. Similar gradient was observed for talin-2 expression in LITA controls but was not detected in plaques (Article I, Fig.3B). This suggests that impaired tissue mechanostability affects the tissue remodeling and healing capabilities leading to development of unstable plaques.

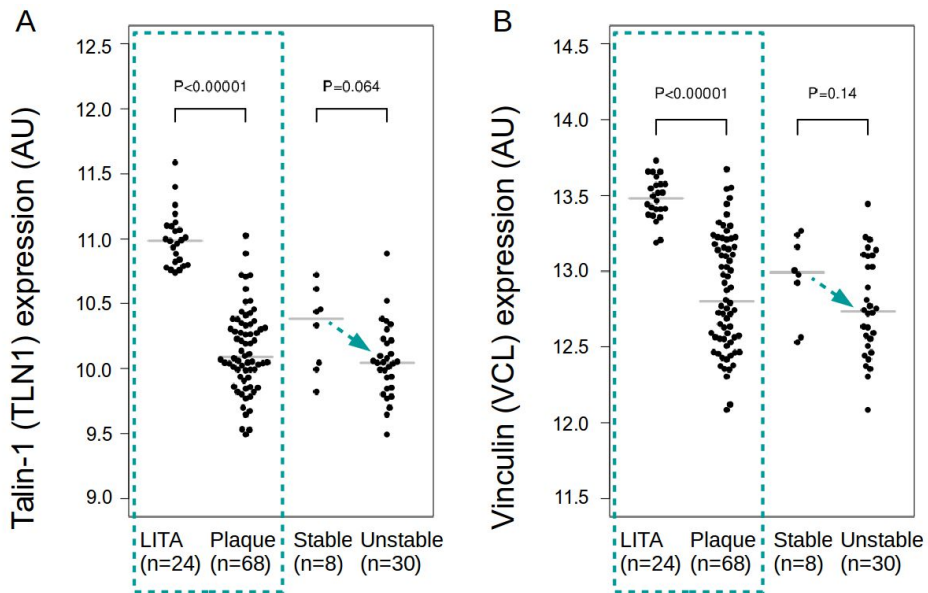


**Figure 16. Expression of talin (TLN) and vinculin (VCL) in atherosclerotic plaque and healthy tissue.** Results of microarray analysis (MA). Expression levels of talin (A) and vinculin (B) in healthy tissue represented by LITA controls and all, stable and unstable atherosclerotic plaques. The expression of talin and vinculin was significantly downregulated in plaques compared to healthy tissue (highlighted with cyan rectangle). Between stable and unstable plaque a protein expression decreasing trend was observed (highlighted with cyan arrow). Modified from Article I. doi:10.1016/j.atherosclerosis.2016.10.031. Reprinted with permission © 2016 Elsevier Ireland Ltd. All rights reserved.

## 5.3 Talin mutagenesis (II)

Despite intensive research of talin protein and talin mechanobiology, the mechanisms of its activation and function remain largely unknown. Since no talin-1 disease linked mutations have been discovered to date, we designed a hypothetical situation to observe the severity of impact on the overall cell motility, proliferation and vitality (II). We have designed a series of destabilizing mutations in talin R3 domain (see **Figure 17B-D**) in order to finally link talin mechanical stability to the cellular response.

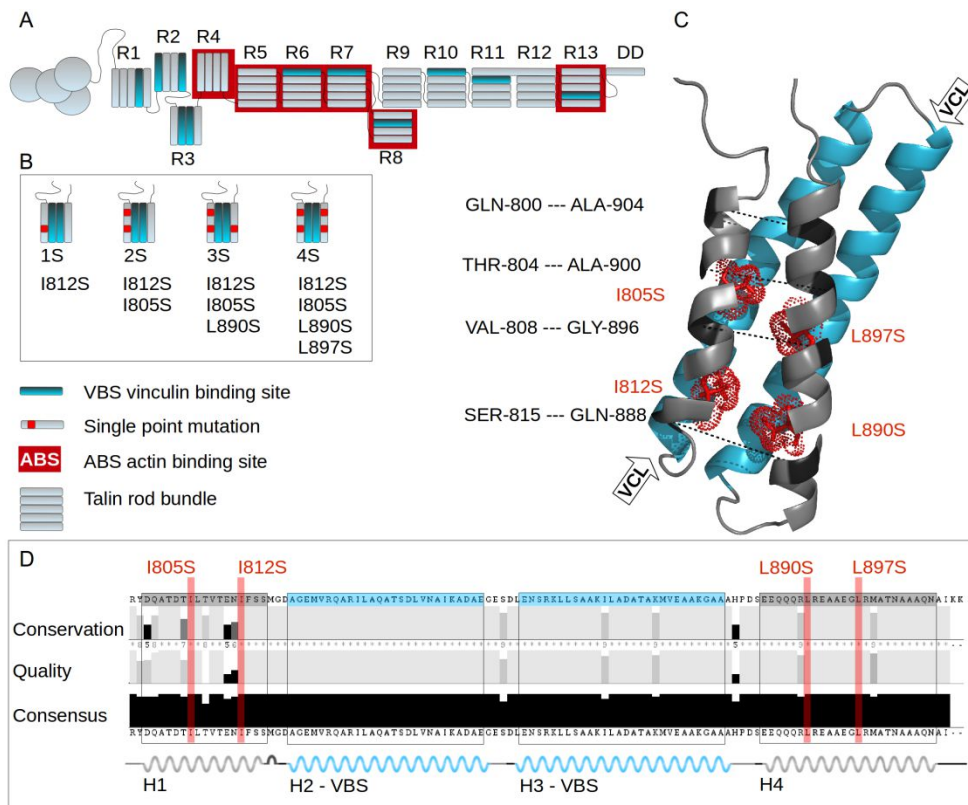


**Figure 17. Talin destabilization mutation design.** (A) Talin structure and domain organization with vinculin binding sites (VBSs) (cyan) and actin binding sites (ABSs) (red). (B) Talin R3 domain and a series of destabilizing mutation in the N- and C-terminal helix, R3H1 and R3H4, respectively. (C) Detail study of talin R3 structure with residues targeted with the mutagenesis design (*in red*) and residues in the terminal helices used in the identification of pulling points for consequent steered molecular dynamics (SMD) simulation (*in black*). Helices R3H2 and R3H3 containing VBSs are shown in cyan. (D) Multiple sequence alignment over species showing high amino acid (aa) conservation. The locations of

residues targeted for mutagenesis are highlighted in *red*, VBSs in *cyan*. A secondary structure guide with corresponding color code is provided below the alignment for orientation. Figure modified from Article II. Published in Scientific Reports, doi:10.1038/s41598-017-03335-2, licensed under CC BY 4.0.

Talin R3 subdomain mechanical stability is rather low compared to other talin rod subdomains. This is due to the presence of hydrophilic threonine belt in the otherwise hydrophobic core of the R3 bundle<sup>206</sup>. With our mutation design we aimed to further destabilize the R3 subdomain. For this purpose we targeted highly conserved hydrophobic residues in the R3 core, isoleucines and leucines. These were mutated into hydrophilic and small amino acid serine in each instance. The selected residues oriented their side chains into the bundle core, they were located at sufficient distances from each other as well as from other polar residues in the existing polar belt. This ensured that formation of new stabilizing polar planes was unlikely. Finally, four talin mutants were produced containing one to four destabilizing mutations. Locations in the R3 subdomain and the panel of final mutants are available in **Figure 17B-D**.

## 5.4 Talin destabilization in SMD (II)

The panel of the destabilized mutants was analyzed utilizing helix-helix stretching in computational SMD investigation. We observed only mild changes in the bundle stability over 10 ns of SMD simulation under 150 pN constant force helix-helix pulling (**Figure 18F, G**).

To provide an objective comparison, the penetrating water molecules were analyzed and count plotted to provide visual comparison (**Figure 18H**). The results showed decreasing mechanical stability with the increasing number of single point destabilizing mutations in the R3 bundle. In more detail, the increase in the penetrating water molecules reflected an increase in the bundle volume when stretched, as illustrated in **Figure 18D** and correlated with the number of the point mutations.

The ability of the destabilized mutants to withstand mechanical force was further analyzed by following the opening of the bundle based on distance changes between the pulled helices R3H1 and R3H4. Previously, we have defined four C $\alpha$  atoms in R3H1 and four C $\alpha$  atoms in R3H4 in order to specify the pulling origins. The distances d1, d2, d3 and d4 between these complements between R3H1 and

R3H4 were the analyzed distances, plotted in **Figure 19** as a distance change over the pulling simulation time.

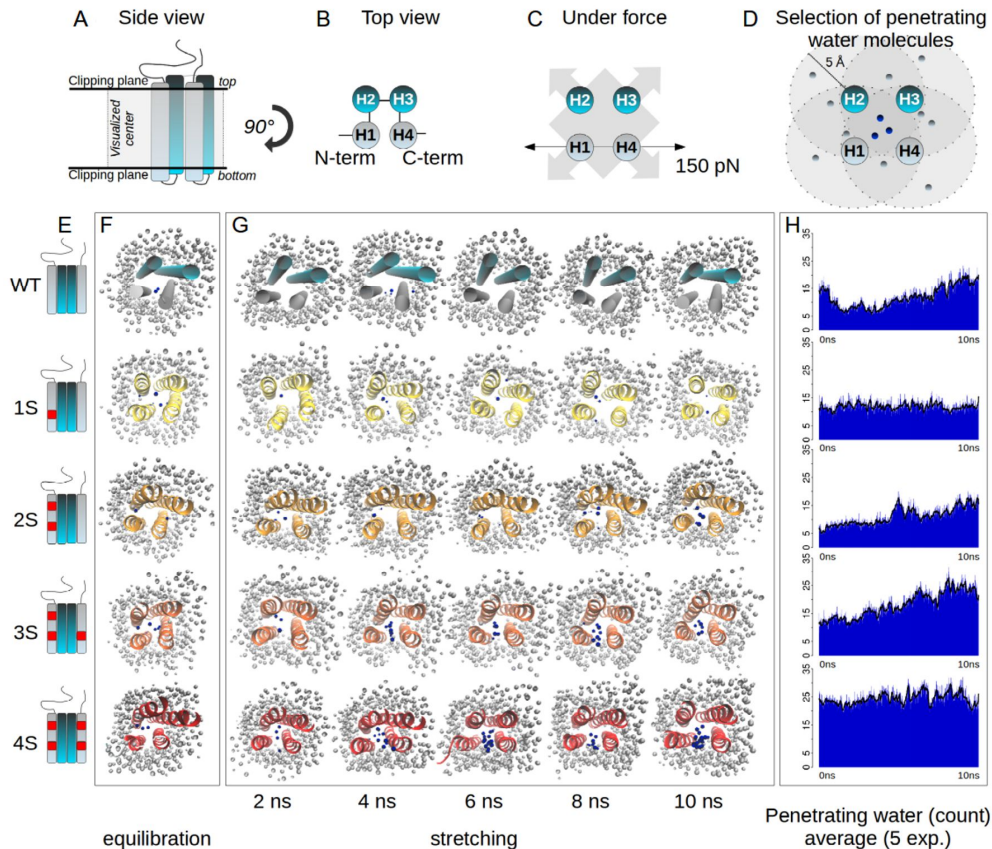


**Figure 18. Destabilizing talin mutations in steered molecular dynamics (SMD) investigation.** (A) Side view of the R3 domain and the use of clipping planes for comprehensive visualization of the water penetration into the bundle core. (B) Top view of the helix organization in the R3 bundle; R3H1 helix at the N-terminal end and R3H4 helix at the C-terminal end were applied pulling force, vinculin binding sites (VBSs) in helices R3H2 and R3H4 are in cyan. (C) Visualization of the 150 pN pulling force effect. The helix-helix pulling caused slight expansion of the R3 bundle. (D) Penetrating water (blue) is the water within 5 Å distance of each helix and in the intersection of all helices. (E) Series of the designed panel of destabilized mutations and schematics. (F) Top view of the bundle organization after 10 ns equilibration. (G) Top view trajectory snapshots over 10 ns SMD with helix-helix stretching with 150 pN. Non-penetrating water in light gray, penetrating water in blue. (H) Penetrating water count over 10 ns SMD with helix-helix stretching with 150 pN. Modified from Article II. Published in Scientific Reports, doi:10.1038/s41598-017-03335-2, licensed under CC BY 4.0.

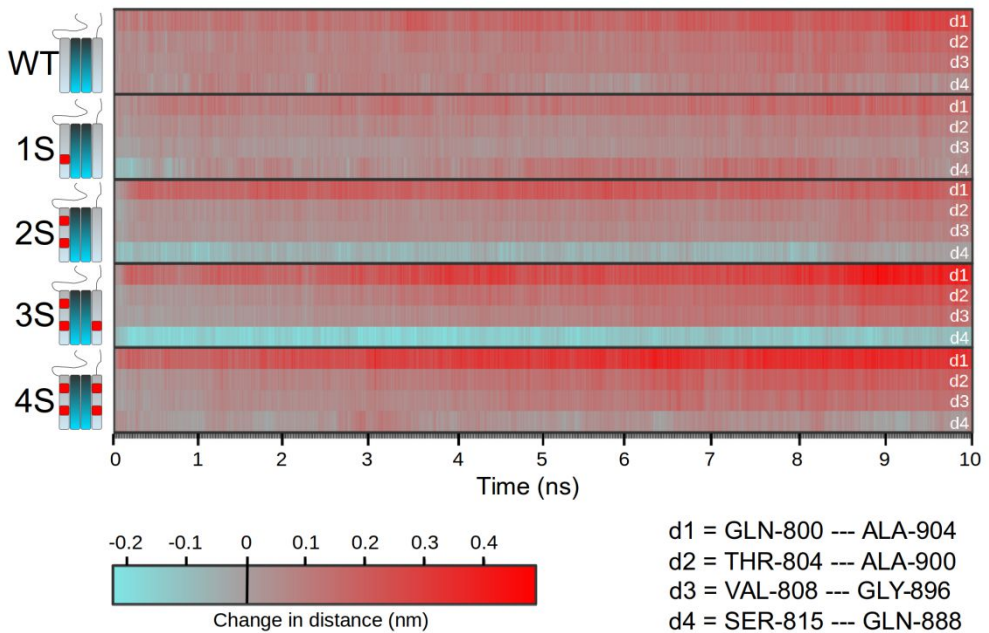


**Figure 19. Destabilization of talin R3 domain and unfolding by N- C- terminal helix-helix constant force pulling over 10 ns at 150 pN.** The mechanical stability is shown on the change in distances between R3H1 and R3H4 helices specified by four vectors, d1-d4. The distances were analyzed over the pulling simulation for wild type R3 domain (WT) and for the panel of destabilized mutants in the R3 domain (1S-4S). Modified from Article II. Published in Scientific Reports, doi:10.1038/s41598-017-03335-2, licensed under CC BY 4.0.

Wild type talin (WT) and 1S talin mutant underwent only negligible changes in the R3H1 and R3H4 helical positions in the range of approx. 0.2 nm. Increase in length in d1 at the top of the bundle and decrease in d4 length at the bottom was observed for 2S mutant. This suggests “opening” of the bundle from the N- and C- terminal ends (the “top” of the bundle) mimicking the classical end-to-end pulling. Similar, yet more intensive, dynamics was observed for 3S and 4S mutants. This suggests that the destabilization in the R3 domain reorganizes the helix positions in the bundle, opens the structure from the N-C- terminal ends and makes the VBS in R3H3 accessible for vinculin binding.

The 4S mutant was also investigated for its ability to refold to its original state. The unfolding and refolding of 4S mutant was followed on the change in d3 distance. The change in d3 vector length located in the center of the bundle was followed over the pulling simulation and consequent classical MD simulation starting from the modestly extended bundle after releasing the pulling points. The d3 distance increased during the pulling simulation, however, returned to its

original length within 7 ns of refolding simulation. This suggests that even the drastically modified R3 domain readily refolded. Also, this showed that the mutagenesis indeed affected mainly the domain mechanical stability, while the domain refolding was not prevented.

## 5.5 Talin destabilization in SMD simulation, biochemical analysis and *in vivo* (II)

This paragraph briefly compares the results of SMD simulation to the experimental biochemical and *in vivo* experiments performed by others and included in Article II.

Even though the observations in the computational simulation were very mild (**Figure 18** and **Figure 19**), biochemical analysis (Article II, Figure 2h-k) and *in vivo* investigation (Article II, Figure 3-5) suggest considerably greater impact of the mutagenesis on the R3 domain stability and overall character. For example, the 3S and 4S were shown to form dimers in gel filtration analysis (Article II, Figure 2i). Also, folding and thermal stability analysis showed that WT and 1S have closely matching folding and thermal stability properties, whereas 2S showed decreased subdomain helicity, analyzed with CD spectroscopy. The decrease in helical properties and thermal stability was further enhanced in 3S and 4S mutants (Article II, Figure 2j-k). This suggests that the drastic mutagenesis in the hydrophobic core decreased helical content, which may have allowed for dimerization through the exposure of normally hidden hydrophobic patches. During the pulling simulations helix bending and torsions in the mutated locations were observed, particularly for 3S and 4S mutants. This leads to similar conclusions of reduced helical stability and domain dissociation.

Cell experiments have shown that the R3 destabilization induces the accumulation of destabilized talin in cell-ECM adhesions (Article II, Figure 3c-e). Furthermore, this accumulation is independent of R4-R12 subdomains suggesting that this accumulation is caused only by affected mechanical stability and not by disrupted autoinhibition conformation or by additional actin binding site (ABS) located in R4-R8 subdomains (Article II, Figure 3f-g).

It was also shown that the R3 destabilization affected traction force generation (measured by elastic substrate and fluorescent microbeads), talin and vinculin mobility and turnover in FAs (analyzed by FRAP) and the rate of cell migration. In detail, talin-1 removal caused dramatic decrease in the average cell area and complete loss of cellular traction. The re-expression of GFP-tagged WT talin-1

rescued cell spreading to full extend and largely rescued force traction (Article II, Figure 4a-c). Re-expression of the destabilized mutants rescued the cell spreading and force traction depending on the mechanical stability. For instance, 1S talin caused only small, statistically insignificant increase in traction force compared to WT talin, while the cell spreading was fully reestablished. Destabilized mutants 2S, 3S and 4S resulted in increasing severity of defects in the traction force generation and cell spreading.

Increased mobility in cell-ECM adhesions of 1S and 4S destabilized talin mutants was detected by FRAP (Article II, Figure 4d) together with significant increase of vinculin fraction in the adhesions (Article II, Figure 4e). The increased vinculin fraction was probably caused by slow exchange rate in destabilized talins.

The effect of the talin destabilization was also observed on the rate of cell migration on a fibronectin coated surface. The introduction of a single point mutation (1S) did not affect the rate of cell migration, while the introduction of 4 point mutations (4S) has significantly reduced the migration rate (Article II, Figure 4f-g).

It was also observed that talin R3 destabilization affects the ECM sensing and talin colocalization with different integrin subtypes (Article II, Figure 5). More precisely, a difference in the colocalization between talin and ECM proteins fibronectin and vitronectin was observed using micropatterned cell culture substrates between the wild-type and mutated talins. Hence the talin destabilization does not affect solely the adhesion dynamics but also the cell-ECM composition and adhesion segregation.

## 5.6 Talin rod and mechanosensitivity (III)

Previously, we showed that talin and its mechanostability provides for the physical and functional link driving the cellular response to mechanosensing (II). In the following, we concentrated on the mechanical properties of talin individual rod bundles under mechanical force to uncover the talin mechanotransduction and mechanosensitive roles in the signaling pathways.

Given two distinct parts in the talin rod characterized by differences in their quaternary structure organization, these parts were assumed distinct functions in the cell's mechanobiology. The N-terminal compact region of the talin rod (R1-R3) was assumed the mechanosensitive and mechanosignaling roles, whereas the elongated C-terminal end (R4-R12), described as "beads on a string" conformation,

was assumed the force propagation function<sup>113</sup>. Undeniably, force-induced talin unfolding and binding activation has been demonstrated by others for a small portion of its rod domain, namely the compact N-terminal region<sup>17,51</sup>.

Because of the abundance of binding sites among the talin rod, buried inside the bundle cores as well as on the bundle surfaces, it was hypothesized that the whole talin rod is mechanosensitive. In other words, also the elongated part of the talin rod was suspected to undergo conformational changes and drive mechanosignaling cascades.

By using single-molecule atomic force microscopy (smAFM) carried out by del Rio group, it was shown that the entire talin rod can be unfolded by mechanical extension. The talin rod was separated into fragments R1-R3, R4-R6, R7-R8, R9-R10, and R11-R12. With the exception of R1-R3 and R7-R8 fragments, the number of unfolding events corresponded to the number of domains (Article III, Figure 2). Fragment R1-R3 showed 2 unfolding events suggesting that one domain unfolded undetected (Article III, Figure 2a, f). This is consistent with previous studies showing that R3 is the most mechanosensitive domain in the talin rod, unfolding with force of approx. 5 pN<sup>29</sup>. This lies below the detection limit of the smAFM methodology used here. Fragment R7-R8 has a unique helix fold, where the 4-helix R8 bundle is inserted into 5-helix R7 and requires complete R7 unfolding prior to its own disintegration. In the smAFM analysis, R8 subdomain showed similar mechanical unstable nature similar to R3 domain unfolding under minimal mechanical force (Article III, Figure 2c, h).

## 5.7 Talin unfolds over a range of forces (III)

Through a combination of smAFM and computational simulation (SMD) it was demonstrated that the different bundles within the talin rod exhibit a distinct hierarchy of mechanical stability. Moreover, the investigated talin rod bundles disintegrated over a physiological range of forces between 10 and 40 pN (Article III, Figure 3a-e). This suggests that all the investigated talin rod subdomains hold a physiologically relevant mechanosensitive function apart from the force propagation roles. In more detail, such a range of mechanical stability over the talin rod proposes that different force regimes control a graduated unfolding of the talin rod in the cell environment. The mechanical unfolding of the rod subdomains switching between talin binding interactions through changes in the binding site

availability, would allow for a fine cellular response to internal or external forces (III).

## 5.8 Unfolding of single talin rod bundles in SMD (III)

The smAFM experiments described above revealed a range of unfolding forces for the fragments of talin rod domains. Also, a certain hierarchy of bundle stability was observed. In the following, computational SMD methods were utilized to assess the stabilities of individual talin rod bundles. The calculated force traces (based on Eq. 1) are presented for R3, R4, R5, R6, R7-R8, R10, R11 and R12 in **Figure 20**. The pulling simulations were performed at constant speed pulling at a rate of 0.1 and 2 nm/ns for individual domains. Both pulling rates simulations revealed similar hierarchy of mechanical stability of the investigated talin rod bundles. The SMD single domain simulations support the findings of the experimental smAFM investigation for talin rod fragments.

Because of the character of the computational simulation, the resulting unfolding forces are considerably higher compared to experimentally measured forces or even so, physiological forces. For that reason, we have compared SMD and smAFM results based on hierarchy or unfolding patterns rather than on absolute force magnitude. For simplicity, we have organized the talin rod bundles into three groups; weak (R3, R4, R6 and R10), intermediate (R7, R11 and R12), and strong (R5 and R9) based on the results of computational and experimental unfolding patterns.

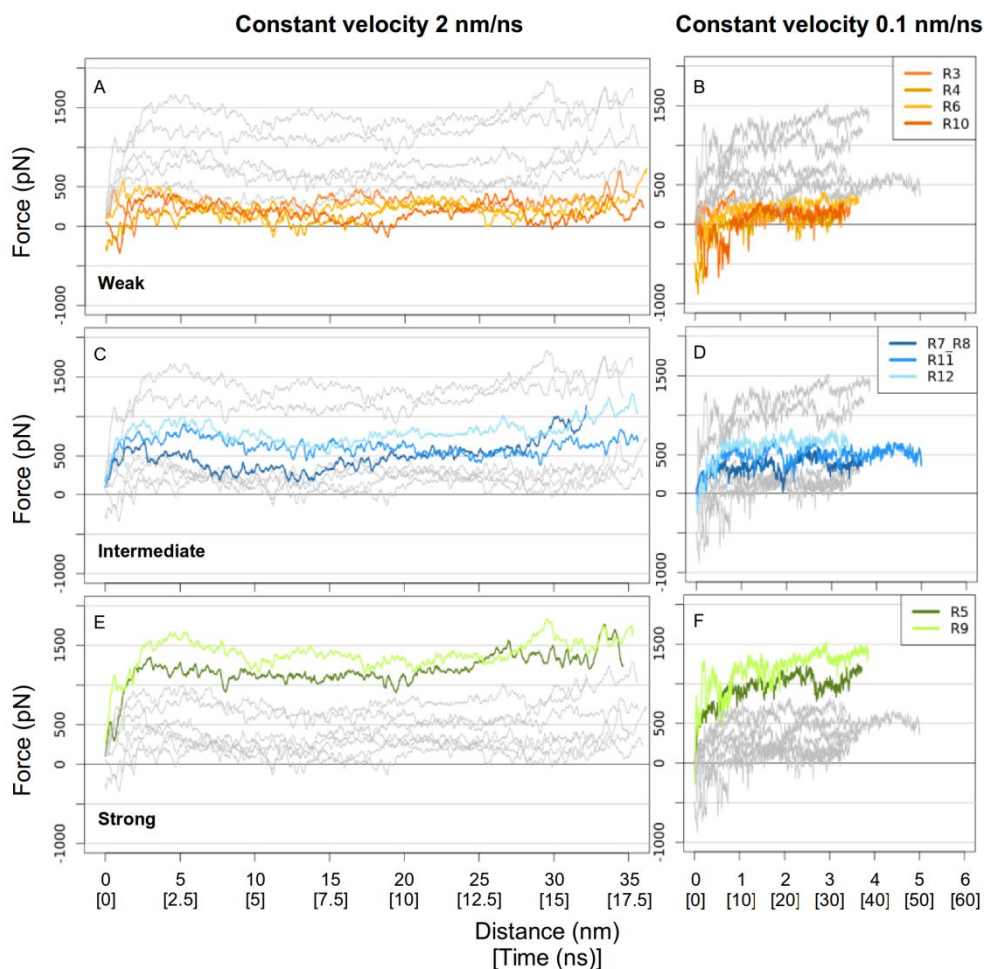


**Figure 20. Talin rod domains (R3-R12) and unfolding force in constant velocity SMD pulling.** Unfolding patterns of weak (A, B) in orange shades, intermediate (C, D) in blue shades, and strong domains (E, F) in green shades are presented for two pulling rates of 2 nm/ns (A,C,E) and 0.1 nm/ns (B, D, F). Modified from Article III. Published in ACS Nano, DOI: 10.1021/acsnano.6b01658, Copyright © 2018 American Chemical Society, licensed under ACS AuthorChoice.

Based on this simplified hierarchy, the talin rod mechanobiology and the location of the different bundle stabilities are drawn in **Figure 21**. It can be seen that the different bundle sensitivities are distributed over the whole rod placing mechanically weak bundles next to or between mechanically stronger subdomains.

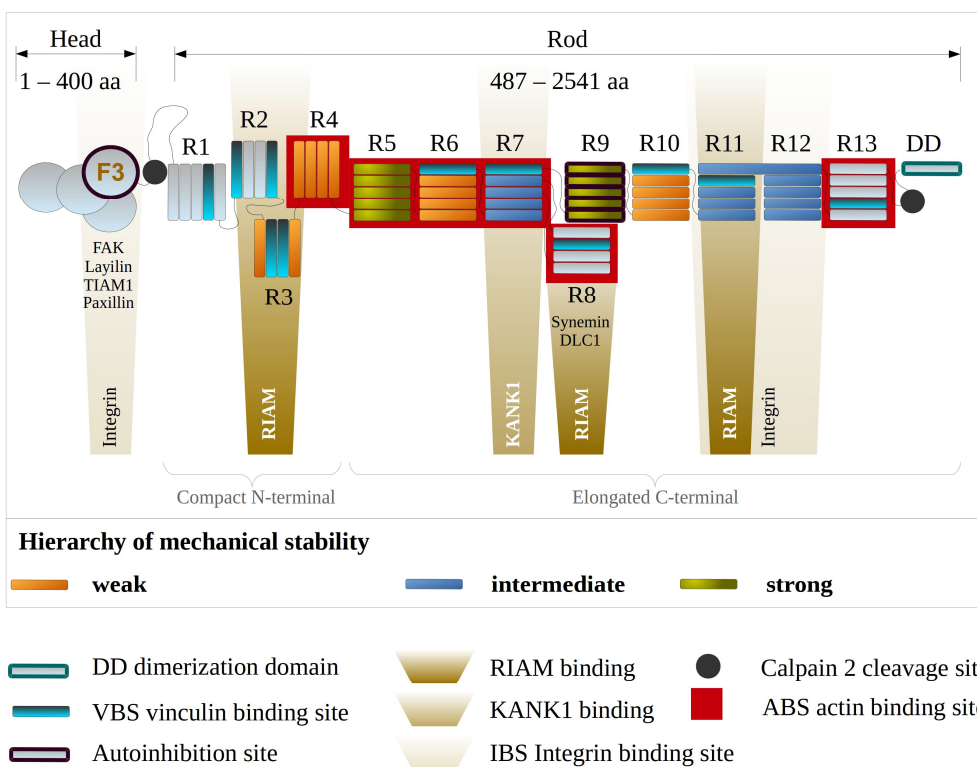


**Figure 21. Hierarchy of mechanical stability among talin rod bundles based on results of constant velocity SMD simulation.** Bundles and helices represented by gray color were excluded from the investigation (R1, R2, R13 and DD) or did not unfold within the total simulation time (R8). Bundles represented by *orange* color (R3, R4, R6 and R10) were weak and unfolded readily or under low mechanical forces. Intermediate bundles R7, R11 and R12 are presented in *blue*. Bundles at the upper force range were described as strong and were assigned *green* color. Bundles with varying mechanical stability are distributed over the talin rod, placing mechanically weak bundles between the mechanically stronger subdomains.

The unfolding dynamics of talin subdomains was further investigated in unfolding simulation of multi-domain fragments. The examples of the unfolding dynamics among the fragments are available in **Figure 22**. Even though the unfolding force peak assignment to individual subdomain collapse was not possible and the overall interpretation of the SMD force traces proved challenging, interesting details of multi-domain system unfolding were observed. In particular, certain inter-domain cooperation and simultaneous unfolding leading to the formation of intermediate states were recognized in multiple instances. The existence of a 3-helix intermediate and the connected investigations are included in the paragraph below concerning Article IV.

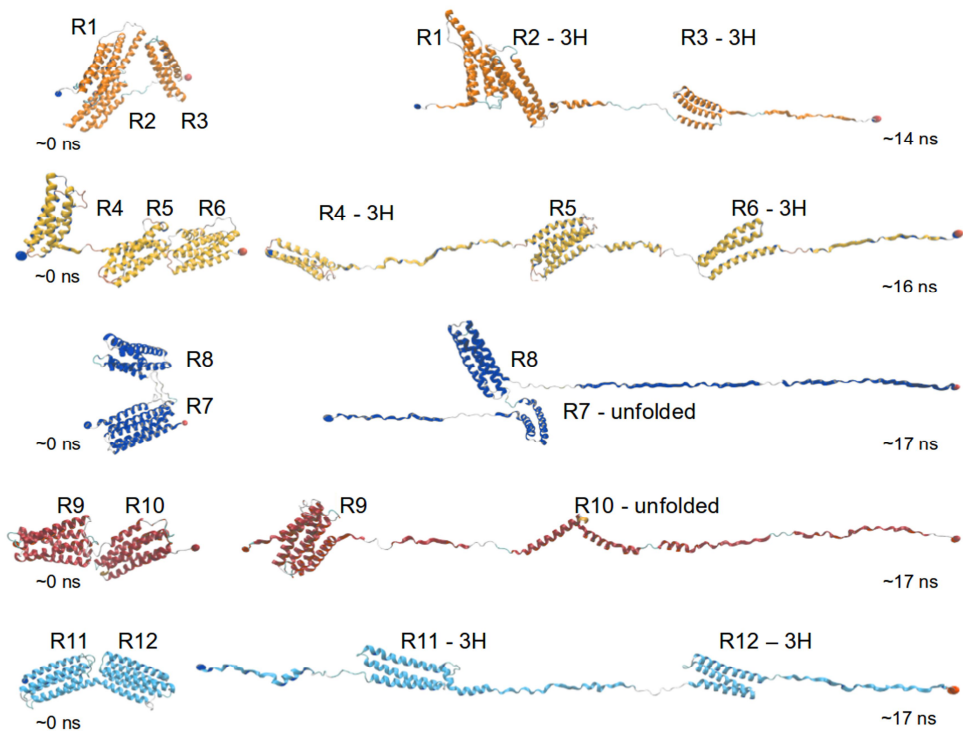


**Figure 22. Unfolding dynamics of talin rod fragments in constant velocity steered molecular dynamics (SMD) investigation.** Talin rod domains with similar mechanostability unfold simultaneously into a 3-helix stable conformation. This unfolding intermediate is present in the unfolding pathway of both 4- and 5-helix subdomains.

## 5.9 3-helix intermediate in 5-helix subdomains (IV)

During our previous computational simulations of talin rod fragments as well as single domains we have observed common intermediate structure among the unfolding trajectories. In order to further investigate such unfolding intermediate, two  $\alpha$ -helical mechanosensory proteins, talin and  $\alpha$ -catenin were selected for the computational and smAFM experiments.

Constant velocity pulling simulation at a 2 nm/ns rate revealed that talin rod 5-helix bundles R9 and R11 unfolded through a stable 3-helix intermediate **Figure 23**). The unfolding force showed two peaks for each individual bundle corresponding to breaking of the 5-helix original state and to the breaking of the 3-helix intermediate state. The 3-helix intermediate core consisted of helices H2,

H3 and H4 after the N- and C- terminal helices (H1 and H5) dissociated from the 5-helix subdomain.

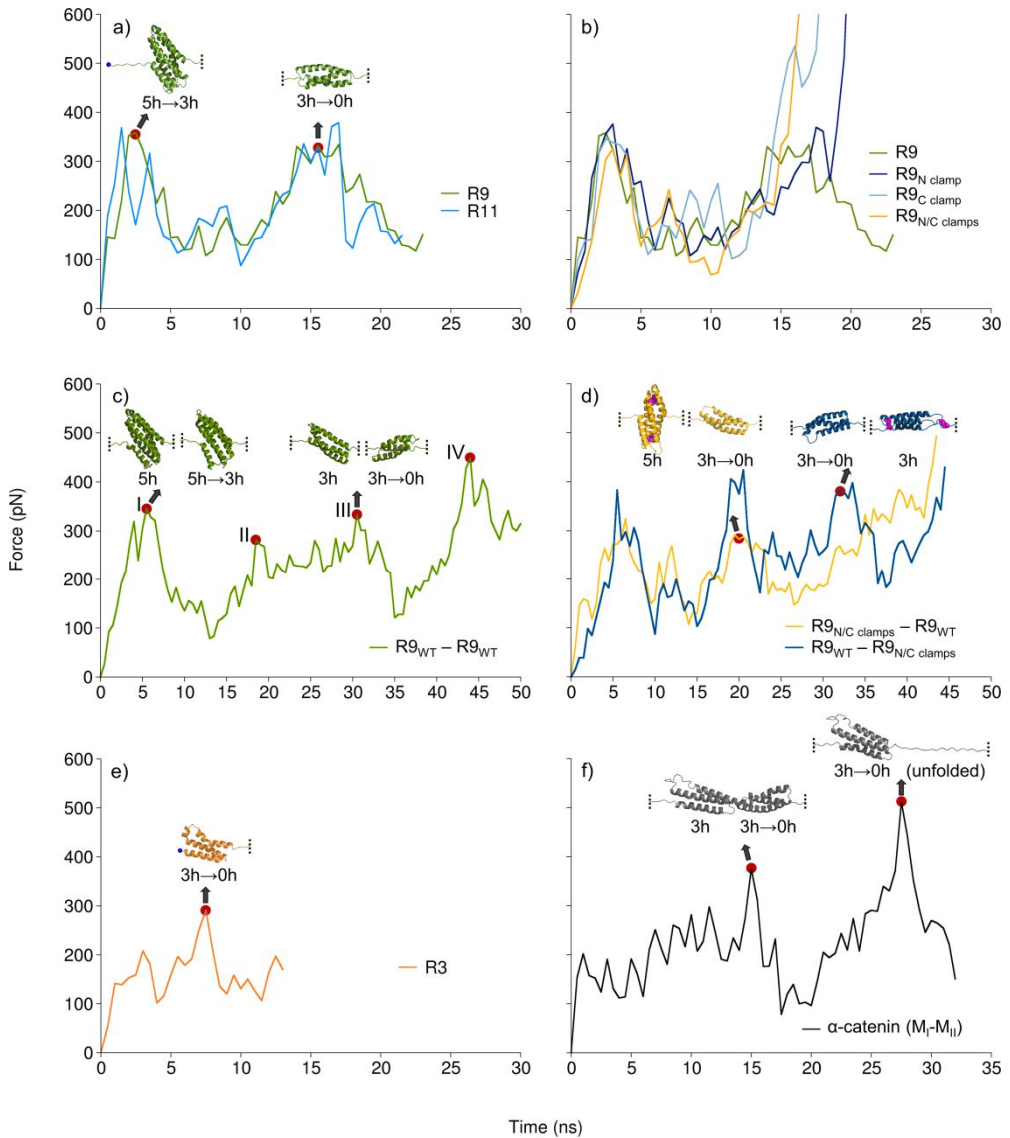


**Figure 23. Unfolding force profiles of talin and  $\alpha$ -catenin subdomains reveal an unfolding 3-helix intermediate in constant velocity SMD.** (a) Unfolding forces of the talin R9 and R11 subdomains showed similar profiles and revealed two force peaks corresponding to the breaking of the 5-helix bundle and 3-helix intermediate. (b) R9 constructs with disulfide clamps protecting the 3-helix state showed similar unfolding peak at the breakage of the 5-helix bundle at approx. 2.5 ns simulation time, absence of a second peak corresponding to 3-helix intermediate reflected efficient blocking of the unfolding. Simultaneous unfolding

through a 3 helix intermediate was recognized for R9<sub>wt</sub>-R9<sub>wt</sub> tandem (c) and for  $\alpha$ -catenin M<sub>I</sub>-M<sub>II</sub> double domain (f). (c) R9<sub>wt</sub>-R9<sub>wt</sub> tandem showed four peaks corresponding to breaking of the R9<sub>5h</sub> – R9<sub>5h->3h</sub> (peak I), R9<sub>5h->3h</sub> – R9<sub>3h</sub> (peak II), R9<sub>3h</sub> – R9<sub>3h->0h</sub> (peak III), and R9<sub>3h->0h</sub> – R9<sub>0h</sub> (peak IV). (d) Tandems with the clamped 3-helix state in one monomer showed three peaks, lacking the peak for unfolding of the clamped 3-helix state. (e) Unfolding force of 4-helix R3 bundle has one peak that corresponds to the 3-helix state disintegration. (f) 4-helix  $\alpha$ -catenin showed two peaks, one peak per 3-helix state break in each subdomain. Cysteine residues in (d) R9 tandems, that form disulfide clamps shown as magenta spheres. Structure snapshots correspond to force peaks are highlighted with *red dots*. Modified from Article IV. Published in PLOS Computational Biology, doi: 10.1371/journal.pcbi.1006126, licensed under CC BY 4.0.

The existence of the intermediate state was confirmed by utilizing point mutation design stabilizing the 3-helix intermediate through creation of disulfide bonds. These clamps were formed in positions L1698C – A1748C to protect the N-terminal end and denoted as N clamp; and in positions A1720C – A1779C to prevent the C-terminal unfolding and denoted as C clamp. R9<sub>N clamp</sub>, R9<sub>C clamp</sub> and R9<sub>N/C clamps</sub> showed similar unfolding forces during the initial 5-helix bundle disintegration compared to the R9<sub>WT</sub> (**Figure 23b**). The use of only one of the clamps, N or C clamp at a time, allowed continuous unfolding of the H4 or H2, respectively. Based on the comparison of the traces and known constructs, it was possible that the unfolding state indeed reflects the 3-helix fold.

## 5.10 3-helix intermediate in 4-helix subdomains (IV)

In the additional experiments the unfolding of 4-helix bundles, talin R3 and  $\alpha$ -catenin modulation domain I and II were investigated. Here, talin R3 domain dissociated its 4-helix bundle under low force and formed a 3-helix intermediate consisting of H1, H2 and H3 helices. The following force trace showed that the unfolding of the intermediate state required considerably higher force compare to the original 4-helix subdomain. Similarly,  $\alpha$ -catenin 4-helix tandem subdomains unfolded to a 3-helix conformation by the dissociation of the N- and C- terminal helices (**Figure 23e, f**).

## 5.11 3-helix intermediate in talin tandem subdomains (IV)

In the following, the force penetration effect on the SMD mechanisms and the intermediate existence in a tandem fragment resembling native talin subdomain

organization were established. Because of previous challenges in the interpretation of the multi-domain unfolding force traces, an artificial R9<sub>WT</sub>-R9<sub>WT</sub> tandem was investigated. By using two identical bundles we assumed identical mechanical stability. Together with disulfide clamp tandem mutants (R9<sub>N/C clamps</sub>-R9<sub>WT</sub>, R9<sub>WT</sub>-R9<sub>N/C clamps</sub>), the setup allowed for the investigation of SMD force penetration as well as for observations of the unfolding principles and comparison of 5- and 3-helix stabilities in multi-domain systems.

The unfolding of R9<sub>WT</sub>-R9<sub>WT</sub> revealed four peaks corresponding to dissociation of both of the 5-helix states (peaks I and II) followed by the collapse of the 3-helix states (peaks III and IV). From the view of the force penetration through the SMD system, the mechanism of the unfolding progressed as follows: R9<sub>5h</sub> – R9<sub>5h->3h</sub> (peak I), R9<sub>5h->3h</sub> – R9<sub>3h</sub> (peak II), R9<sub>3h</sub> – R9<sub>3h->0h</sub> (peak III), and R9<sub>3h->0h</sub> – R9<sub>0h</sub> (peak IV) (**Figure 23c**). This means that the unfolding progressed rather from the C-terminal end, where the pulling force application point was located.

Both tandems containing N/C clamps in the first or second subdomain unfolded with three peaks each (**Figure 23d**). However both tandems showed different unfolding dynamics, which was affected by the orientation of the tandem with respect to the force application point. In other words, the force penetration of the SMD impacted the observed unfolding dynamics. R9<sub>WT</sub>-R9<sub>N/C clamps</sub>, i.e. C-terminal clamp with C-terminal pulling point, unfolded both tandem subdomains into 3-helix intermediate states followed by collapse of R9<sub>WT</sub> 3-helix state resulting in three force peaks. On the other hand R9<sub>N/C clamps</sub>-R9<sub>WT</sub>, i.e. N-terminal clamp with C-terminal pulling point initially unfolded R9<sub>WT</sub> completely before the collapse of 5-helix subdomain of R9<sub>N/C clamps</sub> appeared (Article IV, Figure 3).

## 5.12 3-helix intermediate in constant force SMD

In addition to the constant velocity simulation described above, which is a valuable simulation regime for comparison with AFM experiments, constant force simulation was performed to support the observations. The constant force simulation regime is considered more sensitive for fold stability investigation compared to constant velocity pulling.

Two talin bundles were investigated in the constant force pulling regime, the mechanically weak 4-helix R3 bundle (**Figure 24a**) and the mechanically stable 5-helix R9 subdomain (**Figure 24b**). R3 bundle was subjected to force range between 160 to 200 pN, and unfolded its 4-helix bundle to a 3-helix state even at the lowest

tested force of 160 pN. The 3-helix state remained stable up to 40 ns simulation and unfolded completely during 72 ns pulling.

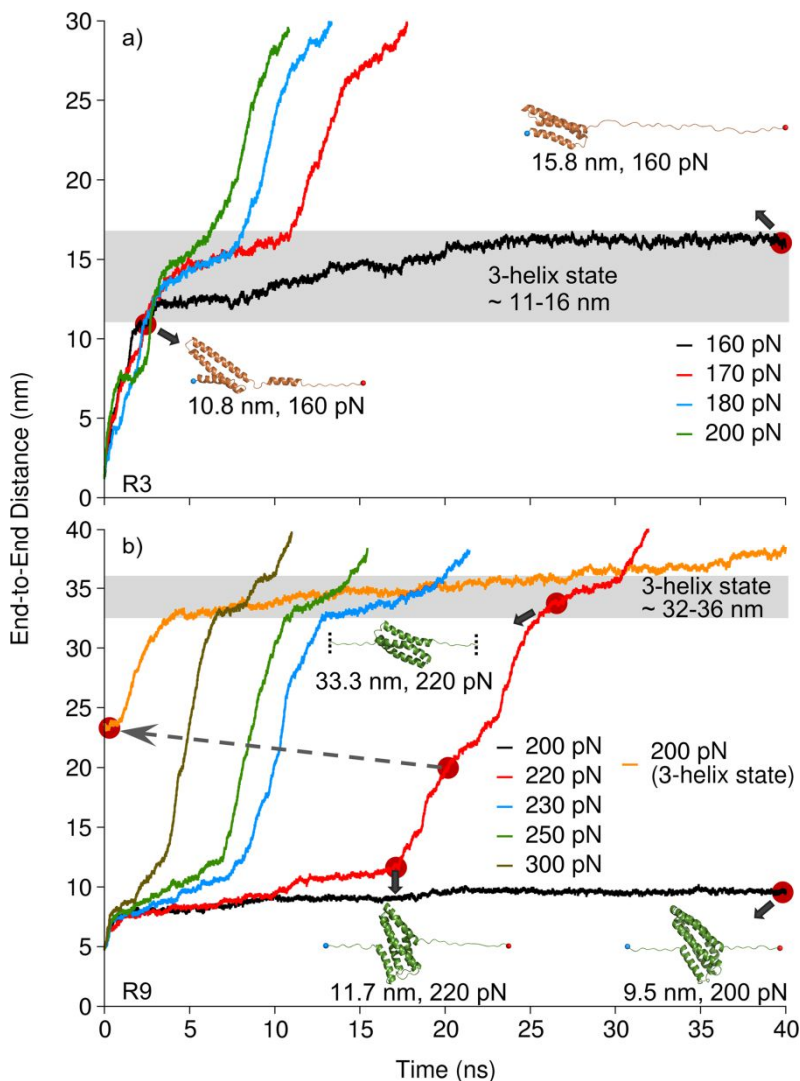


**Figure 24. Stability of 3-helix intermediate state in talin 4- and 5-helix unfolding.** Talin 4-helix bundle R3 (a) and 5-helix bundle R9 (b) were subjected to constant velocity SMD pulling at different force magnitudes. Despite different mechanical stabilities of the investigated bundles, both unfold through a stable 3-helix intermediate (*gray shading*). Mechanically weak R3 subdomain (a) readily unfolded even under low force magnitude of 160 pN (*black* in panel a). Mechanically stable R9 subdomain (b) resisted initial 5-helix disintegration under 200 pN (*black* in panel b). However, when the initial 5-helix domain was broken (with greater force), it unfolded to and above of the 3-helix intermediate at 200 pN (*orange* in panel b). Force of greater magnitude did break initial R9 fold starting at 220 pN force

magnitude. Stable 3-helix intermediate was observed at ~11-16 nm and ~32-36 nm end-to-end distances for 4-helix and 5-helix subdomain, respectively. Modified from Article IV. Published in PLOS Computational Biology, doi: 10.1371/journal.pcbi.1006126, licensed under CC BY 4.0.

R9 subdomain remained intact during 40 ns under 200 pN, it however unfolded to 3-helix state at approx. 86 ns simulation. With higher force in a range between 220 to 300 pN, R9 subdomain unfolded gradually through a 3-helix state. To test the relative stability of the 3-helix state and the 5-helix bundle, the disrupted 5-helix conformation of R9 (resulting from approx. 20 ns of 220 pN) was applied 200 pN force (**Figure 23b**, orange trace). While 5-helix bundle resists the 200 pN pulling force, this magnitude is sufficient to proceed the unfolding towards and through the 3-helix state.

### 5.13 3-helix intermediate in smAFM

smAFM experiments were utilized by del Rio group to investigate the existence of the 3-helix intermediate *in vitro*. smAFM pulling of R9 and R11 revealed two unfolding events for each subdomain (Article IV, Figure 4) implying the existence of a mechanically stable intermediate. Overall the mechanical stability of R9 was higher compared to R11. The first detected distance between the unfolding events was 20-25 nm, which is consistent with the distance change between 5-helix and 3-helix conformations. The second detected distance of 25-35 nm was consisted with a collapse of a 3-helix conformation to fully extended protein.

Tandem R9 constructs showed that domains in smAFM probably collapse completely one after another. However the error margin of the distance/peak assignment provides for uncertainty in drawing conclusions on the unfolding dynamics. Unfolding with the clamped tandems reduced the unfolding peaks from four to three (Article IV, Figure 5a-h).

The unfolding of the  $\alpha$ -catenin tandem showed 2 unfolding events approx. 50 nm apart suggesting that 4-helix bundles unfolded undetected into 3-helix states. The two unfolding events observed correspond to the unfolding of 3-helix states simultaneously in both  $\alpha$ -catenin subdomains (Article IV, Figure 5i-l).

## 6 DISCUSSION

Despite growing awareness of the mechanobiology fields and ongoing intensive research, the fundamental questions in mechanotransduction remain unanswered. It is still not fully understood how cells sense and interpret mechanical forces exerted on them by their environment and how they drive their mechanical response in health and in disease. This thesis introduced several areas from diverse research fields of molecular biology, structural bioinformatics or medicine, and discussed mechanobiology from different angles from submolecular to tissue level. The main focus of the work was on the mechanosensitive protein talin. The work introduced here and performed in cooperation with our collaborators yielded new knowledge in the field of talin mechanobiology and fundamental principles of protein unfolding under applied mechanical load. The results and observations are in detail discussed by topics below.

### 6.1 Mechanotransduction components in disease

The reviewed literature and presented graphics in **Figure 3 - Figure 14** sketched the incredible complexity of the mechanotransduction pathways within single cells and tissues. These graphs emphasize the connections between the components within the cell and between the cell and ECM. More importantly, the links between the different structural components suggest overlapping roles, possible cooperation in cellular mechanotransduction as well as compensation for failed function.

The graphical presentation also shows similarities in structural homology over domains of known mechanosensitive proteins. For example,  $\beta$ -sheet Ig titin-like domains are abundant over large fraction of the proteins in the force bearing apparatus in the cell, ECM, at the cell surface and in the muscle sarcomere. Also  $\alpha$ -helical structures are common in different types of folds with varying number of helices.

We have used the structural homology in the public database searches during the data collection as one of the approaches to investigate all possible mechanosensitive proteins. We propose that the structural homology is a useful

tool in mechanosensor identification. It should be noted though, that mechanosensitive structures comprise of a number of varying domains and folds responsible for varying functions. For example,  $\alpha$ -actinin consists of two calponin homology domains (CH) facilitating actin binding, four spectrin repeats responsible for the mechanotransduction roles and two EF hand domains accounting for calcium binding<sup>97</sup>. These different domains comprising a mechanosensitive protein may be involved in the force sensing and transduction directly or indirectly and on different levels of the signal transduction mechanisms.

## 6.2 Talin and vinculin expression in atherosclerosis

The investigation of the expression levels of the two talin isoforms (talin-1 and talin-2) and two vinculin isoforms (vinculin and meta-vinculin) showed that their expression is significantly reduced in atherosclerotic plaques. It can be speculated that such reduction in the protein expression is one of the initial triggers for the atherosclerotic plaque formation. Talin with the wide variety of binding partners acts as a signaling hub converting mechanical signals into chemical cues<sup>120</sup>. Hence a reduction in its expression in the vascular endothelium may increase susceptibility to injury and promote inflammation<sup>209</sup>. The endothelium also acts as a barrier for large molecules to enter the inner layers of the vascular wall. Malfunctions in the mechanical stability of the endothelial vessel lining, caused by reduced expression of adhesion proteins (talin and vinculin among others) may trigger pathological processes in the inner layers of the vessel wall leading to inflammation, macrophage (M $\Phi$ ) accumulation and plaque formation<sup>210</sup>. Hypothetical talin and vinculin roles in the atherosclerotic plaque formation and progression are visualized in **Figure 25**.

The role of talin and vinculin proteins in the atherosclerosis development may be well justified. However, the cause of the initial expression downregulation remains unknown. One of such downregulation reasons could be an external factor such as change in the blood pressure or viscous properties of the blood suspension causing changes in the shear stress exerted on the vascular wall. The magnitude of shear stress was shown to affect the expression of several adhesion molecules facilitating the leukocyte adhesion. Also the expression of FA proteins of the integrin and kindlin family was altered in progressing atherosclerotic plaque<sup>140,207,211</sup>. Integrin and kindlin family proteins are crucial components in the cellular mechanotransduction. Mechanotransduction and mechanosensing has been

long suspected to affect the DNA packing and control the protein expression in healthy and diseased tissue<sup>13,212</sup>. Likewise, a change in the cell composition in the atherosclerotic plaque may have a significant impact on the ability of cells and tissues to withstand mechanical forces and correctly interpret these signals into normal response.

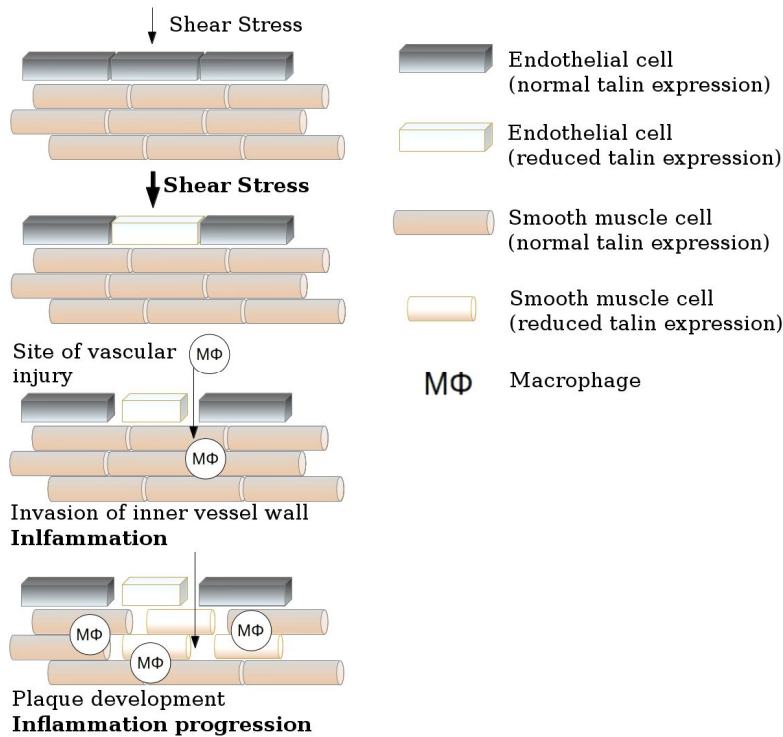


**Figure 25. Simplified speculative model for downregulation of talin expression in vascular endothelium as initial trigger of atherosclerotic plaque formation.** Modified from Article I. doi:10.1016/j.atherosclerosis.2016.10.031. Reprinted with permission © 2016 Elsevier Ireland Ltd. All rights reserved.

Talin was previously shown crucial for embryonic vascular development in mice<sup>12</sup>. Talin expression has recently been intensively investigated in aggressive cancers<sup>179,180,181,182</sup> as well as in hypertrophic myocardium and failing heart<sup>99</sup>. Here, it was shown for the first time that the expression of talin and vinculin isoforms is reduced in atherosclerosis. It was further discussed that these crucial components in the cellular mechanotransduction may hold vital impacts on the atherosclerotic plaque development and disease progression.

## 6.3 Challenges of mechanotransduction disease research

The comprehensive overview of mechanotransduction components and their known association with disease shows that altered expression or functional, missense mutation in different mechanotransduction components may result in similar symptoms and diseases. On the other hand, one mechanotransduction protein may be responsible for number of diverse symptoms and diseases posing a major challenge in the causative investigations.

The diagnostics of diseases is another important challenge in the field. Number of diseases remains asymptotic for long periods of time. Also the detection and screening methods pose limitations in correct symptom or progress of disease assessment. Atherosclerosis is a model example in such problematic disease diagnostics. It is caused or altered by a vast number of external and internal factors including genetics, molecular expression or life style impacts. Even though changes in the inner wall morphology and histology start forming already in the early age, they do not manifest in a serious condition until after several decades<sup>213</sup>.

Progress in genetics research and ongoing whole genome screening projects are constantly providing vast amount of data on gene mutations possibly linked or associated to diseases. However the interpretation of the mutation role in disease pathology is often missing. The problem with the disease effect interpretation on molecular level is mainly the missing information on protein structural data, on principal mechanisms of protein behavior under mechanical load, or the experimental and computational limitation of existing methods. Also differences in population genetics or the availability of patient/control samples become often a major limitation in any multidisciplinary disease cause-to-effect investigation.

The mechanotransduction research overall is facing a major challenge in bringing *ex vivo* experiments closer to physiological conditions. Such need originates from the necessity to observe single molecules and their individual roles separated outside their complex cellular interactions. Moreover, mechanobiological events often require submolecular, atomistic level observations yet close to *in vivo* conditions in order to draw meaningful conclusions. Also to draw biological significance, several parameters should be observed simultaneously<sup>51</sup>, which often poses technical challenges and ingenuity in methodology design.

## 6.4 Talin destabilization in computational and cell investigation

The hypothesis of this study was that the mechanical stabilities of the talin rod subdomains are optimized for cellular mechanotransduction. It was also assumed that the gradual unfolding of talin rod subdomains allows cells to detect local changes in forces at a high resolution and sensitivity. Despite intensive talin-focused research, mechanical modifications in talin have not been previously thoroughly characterized. In particular, the effects of talin destabilization on the regulation of cellular processes remain unknown.

Talin R3 is in many ways unique among the talin rod subdomains. It is a 4-helix bundle containing binding sites for RIAM and vinculin. The binding of the two protein ligands are mutually exclusive since the binding site for RIAM locates to the surface of R3H2 and R3H3 helices and requires folded R3 subdomain. On the other hand, two vinculin binding sites are located in the R3H2 and R3H3 inside of the hydrophobic core. Thus, the binding to vinculin requires structural reorganization of the R3 bundle to reveal the initially hidden hydrophobic residues<sup>113</sup>. Furthermore, the structural reorganization of the R3 subdomain likely acts as a switch releasing RIAM and allowing vinculin binding during adhesion maturation.

In this study, talin R3 destabilization increased talin and vinculin accumulation into cell-matrix adhesions, which indicated a decrease in the unfolding force demand. In other words, lower force was needed to switch between the RIAM-binding and the vinculin-binding conformation. Since the destabilizing mutations were located in the R3H1 and R3H4 they did not directly affect the talin-RIAM or talin-vinculin binding<sup>113</sup>. Indeed, significant difference in RIAM localization between WT and destabilized talin proteins was not recognized.

It has been previously reported that R3 bundle is mechanically unstable, in fact the most unstable of all the rod subdomains<sup>113,206</sup>. Because of its low mechanical stability, R3 subdomain may hold a crucial role in mechanotransduction of low magnitude forces during the maturation of nascent adhesions. In case that talin functions as a cellular mechanosensor, an alteration in adhesion dynamics and cellular mechanical response may be expected as a result in the mechanostability alteration. Previous studies involving R3 mutagenesis, in particular the stabilization of R3 domain in IVVI mutant, reported that the rigidity threshold was mediated by talin unfolding under force and subsequent vinculin binding<sup>214</sup>. The expression of a stabilized R3 mutant has increased this threshold needed for triggering mechanotransduction cascade and cellular traction force generation.

The destabilizing mutations were found to sensitize talin for sensing and propagation of low magnitude forces. This was indicated by the decreases in cell migration rate and traction force generation. Even though talin is recruited to nascent adhesions independent of vinculin or mechanical force, both are crucial for stabilizing talin into cell-matrix adhesions<sup>215</sup>. The destabilization of the talin R3 subdomain stimulated talin accumulation into cell-matrix adhesions accompanied by a decrease in cellular traction forces. This is possibly a result of talin R3 unfolding leading to VBS activation in adhesions where it would normally remain folded. Such talin unfolding and the resulting vinculin binding would possibly trigger downstream signaling cascades that eventually downregulate cellular traction force generation. Decreased traction force as observed in this study would prevent further talin unfolding and result in a decreased vinculin/talin ratio. These findings signify the importance of mechanical force as a regulator of adhesion turnover<sup>215</sup>.

Slow dissociation of the talin-vinculin complex possibly due to affected refolding of talin R3 subdomain after the release of force was also observed. Affected refolding of 3S and 4S mutants in particular was supported by the biochemical analysis where 3S and 4S appeared rather unstable and poorly folded as isolated domains when compared to WT, 1S and 2S. SMD simulation, on the other hand, suggested normal refolding even of 4S mutant. The starting structure of the refolding simulation was, however, only minimally affected by the preceding unfolding and may illustrate certain underestimation of the molecular events in computational simulation.

Based on these observations, it appears that talin destabilization causes modification in cellular mechanosignaling and ultimately decreases the force acting on talin molecule. Furthermore, R3 destabilization also affected the size, shape and protein composition of cell-matrix adhesions. The destabilized talin mutants localized into long, streak-like adhesions often located also in the central parts of the adhering cell. Talin destabilization was found to strongly promote adhesion formation on fibronectin. The destabilized mutants were also observed to prefer different  $\beta$ -integrin subtypes as compared to WT. These observations imply that talin rod subdomain mechanostability regulates the structure and function of FAs at the levels of ECM sensing and integrin activation. Yet, the mechanism explaining talin rod subdomain mechanostability and activation of different integrin subtypes remain to be determined.

This study emphasizes the importance of talin rod subdomain mechanostability as a key component of cellular mechanosensing. The decrease in mechanostability of an individual talin rod subdomain was sufficient to alter a wide range of cellular

processes dependent on mechanical signals and cellular mechanosensing. Our findings therefore indicate that talin together with vinculin function as mechanosensors, which are responsible for adhesion turnover, extracellular substrate sensing and consequently traction force generation and cell migration.

## 6.5 Talin as a fine mechanosensor

Our study presented in Article II showed that the mechanical stability of R3 domain is a key factor in mechanosensing, force traction generation and controlling the adhesion composition and turnover. Such a strong link between talin mechanosensitivity and cell response have highlighted the need for a thorough investigation of talin force response. It has been shown that unfolding of the compact R1-R3 region occur at forces as low as 5 pN and that this unfolding leads to an increase in affinity for vinculin<sup>17,51,206</sup>. Recent investigations have, however, indicated that the subdomains of the elongated region (R4–R12) may be actively involved in talin mechanosensing. For example, it was shown that the distance between the N- and C-terminal varied between 50 and 350 nm<sup>124</sup>, which would require unfolding in the elongated region of the rod in addition to the compact R1–R3. The mechanosensitivity of the whole rod is indicated also through the locations of vinculin binding occurring along the full rod, including subdomains R4–R13<sup>216</sup>.

Further investigation of talin rod (Article III) showed that the subdomains R4–R12 are vulnerable to mechanical force and undergo conformational rearrangement comparable to that of R1–R3. The application of mechanical force resulted in characteristic unfolding events and end-to-end protein extension explaining the varying talin length in cells. Such full rod unfolding also provides a mechanism of cryptic vinculin binding site activation. Crucially this force induced elongation occurs within a physiological force range between 10 – 40 pN. For context, single integrin molecules have been shown to experience forces up to 40 pN<sup>217</sup>. Different talin subdomains were shown to experience tension between 5 and 20 pN measured by magnetic tweezers<sup>29</sup>, and <7 and <10 pN analyzed with tension scissors<sup>218</sup>.

Within this physiological range, a hierarchy of talin subdomain stability was observed as demonstrated by SMD and smAFM unfolding. It was shown that the full talin rod possesses a gradual response to force where low forces can unfold only the weakest bundles and mechanically stronger bundles unfolded only with

increased force (Article III, Figure 6). Furthermore, such graduated force response of the talin rod could result in a similarly graduated cellular response to force through the gradual activation of cryptic VBSs located along the rod subdomains. In addition, the binding of other talin binding partners could be driven by the talin rod gradual unfolding and by the magnitude of the acting force. The talin rod subdomains investigated here comprise binding sites for various signaling or scaffolding proteins (RIAM, deleted in liver cancer 1 (DLC1), or synemin) (**Figure 9**). The binding sites of these proteins often locate close to cryptic VBSs and are suspected to compete for binding to talin<sup>113</sup>. In other words, a small range of physiological forces may change the talin conformation and switch between binding various ligands to control cellular function.

## 6.6 Fundamental principles of protein unfolding

Numerous studies concerning  $\alpha$ -helical mechanosensitive proteins have provided information on regulation switches between binding partners through mechanically induced conformational changes. However, detailed mechanisms and fundamental principles of such unfolding events remain largely unknown. Our observation of talin multi-domain fragment unfolding (**Figure 22**) revealed a possible stable 3-helix intermediate in SMD simulation. Because of the complexity of the SMD and smAFM data (Article III, Figure 2) we were not able to locate the 3-helix intermediate among the force traces of multi-domain fragment unfolding. However, we observed simultaneous unfolding of talin subdomains exhibiting similar mechanostability (**Figure 22**). Therefore, we examined the detailed unfolding mechanisms of  $\alpha$ -helical talin rod bundles to verify any existence of a stable intermediate or partial unfolded state. To investigate possible generalization of the unfolding intermediate among other helical protein, we included  $\alpha$ -catenin double domain  $M_I - M_{II}$ .

We demonstrated by a combination of SMD and smAFM that talin 5-helix rod bundles (R9 and R11) unfold with two peaks in the force traces. These correspond to the breaking of the 5- and 3-helix states (**Figure 23**). The 4-helix bundles (talin R3 and  $\alpha$ -catenin  $M_I - M_{II}$ ) also unfolded through a stable 3-helix intermediate. This 3-helix state was recognized as the most mechanically stable conformation among the 4-helix domains (**Figure 24**). An indirect evidence of unfolding intermediates in  $\alpha$ -helical proteins can be found in the literature. The computational and experimental investigation of the talin R3 subdomain revealed a

3-helix intermediate possibly able to instantly activate and bind vinculin. In detail, the deletion of R3H4 leads to a super-active R3 subdomain, which efficiently localizes in cell-surface contacts (Article IV, Figure S6). Furthermore, the talin R3 destabilization by mutations in R3H1 was sufficient to promote the bundle unfolding, consequently increase the activation and vinculin binding introducing a strong cellular phenotype. The phenotype of the 4S destabilized R3 subdomain modified with four point mutations was comparable to the super-active R3, which potentially indicates immediate domain dissociation into a 3-helix state. Further evidence of a 3-helix state in R3 domain is found in a recent study by Baxter et al.<sup>190</sup>. Here, high pressure conditions caused dissociation of R3H1 and created R3 in a 3-helix open state. Similar was observed even for the talin R1 bundle. The deletion of R1H5 resulted in the exposure of the VBS located in R1H4 and an active conformation<sup>125</sup>. It was also suggested that the deletion of H5, resulting in a 4-helix partial bundle, causes destabilization leading to partial unfolding of the R1 H1-H4 partial domain. In this study we showed that the 4-helix fold is a fragile conformation, which disintegrates under low mechanical load to form a mechanically more stable 3-helix state (**Figure 23**). Finally, even previous computational investigation concerning talin R1 suggested that only partial unfolding of talin subdomains described by minimal protein extension is sufficient for VBS activation<sup>126</sup>.

Our implementation of tandem fragments and force resisting disulfide clamps allowed for closer investigation of the unfolding principles. Indeed such methodology proved useful in the unfolding dynamics assessment and for comparison between methodologies. Overall, the unfolding force required for the unfolding of the 3-helix intermediate state is similar to that needed for the unfolding of 5-helix state.

In the experimental and simulation setup we observed talin unfolding further to the 3-helix intermediate. However, whether this complete unfolding takes place *in vivo*, or whether the 3-helix state is the final unfolding conformation remains unclear. Notions of both possibilities can be found in the literature. For example, vinculin binding to unfolded talin or  $\alpha$ -catenin domains inhibits domain refolding<sup>206,219</sup> while at the same time, vinculin binding may protect the 3-helix state from complete unfolding<sup>124</sup>. The notion of partial unfolding is also supported by the studies of talin maximal length in living cells, at approx. 400 nm in the absence of vinculin<sup>124</sup>. Recently published work revealed a force gradient across the talin rod domain<sup>191</sup>, which may be an interesting aspect to the complete 3-helix unfolding dynamics. To elucidate, in the presence of vinculin, greater force was measured at

the N-terminal end compared to the C terminal. Such force gradient leads to N-terminal bundle unfolding and activation for vinculin binding. As vinculin binds to activated talin and to actin, the force acting on the talin rod becomes dissipated and reduced towards the C-terminal end. We may speculate that such force reduction becomes insufficient to unfold stable 5-helix subdomains located at the talin C-terminal end. To support the complete unfolding hypothesis, we showed that the 3-helix intermediate resulting from 4-helix was mechanically weaker compared to the 3-helix intermediate of a 5-helix subdomain. The complete unfolding of 4-helix bundles at the N-terminal end of the talin rod may be, therefore, possible. Based on the work by Yao et al., we may assume that complete yet reversible unfolding of R3 domain takes place under low force load. It was shown that at 4.8 pN of constant force load exerted on the full length talin, R3 occupies two distinct conformations undergoing an end-to-end elongation of approx. 19 nm. However, which states these in fact are remains unclear<sup>29</sup>. It is possible that only the attachment to the pulling device would initiate elongation under low force load. Low force would, indeed, be sufficient to collapse mechanically unstable R3 subdomain into an activated 3-helix state. Such immediate conformational change would not necessarily result into an observable difference in the total end-to-end elongation compared to the R3 conformation in solution (Article IV, Figure S5). Similar elongation of approx. 19 nm between the 3-helix intermediate and the completely unfolded state was shown in our SMD results (**Figure 24**). Here we also see that the 3-helix intermediate remained stable even though the end-to-end distance increased by 5 nm caused by the uncoiling of H4.

The existence of a stable 3-helix intermediate may contribute to the complexity of cellular mechanotransduction with yet another level in the mechanoregulation process. The existence of the unfolding intermediate also contributes to the major challenge in mutation impact assessment from the view of mechanotransduction disease investigation. The understanding of these molecular mechanisms could guide new treatment solutions. We may also speculate that the existence of a 3-helix intermediate, whether undergoing full unfolding or not, may provide an additional structural support similar to the structure and function of spectrin or  $\alpha$ -actinin. It might also function as a molecular bumper reducing the impact of functional mutations present in the mechanosensitive protein. In other words, with additional level of mechanoregulation, the mutation effect on the cells behavior may be defused with only moderate effect on the cells fitness. Such theory could be of interest especially for talin mechanobiology since despite its vital roles only one

mutation in talin-2 located outside the mechanosensitive region has been linked to a disease<sup>176</sup>.

## 6.7 Model of talin mechanobiology

Based on the observations presented in this thesis supported by research published by other researchers, a model of talin unfolding under different force regimes was prepared. The organization of the talin subdomains after the release of autoinhibition state between talin head F3 and talin rod R9 bundle, and the mechanical stability of the rod subdomains is available in **Figure 26A**. In the absence of mechanical force,  $\alpha$ -helical bundles remain in a folded conformation capable of binding for example RIAM or DLC1<sup>107</sup>. The domains R1 and R2 were not included in the simulations considered in Article III and are not assigned mechanical stability in these models. Based on our observations of the mechanical characteristics of 4- and 5-helical subdomains, R2 could be assumed a weak subdomain and R1 intermediate/strong bundle. The experiments by Yao et al., however, report for the fragment R1-R3 one extremely weak bundle corresponding to R3 (unfolding at approx. 5 pN), one of high stability group III (unfolding force magnitude at 15-20 pN) and one with the highest mechanostability of group IV (unfolding force magnitude at 20-25 pN)<sup>29</sup>. These observations, however, propose similar hierarchy to our mechanostability assessments.

**Figure 26B-C** shows simplified model of the talin rod unfolding after N-terminal binding to integrin and C-terminal binding to actin. We hypothesize that only this initial binding might produce sufficient stimuli for R3 subdomain dissociation. Indeed, Yao et al. showed R3 domain in equilibrium between two states at force below 5 pN at an extension of 19 nm<sup>29</sup>. Nonetheless, these states of the bundle fold have not been assigned. It is therefore possible that even lower forces under 4.8 pN may cause dissociation of unstable R3 and its activation for vinculin binding. For detail, a study of R3 unfolding with the R3 dimensions at different stages of the unfolding is available in Article IV, Supplementary Figure S5. We may hypothesize that VBS in a folded 3-helix state is already available for vinculin binding especially in subdomains structurally similar to R3. In the R3 subdomain, the VBS containing helices R3H2 and R3H3 are considerably longer compared to R3H1 or R3H4 (**Figure 17C**). These may be partially accessible for vinculin binding already in the 3-helix state. It should be noted, that it is still not clear which of the helices dissociates from the R3 bundle first, and whether it is of

functional importance in the response to mechanical stimuli. Our simulations suggest C-terminal dissociation of R3H4, while recent publication reports on N-terminal dissociation of R3H1 under high pressure<sup>190</sup>. At the same time, the partial unfolding of the bundles causes disturbance in the binding sites for other partners located on the bundle surface<sup>113</sup>.

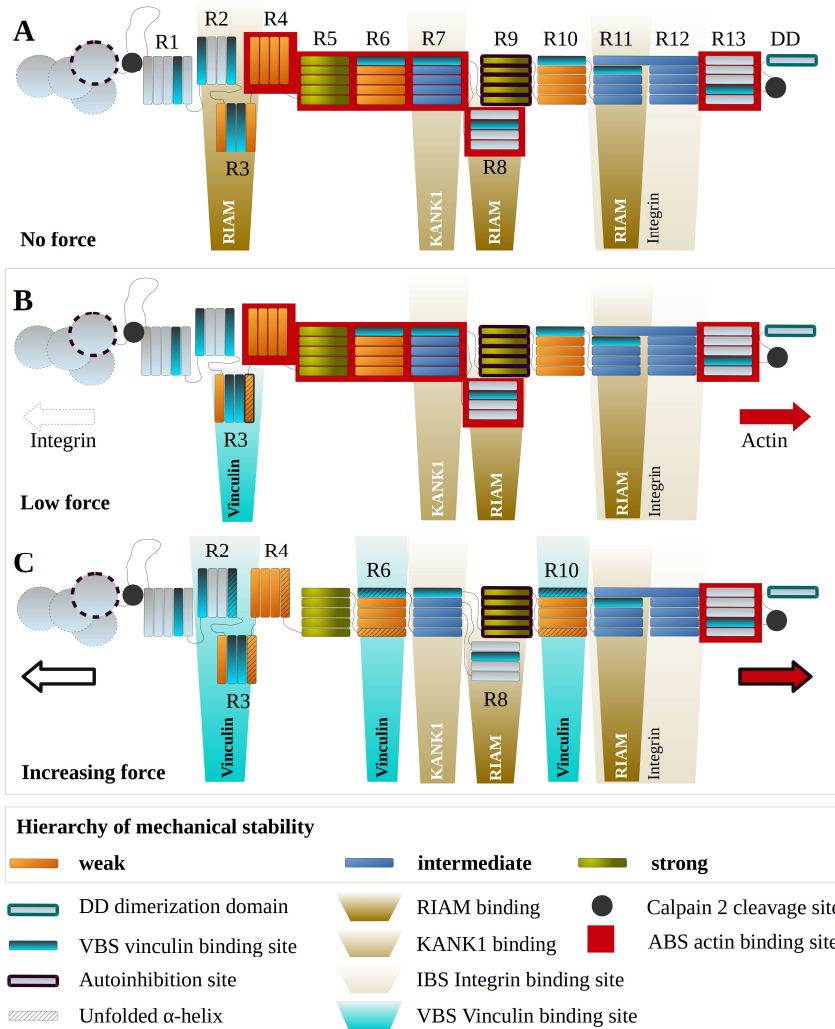


**Figure 26. Simplified model of talin mechanobiology under low and intermediate mechanical force magnitude.** End-to-end unfolding initiated by N-terminal binding to integrin and C-terminal binding to actin causes conformational changes in the talin rod subdomains. A) Talin rod after release of autoinhibition state between F3-R9 without presence of force. B) after N-terminal integrin binding and C-terminal actin binding the weakest R3 subdomain dissociates under low force regime and reveals its cryptic VBSs for vinculin binding. C)

With increasing force, other mechanically weak subdomains (R4, R6 and R10) undergo conformational changes disrupting existing binding sites and revealing cryptic other binding sites.  $\alpha$ -helices dissociated from the original subdomain fold are illustrated with hatching.

With increasing force other subdomains would unfold to the 3-helix intermediate starting from the mechanically weak bundles R4, R6 and R10 switching from a mechanoregulatory role to a structural reinforcement role. Such reinforcement scaffolding role, comparable to that of spectrin or  $\alpha$ -actinin, is assumed based on the similarity in conformations of the 3-helix state to the spectrin fold. Subdomains R6 and R10 contain one VBS each and would become activated to bind vinculin after the domain dissociation. Furthermore, actin binding site is located in the central rod region within the R4-R8 subdomains<sup>220</sup>. It is possible that the unfolding of the bundles R4 and R6 would disrupt the ABS making it inaccessible for actin binding. Alteration in the unfolding in the central rod, by alteration of the mechanical stability by mutation, might therefore modify mechanotransduction in different tissues and lead to pathological development<sup>108</sup>.

Finally, at a high force some of the talin bundles may unfold completely, or proceed to unfold all remaining subdomains to the 3-helix intermediate. Completely unfolded bundles would lose the ability to support ligand binding as well as provide structural function<sup>206</sup>. Such model would enable rich mechanosignaling through the talin signaling hub via several different binding partners<sup>221,222</sup>. Also in such model, the 3-helix intermediate could hold an essential role in binding regulations. **Figure 27** presents the hypothesis of an alternative talin rod unfolding under high force in a simplified model.

On the other hand, it was shown recently that the mechanical load across talin is not homogeneous, providing further variation in the regulation of talin functions<sup>191</sup>. After initial vinculin binding, talin rod experiences a force gradient where the local stress may become modulated and insufficient to unfold the 3-helix state. The 3-helix state may thus represent abundant talin rod subdomain conformation in living cells. Alternatively, the force distribution through vinculin and ABS2 (R4-R8) actin binding could be insufficient for dissociation of stable subdomains in the elongated rod, which would under normal conditions protect the elongated talin rod from extensive unfolding conserving crucial binding sites for RIAM or for integrin (**Figure 27C**). Needless to note, these mechanisms and the extent of the unfolding/protection of the elongated talin rod may differ in various tissue types and control tissue/organ development<sup>108</sup>. However, these models require further investigation. For instance, the ABS2 activation in the central talin rod (R4-R8) and actin binding, the underlining conditions and effects

of the force dissipation as well as the gradient across the talin rod are not yet understood.

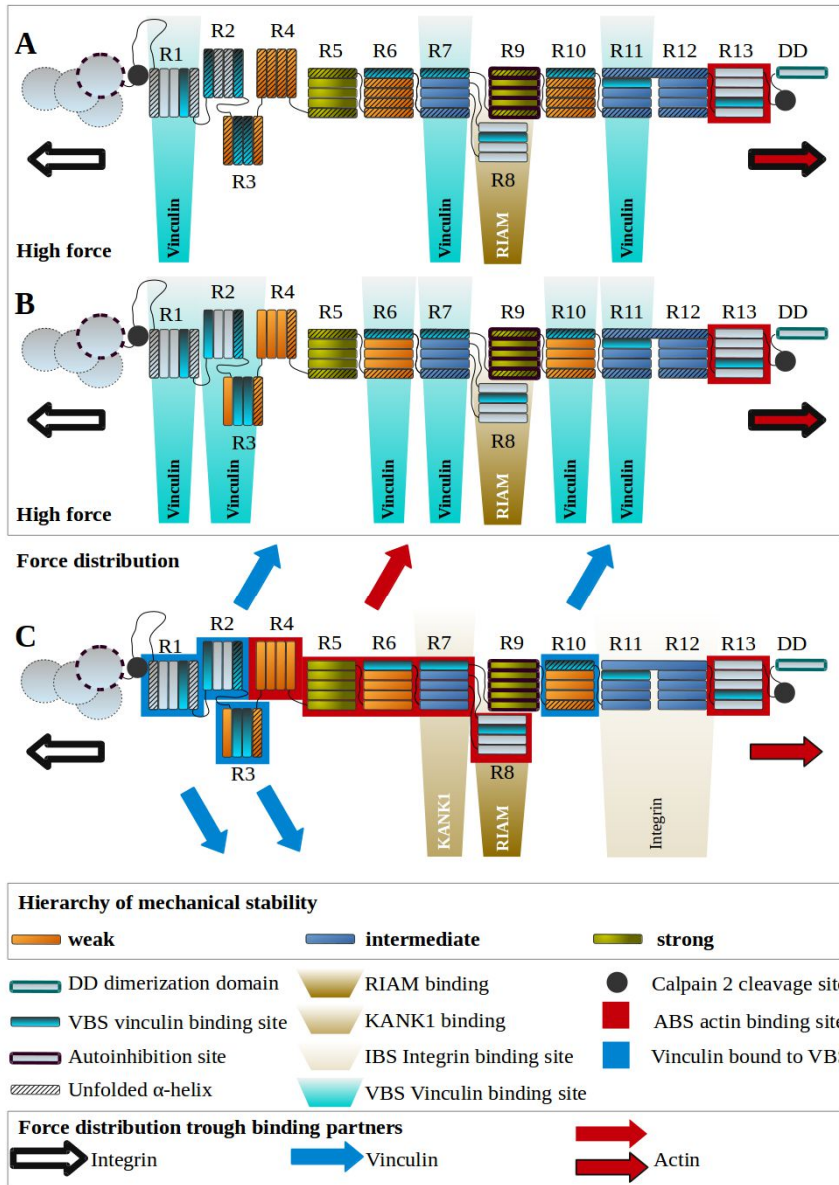


**Figure 27. Simplified model of alternative talin subdomain unfolding under high mechanical load and force distribution through binding partners resulting to force gradient among talin rod.** Under high force regime, talin rod could undergo either complete or partial unfolding with 3-helix state as final unfolding conformation. In the presence of vinculin bound to the activated compact N-terminal rod, and actin bound to the central

region of the talin rod, the force would be distributed through these binding partners. At the same time, the vinculin bound 3-helix intermediates would be protected from further unfolding. The resulting force gradient with decreased force acting at the C-terminal end of the rod would become insufficient to unfold mechanically stable subdomains or 3-helix intermediates.

It is possible that only vinculin binding to an active 3-helix state at the compact N-terminal end (R1-R3) containing 5 VBSs is sufficient to cause the above-mentioned force distribution leading to the reported force gradient. However, to what extent does this affect the elongated region of the talin rod has not yet been studied.

As previously discussed, the mechanical unfolding of full talin rod with magnetic tweezers showed that at a very low force of approx. 4.8 pN, R3 domain switches between two conformations<sup>29</sup>; folded 4-helix or 3-helix intermediate and an unfolded state. Whether all of the domains possess similar equilibrium force allowing fluent unfolding and refolding at varying force regimes remains unclear. Such characteristics however would bring another step in the talin mechanoregulation machinery. **Figure 28** provides a speculation of refolding events under fluctuating force leading to structural reorganization of the original helix subdomains in the talin rod. Such reorganization might also change the availability of previously accessible binding sites as a result of high force reduction.

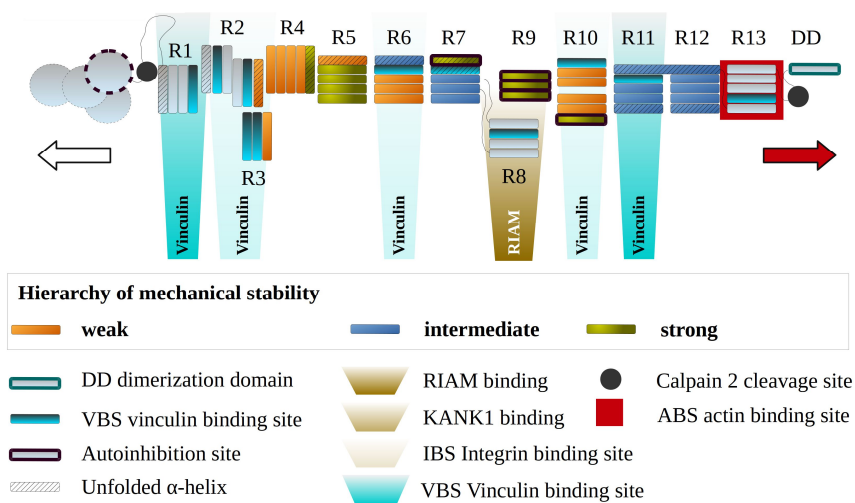


**Figure 28. Hypothetical refolding of talin subdomains under fluctuating force causing reorganization of talin subdomains and helices.**

Because the range of talin subdomain mechanical stabilities depends on minor differences in the structures, we also hypothesize that changes in the mechanical stability of the talin rod subdomains can be altered by a small number of single-point mutations. This was well presented by the destabilization of the R3 subdomain. These modifications in mechanical stability may lead to a misinterpretation of the mechanical impulse and an abnormal cellular response. Such false interpretation might theoretically lead into pathological changes in cell differentiation, tissue homeostasis and tissue maintenance leading to pathological development.

The models of talin mechanobiology presented here are highly simplified hypothetical models of the talin rod unfolding. For simplicity of presentation I have included only major talin rod interactions in a single talin molecule. Networks and crosslinks between the constituents of FAs may further complicate the proposed models. Even though the mechanisms presented in this chapter are theoretical, they provide a basis for talin-focused research in the future. Furthermore, the presented model is hypothesized for the talin rod mechanobiology, however, its validity may be applicable also for other  $\alpha$ -helical multi-domain mechanosensors.

## 6.8 Computational methods: advantages and limitations

During the protein activation under mechanical force, involved conformational changes happen on atom scale level. These changes are therefore challenging to observe and track *in vivo* and *in vitro*. Despite existing limitations, *in silico* methods provide an atomic and molecular insight into these processes and activation events. On many occasions computational methods, classical molecular dynamics (MD) and steered molecular dynamics (SMD), have proven rather accurate and even predictive. Therefore these methods are often utilized to link experiments and theory<sup>192</sup>.

The protein unfolding force magnitude is pulling rate dependent and therefore affected by the methodology. All-atom simulations are typically six to eight orders of magnitude faster, which leads to larger force magnitudes than those observed in experiments. For that reason, in our multidisciplinary research interlinking results of smAFM experiments with SMD computational simulation, we compared force patterns between domains rather than absolute force magnitude. Also our use of artificial tandem domains in a combination with disulfide clamps resisting

unfolding under forces typical for  $\alpha$ -helical proteins has proven valuable for the comparisons between different methods.

We further hypothesize that the MD/SMD parameter setup and the method of the theoretical force analysis may affect the force magnitude itself, the pattern of the force trace as well as the observed protein unfolding dynamics and the existence of intermediate states. The simulation setup and the force calculation presented in Article III retained the force magnitude at a rather similar level after reaching the initial unfolding event. Such lack of force release and revealing of local minima, probably caused by the parametrization and by the force extraction method, pose challenges in the data interpretation.

In the SMD methods some events may be enhanced or magnified compared to experimental results. For instance the unfolding force magnitudes are much higher compared to *in vitro* and *in vivo* forces. Also other parametrization such as the choice of force field or solvent parameters may affect the behavior of the protein in the simulation and cause decreased or increased helicity, twisting of domains or bundles. Hence, the fine molecular dynamics events have to be assessed critically. On other occasions, SMD results may appear numb to certain events. Such as in our destabilized mutants assessment, where computation offered only mild effects on the domain destabilization whereas the consequent biochemical analysis and cell experiments presented significant change in the helicity, thermal and mechanical stability and final effect on the cells' motility and overall fitness.

$\alpha$ -helices and  $\alpha$ -helical structures and their unique properties pose additional challenges in the SMD simulation. For instance, the helices stretch substantially upon force induced unfolding, and the interactions between helices are dictated by entropy-mediated interactions. These characteristics may cause possible bias in the relevance of the absolute force determined.

However, despite these limitations, we propose that SMD simulations are useful and reliable for the determination of relative mechanical stabilities, especially when used in a combination with experimental methods such as smAFM or magnetic tweezers.

## 7 CONCLUSIONS

Despite growing awareness of the mechanobiology field and ongoing intensive research, the fundamental questions in mechanotransduction remain unanswered. The perception of cellular mechanosensing and mechanical stimuli interpretation in the context of disease development is still incomplete.

The comprehensive overview of the known and suspected mechanotransducers and their interactions show that numerous subcellular and protein structures involved in the force sensing and propagation are associated with or linked to diverse diseases of mechanotransduction. For instance, diseases of heart, muscle and bone or cancer, among other conditions, are identified in the mechanotransduction pathways. Despite intensive research, the link between the pathological development and modified function on molecular and submolecular level remains largely unknown.

The presented research communicates the role of  $\alpha$ -helical proteins in mechanosensing. The focus of this thesis is key FA protein, talin; its disease connection and fundamental principles of behavior under mechanical force.

First we investigated the role of talin and vinculin isoforms in atherosclerosis. We conclude that talin-1, talin-2, meta-vinculin and vinculin expression is downregulated in atherosclerotic plaque. The expression of the investigated genes is downregulated in plaques from all of the studied peripheral arterial beds (carotid, abdominal aortic and femoral). The key role of talin in FAs proposes that the tissue decomposition in atherosclerosis could be partially driven by downregulation of talin, leading to loosening of cell-ECM adhesion interactions and reorganization of the tissue. In conclusion, proteins contributing to mechanosensing (talin and vinculin) may have important roles in atherosclerotic plaque formation and atherosclerosis progression.

Furthermore, our study with talin destabilization emphasizes the talin rod mechanostability and its importance as a key player in cellular mechanosensing. We demonstrate that the alteration in the mechanostability of only one talin rod subdomain is sufficient to affect a wide range of cellular processes dependent on mechanical signals and cellular mechanosensing. Our results suggest that talin acts as a mechanosensor together with vinculin and is responsible for controlling

adhesion turnover, ECM sensing and consequently traction force generation and cell migration.

The combination of SMD and smAFM provides a valuable insight into the molecular behavior of talin when exposed to mechanical force and associated biological mechanisms. A physiological force range of 10 – 40 pN is found to affect the entire talin rod. The talin rod bundles also exhibit certain hierarchy of mechanical stability. In conclusion, we hypothesize that talin acts as a delicate force meter sensitive to a range of small mechanical forces. Such fine mechanosensing could control the affinity towards ligand binding triggering biochemical cascades that control strength of surface adhesion, guide spreading or locomotion.

Finally, we show that  $\alpha$ -helical proteins unfold via stable 3-helix intermediates, which represent biologically active states. Our results suggest that talin is a central scaffolding hub in FAs with multiple discrete unfolding states, acting as a sophisticated mechanosensor and an important regulatory switch. We further propose that the mechanical stability of  $\alpha$ -helical domains as well as the mechanical stability of their unfolding intermediates should be considered in mechanoregulation models of other  $\alpha$ -helical proteins.

Despite the limitations of computational simulation methods, our data and techniques clearly present their benefits especially when utilized in combination with experimental methods. Such multidisciplinary approach may be useful in the future to design talin mutants of varying mechanostability in order to evaluate the contribution of talin-mediated mechanosensing in cellular differentiation, tissue maintenance and healing or fundamental biology processes during development.

## 8 REFERENCES

1. Turner CH, Warden SJ, Bellido T, et al. Mechanobiology of the skeleton. *Sci Signal*. 2009. doi:10.1126/scisignal.268pt3.
2. Malik T. *Space Station Astronauts Lose Bone Strength Fast*; 2009. <https://www.space.com/6354-space-station-astronauts-lose-bone-strength-fast.html>. Accessed June 25, 2018.
3. Ulstrup KA. Biomechanical concepts of fracture healing in weight-bearing long bones. *Acta Orthop Belg*. 2008.
4. Zhang J, He F, Zhang W, Zhang M, Yang H, Luo ZP. Mechanical force enhanced bony formation in defect implanted with calcium sulphate cement. *Bone Res*. 2015. doi:10.1038/boneres.2014.48.
5. Califano JP, Reinhart-King CA. Exogenous and endogenous force regulation of endothelial cell behavior. *J Biomech*. 2010. doi:10.1016/j.jbiomech.2009.09.012.
6. Keaney JF. Atherosclerosis: From lesion formation to plaque activation and endothelial dysfunction. *Mol Aspects Med*. 2000. doi:10.1016/S0098-2997(00)00005-4.
7. Ando J, Yamamoto K. Vascular Mechanobiology. *Circ J*. 2009. doi:10.1253/circj.CJ-09-0583.
8. McCain ML, Parker KK. Mechanotransduction: The role of mechanical stress, myocyte shape, and cytoskeletal architecture on cardiac function. *Pflugers Arch Eur J Physiol*. 2011. doi:10.1007/s00424-011-0951-4.
9. Schwander M, Kachar B, Müller U. The cell biology of hearing. *J Cell Biol*. 2010. doi:10.1083/jcb.201001138.
10. Reichelt J. Mechanotransduction of keratinocytes in culture and in the epidermis. *Eur J Cell Biol*. 2007. doi:10.1016/j.ejcb.2007.06.004.
11. Hytönen VP, Wehrle-Haller B. Mechanosensing in cell-matrix adhesions - Converting tension into chemical signals. *Exp Cell Res*. 2016. doi:10.1016/j.yexcr.2015.10.027.
12. Monkley SJ, Kostourou V, Spence L, et al. Endothelial cell talin1 is essential for embryonic angiogenesis. *Dev Biol*. 2011. doi:10.1016/j.ydbio.2010.11.010.
13. Zwerger M, Ho CY, Lammerding J. Nuclear mechanics in disease. *Annu Rev Biomed Eng*. 2011. doi:10.1146/annurev-bioeng-071910-124736.
14. Kopp PM, Bate N, Hansen TM, et al. Studies on the morphology and spreading of human endothelial cells define key inter- and intramolecular interactions for talin1. *Eur J Cell Biol*. 2010. doi:10.1016/j.ejcb.2010.05.003.
15. Gingras AR, Bate N, Goult BT, et al. The structure of the C-terminal actin-binding domain of talin. *EMBO J*. 2008. doi:10.1038/.
16. Jahed Z, Shams H, Mehrbod M, Mofrad MRK. Mechanotransduction pathways linking the extracellular matrix to the nucleus. *Int Rev Cell Mol Biol*. 2014. doi:10.1016/B978-0-12-800180-6.00005-0.

17. Hytönen VP, Vogel V. How force might activate talin's vinculin binding sites: SMD reveals a structural mechanism. *PLoS Comput Biol.* 2008. doi:10.1371/journal.pcbi.0040024.
18. Jacobs CR, Huang H, Kwon RY. *Introduction to Cell Mechanics and Mechanobiology.* Garland Science; 2013.
19. Ingber DE. Cellular mechanotransduction: putting all the pieces together again. *FASEB J.* 2006. doi:10.1096/fj.05-5424rev.
20. Yang X, Sachs F. Block of stretch-activated ion channels in *Xenopus* oocytes by gadolinium and calcium ions. *Science.* 1989. doi:10.1126/science.2466333.
21. Artemenko Y, Axiotakis L, Borleis J, Iglesias P a., Devreotes PN. Chemical and mechanical stimuli act on common signal transduction and cytoskeletal networks. *Proc Natl Acad Sci.* 2016. doi:10.1073/pnas.1608767113.
22. Goncharova EJ, Kam Z, Geiger B. The involvement of adherens junction components in myofibrillogenesis in cultured cardiac myocytes. *Development.* 1992. <http://www.ncbi.nlm.nih.gov/pubmed/1576958>.
23. Henry MD, Campbell KP. Dystroglycan: An extracellular matrix receptor linked to the cytoskeleton. *Curr Opin Cell Biol.* 1996. doi:10.1016/S0955-0674(96)80103-7.
24. Anderson JM, Van Itallie CM. Physiology and Function of the Tight Junction. *Cold Spring Harb Perspect Biol.* 2009. doi:10.1101/cshperspect.a002584.
25. Monkley SJ, Zhou XH, Kinston SJ, et al. Disruption of the talin gene arrests mouse development at the gastrulation stage. *Dev Dyn.* 2000. doi:10.1002/1097-0177(2000)9999:9999<::AID-DVDY1079>3.0.CO;2-Y.
26. Rahikainen R, Von Essen M, Schaefer M, et al. Mechanical stability of talin rod controls cell migration and substrate sensing. *Sci Rep.* 2017. doi:10.1038/s41598-017-03335-2.
27. Johnson CP, Tang H-Y, Carag C, Speicher DW, Discher DE. Forced Unfolding of Proteins Within Cells. *Science.* 2007. doi:10.1126/science.1139857.
28. Rognoni L, Stigler J, Pelz B, Ylanne J, Rief M. Dynamic force sensing of filamin revealed in single-molecule experiments. *Proc Natl Acad Sci.* 2012. doi:10.1073/pnas.1211274109.
29. Yao M, Goult BT, Klapholz B, et al. The mechanical response of talin. *Nat Commun.* 2016. doi:10.1038/ncomms11966.
30. Forman JR, Clarke J. Mechanical unfolding of proteins: insights into biology, structure and folding. *Curr Opin Struct Biol.* 2007. doi:10.1016/j.sbi.2007.01.006.
31. Carrion-Vazquez M, Oberhauser AF, Fisher TE, et al. Mechanical design of proteins-studied by single-molecule force spectroscopy and protein engineering. *Prog Biophys Mol Biol.* 2003. doi:10.1016/S0079-6107(00)00017-1.
32. Valbuena a., Oroz J, Hervas R, et al. On the remarkable mechanostability of scaffoldins and the mechanical clamp motif. *Proc Natl Acad Sci.* 2009. doi:10.1073/pnas.0813093106.
33. Lemke SB, Schnorrer F. Mechanical forces during muscle development. *Mech Dev.* 2017. doi:10.1016/j.mod.2016.11.003.
34. Oberhauser a. F, Hansma PK, Carrion-Vazquez M, Fernandez JM. Stepwise unfolding of titin under force-clamp atomic force microscopy. *Proc Natl Acad Sci.* 2001. doi:10.1073/pnas.98.2.468.
35. Puchner EM, Alexandrovich A, Kho AL, et al. Mechanoenzymatics of titin kinase. *PNAS.* 2008.

36. Grodzinsky AJ, Levenston ME, Jin M, Frank EH. Cartilage Tissue Remodelling in Response to Mechanical Forces. *Annu Rev Biomed Eng.* 2000.
37. Ingber DE. Mechanical signaling and the cellular response to extracellular matrix in angiogenesis and cardiovascular physiology. *Circ Res.* 2002. doi:10.1161/01.RES.0000039537.73816.E5.
38. Tschumperlin DJ, Dai G, Maly I V., et al. Mechanotransduction through growth-factor shedding into the extracellular space. *Nature.* 2004. doi:10.1038/nature02543.
39. Han B, Bai XH, Lodyga M, et al. Conversion of mechanical force into biochemical signaling. *J Biol Chem.* 2004. doi:10.1074/jbc.M406880200.
40. Sikora M, Cieplak M. Mechanical stability of multidomain proteins and novel mechanical clamps. *Proteins Struct Funct Bioinforma.* 2011. doi:10.1002/prot.23001.
41. Li H, Linke WA, Oberhauser AF, et al. Reverse engineering of the giant muscle protein titin. *Nature.* 2002.
42. Berman HM, Westbrook J, Feng Z, et al. The protein data bank. *Nucleic Acids Res.* 2000. doi:10.1093/nar/28.1.235.
43. Ng SP, Rounsevell RWS, Steward A, et al. Mechanical unfolding of TNfn3: The unfolding pathway of a fnIII domain probed by protein engineering, AFM and MD simulation. *J Mol Biol.* 2005. doi:10.1016/j.jmb.2005.04.070.
44. Mai SL. Secondary structure, mechanical stability, and location of transition state of proteins. *Biophys J.* 2007. doi:10.1529/biophysj.107.106138.
45. Lee G, Abdi K, Jiang Y, Michaely P, Bennett V, Marszalek PE. Nanospring behaviour of ankyrin repeats. *Nature.* 2006. doi:10.1038/nature04437.
46. Schwaiger I, Sattler C, Hostetter DR, Rief M. The myosin coiled-coil is a truly elastic protein structure. *Nat Mater.* 2002. doi:10.1038/nmat776.
47. Toofanny RD, Williams PM. Simulations of multi-directional forced unfolding of titin I27. *J Mol Graph Model.* 2006. doi:10.1016/j.jmgm.2005.09.005.
48. West DK, Brockwell DJ, Olmsted PD, Radford SE, Paci E. Mechanical resistance of proteins explained using simple molecular models. *Biophys J.* 2006. doi:10.1529/biophysj.105.071035.
49. Nord AL, Gachon E, Perez-Carrasco R, et al. Catch bond drives stator mechanosensitivity in the bacterial flagellar motor. *Proc Natl Acad Sci.* 2017. doi:10.1073/pnas.1716002114.
50. Ohashi T, Kiehart DP, Erickson HP. Dynamics and elasticity of the fibronectin matrix in living cell culture visualized by fibronectin-green fluorescent protein. *Proc Natl Acad Sci U S A.* 1999. doi:10.1073/pnas.96.5.2153.
51. Del Rio A, Perez-Jimenez R, Liu R, Roca-Cusachs P, Fernandez JM, Sheetz MP. Stretching single talin rod molecules activates vinculin binding. *Science.* 2009. doi:10.1126/science.1162912.
52. Bhasin N, Carl P, Harper S, et al. Chemistry on a single protein, vascular cell adhesion molecule-1, during forced unfolding. *J Biol Chem.* 2004. doi:10.1074/jbc.M404103200.
53. Lu P, Takai K, Weaver V, Werb Z. Extracellular matrix degradation and remodeling in development and disease. *Cold Spring Harb.* 2011. doi:10.1101 / cshperspect.a005058.
54. Humphrey JD, Dufresne ER, Schwartz M a. Mechanotransduction and extracellular matrix homeostasis. *Nat Rev Mol Cell Biol.* 2015. doi:10.1038/nrm3896.Mechanotransduction.

55. Hynes RO, Naba A. Overview of the Matrisome—An Inventory of Extracellular Matrix Constituents and Functions. 2012. doi:10.1101/cshperspect.a004903.
56. Ricard-Blum S. The Collagen Family. *Cold Spring Harb Perspect Biol.* 2011. doi:10.1101/cshperspect.a004978.
57. Yurchenco PD. Membranes: Cell Scaffoldings and Signaling Platforms. 2011. doi:10.1101/cshperspect.a004911.
58. Ida-Yonemochi H. Role of perlecan, a basement membrane-type heparan sulfate proteoglycan, in enamel organ morphogenesis. *J Oral Biosci.* 2013. doi:10.1016/j.job.2012.12.004.
59. Schwarzbauer JE, DeSimone DW. Fibronectins, their fibrillogenesis, and in vivo functions. *Cold Spring Harb Perspect Biol.* 2011. doi:10.1101/cshperspect.a005041.
60. Chiquet-Ehrismann R, Tucker RP. Tenascins and the importance of adhesion modulation. *Cold Spring Harb Perspect Biol.* 2011. doi:10.1101/cshperspect.a004960.
61. Barros CS, Franco SJ, Müller U. Extracellular Matrix: Functions in the nervous system. *Cold Spring Harb Perspect Biol.* 2011. doi:10.1101/cshperspect.a005108.
62. Bergmeier W, Hynes RO. and Thrombosis. *Curr Ther Vasc Endovasc Surg.* 2012. doi:10.1016/B978-1-4557-0984-7.00267-2.
63. Teng YHF, Aquino RS, Park PW. Molecular functions of syndecan-1 in disease. *Matrix Biol.* 2012. doi:10.1016/j.matbio.2011.10.001.
64. Martins-Green M, Bissell MJ. Cell-ECM interactions in development. *Semin Dev Biol.* 1995. doi:10.1016/S1044-5781(06)80024-1.
65. Lokeshwar VB, Fregien N, Bourguignon LYW. Ankyrin-binding domain of CD44(GP85) is required for the expression of hyaluronic acid-mediated adhesion function. *J Cell Biol.* 1994. doi:10.1083/jcb.126.4.1099.
66. Juliano RL. Signal Transduction by Cell Adhesion Receptors and the Cytoskeleton: Functions of Integrins, Cadherins, Selectins, and Immunoglobulin-Superfamily Members. *Annu Rev Pharmacol Toxicol.* 2002.
67. Hynes RO. Cell adhesion: old and new questions. *Trends Cell Biol.* 1999. doi:10.1016/S0962-8924(99)01667-0.
68. Luis Alonso J, H. Goldmann W. Cellular mechanotransduction. *AIMS Biophys.* 2016. doi:10.3934/biophy.2016.1.50.
69. Constantin B. Dystrophin complex functions as a scaffold for signalling proteins. *Biochim Biophys Acta - Biomembr.* 2014. doi:10.1016/j.bbamem.2013.08.023.
70. Chitaev N a, Troyanovsky SM. Direct Ca<sup>2+</sup>-dependent Heterophilic Interaction between Desmosomal Cadherins, Desmoglein and Desmocollin, Contributes to Cell-Cell Adhesion. *Cell.* 1997.
71. Yin T, Green KJ. Regulation of desmosome assembly and adhesion. *Semin Cell Dev Biol.* 2004. doi:10.1016/j.semcdb.2004.09.005.
72. Hartsock A, Nelson WJ. Adherens and Tight Junctions: Structure, Function and Connection to the Actin Cytoskeleton. *Biochim Biophys Acta.* 2008. doi:10.1016/j.bbamem.2007.07.012.Adherens.
73. Kumar NM, Gilula NB. The Gap Junction Review Communication Channel. *Cell.* 1996. doi:S0092-8674(00)81282-9.
74. Venkatakrishnan AJ, Deupi X, Lebon G, Tate CG, Schertler GF, Madan Babu M. Molecular signatures of G-protein-coupled receptors. *Nature.* 2013. doi:10.1038/nature11896.
75. Machnicka B, Czogalla A, Hryniewicz-Jankowska A, et al. Spectrins: A structural platform for stabilization and activation of membrane channels, receptors and

- transporters. *Biochim Biophys Acta - Biomembr.* 2014. doi:10.1016/j.bbamem.2013.05.002.
76. Metral S, Machnicka B, Bigot S, Colin Y, Dhermy D, Lecomte MC.  $\alpha$ II-spectrin is critical for cell adhesion and cell cycle. *J Biol Chem.* 2009. doi:10.1074/jbc.M801324200.
  77. Li L. Cytoskeleton. *Biol Dict.* 2014:7-8. <https://biologydictionary.net/cytoskeleton/>. Accessed April 24, 2018.
  78. Mollinedo F, Gajate C. Microtubules, microtubule-interfering agents and apoptosis. *Apoptosis.* 2003. doi:10.1023/A:1025513106330.
  79. Fuchs E, Yang Y. Crossroads on cytoskeletal highways. *Cell.* 1999. doi:10.1016/S0092-8674(00)80041-0.
  80. Leung CL, Green KJ, Liem RKH. Plakins: A family of versatile cytolinker proteins. *Trends Cell Biol.* 2002. doi:10.1016/S0962-8924(01)02180-8.
  81. Prins KW, Humston JL, Mehta A, Tate V, Ralston E, Ervasti JM. Dystrophin is a microtubule-associated protein. *J Cell Biol.* 2009. doi:10.1083/jcb.200905048.
  82. Bailly M, Condeelis J. Cell motility: Insights from the backstage. *Nat Cell Biol.* 2002. doi:10.1038/ncb1202-e292.
  83. Lee SH, Dominguez R. Regulation of actin cytoskeleton dynamics in cells. *Mol Cells.* 2010. doi:10.1007/s10059-010-0053-8.
  84. Verma SK, Lal H, Golden HB, et al. Rac1 and RhoA differentially regulate angiotensinogen gene expression in stretched cardiac fibroblasts. *Cardiovasc Res.* 2011. doi:10.1093/cvr/cvq385.
  85. Otomo T, Tomchick DR, Otomo C, Panchal SC, Machius M, Rosen MK. Structural basis of actin filament nucleation and processive capping by a formin homology 2 domain. *Nature.* 2005. doi:10.1038/nature03251.
  86. Broderick MJ, Winder SJ. Spectrin,  $\alpha$ -actinin, and dystrophin. *Adv Protein Chem.* 2005. doi:10.1016/S0065-3233(04)70007-8.
  87. Henne WM, Kent HM, Ford MGJ, et al. Structure and Analysis of FCHO2 F-BAR Domain: A Dimerizing and Membrane Recruitment Module that Effects Membrane Curvature. *Structure.* 2007. doi:10.1016/j.str.2007.05.002.
  88. Herrmann H, Bär H, Kreplak L, Strelkov S V., Aebi U. Intermediate filaments: From cell architecture to nanomechanics. *Nat Rev Mol Cell Biol.* 2007. doi:10.1038/nrm2197.
  89. Gruenbaum Y, Margalit A, Goldman RD, Shumaker DK, Wilson KL. The nuclear lamina comes of age. *Nat Rev Mol Cell Biol.* 2005. doi:10.1038/nrm1550.
  90. Tzur YB, Wilson KL, Gruenbaum Y. SUN-domain proteins: "Velcro" that links the nucleus to the cytoskeleton. *Nat Rev Mol Cell Biol.* 2006. doi:10.1038/nrm2003.
  91. Wilhelmsen K, Litjens SHM, Kuikman I, et al. Nesprin-3, a novel outer nuclear membrane protein, associates with the cytoskeletal linker protein plectin. *J Cell Biol.* 2005. doi:10.1083/jcb.200506083.
  92. Zierath JR, Hawley J a. Skeletal muscle fiber type: Influence on contractile and metabolic properties. *PLoS Biol.* 2004. doi:10.1371/journal.pbio.0020348.
  93. Scott W, Stevens J, Stuart a, Scott W, Stevens J, Binder-macleod S a. Human Skeletal Muscle Fiber Type Classifications. 2001.
  94. Sehnert AJ, Huq A, Weinstein BM, Walker C, Fishman M, Stainier DYR. Cardiac troponin T is essential in sarcomere assembly and cardiac contractility. *Nat Genet.* 2002. doi:10.1038/ng875.

95. Agarkova I, Ehler E, Lange S, Schoenauer R, Perriard JC. M-band: A safeguard for sarcomere stability? *J Muscle Res Cell Motil.* 2003. doi:10.1023/A:1026094924677.
96. Monti RJ, Roy RR, Hodgson J a., Reggie Edgerton V. Transmission of forces within mammalian skeletal muscles. *J Biomech.* 1999. doi:10.1016/S0021-9290(98)00189-4.
97. Bateman A, Martin MJ, O'Donovan C, et al. UniProt: The universal protein knowledgebase. *Nucleic Acids Res.* 2017. doi:10.1093/nar/gkw1099.
98. Uhlen M, Fagerberg L, Hallstrom BM, et al. Tissue-based map of the human proteome. *Science.* 2015. doi:10.1126/science.1260419.
99. Manso AM, Li R, Monkley SJ, et al. Talin 1 has unique expression versus talin 2 in the heart and modifies the hypertrophic response to pressure overload. *J Biol Chem.* 2013. doi:10.1074/jbc.M112.427484.
100. Goult BT, Bouaouina M, Elliott PR, et al. Structure of a double ubiquitin-like domain in the talin head: A role in integrin activation. *EMBO J.* 2010. doi:10.1038/emboj.2010.4.
101. Calderwood D a., Zent R, Grant R, Rees DJG, Hynes RO, Ginsberg MH. The talin head domain binds to integrin  $\beta$  subunit cytoplasmic tails and regulates integrin activation. *J Biol Chem.* 1999. doi:10.1074/jbc.274.40.28071.
102. Chen HC, Appeddu P a., Parsons JT, Hildebrand JD, Schaller MD, Guan JL. Interaction of focal adhesion kinase with cytoskeletal protein talin. *J Biol Chem.* 1995. doi:10.1074/jbc.270.28.16995.
103. Martel V, Racaud-Sultan C, Dupe S, et al. Conformation, Localization, and Integrin Binding of Talin Depend on Its Interaction with Phosphoinositides. *J Biol Chem.* 2001. doi:10.1074/jbc.M102373200.
104. Bono P, Rubin K, Higgins JM, Hynes RO. Layilin, a novel integral membrane protein, is a hyaluronan receptor. *Mol Biol Cell.* 2001. doi:10.1091/mbc.12.4.891.
105. Wang S, Watanabe T, Matsuzawa K, et al. Tiam1 interaction with the PAR complex promotes talin-mediated Rac1 activation during polarized cell migration. *J Cell Biol.* 2012. doi:10.1083/jcb.201202041.
106. Tadokoro S, Shattil SJ, Eto K, et al. Talin binding to integrin  $\beta$  tails: A final common step in integrin activation. *Science.* 2003. doi:10.1126/science.1086652.
107. Calderwood D a., Campbell ID, Critchley DR. Talins and kindlins: Partners in integrin-mediated adhesion. *Nat Rev Mol Cell Biol.* 2013. doi:10.1038/nrm3624.
108. Klapholz B, Herbert SL, Wellmann J, Johnson R, Parsons M, Brown NH. Alternative Mechanisms for Talin to Mediate Integrin Function. *Curr Biol.* 2015. doi:10.1016/j.cub.2015.01.043.
109. Hemmings L, Hemmings L, Rees DJ, et al. Talin contains three actin-binding sites each of which is adjacent to a vinculin-binding site. *J Cell Sci.* 1996.
110. IZARD T, BROWN DT. Mechanisms and Functions of Vinculin Interactions with Phospholipids at Cell Adhesion Sites. *J Biol Chem.* 2016. doi:10.1074/jbc.R115.686493.
111. Goult BT, Bate N, Anthis NJ, et al. The structure of an interdomain complex that regulates Talin activity. *J Biol Chem.* 2009. doi:10.1074/jbc.M900078200.
112. Gingras AR, Ziegler WH, Frank R, et al. Mapping and consensus sequence identification for multiple vinculin binding sites within the talin rod. *J Biol Chem.* 2005. doi:10.1074/jbc.M508060200.
113. Goult BT, Zacharchenko T, Bate N, et al. RIAM and vinculin binding to talin are mutually exclusive and regulate adhesion assembly and turnover. *J Biol Chem.* 2013. doi:10.1074/jbc.M112.438119.

114. Li G, Du X, Vass WC, Papageorge a. G, Lowy DR, Qian X. Full activity of the deleted in liver cancer 1 (DLC1) tumor suppressor depends on an LD-like motif that binds talin and focal adhesion kinase (FAK). *Proc Natl Acad Sci.* 2011. doi:10.1073/pnas.1112122108.
115. Bouchet BP, Gough RE, Ammon YC, et al. Talin-KANK1 interaction controls the recruitment of cortical microtubule stabilizing complexes to focal adhesions. *Elife.* 2016. doi:10.7554/eLife.18124.
116. Sun N, Critchley DR, Paulin D, Li Z, Robson RM. Identification of a repeated domain within mammalian alpha-synemin that interacts directly with talin. *Exp Cell Res.* 2008. doi:10.1016/j.yexcr.2008.01.034.
117. Gingras AR, Ziegler WH, Bobkov AA, et al. Structural determinants of integrin binding to the talin rod. *J Biol Chem.* 2009. doi:10.1074/jbc.M805937200.
118. Franco-Cea A, Ellis SJ, Fairchild MJ, Yuan L, Cheung TYS, Tanentzapf G. Distinct developmental roles for direct and indirect talin-mediated linkage to actin. *Dev Biol.* 2010. doi:10.1016/j.ydbio.2010.06.027.
119. Lawson C, Lim ST, Uryu S, Chen XL, Calderwood D a., Schlaepfer DD. FAK promotes recruitment of talin to nascent adhesions to control cell motility. *J Cell Biol.* 2012. doi:10.1083/jcb.201108078.
120. Hytönen VP, Wehrle-Haller B. Protein conformation as a regulator of cell-matrix adhesion. *Phys Chem Chem Phys.* 2014. doi:10.1039/c3cp54884h.
121. Choi CK, Vicente-Manzanares M, Zareno J, Whitmore, A. L, Mogilner A, Horwitz AR. Actin and  $\alpha$ -actinin orchestrate the assembly and maturation of nascent adhesions in a myosin II motor-independent manner. *Nat Cell Biol.* 2008.
122. Zaidel-Bar R, Cohen M, Addadi L, Geiger B. Hierarchical assembly of cell-matrix adhesion complexes. *Biochem Soc Trans.* 2004. doi:10.1042/bst0320416.
123. Sun Z, Guo SS, Fässler R. Integrin-mediated mechanotransduction. *J Cell Biol.* 2016. doi:10.1083/jcb.201609037.
124. Margadant F, Chew LL, Hu X, et al. Mechanotransduction in vivo by repeated talin stretch-relaxation events depends upon vinculin. *PLoS Biol.* 2011. doi:10.1371/journal.pbio.1001223.
125. Papagrigoriou E, Gingras AR, Barsukov IL, et al. Activation of a vinculin-binding site in the talin rod involves rearrangement of a five-helix bundle. *EMBO J.* 2004. doi:10.1038/.
126. Lee SE, Kamm RD, Mofrad MRK. Force-induced activation of Talin and its possible role in focal adhesion mechanotransduction. *J Biomech.* 2007. doi:10.1016/j.jbiomech.2007.04.006.
127. Muretta JM, Thomas DD. Mutation that causes hypertrophic cardiomyopathy increases force production in human  $\beta$ -cardiac myosin. *Proc Natl Acad Sci.* 2013. doi:10.1073/pnas.1310669110.
128. Mogensen J, Perrot A, Andersen P, et al. Clinical and genetic characteristics of  $\alpha$  cardiac actin gene mutations in hypertrophic cardiomyopathy. *J Med Genet.* 2004. doi:10.1136/jmg.2004.019257.
129. Satoh M, Takahashi M, Sakamoto T, Hiroe M, Marumo F, Kimura A. Structural analysis of the titin gene in hypertrophic cardiomyopathy: Identification of a novel disease gene. *Biochem Biophys Res Commun.* 1999. doi:10.1006/bbrc.1999.1221.
130. Jääskeläinen P, Heliö T, Aalto-Setälä K, et al. Two founder mutations in the alpha-tropomyosin and the cardiac myosin-binding protein C genes are common causes of

- hypertrophic cardiomyopathy in the Finnish population. *Ann Med*. 2013. doi:10.3109/07853890.2012.671534.
131. Wang H, Li Z, Wang J, et al. Mutations in NEXN, a Z-Disc gene, are associated with hypertrophic cardiomyopathy. *Am J Hum Genet*. 2010. doi:10.1016/j.ajhg.2010.10.002.
  132. Watkins H, McKenna W, Thierfelder L, et al. Mutations in the genes for cardiac troponin T and  $\alpha$ -tropomyosin in hypertrophic cardiomyopathy. *N Engl J Med*. 1995.
  133. Landstrom AP, Parvatiyar MS, Pinto JR, et al. Molecular and Functional Characterization of Novel Hypertrophic Cardiomyopathy Susceptibility Mutations in TNNC1- Encoded Troponin C. *J Mol Cell Cardiol*. 2008. doi:10.1016/j.yjmcc.2008.05.003.Molecular.
  134. Mohapatra B, Jimenez S, Lin JH, et al. Mutations in the muscle LIM protein and  $\alpha$ -actinin-2 genes in dilated cardiomyopathy and endocardial fibroelastosis. *Mol Genet Metab*. 2003. doi:10.1016/S1096-7192(03)00142-2.
  135. Li D, Tapscoft T, Gonzalez O, et al. Desmin mutation responsible for idiopathic dilated cardiomyopathy. *Circulation*. 1999. doi:10.1161/01.CIR.100.5.461.
  136. Vasile VC, Will ML, Ommen SR, Edwards WD, Olson TM, Ackerman MJ. Identification of a metavinculin missense mutation, R975W, associated with both hypertrophic and dilated cardiomyopathy. *Mol Genet Metab*. 2006. doi:10.1016/j.ymgme.2005.08.006.
  137. Song K, Dubé MP, Lim J, Hwang I, Lee I, Kim J-J. Lamin A/C mutations associated with familial and sporadic cases of dilated cardiomyopathy in Koreans. *Exp Mol Med*. 2007. doi:10.1038/emm.2007.13.
  138. Tsubata S, Bowles KR, Vatta M, et al. Mutations in the human delta-sarcoglycan gene in familial and sporadic dilated cardiomyopathy. *J Clin Invest*. 2000. doi:10.1172/JCI9224.
  139. Milewicz DM, Østergaard JR, Ala-kokko LM, et al. De Novo ACTA2 Mutation Causes a Novel Syndrome of Multisystemic Smooth Muscle Dysfunction. *Am J Med Genet*. 2010. doi:10.1002/ajmg.a.33657.
  140. Oksala N, Pärssinen J, Seppälä I, et al. Kindlin 3 (FERMT3) is associated with unstable atherosclerotic plaques, anti-inflammatory type II macrophages and upregulation of beta-2 integrins in all major arterial beds. *Atherosclerosis*. 2015. doi:10.1016/j.atherosclerosis.2015.06.058.
  141. Gallagher PG, Tse WT, Coetzer T, et al. A common type of the spectrin  $\alpha$ I 46-50a-kD peptide abnormality in hereditary elliptocytosis and pyropoikilocytosis is associated with a mutation distant from the proteolytic cleavage site: Evidence for the functional importance of the triple helical model. *J Clin Invest*. 1992. doi:10.1172/JCI115669.
  142. Bassères DS.  $\beta$ -Spectrin São Paulo II , a novel frameshift mutation of the  $\beta$ -spectrin gene associated with hereditary spherocytosis and instability of the mutant mRNA. 2002.
  143. Hanspal M, Hanspal JS, Sahr KE, Fibach E, Nachman J, Palek J. Molecular basis of spectrin deficiency in hereditary pyropoikilocytosis. *Blood*. 1993.
  144. Gresele P, Falcinelli E, Giannini S, et al. Dominant inheritance of a novel integrin  $\beta$ 3 mutation associated with a hereditary macrothrombocytopenia and platelet dysfunction in two Italian families. *Haematologica*. 2009. doi:10.3324/haematol.2008.002246.

145. Kunishima S, Okuno Y, Yoshida K, et al. ACTN1 mutations cause congenital macrothrombocytopenia. *Am J Hum Genet.* 2013. doi:10.1016/j.ajhg.2013.01.015.
146. Corrado A. *Muscular Dystrophy Cause and Management.* Vol (Corrado A, ed.). Nova Science Publishers, Inc., New York; 2013.
147. Punnoose A, Burke AE., Golub R. Muscular dystrophy. *JAMA.* 2011.
148. Nowak KJ, Davies KE. Duchenne muscular dystrophy and dystrophin: Pathogenesis and opportunities for treatment: Third in molecular medicine review series. *EMBO Rep.* 2004. doi:10.1038/sj.embor.7400221.
149. Live D, Wells L, Boons G-L. Dissecting the Molecular Basis of the Role of the O-Mannosylation Pathway in Disease: a-Dystroglycan and Forms of Muscular Dystrophy. 2013. doi:10.1002/cbic.201300417.
150. Vainzof M, Passos-Bueno MR, Canovas M, et al. The sarcoglycan complex in the six autosomal recessive limb-girdle muscular dystrophies. *Hum Mol Genet.* 1996. doi:10.1093/hmg/5.12.1963.
151. Cetin N, Balci-Hayta B, Gundesli H, et al. A novel desmin mutation leading to autosomal recessive limb-girdle muscular dystrophy: Distinct histopathological outcomes compared with desminopathies. *J Med Genet.* 2013. doi:10.1136/jmedgenet-2012-101487.
152. Fulizio L, Nascimbeni AC, Fanin M, et al. Molecular and muscle pathology in a series of caveolinopathy patients. *Hum Mutat.* 2005. doi:10.1002/humu.20119.
153. Zhang Q, Bethmann C, Worth NF, et al. Nesprin-1 and -2 are involved in the pathogenesis of Emery - Dreifuss muscular dystrophy and are critical for nuclear envelope integrity. *Hum Mol Genet.* 2007. doi:10.1093/hmg/ddm238.
154. Muchir a, Bonne G, van der Kooi a J, et al. Identification of mutations in the gene encoding lamins A/C in autosomal dominant limb girdle muscular dystrophy with atrioventricular conduction disturbances (LGMD1B). *Hum Mol Genet.* 2000. doi:ddd158.
155. Garavelli L, D'Apice MR, Rivieri F, et al. Mandibuloacral dysplasia type A in childhood. *Am J Med Genet Part A.* 2009. doi:10.1002/ajmg.a.33005.
156. Callewaert BL, Loeyls BL, Ficcadenti A, et al. Comprehensive clinical and molecular assessment of 32 probands with congenital contractural arachnodactyly: Report of 14 novel mutations and review of the literature. *Hum Mutat.* 2009. doi:10.1002/humu.20854.
157. Krakow D, Robertson SP, King LM, et al. Mutations in the gene encoding filamin B disrupt vertebral segmentation, joint formation and skeletogenesis. *Nat Genet.* 2004. doi:10.1038/ng1319.
158. Bicknell LS, Farrington-Rock C, Shafeghati Y, et al. A molecular and clinical study of Larsen syndrome caused by mutations in FLNB. *J Med Genet.* 2007. doi:10.1136/jmg.2006.043687.
159. Rivière JB, Van Bon BWM, Hoischen A, et al. De novo mutations in the actin genes ACTB and ACTG1 cause Baraitser-Winter syndrome. *Nat Genet.* 2012. doi:10.1038/ng.1091.
160. Verloes A, Di Donato N, Masliah-Planchon J, et al. Baraitser-Winter cerebrofrontofacial syndrome: Delineation of the spectrum in 42 cases. *Eur J Hum Genet.* 2015. doi:10.1038/ejhg.2014.95.
161. Barnes AM, Chang W, Morello R, et al. Deficiency of cartilage-associated protein in recessive lethal osteogenesis imperfecta. *N Engl J Med.* 2006. doi:10.1056/NEJMoa063804.

162. Van Dijk FS, Zillikens MC, Micha D, et al. *PLS3* Mutations in X-Linked Osteoporosis with Fractures. *N Engl J Med*. 2013. doi:10.1056/NEJMoa1308223.
163. Kim TH, Rowat AC, Sloan EK. Neural regulation of cancer: From mechanobiology to inflammation. *Clin Transl Immunol*. 2016. doi:10.1038/cti.2016.18.
164. Irianto J, Pfeifer CR, Ivanovska IL, Swift J, Discher DE. Nuclear Lamins in Cancer. *Cell Mol Bioeng*. 2016. doi:10.1007/s12195-016-0437-8.
165. Makale M. Cellular mechanobiology and cancer metastasis. *Birth Defects Res Part C - Embryo Today Rev*. 2007. doi:10.1002/bdrc.20110.
166. Yabuta T, Shinmura K, Tani M, et al. E-cadherin gene variants in gastric cancer families whose probands are diagnosed with diffuse gastric cancer. *Int J Cancer*. 2002. doi:10.1002/ijc.10633.
167. Masciari S, Larsson N, Senz J, et al. Germline E-cadherin mutations in familial lobular breast cancer. *J Med Genet*. 2007. doi:10.1136/jmg.2007.051268.
168. Risinger JI, Berchuck A, Kohler MF, Boyd J. Mutations of the E-cadherin gene in human gynecologic cancers. *Nat Genet*. 1994. doi:10.1038/ng0594-98.
169. Siegel DH, Ashton GHS, Penagos HG, et al. Loss of Kindlin-1, a Human Homolog of the *Caenorhabditis elegans* Actin-Extracellular-Matrix Linker Protein UNC-112, Causes Kindler Syndrome. *Am J Hum Genet*. 2003. doi:10.1086/376609.
170. Fine JD, Eady R a. J, Bauer E a., et al. The classification of inherited epidermolysis bullosa (EB): Report of the Third International Consensus Meeting on Diagnosis and Classification of EB. *J Am Acad Dermatol*. 2008. doi:10.1016/j.jaad.2008.02.004.
171. Has C, Spartà G, Kiritsi D, et al. Integrin  $\alpha_3$  Mutations with Kidney, Lung, and Skin Disease. *N Engl J Med*. 2012. doi:10.1056/NEJMoa1110813.
172. Zekanowski C, Golan MP, Krzyśko K a., et al. Two novel presenilin 1 gene mutations connected with frontotemporal dementia-like clinical phenotype: Genetic and bioinformatic assessment. *Exp Neurol*. 2006. doi:10.1016/j.expneurol.2006.01.022.
173. Gros-Louis F, Dupré N, Dion P, et al. Mutations in SYNE1 lead to a newly discovered form of autosomal recessive cerebellar ataxia. *Nat Genet*. 2007. doi:10.1038/ng1927.
174. Conti FJ, Monkley SJ, Wood MR, Critchley DR, Müller U. Talin 1 and 2 are required for myoblast fusion, sarcomere assembly and the maintenance of myotendinous junctions. *Development*. 2009. doi:10.1242/dev.035857.
175. McKusick-Nathans (Institute of Genetic Medicine, John Hopkins University Baltimore M. Online Mendelian Inheritance in Man, OMIM®. <http://www.omim.org/>.
176. Deng H, Deng S, Xu H, et al. Exome sequencing of a pedigree reveals S339L mutation in the TLN2 gene as a cause of fifth finger camptodactyly. *PLoS One*. 2016. doi:10.1371/journal.pone.0155180.
177. Wu Q, Zhang J, Koh W, et al. Talin1 is required for cardiac Z-disk stabilization and endothelial integrity in zebrafish. *FASEB J*. 2015. doi:10.1096/fj.15-273409.
178. Manevich-Mendelson E, Grabovsky V, Feigelson SW, et al. Talin1 is required for integrin-dependent B lymphocyte homing to lymph nodes and the bone marrow but not for follicular B cell maturation in the spleen Talin1 is required for integrin-dependent B lymphocyte homing to lymph nodes and the bone marrow but no. *Blood*. 2010. doi:10.1182/blood-2010-06-293506.

179. Zhang J-L, Qian Y-B, Zhu L-X, Xiong Q-R. Talin1, a valuable marker for diagnosis and prognostic assessment of human hepatocellular carcinomas. *Asian Pac J Cancer Prev*. 2011.
180. Sakamoto S, McCann RO, Dhir R, Kyprianou N. Talin1 promotes tumor invasion and metastasis via focal adhesion signaling and anoikis resistance. *Cancer Res*. 2010. doi:10.1158/0008-5472.CAN-09-2833.
181. Beaty BT, Wang Y, Bravo-Cordero JJ, et al. Talin regulates moesin-NHE-1 recruitment to invadopodia and promotes mammary tumor metastasis. *J Cell Biol*. 2014. doi:10.1083/jcb.201312046.
182. Tang H, Yao L, Tao X, et al. MiR-9 functions as a tumor suppressor in ovarian serous carcinoma by targeting TLN. *Int J Mol Med*. 2013. doi:10.3892/ijmm.2013.1400.
183. Sen S, Ng WP, Kumar S. Contributions of talin-1 to glioma cell-matrix tensional homeostasis. *J R Soc Interface*. 2012. doi:10.1098/rsif.2011.0567.
184. Xu Y-F, Ren X-Y, Li Y-Q, et al. High expression of Talin-1 is associated with poor prognosis in patients with nasopharyngeal carcinoma. *BMC Cancer*. 2015. doi:10.1186/s12885-015-1351-5.
185. Forbes S a., Beare D, Boutselakis H, et al. COSMIC: Somatic cancer genetics at high-resolution. *Nucleic Acids Res*. 2017. doi:10.1093/nar/gkw1121.
186. Fröbel J, Cadeddu R-P, Hartwig S, et al. Platelet Proteome Analysis Reveals Integrin-dependent Aggregation Defects in Patients with Myelodysplastic Syndromes. *Mol Cell Proteomics*. 2013. doi:10.1074/mcp.M112.023168.
187. Ye F, Snider AK, Ginsberg MH. Talin and kindlin: The one-two punch in integrin activation. *Front Med China*. 2014. doi:10.1007/s11684-014-0317-3.
188. Zerbino DR, Achuthan P, Akanni W, et al. Ensembl 2018. *Nucleic Acids Res*. 2018. doi:10.1093/nar/gkx1098.
189. Agarwala R, Barrett T, Beck J, et al. Database Resources of the National Center for Biotechnology Information. *Nucleic Acids Res*. 2017. doi:10.1093/nar/gkw1071.
190. Baxter NJ, Zacharchenko T, Barsukov IL, Williamson MP. Pressure-Dependent Chemical Shifts in the R3 Domain of Talin Show that It Is Thermodynamically Poised for Binding to Either Vinculin or RIAM. *Structure*. 2017. doi:10.1016/j.str.2017.10.008.
191. Ringer P, Weißl A, Cost AL, et al. Multiplexing molecular tension sensors reveals piconewton force gradient across talin-1. *Nat Methods*. 2017. doi:10.1038/nmeth.4431.
192. Vendruscolo M, Paci E. Protein folding: Bringing theory and experiment closer together. *Curr Opin Struct Biol*. 2003. doi:10.1016/S0959-440X(03)00007-1.
193. Abraham M, Hess B, Spoel D van der, Lindahl E, GROMACS development team. Gromacs 5.1.3 Reference Manual. www.gromacs.org.
194. Lindorff-Larsen K, Maragakis P, Piana S, Eastwood MP, Dror RO, Shaw DE. Systematic validation of protein force fields against experimental data. *PLoS One*. 2012. doi:10.1371/journal.pone.0032131.
195. NosÉ S. A molecular dynamics method for simulations in the canonical ensemble. *Mol Phys*. 2002. doi:10.1080/00268970110089108.
196. Berendsen HJC, Postma JPM, Van Gunsteren WF, Dinola a., Haak JR. Molecular dynamics with coupling to an external bath. *J Chem Phys*. 1984. doi:10.1063/1.448118.

197. Bussi G, Donadio D, Parrinello M. Canonical sampling through velocity rescaling. *J Chem Phys*. 2007. doi:10.1063/1.2408420.
198. Sotomayor M, Schulten K. Single-Molecule Experiments in Vitro and in Silico. 2007. doi:10.1126/science.1137591.
199. Sikora M, Cieplak M, Sulkowska, Joanna I. Witkowski BS. Bio-molecule Stretching Database (BSDB). 2010. <http://jowisz.ifpan.edu.pl/BSDB/index.php>.
200. Li H, Fernandez JM. Mechanical design of the first proximal Ig domain of human cardiac titin revealed by single molecule force spectroscopy. *J Mol Biol*. 2003. doi:10.1016/j.jmb.2003.09.036.
201. Fowler SB, Best RB, Toca Herrera JL, et al. Mechanical unfolding of a titin Ig domain: Structure of unfolding intermediate revealed by combining AFM, molecular dynamics simulations, NMR and protein engineering. *J Mol Biol*. 2002. doi:10.1016/S0022-2836(02)00805-7.
202. Kumar S, Li MS. Biomolecules under mechanical force. *Phys Rep*. 2010. doi:10.1016/j.physrep.2009.11.001.
203. Li H, Oberhauser a F, Fowler SB, Clarke J, Fernandez JM. Atomic force microscopy reveals the mechanical design of a modular protein. *Proc Natl Acad Sci U S A*. 2000. doi:10.1073/pnas.120048697.
204. Rief M, Gautel M, Oesterhelt F, Fernandez JM, Gaub HE. Reversible unfolding of individual titin immunoglobulin domains by AFM. *Science*. 1997. doi:10.1126/science.276.5315.1109.
205. Watanabe K, Muhle-Goll C, Kellermayer MSZ, Labeit S, Granzier H. Different molecular mechanics displayed by titin's constitutively and differentially expressed tandem Ig segments. *J Struct Biol*. 2002. doi:10.1006/jsbi.2002.4458.
206. Yao M, Goult BT, Chen H, Cong P, Sheetz MP, Yan J. Mechanical activation of vinculin binding to talin locks talin in an unfolded conformation. *Sci Rep*. 2014. doi:10.1038/srep04610.
207. Galkina E, Ley K. Vascular adhesion molecules in atherosclerosis. *Arterioscler Thromb Vasc Biol*. 2007. doi:10.1161/ATVBAHA.107.149179.
208. Olson TM, Illenberger S, Kishimoto NY, Huttelmaier S, Keating MT, Jockusch BM. Metavinculin mutations alter actin interaction in dilated cardiomyopathy. *Circulation*. 2002. doi:10.1161/hc0402.102930.
209. Davies PF. Hemodynamic shear stress and the endothelium in cardiovascular pathophysiology. *Nat Clin Pract Cardiovasc Med*. 2009. doi:10.1038/ncpcardio1397.
210. Tarbell JM. Shear stress and the endothelial transport barrier. *Cardiovasc Res*. 2010. doi:10.1093/cvr/cvq146.
211. Nagel T, Resnick N, Atkinson WJ, Dewey CF, Gimbrone MA. Shear stress selectively upregulates intercellular adhesion molecule-1 expression in cultured human vascular endothelial cells. *J Clin Invest*. 1994. doi:10.1172/JCI117410.
212. Yim EK, Sheetz MP. Force-dependent cell signaling in stem cell differentiation. *Stem Cell Res Ther*. 2012. doi:10.1186/scrt132.
213. Aird WC. Endothelial cell heterogeneity. *Cold Spring Harb Perspect Med*. 2012. doi:10.1101/cshperspect.a006429.
214. Elosegui-Artola A, Oria R, Chen Y, et al. Mechanical regulation of a molecular clutch defines force transmission and transduction in response to matrix rigidity. *Nat Cell Biol*. 2016. doi:10.1038/ncb3336.

215. Carisey A, Tsang R, Greiner AM, et al. Vinculin regulates the recruitment and release of core focal adhesion proteins in a force-dependent manner. *Curr Biol*. 2013. doi:10.1016/j.cub.2013.01.009.
216. Liu J, Wang Y, Goh WI, et al. Talin determines the nanoscale architecture of focal adhesions. *Proc Natl Acad Sci*. 2015. doi:10.1073/pnas.1512025112.
217. Wang X, Ha T. Defining single molecular forces required to activate integrin and Notch signaling. *Science*. 2013. doi:10.1126/science.1231041.
218. Austen K, Ringer P, Mehlich A, et al. Extracellular rigidity sensing by talin isoform-specific mechanical linkages. *Nat Cell Biol*. 2015. doi:10.1038/ncb3268.
219. Yao M, Qiu W, Liu R, et al. Force-dependent conformational switch of  $\alpha$ -catenin controls vinculin binding. *Nat Commun*. 2014. doi:10.1038/ncomms5525.
220. Gingras AR, Bate N, Goult BT, et al. Central region of talin has a unique fold that binds vinculin and actin. *J Biol Chem*. 2010. doi:10.1074/jbc.M109.095455.
221. Bouchet BP, Gough RE, Ammon YC, et al. Talin-KANK1 interaction controls the recruitment of cortical microtubule stabilizing complexes to focal adhesions. *Elife*. 2016. doi:10.7554/eLife.18124.
222. Zacharchenko T, Qian X, Goult BTT, et al. LD Motif Recognition by Talin: Structure of the Talin-DLC1 Complex. *Structure*. 2016. doi:10.1016/j.str.2016.04.016.

## 9 ORIGINAL PUBLICATIONS



## Talin and vinculin are downregulated in atherosclerotic plaque; Tampere Vascular Study



Magdaléna von Essen <sup>a,1</sup>, Rolle Rahikainen <sup>a,1</sup>, Niku Oksala <sup>b,c</sup>, Emma Raitoharju <sup>b</sup>, Ilkka Seppälä <sup>b</sup>, Ari Mennander <sup>d</sup>, Thanos Sioris <sup>d</sup>, Ivana Kholová <sup>e</sup>, Norman Klopp <sup>f</sup>, Thomas Illig <sup>f,g,h</sup>, Pekka J. Karhunen <sup>i</sup>, Mika Kähönen <sup>j</sup>, Terho Lehtimäki <sup>b,2</sup>, Vesa P. Hytönen <sup>a,\*,2</sup>

<sup>a</sup> BioMediTech, University of Tampere and Fimlab Laboratories, Tampere, Finland

<sup>b</sup> Dep. of Clinical Chemistry, Fimlab Laboratories, Tampere University Hospital and School of Medicine, University of Tampere, Tampere, Finland

<sup>c</sup> Division of Vascular Surgery, Department of Surgery, Tampere University Hospital, Tampere, Finland

<sup>d</sup> Heart Center, Tampere University Hospital, Tampere, Finland

<sup>e</sup> Department of Pathology, Fimlab Laboratories, Tampere University Hospital and School of Medicine, University of Tampere, Tampere, Finland

<sup>f</sup> Hannover Unified Biobank, Hannover Medical School, Hannover, Germany

<sup>g</sup> Institute of Human Genetics, Hannover Medical School, Hannover, Germany

<sup>h</sup> Research Unit of Molecular Epidemiology, Helmholtz Zentrum München, German Research Center for Environmental Health, Neuherberg, Germany

<sup>i</sup> School of Medicine, University of Tampere and Fimlab Laboratories, Tampere University Hospital, Tampere, Finland

<sup>j</sup> Department of Clinical Physiology, Tampere University Hospital and School of Medicine, University of Tampere, Tampere, Finland

### ARTICLE INFO

#### Article history:

Received 9 June 2016

Received in revised form

12 October 2016

Accepted 14 October 2016

Available online 15 October 2016

#### Keywords:

Mechanobiology

Atherosclerosis

Focal adhesion

Talin

Vinculin

### ABSTRACT

**Background and aims:** Focal adhesions (FA) play an important role in the tissue remodeling and in the maintenance of tissue integrity and homeostasis. Talin and vinculin proteins are among the major constituents of FAs contributing to cellular well-being and intercellular communication.

**Methods:** Microarray analysis (MA) and qRT-PCR low-density array were implemented to analyze talin-1, talin-2, meta-vinculin and vinculin gene expression in circulating blood and arterial plaque.

**Results:** All analyzed genes were significantly and consistently downregulated in plaques (carotid, abdominal aortic and femoral regions) compared to left internal thoracic artery (LITA) control. The use of LITA samples as controls for arterial plaque samples was validated using immunohistochemistry by comparing LITA samples with healthy arterial samples from a cadaver. Even though the differences in expression levels between stable and unstable plaques were not statistically significant, we observed further negative tendency in the expression in unstable atherosclerotic plaques. The confocal tissue imaging revealed gradient of talin-1 expression in plaque with reduction close to the vessel lumen. Similar gradient was observed for talin-2 expression in LITA controls but was not detected in plaques. This suggests that impaired tissue mechanostability affects the tissue remodeling and healing capabilities leading to development of unstable plaques.

**Conclusions:** The central role of talin and vinculin in cell adhesions suggests that the disintegration of the tissue in atherosclerosis could be partially driven by downregulation of these genes, leading to loosening of cell-ECM interactions and remodeling of the tissue.

© 2016 Elsevier Ireland Ltd. All rights reserved.

\* Corresponding author. BioMediTech, Lääkärintätkatu 1, FI-33520, Tampere, Finland.

E-mail address: [vesa.hytonen@uta.fi](mailto:vesa.hytonen@uta.fi) (V.P. Hytönen).

<sup>1</sup> These authors contributed equally to this work.

<sup>2</sup> These authors contributed equally to this work.

### 1. Introduction

Atherosclerosis is a disease of the vasculature with a complex etiology. Risk factors include age, sex, family history, dyslipidemia, high blood pressure and high body mass index (BMI), stress and dietary factors. The disease develops over a long time period and may remain asymptomatic over decades. It is characterized by

## Abbreviations

BMI	body mass index
CAD	coronary artery disease
ECM	extracellular matter
FA	focal adhesion
FC	focal complex
fc	fold change
HUVEC	human umbilical vein endothelial cell
ICAM	intercellular adhesion molecule
LDA	low density array
LITA	left internal thoracic artery
MA	microarray analysis
M $\Phi$	macrophage
PECAM	platelet endothelial cell adhesion molecule
SMC	smooth muscle cell
TVS	Tampere Vascular Study
VBS	vinculin binding site
VCAM	vascular cell adhesion molecule
FFPE	formalin-fixed, paraffin-embedded
HE	hematoxylin-eosin

chronic inflammation of the arterial wall, by infiltration of macrophages (M $\Phi$ ) and accumulation of oxidized low-density lipoproteins leading to M $\Phi$  conversion to foam cells [1].

The vasculature is continuously exposed to cyclical fluctuations of blood flow, pressure and fluid shear stress and also exhibits diurnal variation. The blood mechanical impacts of varying magnitudes exert significant influences on physiological and pathophysiological processes [2–4]. For illustration, veins and arteries are composed of several tissue layers with different cell and extracellular matter (ECM) content. This cell and ECM composition determines the tissue characteristics in terms of physicochemical properties [5,6]. Hence, each vessel layer possesses different ability to withstand, produce or transduce mechanical forces [5]. The mechanical pressure sensed by the endothelial cells is transferred from the extracellular space through the actin cytoskeletal network towards the nucleus [7,8].

To date, a number of genes implicated in cellular mechanostability and their altered expression has been associated with the progress of atherosclerosis. For example, ADAM metalloprotease disintegrins have been linked with cell-cell/surface adhesion and inflammation progression in the atherosclerotic plaque [9]. Moreover, the expression levels of integrin and kindlin family proteins were found to be altered in progressing atherosclerotic plaques [10]. Integrin and kindlin proteins support leukocyte adhesion, transendothelial migration, platelet aggregation and thrombosis. Furthermore, integrins and kindlins are together with talin and vinculin among the major components of focal adhesions (FA). FAs are key attachments between cells and ECM and play an important role in cell morphology, differentiation, locomotion and intercellular communication. FAs are crucial for the tissue remodeling, integrity and homeostasis through the maintenance of intercellular gaps and cell adhesion supervision.

Talin is a large flexible protein [11] binding to transmembrane integrins (N-terminal FERM domain) [12] and to cytoskeletal actin (C-terminal rod) [13] providing a vital link between the intra- and extracellular space and allowing the communication between the ECM and nucleus [8]. Talin plays a significant role in the actin filament assembly and in spreading and migration of various cell types. During the adhesion maturation, talin recruits vinculin to

crosslink with F-actin filaments and stabilize the adhesion complex. For this purpose talin rod contains several binding sites for vinculin [14]. Vinculin binding sites (VBSs) are buried inside the structural bundles and require a major conformational change in the bundle organization prior to vinculin binding [15]. Mechanical force has been suspected to mediate such domain reorganization and talin-vinculin binding [16,17]. Talin interacts with several ligands making it a vital component of numerous mechanosensor and chemical signaling pathways [18–21].

Vinculin is a cytoskeletal protein crosslinking talin and F-actin. Vinculin is ubiquitously expressed with high expression in skeletal, cardiac and smooth muscle. Vinculin head at the N-terminal end binds to talin's VBSs [22]. Vinculin tail at the C-terminal end binds F-actin [23]. Also other important interactions of vinculin have been recognized, for example with paxilin [24] and  $\alpha$ -actinin [25]. These ligands make vinculin an important contributor to focal adhesion complex, as well as to the cytoskeletal assembly and stability.

The progress and the causatives of atherosclerosis have been intensively investigated during the past decades. Still, the mechanisms behind the disease development are not fully understood. In more detail, the mechanical impact of shear stress on the cell and tissue integrity has risen to attention only recently. We hypothesize that the cellular mechanostability and maintenance of tissue integrity through focal adhesions is an important factor in all stages of atherosclerotic plaque development. We speculate that the function of focal adhesions is compromised by altered expression of cell adhesion proteins talin and vinculin in atherosclerotic plaque as compared to non-atherosclerotic vessel wall.

In this work, we followed talin and vinculin expression in atherosclerotic plaque samples collected in ongoing Tampere Vascular Study (TVS) series. Gene expression in carotid, abdominal aortic and femoral plaque samples was compared to expression values in left internal thoracic artery (LITA) controls. Expression levels were determined by microarray analysis and low-density qRT-PCR-array. Results are supported by smooth muscle cell (SMC) and macrophage (M $\Phi$ ) marker co-expression analysis. The tissue localization of talin and vinculin was investigated by confocal immunofluorescence study.

## 2. Materials and methods

### 2.1. Vascular samples

Arterial sample series from Tampere Vascular Study (TVS) [9,10,26], including samples from femoral, carotid and abdominal aortic regions, were obtained during open vascular procedures between 2005 and 2015. The patients fulfilled the following inclusion criteria: (1) carotid endarterectomy performed because of asymptomatic or symptomatic and hemodynamically significant carotid stenosis (>70%); (2) femoral or (3) aortic endarterectomy with aortoiliac or aortobifemoral bypass based on symptomatic peripheral arterial disease. The left internal thoracic artery (LITA) controls were obtained during coronary artery bypass surgery due to coronary artery disease (CAD). The samples were collected from patients subjected to open vascular surgery in the Division of Vascular Surgery and Heart Center, Tampere University Hospital. The patient's denial to participate in the study was used as a measure of exclusion. The vascular samples were classified according to American Heart Association recommendation [27]. The type V and VI atherosclerotic lesions were further histologically classified as stable and unstable according to the presence of fissure, rupture, hemorrhage or thrombosis. Gene expression was analyzed from carotid (n = 29), abdominal aortic (n = 15), and femoral (n = 24) plaques (cases) and compared to atherosclerosis-

free LITA samples ( $n = 28$ ) (controls). The study has been approved by the Ethics Committee of Tampere Hospital District. All studies were conducted according to the declaration of Helsinki, with the informed consent from individual patient involved.

## 2.2. Whole blood and circulating monocyte fractions

TVS whole blood and monocyte fractions were collected during 2008. The angiographically verified samples were selected from a larger population-based cross-sectional study [28] collected between 2001 and 2004 comprising patients subjected to an exercise test at Tampere University Hospital (treatment according to the Finnish Current Care Guidelines). RNA was isolated from the whole blood and monocyte fractions of individuals with CAD ( $n = 55$ ) and without coronary artery lesions ( $n = 45$ ). Patient history data were based on hospital records and patient interviews. These data covered the demographics such as age, sex, weight, lifestyle information and classical cardiovascular risk factors and symptoms.

## 2.3. RNA isolation and microarrays

The fresh arterial tissue samples were soaked in RNALater solution (Ambion Inc, Austin, TX) and isolated with Trizol reagent (Invitrogen, Carlsbad, CA) and the RNeasy Kit with DNase Set (Qiagen, Valencia, CA). From the whole blood fraction, the RNA was isolated with PAXgene tubes (BD, Franklin Lakes, NJ) and PAXgene Blood RNA Kit (Qiagen) with DNase Set. Peripheral mononuclear cells were isolated from the whole blood samples by Ficoll-Paque density-gradient centrifugation (Amersham Pharmacia Biotech UK Limited, Buckinghamshire, England). Total RNA was then extracted using RNeasy Mini Kit (Qiagen). Manufacturers' instructions were followed in all isolation protocols. The quality of the RNA samples was evaluated spectrophotometrically and stored at  $-80\text{ }^{\circ}\text{C}$ .

The expression levels of arterial and whole blood samples were analyzed with Illumina HumanHT-12 v3 Expression BeadChip (Illumina, San Diego, CA) analyzing 47,000 transcripts of all known genes, gene candidates, and splice variants. The microarray experiments with the monocyte RNA were performed using Sentrix Human-6 Expression BeadChips analyzing >46,000 transcripts (Illumina). Both arrays were run according to given instructions by the manufacturer and scanned with the Illumina iScan system. Further details of the methodology can be found in work by Turpeinen et al. [29].

## 2.4. Microarray data analysis

After background subtraction, raw intensity data were exported using the Illumina GenomeStudio software. Raw expression data were imported into R software,  $\log_2$  transformed and normalized by the locally estimated scatterplot smoothing normalization method implemented in the R/Bioconductor package Lumi. Locally estimated scatterplot smoothing normalization returned the best accuracy to detect differentially expressed genes in comparison with quantitative reverse transcription polymerase chain reaction using the control artery (LITA) and atherosclerotic plaque samples from the TVS study [30]. All samples fulfilled following data quality control criteria; detection of outlier arrays based on the low number of robustly expressed genes and hierarchical clustering. Probes were considered robustly expressed if the detection was  $p < 0.05$  for minimum of 50% of the samples in the data set. *TLN1* (microarray element probe ILMN\_1696643), *TLN2* (microarray element probe ILMN\_1700042) and *VCL* (transcript variant 1, microarray element probe ILMN\_1795429; transcript variant 2, microarray element probe ILMN\_2413527) genes were selected for differential

expression and correlation analyses. These results were further confirmed by low-density qRT-PCR array.

## 2.5. Low-density qRT-PCR-array (LDA)

The quantitative real-time polymerase chain reaction (qRT-PCR) was performed with TaqMan low-density array (LDAs; Applied Biosystems) according to the manufacturer's instructions. The functionality of TaqMan assays, the optimal amounts of RNA in cDNA synthesis and optimal amount of cDNA in qRT-PCR were first optimized for functional range and validated for inhibition using several concentrations in separate TaqMan assays. Sufficient RNA was available for 19 out of 24 LITAs (79.2%) and 64 out of 68 plaque (94.2%) samples. 60 (30 cases and 30 controls) out of 96 blood samples (62.5%) were selected for analysis based on pairwise matching according to BMI, age, gender and smoking status. In detail, 500 ng of total RNA per sample was transcribed to cDNA using the High Capacity cDNA Kit (Applied Biosystems). For the qPCR, LDAs were loaded with 7  $\mu\text{l}$  cDNA synthesis product (175 ng of RNA), 43  $\mu\text{l}$   $\text{H}_2\text{O}$  and 50  $\mu\text{l}$  PCR Universal Master Mix (Applied Biosystems). The array contained technical triplicates. Glyceraldehyde-3-phosphate dehydrogenase (GAPDH, assayID Hs99999905\_m1) was used as housekeeping gene control. The qRT-PCR data was analyzed with Expression suite software (Applied biosystems) using the  $2^{-\Delta\Delta\text{CT}}$  method.

## 2.6. Hierarchical clustering and correlation analyses

*TLN1*, *TLN2*, *VCL* and well-characterized biomarkers of inflammation (cluster of differentiation 68 (CD68) and arachidonate 5-lipoxygenase (ALOX5)), and SMCs markers (calponin 1 (CNN1), smoothelin (SMTN)) [31] were used in the hierarchical clustering analysis to assess whether subgroups of samples had similar marker profiles. Furthermore, similarity of the expression levels (*TLN1*, *TLN2* and *VCL*) across the samples was studied. The procedure was performed using the heatmap.2 function from the gplots R library on all 68 artery samples. Pearson dissimilarity and average linkage were used for the hierarchical clustering of both genes and samples. To further investigate the *TLN1*, *TLN2* and *VCL* genes as measures of plaque cell composition, correlation analyses were performed using previously established macrophage and SMC-rich plaque signatures [31].

## 2.7. Confocal immunofluorescence study of frozen and paraffin-embedded samples

For immunofluorescence labeling of frozen tissue sections, vascular samples from LITA and from atherosclerotic carotid artery were embedded into TissueTek O.C.T compound (Sakura Finetek, USA), frozen in liquid nitrogen and stored at  $-80\text{ }^{\circ}\text{C}$ . Leica CM 3050S (Leica Biosystems, Nussloch, Germany) cryostat was used to cut 6  $\mu\text{m}$  sections of the frozen tissues. Before antibody staining, the tissue sections were air-dried at room temperature for 20 min and fixed with acetone at  $-20\text{ }^{\circ}\text{C}$  for 10 min. Fixed samples were air-dried for 15 min at room temperature, immersed into PBS (pH 7.4) and transferred to Shandon Sequenza (Thermo Shandon Ltd, Runcorn, UK) immunostaining cassettes. Nonspecific antibody binding was blocked by preincubating the tissue sections in blocking buffer containing 1% BSA and 0.3% Triton-X100 diluted in PBS (pH 7.4). All antibodies were diluted into the blocking buffer. The following primary antibodies were used to detect adhesion proteins and vascular cell markers in adjacent sections: mouse-anti-human PECAM-1 antibody (CD31, clone JC70A, Dako Agilent Technologies, Glostrup, Denmark) diluted 1:20 was used as a marker of endothelial cells, rabbit-anti-human Tal1 (clone ab71333,

Abcam, Cambridge, UK) diluted 1:80 was used for talin-1, mouse-anti-human Tal2, (clone 68E7, Cancer Research Technology, London, UK) diluted 1:100 was used for talin-2 and rabbit anti human Vin (clone ab61186, Abcam, Cambridge, UK) diluted 1:50 was used vinculin. Samples were incubated with diluted primary antibodies at +4 °C overnight, followed by washing 3 times with PBS. AlexaFluor-568 labeled goat-anti-mouse IgG (Cat # A11004, Thermo Fisher Scientific) and AlexaFluor-488 labeled donkey-anti-rabbit IgG (Cat # A21206, Thermo Fisher Scientific) antibodies diluted 1:100 were incubated on the samples for 1 h at room temperature to detect the bound primary antibodies. Immunostained samples were washed 5 times with PBS, followed by one wash with deionized water. Glass coverslips were mounted on the samples by using Prolong Diamond (Cat # P36962, Thermo Fisher Scientific) containing DAPI for nuclear staining.

For immunofluorescence staining of formalin-fixed and paraffin-embedded (FFPE) samples, 4 µm sections were cut from paraffin-embedded samples of LITA and healthy carotid artery and abdominal aorta. Samples of LITA were collected from patients diagnosed with atherosclerosis, while the samples of carotid artery and abdominal aorta were collected from a cadaver with no coronary artery disease. Hematoxylin-eosin (HE) stained tissue sections were used to confirm normal tissue morphology of these samples. All tissue sections were deparaffinized and rehydrated by incubating them in xylene and in 99%, 95%, 70% and 50% ethanol solution for 10 min in each. For antigen retrieval, tissue sections were boiled in 10 mM sodium citrate buffer (pH 6) with 0.05% Tween-20 for 20 min in a microwave oven and allowed to slowly cool back to room temperature. Samples were washed 3 times with PBS (pH 7.4) and treated with 0.1% Sudan Black B for 20 min at room temperature to quench tissue autofluorescence. Samples were washed 3 times 10 min with PBS and immunostained using the same methods used for the frozen tissue sections. Antibody specificity was confirmed by using control samples with no primary antibodies.

The immunolabeled sections were examined under a laser scanning confocal microscope (Zeiss Cell Observer.Z1 equipped with a 63x/NA 1.4 oil immersion objective and Zeiss LSM780 confocal unit, Carl Zeiss Microscopy, Jena, Germany). For fluorescence excitation, 480 nm argon laser and 405 nm and 561 nm diode lasers were used together with suitable filter sets. For comparative analysis, the laser intensities, PMT gains and other settings were kept constant for all samples. Serial plane images were collected throughout the whole thickness of the sample at 200 nm intervals. During image processing, maximum intensity projections were used to extract high intensity areas from the image stacks into single images.

## 2.8. Statistical analyses

Statistical analyses were performed using R version 2.15.0. To estimate fold changes between groups in microarray analysis (MA), differences between medians (in log<sub>2</sub> scale) were calculated. The log ratios were back-transformed to fold changes. To ease the interpretation, fold-change values < 1 were replaced by the negative of its inverse. Statistical significance of differences in gene expression was assessed using the nonparametric Wilcoxon signed-rank test and the log-transformed data. For associations between *TLN1*, *TLN2*, *meta-VCL* and *VCL* expression levels and SMC-rich plaque/macrophage markers, the Spearman correlation coefficient was used. To test the effect of covariates on expression levels of *TLN1*, *TLN2*, *meta-VCL* and *VCL*, Wilcoxon rank-sum test and Spearman correlation were used. The associations between covariates and expression levels were tested in the atherosclerotic plaque and LITA samples separately and were considered

significant when  $p < 0.05/42$  to 0.001 according to the Bonferroni correction for multiple testing. Differences were considered significant when  $p < 0.05$ .

## 2.9. Limitations of the study

Due to the poor availability of control arterial samples from healthy persons with no coronary artery disease, LITA samples obtained during coronary artery bypass surgery were used as controls for the studied plaque samples. LITA samples were collected from patients diagnosed with coronary artery disease. Therefore, the levels of talin-1, talin-2 and vinculin transcript expression profiles in LITA may not exactly match their expression profile in artery samples from healthy subjects with no diagnosed CAD. Therefore, immunostaining of talin-1 was used to confirm similar expression pattern of talin-1 in the LITA samples from CAD patients and in artery samples from a healthy subject (Fig. 4). In addition, similar artery morphology for these samples was confirmed by observing tissue sections with HE-staining (Fig. 4). Another limitation of our study is the relatively small sample group size used. The small sample group size results from the poor availability of suitable patient samples and it was taken into consideration in the interpretation of the results.

## 3. Results

### 3.1. Characteristics of the subjects and studied samples

The demographics and risk factors of studied population are presented in Table 1. All internal arteries used as controls were verified microscopically as normal. Body mass index, occurrence of hypercholesterolemia, high blood pressure, coronary artery disease and history of myocardial infarction differed significantly between control group and group with atherosclerotic plaques. For mononuclear and whole blood analysis, patients with coronary artery disease considered as case group differed significantly in hypercholesterolemia occurrence, statin medication use and history of myocardial infarction from the control group. Because of these significant differences in the population, the gene expression was analyzed separately between these groups.

### 3.2. *Talin-1*, *talin-2* and *vinculin* transcripts are robustly expressed in left internal thoracic artery (LITA) controls with significant reduction in plaques

The gene expression profiles of talin-1, talin-2 and vinculin were investigated to understand the molecular mechanisms behind atherosclerosis. All three transcripts were robustly expressed in LITA samples (Supplementary Table 1A) and in all plaque samples of the three analyzed arterial beds (Supplementary Table 1B). Microarray analysis (MA) and low-density qRT-PCR (LDA) array showed that all tested talin and vinculin transcripts were downregulated in atherosclerotic plaques ( $fc < -1.6$ , for all plaques, with MA and LDA,  $p < 0.00001$  (Supplementary Table 2, Fig. 1A–D). In more detail, all transcripts were downregulated in plaques of carotid, abdominal aortic and femoral arterial beds in comparison to LITA (Supplementary Table 2, Fig. 1E–H). The downregulation of talin-1 and talin-2 was most substantial in femoral plaques in comparison to LITA, whilst meta-vinculin was most downregulated in carotid plaques and vinculin in abdominal aortic plaques in comparison to LITA.

**Table 1**  
Demographics and risk factors of the study patients included in the Tampere Vascular Study [10].

	Arterial	Plaque	Mononuclear/whole blood	
	Control	Case	CAD Control	CAD Case
No. of subjects	24	68	44	52
Age, y (median, SD)	69.0 (8.6)	70.0 (10.4)	57.0 (8.6)	56.5 (8.6)
Men (%)	82.1	67.6	63.0	61.5
Body mass index, kg/m <sup>2</sup> (median, SD)	28.2 (5.1)	26.0 (4.0)*	27.7 (4.2)	26.9 (4.3)
History of smoking, %	64.3	75.0	53.3	65.4
Diabetes mellitus, %	32.1	23.5	8.7	19.2
Hypercholesterolemia, %	85.7	67.6*	52.2	76.9*
Hypertension, %	100.0	82.4*	84.8	96.2
Antihypertensive medication, %	92.9	80.9	80.4	92.3
Statin medication, %	82.1	73.5	20.4	73.1*
Coronary artery disease, %	100.0	29.4**	0.0	100.0***
Myocardial infarction, %	40.7	13.2*	23.9	57.7***

Pearson Chi-square test and Wilcoxon signed-rank test was used for categorical and continuous risk factors, respectively.  $p < 0.05^*$ ,  $p < 0.01^{**}$ ,  $p < 0.001^{***}$ .

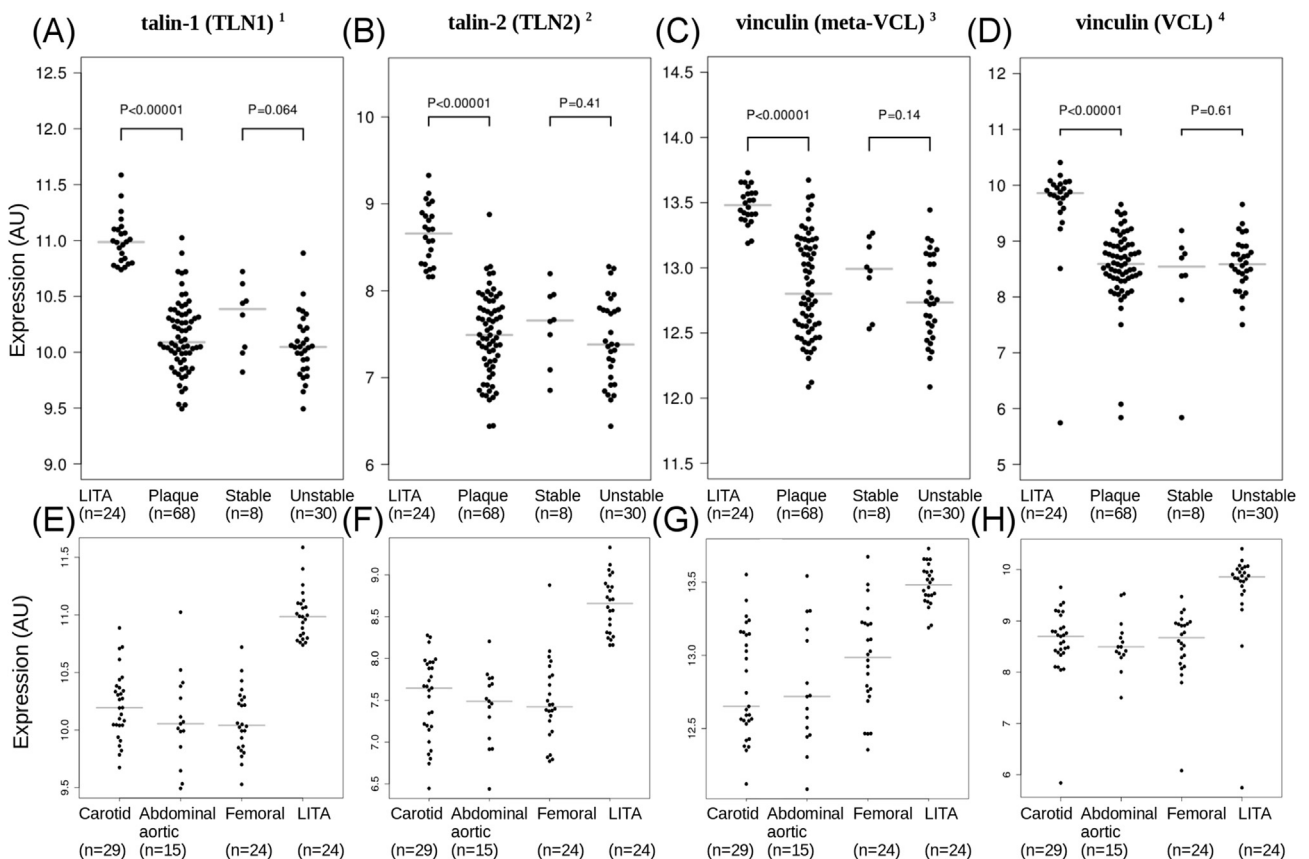
### 3.3. Expression of talin-1, talin-2 and vinculin transcripts is downregulated in both stable and unstable atherosclerotic plaques

We further characterized the expression profiles as a function of disease progression. According to microarray analysis, all tested transcripts were downregulated in all plaques in comparison with LITA controls (Supplementary Table 2, Fig. 1A–D). Even though no significant reduction was observed between the stable and unstable atherosclerotic plaque, a negative tendency in expression was seen for talin-1, talin-2 and meta-vinculin between the stable and

unstable plaques (Fig. 1A–D).

### 3.4. Talin-1 and vinculin transcripts are expressed in whole blood and circulating monocytes

In order to evaluate if the expression profiles could be monitored using blood samples, whole blood and circulating monocytes were analyzed. Talin-1, meta-vinculin and vinculin were robustly expressed in whole blood samples while talin-2 was not detected in whole blood (Supplementary Table 1A). No significant difference



<sup>1</sup> ILMN\_1696643, <sup>2</sup> ILMN\_1700042, <sup>3</sup> ILMN\_1795429, <sup>4</sup> ILMN\_2413527

**Fig. 1. Expression of talin (TLN) and vinculin (VCL) transcripts.** Results of microarray analysis (MA). (A–D) Expression levels in LITA controls and all, stable and unstable atherosclerotic plaques. (E–H) Expression levels in carotid, abdominal aortic and femoral arterial bed compared to LITA controls.

was observed between patients with history of coronary artery disease (CAD) and controls in the whole blood expression levels of talin-1, talin-2, meta-vinculin and vinculin in MA (fold change (fc) =  $-1.01$ – $1.03$ , for all,  $p > 0.3$ ) or in LDA analysis (fold change (fc) =  $-1.13$ – $1.05$ , for all,  $p > 0.3$ ). Moreover, no significant differences were observed in the whole blood samples of the patients with hypercholesterolemia, statin usage or patients with myocardial infarction. Expression in circulating monocytes was statistically insignificant between controls and CAD patients for talin-1, talin-2, meta-vinculin or vinculin transcripts. Nominally significantly reduced expression was however observed for patients with myocardial infarction events for talin-1 (fc =  $-1.13$ ,  $p = 0.026$ ) and for vinculin (fc =  $-1.12$ ,  $p = 0.03$ ) in circulating monocytes. However, no associations between gene expression and clinical risk factors remained statistically significant after correcting for multiple testing.

### 3.5. Hierarchical clustering analysis; association of talin-1, talin-2 and vinculin transcripts with SMC and inflammation markers

Hierarchical clustering based on the expression of the two inflammatory and two SMC markers showed distinct separation of plaque samples from the LITA controls. Expression of talin-1, talin-2 and vinculin was dependent on expression of SMC markers (*CNN1* and *SMTN*). Furthermore, high expression of *TLN1*, *TLN2*, *VCL* and SMC markers with low expression of inflammatory biomarkers *CD68* and *ALOX5* was observed in LITA controls (Fig. 2). Also plaque samples of all tested arterial beds separated into two distinct branches of the dendrogram. The samples exhibiting greater reduction in *TLN1*, *TLN2* and *VCL* expression contained mainly carotid arterial samples, whereas majority of femoral arterial beds showed smaller changes in the expression reduction.

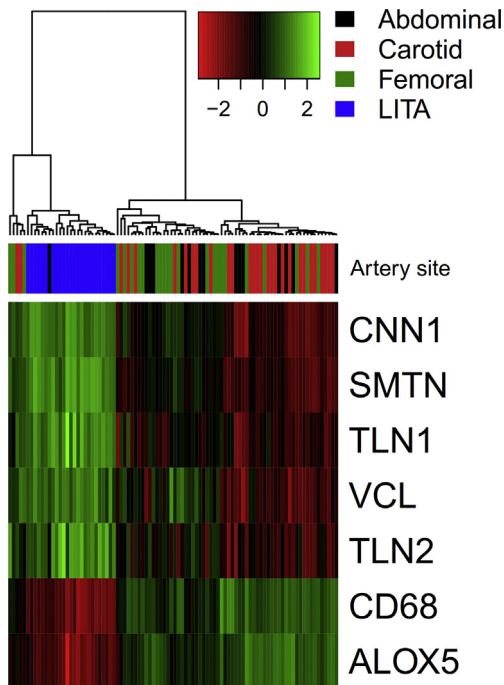


**Fig. 2.** Heat maps of  $\log_2$  expression values. Talin-1 (*TLN1*), talin-2 (*TLN2*) and vinculin (*VCL*) co-expression with biomarkers of inflammation (*CD68*, *ALOX5*) and smooth muscle cells markers (*CNN1*, *SMTN*). The expression values of each row (gene) are scaled to z-scores, color-code for expression values and arterial site is presented in the top-right corner. The dendrogram illustrates hierarchical clustering based on the seven robustly expressed genes. The top bar represents the arterial site origin of the sample tissue.

### 3.6. Talin-1, talin-2 and vinculin transcripts expression levels correlate with SMC-rich atherosclerotic plaque signature

To study the connection between gene expression and plaque composition, the expression profiles were correlated with the known markers of smooth muscle cells (SMC). Utilizing markers of M1 and M2 macrophages and SMC-rich plaque signature, we found that *talin-1*, *talin-2* and both *vinculin* transcripts correlate positively with SMC-rich plaque signature and in majority negatively with M1 and M2 macrophage signatures (Supplementary Fig. 1).

### 3.7. Talin-1, talin-2 and vinculin localization in the atherosclerotic plaque cells according to confocal immunofluorescence analysis

To get information about the protein localization within the blood vessel samples, immunofluorescence staining of frozen tissue sections from atherosclerotic plaque and LITA controls were used to study adhesion protein localization and expression in advanced disease. Talin-1 was found to be highly expressed in the vascular endothelial cells of LITA samples (Fig. 3A). On the contrary, talin-1 staining was not observed in the endothelial cells of an atherosclerotic artery. Furthermore, in the thickened tunica intima (I) underlying the endothelial cells, gradual increase in talin-1 expression was seen towards tunica media (M).

Antibody staining for talin-2 was observed to only partially colocalize with talin-1 staining in the tunica intima (I) and tunica media (M) in LITA samples (Fig. 3B). Interestingly, in tunica media of LITA controls, talin-2 expression was higher in the luminal side and gradually decreased towards tunica adventitia (A). In plaque samples, talin-2 expression in the endothelial cells was decreased, but not to the same extent as talin-1 expression. In LITA samples, vinculin was found to be expressed in both tunica intima (I) and tunica media (M), but not in tunica adventitia (A).

In tunica media, vinculin expression was higher close to the lumen and lower deeper inside the vessel wall (Fig. 3C). In plaque samples, decreased expression of vinculin in endothelial cells was observed, but in the lower parts of the thickened intima vinculin was still expressed. As expected, the expression of endothelial adhesion molecule PECAM-1 was found to be higher in the endothelium of atherosclerotic plaques compared to the control samples from healthy arteries [32] (Fig. 3A, C).

### 3.8. Samples from LITA and healthy carotid artery and abdominal aorta show similar tissue morphology and talin-1 expression patterns

To confirm similar tissue morphology and talin-1 expression patterns in healthy carotid artery and abdominal aorta and in the LITA samples used as a control in this study, tissue sections of formalin-fixed and paraffin-embedded (FFPE) samples were stained with talin-1 antibody and hematoxylin-eosin (HE) staining. Immunofluorescence staining of FFPE samples with talin-1 antibody showed strong specific staining of talin-1 in tunica intima (I) and tunica media (M) in samples from LITA and from healthy carotid artery and abdominal aorta (Fig. 4). Similarly to the sections from frozen LITA, the analyzed FFPE sections from LITA or healthy arteries showed uniform talin-1 staining intensity, suggesting that the talin-1 gradient observed in plaque samples is unique feature. In addition, HE staining of the FFPE samples showed similar tissue morphology for samples from LITA and carotid artery and abdominal aorta (Fig. 4). These experiments confirm the feasibility of using LITA samples from CAD patients as negative controls for samples from atherosclerotic plaques when studying expression patterns of focal adhesion proteins.

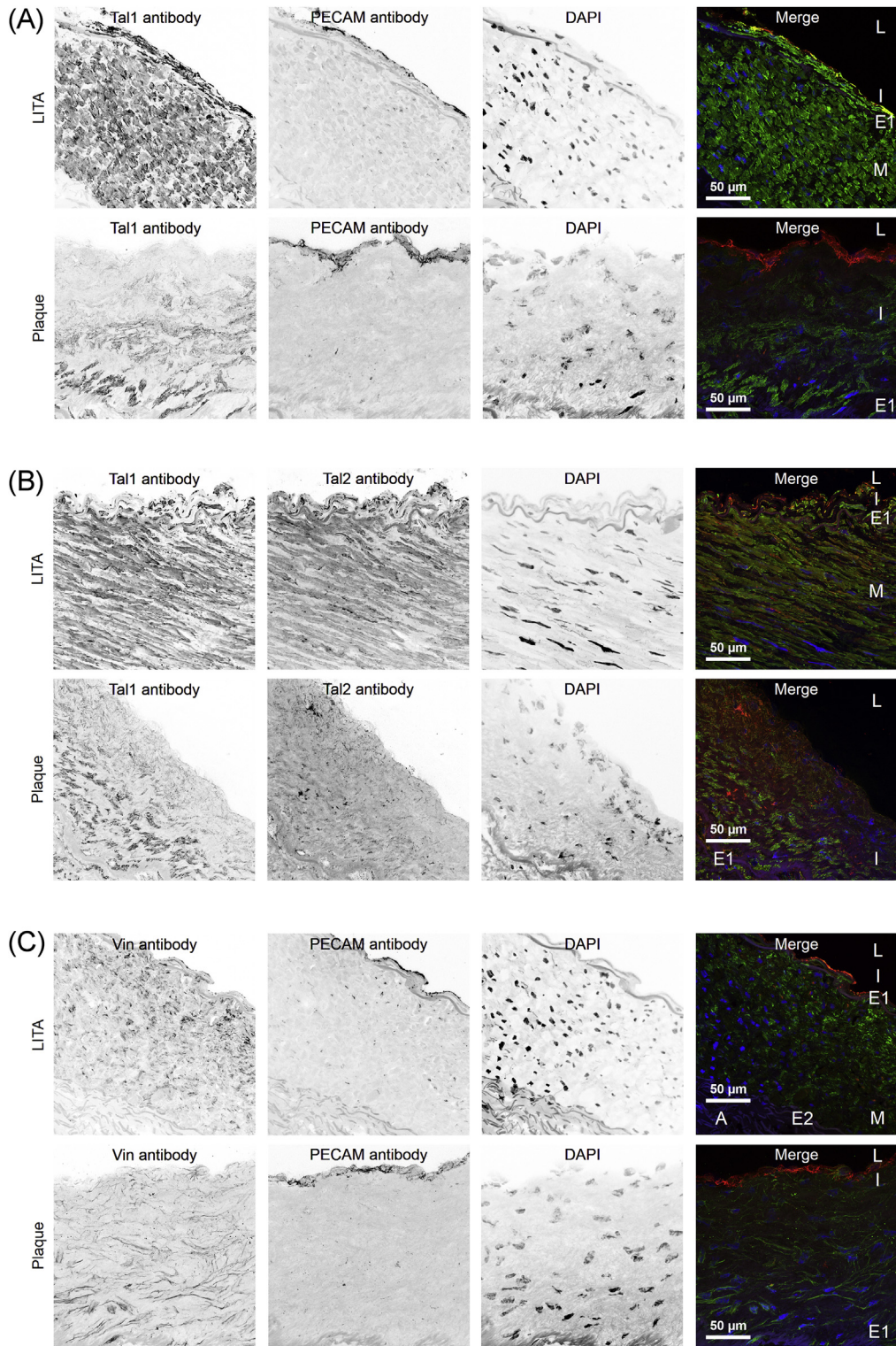


**Fig. 3. Tissue localization of talin-1, talin-2 and vinculin in atherosclerotic plaque from carotid artery and left internal thoracic (LITA) control.** (A) Talin-1 and PECAM-1, (B) talin-1 and talin-2, (C) vinculin and PECAM-1. Talin-1 was expressed in the endothelial cells of LITA, while talin-1 expression in plaque endothelial cells was not observed (A). Talin-2 expression was decreased in plaque endothelium as compared to LITA, but not as strongly as talin-1 expression (B). In LITA, high vinculin expression was observed in tunica intima and at the luminal side of tunica media. In plaque samples, decreased vinculin expression was observed in the thickened tunica intima (C). PECAM-1 expression was found to be increased in plaque endothelium (A, C). L, lumen; I, tunica intima; E1, internal elastic lamina; E2, external elastic lamina; M, tunica media; A, tunica adventitia.

#### 4. Discussion

In this study, we show for the first time that the gene expression of talin-1, talin-2, meta-vinculin and vinculin is significantly

reduced in atherosclerotic plaques. Significant downregulation of expression was observed in all of the studied carotid, abdominal aortic and femoral arterial beds compared to LITA controls. However, expression of neither gene was changed in circulating

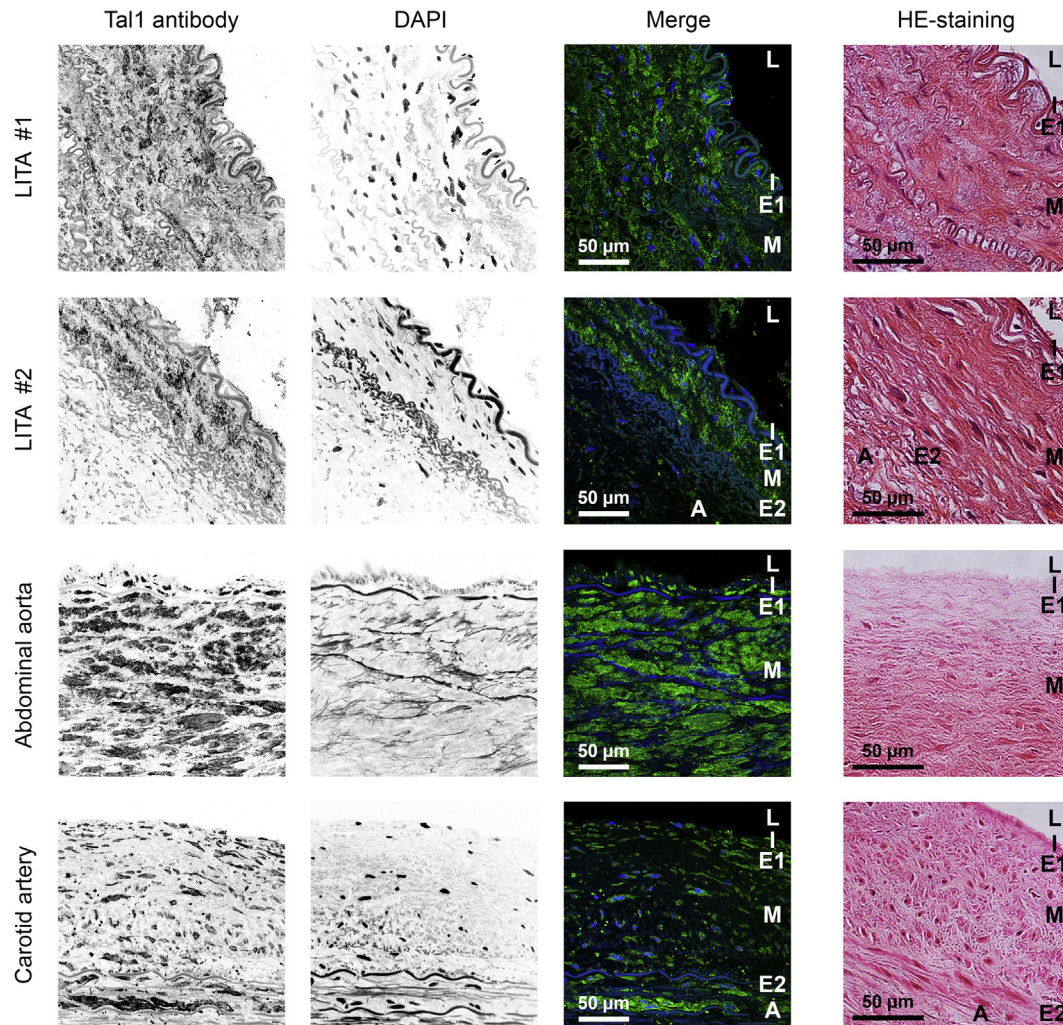


**Fig. 4.** Tissue morphology and localization of talin-1 in immunostained FFPE sections of LITA from patients with coronary artery disease and in sections of healthy abdominal aorta and carotid artery. Uniform talin-1 immunostaining was observed in tunica intima and tunica media in both immunostained LITA samples, as well as in the samples from healthy abdominal aorta and carotid artery. HE-staining showed normal tissue morphology for all of the analyzed samples. In the merged images, talin-1 immunostaining is shown as green and DAPI chromatin staining as blue. L, lumen; I, tunica intima; E1, internal elastic lamina; E2, external elastic lamina; M, tunica media; A, tunica adventitia. (For interpretation of the references to colour in this figure legend, the reader is referred to the web version of this article.)

monocytes or in whole blood samples in CAD patients compared to controls.

We speculate that reduction in talin-1 expression in the endothelium may be one of the initial triggers for the atherosclerotic plaque formation (Fig. 5). Such downregulation could be caused by an external factor such as altered shear stress and increased blood pressure. It has long been suspected that the mechanosensing and mechanotransduction affects the DNA packing and may contribute to changes in the protein expression in health and in disease [33,34]. Another reason may lie in the mutation affected control of gene expression levels leading to changes in the cell mechanobiology and susceptibility to plaque development. In addition, recently the importance of miRNAs in the regulation of gene expression in endothelial dysfunction has become evident, as discussed by Novák et al. [35]. Furthermore, one of the contributing factors of detected downregulation in this study may be the changed cell composition in the advanced atherosclerotic plaque which can be seen on the confocal images. Changes in acting mechanical force may also alter the signaling pathways related to focal adhesions and affect the expression levels. In connection to atherosclerosis, the magnitude of shear stress was shown to affect

the expression of adhesion molecules facilitating endothelial cell-leukocyte adhesion at the vascular lumen (vascular cell adhesion molecule (VCAM), intercellular cell adhesion molecule (ICAM) or platelet endothelial cell adhesion molecule (PECAM) [32,36]. Our previous studies have also shown that the focal adhesions are compromised by reduced expression of integrin family proteins and kindlin-2 in the endothelium and SMCs in the atherosclerotic plaque (*ITGA1*, *ITGAV*, *ITGB1*, *ITGB3*, *ITGB5*, *FERMT2*), while the leukocyte adhesion is accelerated by increased expression of leukocyte integrin-B2 and kindlin-3 [10]. The exact reasons for the observed reduction of the talin and vinculin expression level remain, however, unclear and require attention in future studies.

Altered expression of talin-1, talin-2, meta-vinculin and vinculin may have severe impact on the cell's ability to withstand varying magnitudes of acting mechanical forces, affect cell locomotion, cell/cell and cell-ECM communication since both; talin and vinculin are among the major constituents of the focal adhesion complexes and are essential for cellular well-being [37]. Talin acts as molecular scaffolding protein and may contribute to adhesion signaling via its binding partners, converting mechanical signals to chemical cues [38]. Therefore, a reduction in talin-1 expression could render the

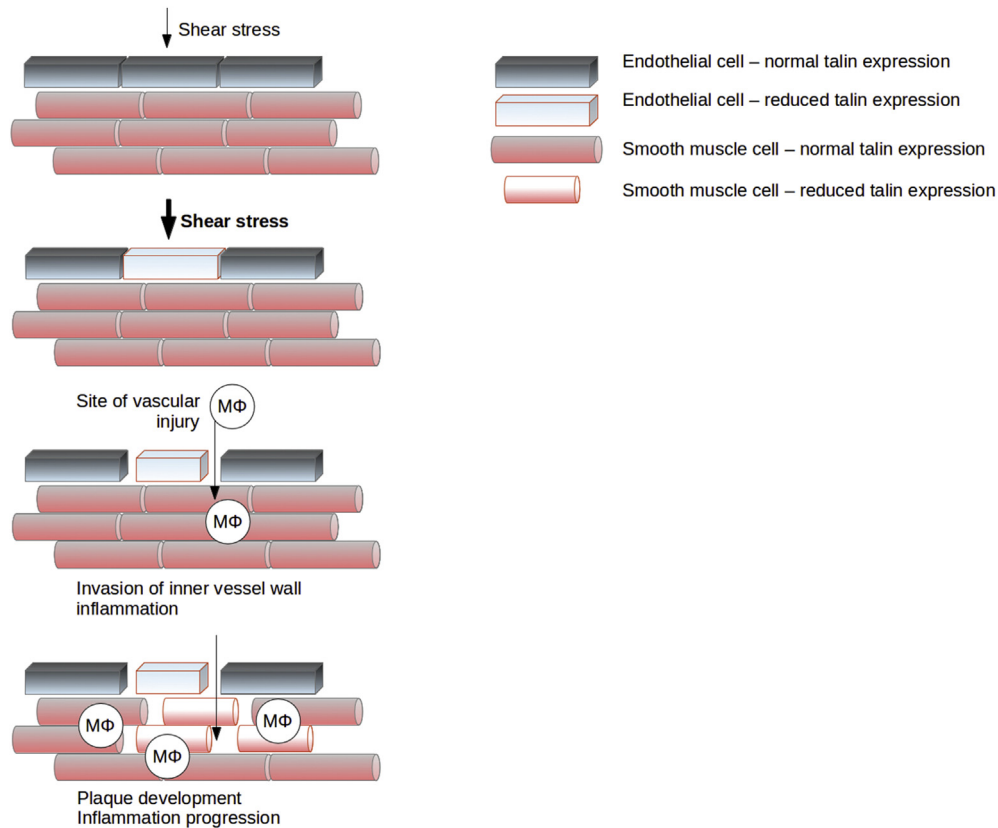


**Fig. 5.** Simplified speculative model for downregulation of talin expression in vascular endothelium as initial trigger of atherosclerotic plaque formation.

endothelium and the vascular wall prone to endothelial injury compared to mechanically stable endothelial cell [39]. Endothelial injury triggers leukocyte adhesion and promotes inflammatory response at the intima due to exposure of subendothelial collagen and other ECM components. Confocal microscopy images of atherosclerotic plaque show increased PECAM-1 staining in the intima, which points to increased leukocyte adhesion molecules and progression of inflammation at the intima.

In addition, endothelium functions as a barrier for large molecules to enter the vessel wall and trigger pathological processes in the inner vessel layers [40,41]. In other words, the mechanostability of endothelial cells including the endothelial intercellular gap and tight junction maintenance is crucial for healthy vessel wall. Experiments with talin knockout cells show dramatically decreased capability of cells to adhere, revealing the central role of talin in mediating the intracellular-extracellular connection. The reduction in talin-1, talin-2, meta-vinculin and vinculin expression in the endothelium may affect the ability of endothelial cells to adhere to each other and to ECM to form consistent blood-tissue barrier. This could allow the inflammatory agents to progress into the tunica media and trigger macrophage accumulation in the intima and media leading to arterial wall thickening and plaque formation. Such effect can be observed in the presented tissue images where plaque staining shows dramatically thickened intima layer with gross disorganization of the cells and low talin-1 and talin-2 intensity (reduced expression of talin-1 and talin-2 in plaque sample).

Studies by others have also shown the importance of talin-1 and talin-2 for cell, tissue and organ development [42,43]. Such importance of talin proteins on development was illustrated by talin-1 knockout experiments in HUVEC cells [44,45] leading to

severe phenotypes in mice embryos. The phenotype is represented by abnormal vascular development affecting the growth of other major tissues [45]. Furthermore, increased talin-1 expression has been detected in aggressive cancers as well as in hypertrophic myocardium and failing heart [46–48]. Even though the downregulation of neither talin-1 nor talin-2 has been to date directly linked to or associated with a disease, the reduced expression may affect the vessel tissue formation, remodeling or healing and recovery. The confocal images of the atherosclerotic plaque show gross disorganization of the cells in the vessel wall. Such additional effects may lead into worsening of the site inflammation and progress of the disease to severe, unstable atherosclerotic plaques. Even though the difference in expression between stable and unstable atherosclerotic plaque reported here was not significant for the investigated transcripts, negative tendency in expression levels was observed for talin-1, talin-2 and meta-vinculin. This suggests that the expression of these genes is further reduced in the advanced disease.

The expression of talin-1 and talin-2 may also differ among the cells depending on the position in the vessel wall layer. As can be seen in the talin-2 LITA staining, the intensity of talin-2 expression in smooth muscle is higher in the layers closer to the intima where the mechanical impacts are expected higher. Similar stratification has not been observed for talin-1 or vinculin in LITA controls. Whether such stratification in healthy tissue is biologically and physiologically important remains open for further investigation.

Talin-1, talin-2, meta-vinculin and vinculin expression is downregulated in atherosclerotic plaque. Downregulation of expression was observed in plaques from all of the studied peripheral arterial beds (carotid, abdominal aortic and femoral).

The central role of talin in cell adhesion proposes that the

disintegration of the tissue in atherosclerosis could be partially driven by downregulation of talin, leading to loosening of cell-ECM interactions and reorganization of the tissue.

In conclusion, we state that proteins contributing to mechanosensing, talin and vinculin, may have important roles in atherosclerotic plaque formation and disease progression.

### Conflict of interest

The authors declared they do not have anything to disclose regarding conflict of interest with respect to this manuscript.

### Financial support

This work was supported by the Academy of Finland: grants 290506, 273192, 136288 (V.P.H.), 286284 (T.L.), 285902 (E.R.), 134309; the Tampere University Hospital Medical Funds (grant X51001 (T.L.), 9S054 (E.R.) and X51410 (V.P.H.)); the Finnish Foundation for Cardiovascular Research (T.L.); the Finnish Cultural Foundation (R.R.); the Tampere Tuberculosis Foundation (T.L. and N.O.); the Emil Aaltonen Foundation (T.L. and N.O.); and the Yrjö Jahnsson Foundation (T.L. and N.O.). This work was also supported by the European Union 7th Framework Programme funding for the AtheroRemo project [201668] and Fimlab Laboratories. We thank the University of Tampere for financial support via the TGPBB graduate school (M.v.E.).

### Appendix A. Supplementary data

Supplementary data related to this article can be found at <http://dx.doi.org/10.1016/j.atherosclerosis.2016.10.031>.

### References

- [1] A.S. Antonov, F.D. Kolodgie, D.H. Munn, R.G. Gerrity, Regulation of macrophage foam cell formation by alphaVbeta3 integrin: potential role in human atherosclerosis, *Am. J. Pathol.* 165 (1) (2004) 247–258.
- [2] P.F. Davies, Flow-mediated endothelial mechanotransduction, *Physiol. Rev.* 75 (3) (1995) 519–560.
- [3] W.C. Aird, Endothelial cell heterogeneity, *Cold Spring Harb. Perspect. Med.* 2 (1) (2012) a006429.
- [4] W.C. Aird, Spatial and temporal dynamics of the endothelium, *J. Thromb. Haemost.* 3 (2005) 1392–1406.
- [5] J.P. Califano, C.A. Reinhart-King, Exogenous and endogenous force regulation of endothelial cell behavior, *J. Biomech.* 43 (1) (2010) 79–86.
- [6] J.F. Keane, Atherosclerosis: from lesion formation to plaque activation and endothelial dysfunction, *Mol. Asp. Med.* 21 (4–5) (2000) 99–166.
- [7] T.J. Chancellor, J. Lee, C.K. Thodeti, T. Lele, Actomyosin tension exerted on the nucleus through nesprin-1 connections influences endothelial cell adhesion, migration, and cyclic strain-induced reorientation, *Biophys. J.* 99 (1) (2010) 115–123.
- [8] Z. Jahed, H. Shams, M. Mehrbod, M.R.K. Mofrad, Mechanotransduction pathways linking the extracellular matrix to the nucleus, *Int. Rev. Cell Mol. Biol.* 310 (171) (2014) e220.
- [9] N. Oksala, M. Levula, N. Airla, M. Pelto-Huikko, R.M. Ortiz, O. Järvinen, J.-P. Salenius, B. Ozsait, E. Komurcu-Bayrak, N. Erginel-Unaltuna, A.-P.J. Huovila, L. Kytömäki, J.T. Soini, M. Kähönen, P.J. Karhunen, R. Laaksonen, T. Lehtimäki, ADAM-9, ADAM-15, and ADAM-17 are upregulated in macrophages in advanced human atherosclerotic plaques in aorta and carotid and femoral arteries—Tampere vascular study, *Ann. Med.* 41 (4) (2009) 279–290.
- [10] N. Oksala, J. Pärssinen, I. Seppälä, N. Klopp, T. Illig, R. Laaksonen, M. Levula, E. Raitoharju, I. Kholova, T. Sioris, M. Kähönen, T. Lehtimäki, V.P. Hytönen, Kindlin 3 (FERMT3) is associated with unstable atherosclerotic plaques, anti-inflammatory type II macrophages and upregulation of beta-2 integrins in all major arterial beds, *Atherosclerosis* 242 (1) (2015) 145–154.
- [11] J. Winkler, H. Lünsdorf, B.M. Jockusch, Energy-filtered electron microscopy reveals that talin is a highly flexible protein composed of a series of globular domains, *Eur. J. Biochem.* 243 (1997) 430–436.
- [12] A.R. Gingras, W.H. Ziegler, A.A. Bobkov, M.G. Joyce, D. Fasci, M. Himmel, S. Rothmund, A. Ritter, J.G. Grossmann, B. Patel, N. Bate, B.T. Goult, J. Emsley, I.L. Barsukov, G.C.K. Roberts, R.C. Liddington, M.H. Ginsberg, D.R. Critchley, Structural determinants of integrin binding to the talin rod, *J. Biol. Chem.* 284 (13) (2009) 8866–8876.
- [13] A.R. Gingras, N. Bate, B.T. Goult, L. Hazelwood, I. Canestrelli, J. Gü Nter Grossmann, H. Liu, N. Sm Putz, G.C. Roberts, N. Volkmann, D. Hanein, I.L. Barsukov, D.R. Critchley, The structure of the C-terminal actin-binding domain of talin, *EMBO J.* 27 (2008) 458–469.
- [14] B.T. Goult, A.R. Gingras, N. Bate, I.L. Barsukov, D.R. Critchley, G.C.K. Roberts, The domain structure of talin: residues 1815–1973 form a five-helix bundle containing a cryptic vinculin-binding site, *FEBS Lett.* 584 (2010) 2237–2241.
- [15] E. Papagrigoriou, A.R. Gingras, I.L. Barsukov, N. Bate, I.J. Fillingham, B. Patel, R. Frank, W.H. Ziegler, G.C. Roberts, D.R. Critchley, J. Emsley, Activation of a vinculin-binding site in the talin rod involves rearrangement of a five-helix bundle, *EMBO J.* 23 (2004) 2942–2951.
- [16] V.P. Hytönen, V. Vogel, How force might activate talin's vinculin binding sites: SMD reveals a structural mechanism, *PLoS Comput. Biol.* 4 (2) (2008) e24.
- [17] A. del Rio, R. Perez-Jimenez, R. Liu, P. Roca-Cusachs, J.M. Fernandez, M.P. Sheetz, Stretching single talin rod molecules activates vinculin binding, *Science* 323 (5914) (2009) 638–641.
- [18] B.T. Goult, T. Zacharchenko, N. Bate, R. Tsang, F. Hey, A.R. Gingras, P.R. Elliott, G.C.K. Roberts, C. Ballestrem, D.R. Critchley, I.L. Barsukov, RIAM and vinculin binding to talin are mutually exclusive and regulate adhesion assembly and turnover, *J. Biol. Chem.* 288 (12) (2013) 8238–8249.
- [19] G. Di Paolo, L. Pellegrini, K. Letinic, G. Cestra, R. Zoncu, S. Voronov, S. Chang, J. Guo, M.R. Wenk, P. De Camilli, Recruitment and regulation of phosphatidylinositol phosphate kinase type 1 gamma by the FERM domain of talin, *Nature* 420 (6911) (2002) 85–89.
- [20] G. Luo, A.H. Herrera, R. Horowitz, Molecular interactions of N-RAP, a nebulin-related protein of striated muscle myotendon junctions and intercalated disks, *Biochemistry* 38 (19) (1999) 6135–6143.
- [21] N. Sun, D.R. Critchley, D. Paulin, Z. Li, R.M. Robson, Identification of a repeated domain within mammalian alpha-synemin that interacts directly with talin, *Exp. Cell Res.* 314 (8) (2008) 1839–1849.
- [22] R.A. Borgon, C. Vonnrhein, G. Bricogne, P.R.J. Bois, T. Izard, Crystal structure of human vinculin, *Structure* 12 (7) (2004) 1189–1197.
- [23] S. Hüttelmaier, P. Bubeck, M. Rüdiger, B.M. Jockusch, Characterization of two F-actin-binding and oligomerization sites in the cell-contact protein vinculin, *Eur. J. Biochem.* 247 (1997) 1136–1142.
- [24] C.K. Wood, C.E. Turner, P. Jackson, D.R. Critchley, Characterisation of the paxillin-binding site and the C-terminal focal adhesion targeting sequence in vinculin, *J. Cell Sci.* 107 (1994) 709–717.
- [25] M. Kroemker, A.H. Rüdiger, B.M. Jockusch, M. Rüdiger, Intramolecular interactions in vinculin control alpha-actinin binding to the vinculin head, *FEBS Lett.* 355 (1994) 259–262.
- [26] N. Oksala, J. Pärssinen, I. Seppälä, E. Raitoharju, I. Kholová, J. Hernesniemi, L.P. Lyytikäinen, M. Levula, K.M. Mäkelä, T. Sioris, M. Kähönen, R. Laaksonen, V. Hytönen, T. Lehtimäki, Association of neuroimmune guidance cue netrin-1 and its chemorepulsive receptor UNC5B with atherosclerotic plaque expression signatures and stability in human(s) Tampere Vascular Study (TVS), *Circ. Cardiovasc. Genet.* 6 (2013) 579–587.
- [27] H.C. Stary, A.B. Chandler, S. Glagov, J.R. Guyton, W. Insull, M.E. Rosenfeld, S.A. Schaffer, C.J. Schwartz, W.D. Wagner, R.W. Wissler, A definition of initial, fatty streak, and intermediate lesions of atherosclerosis. A report from the Committee on Vascular Lesions of the Council on Arteriosclerosis, American Heart Association, *Circulation* 89 (5) (1994) 2462–2478.
- [28] T. Nieminen, R. Lehtinen, J. Viik, T. Lehtimäki, K. Niemelä, K. Nikus, M. Niemi, J. Kallio, T. Kööbi, V. Turjanmaa, M. Kähönen, The Finnish Cardiovascular Study (FINCAVAS): characterising patients with high risk of cardiovascular morbidity and mortality, *BMC Cardiovasc. Disord.* 6 (1) (2006) 9.
- [29] H. Turpeinen, I. Seppälä, L.-P. Lyytikäinen, E. Raitoharju, N. Huutri-Kähönen, M. Levula, N. Oksala, M. Waldenberger, N. Klopp, T. Illig, N. Mononen, R. Laaksonen, O. Raitakari, M. Kähönen, T. Lehtimäki, M. Pesu, A genome-wide expression quantitative trait loci analysis of proprotein convertase subtilisin/kexin enzymes identifies a novel regulatory gene variant for FURIN expression and blood pressure, *Hum. Genet.* 134 (6) (2015) 627–636.
- [30] E. Raitoharju, I. Seppälä, L.P. Lyytikäinen, M. Levula, N. Oksala, N. Klopp, T. Illig, R. Laaksonen, M. Kähönen, T. Lehtimäki, A comparison of the accuracy of Illumina HumanHT-12 v3 Expression BeadChip and TaqMan qRT-PCR gene expression results in patient samples from the Tampere Vascular Study, *Atherosclerosis* 226 (1) (2013) 149–152.
- [31] O. Puig, J. Yuan, S. Stepanians, R. Zieba, E. Zycband, M. Morris, S. Coulter, X. Yu, J. Menke, J. Woods, F. Chen, D.R. Ramey, X. He, E.A. O'Neill, E. Hailman, D.G. Johns, B.K. Hubbard, P.Y. Lum, S.D. Wright, M.M. DeSouza, A. Plump, V. Reiser, A gene expression signature that classifies human atherosclerotic plaque by relative inflammation status, *Circ. Cardiovasc. Genet.* 4 (6) (2011) 595–604.
- [32] E. Galkina, K. Ley, Vascular adhesion molecules in atherosclerosis, *Arterioscler. Thromb. Vasc. Biol.* 27 (2007) 2292–2301.
- [33] E.K. Yim, M.P. Sheetz, Force-dependent cell signaling in stem cell differentiation, *Stem Cell Res. Ther.* 3 (5) (2012) 1.
- [34] M. Zwerger, C.Y. Ho, J. Lammerding, Nuclear mechanics in disease, *Annu. Rev. Biomed. Eng.* 13 (2011) 397–428.
- [35] J. Novák, V. Olejníčková, N. Tkáčová, G. Santulli, Mechanistic role of microRNAs in coupling lipid metabolism and atherosclerosis, *Adv. Exp. Med. Biol.* 887 (2015) 79–100.
- [36] T. Nagel, N. Resnick, W.J. Atkinson, C.F. Dewey, M.A. Gimbrone, Shear stress selectively upregulates intercellular adhesion molecule-1 expression in cultured human vascular endothelial cells, *J. Clin. Invest.* 94 (2) (1994) 885–891.

- [37] K. Austen, P. Ringer, A. Mehlich, A. Chrostek-Grashoff, C. Kluger, C. Klingner, B. Sabass, R. Zent, M. Rief, C. Grashoff, Extracellular rigidity sensing by talin isoform-specific mechanical linkages, *Nat. Cell Biol.* 17 (12) (2015) 1597–1606.
- [38] V.P. Hytönen, B. Wehrle-Haller, Protein conformation as a regulator of cell-matrix adhesion, *Phys. Chem. Chem. Phys.* 16 (14) (2014) 6342–6357.
- [39] P.F. Davies, Hemodynamic shear stress and the endothelium in cardiovascular pathophysiology, *Nat. Clin. Pract. Cardiovasc. Med.* 6 (1) (2009) 16–26.
- [40] G. Satha, S.B. Lindström, A. Klarbring, G. Satha, S.B. Lindström, A. Klarbring, A. Klarbring, A goal function approach to remodeling of arteries uncovers mechanisms for growth instability, *Biomech. Model Mechanobiol.* 13 (2014) 1243–1259.
- [41] J.M. Tarbell, Shear stress and the endothelial transport barrier, *Cardiovasc. Res.* 87 (2) (2010) 320–330.
- [42] S.J. Monkley, X.H. Zhou, S.J. Kinston, S.M. Giblett, L. Hemmings, H. Priddle, J.E. Brown, C.A. Pritchard, D.R. Critchley, R. Fassler, Disruption of the talin gene arrests mouse development at the gastrulation stage, *Dev. Dyn.* 219 (4) (2000) 560–574.
- [43] F.J. Conti, S.J. Monkley, M.R. Wood, D.R. Critchley, U. Müller, Talin 1 and 2 are required for myoblast fusion, sarcomere assembly and the maintenance of myotendinous junctions, *Development* 136 (21) (2009) 3597–3606.
- [44] P.M. Kopp, N. Bate, T.M. Hansen, N.P.J. Brindle, U. Praekelt, E. Debrand, S. Coleman, D. Mazzeo, B.T. Goult, A.R. Gingras, C.A. Pritchard, D.R. Critchley, S.J. Monkley, Studies on the morphology and spreading of human endothelial cells define key inter- and intramolecular interactions for talin1, *Eur. J. Cell Biol.* 89 (9) (2010) 661–673.
- [45] S.J. Monkley, V. Kostourou, L. Spence, B. Petrich, S. Coleman, M.H. Ginsberg, C.A. Pritchard, D.R. Critchley, Endothelial cell talin1 is essential for embryonic angiogenesis, *Dev. Biol.* 349 (2) (2011) 494–502.
- [46] S. Sakamoto, R.O. McCann, R. Dhir, N. Kyprianou, Talin1 promotes tumor invasion and metastasis via focal adhesion signaling and anoikis resistance, *Cancer Res.* 70 (5) (2010) 1885–1895.
- [47] K. Fang, W. Dai, Y.-H. Ren, Y.-C. Xu, S. Zhang, Y.-B. Qian, Both Talin-1 and Talin-2 correlate with malignancy potential of the human hepatocellular carcinoma MHCC-97 L cell, *BMC Cancer* 16 (1) (2016) 45.
- [48] A.M. Manso, R. Li, S.J. Monkley, N.M. Cruz, S. Ong, D.H. Lao, Y.E. Koshman, Y. Gu, K.L. Peterson, J. Chen, E.D. Abel, A.M. Samarel, D.R. Critchley, R.S. Ross, Talin1 has unique expression versus talin 2 in the heart and modifies the hypertrophic response to pressure overload, *J. Biol. Chem.* 288 (6) (2013) 4252–4264.

Supplementary data

**Talin and Vinculin are Downregulated in Atherosclerotic Plaque; Tampere Vascular Study**

Magdaléna von Essen, Rolle Rahikainen, Niku Oksala, Emma Raitoharju, Ilkka Seppälä, Ari Mennander, Thanos Sioris, Ivana Kholova, Norman Klopp, Thomas Illig, Pekka Karhunen, Mika Kähönen, Terho Lehtimäki, Vesa P. Hytönen

Supplementary Table S1

*Table S1 Talin (TLN) and vinculin (VCL) transcripts and their expression (expr.) in a) whole blood, left internal thoracic artery (LITA) control and arterial plaques, and b) in carotid, abdominal aortic and femoral arterial beds. Detection level  $p < 0.05$ .*

a)	Symbol	Whole Blood (n = 96)			LITA (n = 24)			Plaque (n = 68)		
		n( $p < 0.05$ )	%	expr.	n( $p < 0.05$ )	%	expr.	n( $p < 0.05$ )	%	expr.
	TLN1 <sup>a</sup>	96	100.0	1	24	100.0	1	68	100.0	1
	TLN2 <sup>b</sup>	4	4.2	0	24	100.0	1	68	100.0	1
	meta-VCL <sup>c</sup>	96	100.0	1	24	100.0	1	68	100.0	1
	VCL <sup>d</sup>	96	100.0	1	24	100.0	1	67	98.5	1

b)	Symbol	Carotid vs. LITA (n = 29)			Abdominal aortic vs. LITA (n = 15)			Femoral vs. LITA (n = 24)		
		n( $p < 0.05$ )	%	expr.	n( $p < 0.05$ )	%	expr.	n( $p < 0.05$ )	%	expr.
	TLN1 <sup>a</sup>	29	100.0	1	15	100.0	1	24	100.0	1
	TLN2 <sup>b</sup>	29	100.0	1	15	100.0	1	24	100.0	1
	meta-VCL <sup>c</sup>	29	100.0	1	15	100.0	1	24	100.0	1
	VCL <sup>d</sup>	28	96.6	1	15	100.0	1	24	100.0	1

Expression (expr.): 1 = detection  $p < 0.05$  for minimum of 50% of samples in the data set, 0 = otherwise; n( $p < 0.05$ ): number of samples in which a probe is robustly expressed with a detection  $p < 0.05$ ; %: percentage of samples in which a probe is robustly expressed with a detection  $p < 0.05$ .

Accession, Probe-ID

<sup>a</sup> NM\_006289.2, ILMN\_1696643

<sup>b</sup> NM\_015059.1, ILMN\_1700042

<sup>c</sup> NM\_014000.2, ILMN\_1795429

<sup>d</sup> NM\_003373.3, ILMN\_2413527

## Supplementary Table S2

Table S2 Talin (TLN) and vinculin (VCL) expression in arterial plaques expressed as a fold change (fc) from expression in left internal thoracic artery (LITA) control. (a) Gene expression analyzed by microarray analysis (MA), (b) Gene expression analyzed by qRT-PCR - LDA gene assay.

	Carotid vs LITA (n = 29)			Abdominal aortic vs LITA (n = 15)			Femoral vs LITA (n = 24)			Plaque vs LITA (n = 68)		
	fc	p		fc	p		fc	p		fc	p	
<b>a) MA</b>												
TLN1 <sup>a</sup>	<b>-1.731</b>	2.49E-13	***	<b>-1.907</b>	5.44E-08	***	<b>-1.925</b>	6.20E-14	***	<b>-1.861</b>	1.95E-12	***
TLN2 <sup>b</sup>	<b>-2.017</b>	5.00E-13	***	<b>-2.250</b>	3.18E-10	***	<b>-2.356</b>	9.90E-11	***	<b>-2.246</b>	3.05E-12	***
meta-VCL <sup>c</sup>	<b>-1.777</b>	4.73E-11	***	<b>-1.696</b>	1.65E-07	***	<b>-1.409</b>	1.96E-07	***	<b>-1.602</b>	2.37E-10	***
VCL <sup>d</sup>	<b>-2.235</b>	5.23E-09	***	<b>-2.575</b>	8.99E-07	***	<b>-2.274</b>	1.88E-08	***	<b>-2.408</b>	6.60E-10	***
<b>b) LDA</b>												
TLN1 <sup>1</sup>	<b>-2.984</b>	7.13E-08	***	<b>-2.973</b>	2.90E-05	***	<b>-3.439</b>	1.28E-07	***	<b>-3.150</b>	9.75E-10	***
TLN2 <sup>2</sup>	<b>-3.606</b>	1.32E-07	***	<b>-3.093</b>	1.00E-05	***	<b>-3.837</b>	5.92E-07	***	<b>-3.533</b>	1.79E-09	***
VCL <sup>3</sup>	<b>-3.371</b>	6.29E-08	***	<b>-3.682</b>	3.00E-06	***	<b>-3.170</b>	2.26E-07	***	<b>-3.316</b>	4.59E-10	***

Wilcoxon signed-rank test.  $p < 0.05$  \*,  $p < 0.01$  \*\*,  $p < 0.001$  \*\*\*

MA - microarray accession code and probe-ID:

<sup>a</sup> NM\_006289.2, ILMN\_1696643

<sup>b</sup> NM\_015059.1, ILMN\_1700042

<sup>c</sup> NM\_014000.2, ILMN\_1795429

<sup>d</sup> NM\_003373.3, ILMN\_2413527

qRT-PCR - LDA gene assay:

<sup>1</sup> TLN1-Hs00196775\_m1

<sup>2</sup> TLN2-Hs00322257\_m1

<sup>3</sup> VCL-Hs00419715\_m1

Supplementary Figure S1

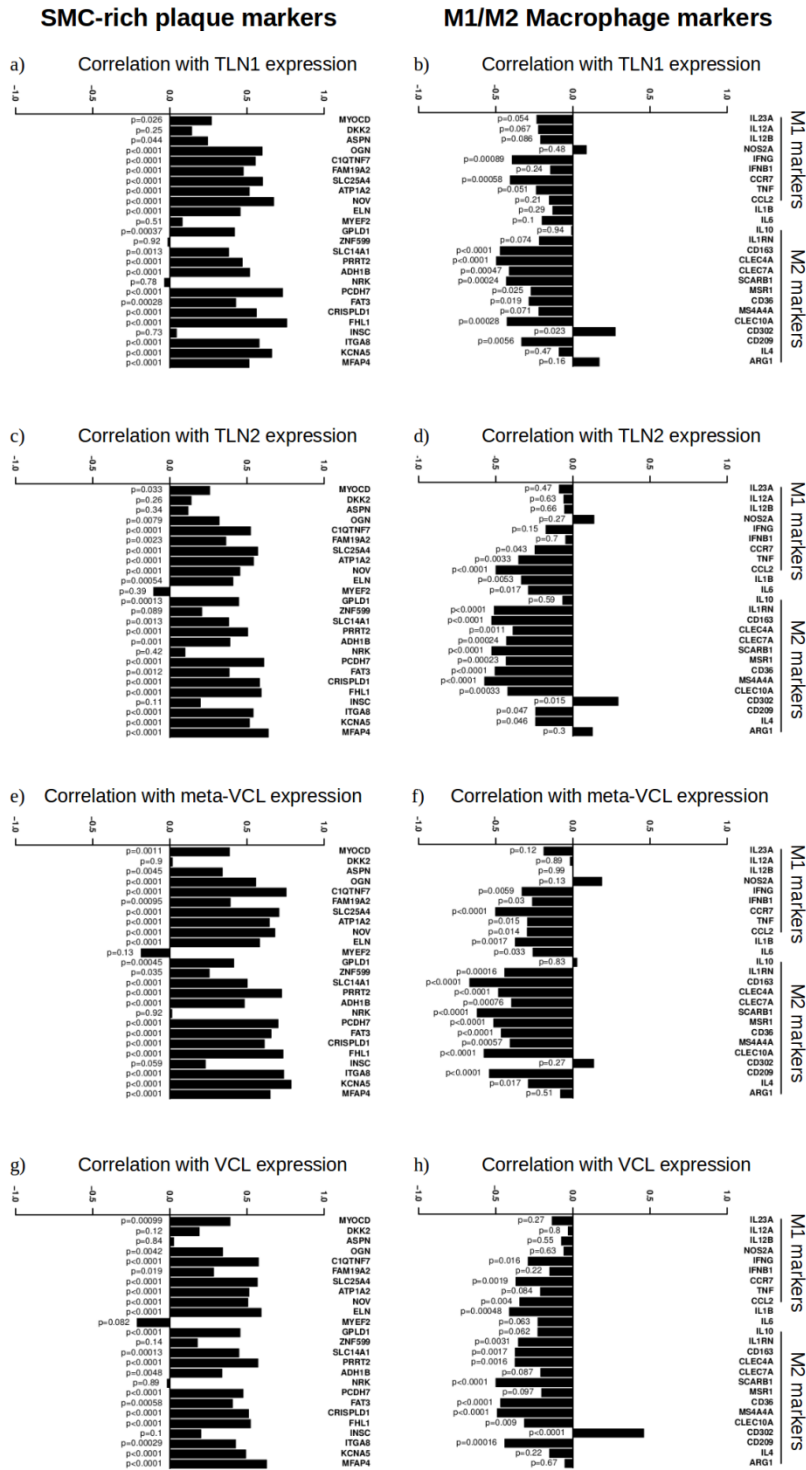
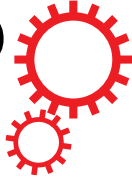


Figure S1 Correlation of talin1 (TLN1), talin-2 (TLN2), meta-vinculin (meta-VCL) and vinculin (VCL) mRNA expression. Results of Microarray Analysis (MA). (a,c,e,g) transcript mRNA levels and top 25 genes differentially expressed between regions of human atherosclerotic plaques enriched in smooth muscle-rich plaque signatures. (b,d,f,h) transcript mRNA levels and established M1/M2 macrophage markers in human atherosclerotic plaque.

# SCIENTIFIC REPORTS



OPEN

## Mechanical stability of talin rod controls cell migration and substrate sensing

Rolle Rahikainen<sup>1</sup>, Magdaléna von Essen<sup>1</sup>, Markus Schaefer<sup>2</sup>, Lei Qi<sup>3</sup>, Latifeh Azizi<sup>1</sup>, Conor Kelly<sup>1</sup>, Teemu O. Ihalainen<sup>1</sup>, Bernhard Wehrle-Haller<sup>4</sup>, Martin Bastmeyer<sup>2</sup>, Cai Huang<sup>3</sup> & Vesa P. Hytönen<sup>1</sup>

Cells adhere to the surrounding tissue and probe its mechanical properties by forming cell-matrix adhesions. Talin is a critical adhesion protein and participates in the transmission of mechanical signals between extracellular matrix and cell cytoskeleton. Force induced unfolding of talin rod subdomains has been proposed to act as a cellular mechanosensor, but so far evidence linking their mechanical stability and cellular response has been lacking. Here, by utilizing computationally designed mutations, we demonstrate that stepwise destabilization of the talin rod R3 subdomain decreases cellular traction force generation, which affects talin and vinculin dynamics in cell-matrix adhesions and results in the formation of talin-rich but unstable adhesions. We observed a connection between talin stability and the rate of cell migration and also found that talin destabilization affects the usage of different integrin subtypes and sensing of extracellular matrix proteins. Experiments with truncated forms of talin confirm the mechanosensory role of the talin R3 subdomain and exclude the possibility that the observed effects are caused by the release of talin head-rod autoinhibition. In conclusion, this study provides evidence into how the controlled talin rod domain unfolding acts as a key regulator of adhesion structure and function and consequently controls central cellular processes such as cell migration and substrate sensing.

Cell-matrix adhesions are large and dynamic membrane spanning protein complexes that physically anchor animal cells to their environment. These complexes connect integrin adhesion receptors to actin fibers providing a mechanical link between the cytoskeleton and the extracellular matrix. In addition to mechanical force, cell-matrix adhesions transmit biochemical signals across the plasma membrane and they have an important role in the regulation of cell anchorage, spreading and migration. The central role of cell-matrix adhesions in force transmission also makes them hotspots for cellular mechanotransduction. Mechanotransduction describes the cellular processes that translate mechanical tension or forces into a chemical or electrical signal. These processes allow cells to probe the mechanical properties of the surrounding tissue and to react to forces exerted on them<sup>1</sup>. Mechanotransduction regulates many processes on the levels of individual cells and complete tissues and it is involved in the development and progression of various diseases<sup>2</sup>. Despite the intense research focusing on the mechanotransduction of cell-matrix adhesions, the primary mechanosensory proteins in these adhesions remain largely unknown.

Talin is a 270 kDa adhesion protein containing a globular N-terminal head domain and a C-terminal rod domain composed of a series of alpha-helical bundles. The head domain (47 kDa) contains binding sites for multiple adhesion proteins and its binding to the  $\beta$ -integrin tail is one of the first steps in the formation of nascent cell-matrix adhesions. The head domain is linked to the rod domain by an unstructured linker region (9 kDa) which, when fully extended, increases the length of the protein by 20 nm and contains a protease cleavage site involved in adhesion turnover<sup>3,4</sup>. Talin rod domain (~210 kDa) consists solely of alpha-helices, assembled into

<sup>1</sup>Faculty of Medicine and Life Sciences and BioMediTech, University of Tampere, Finland and Fimlab Laboratories, Tampere, Finland. <sup>2</sup>Zoological Institute, Cell- and Neurobiology, Karlsruhe Institute of Technology (KIT), Institute of Functional Interfaces (IFG), Karlsruhe, Germany. <sup>3</sup>Markey Cancer Center and Department of Molecular and Biomedical Pharmacology, University of Kentucky, Lexington, KY, USA. <sup>4</sup>Department of Cell Physiology and Metabolism, University of Geneva, Geneva, Switzerland. Rolle Rahikainen and Magdaléna von Essen contributed equally to this work. Correspondence and requests for materials should be addressed to V.P.H. (email: [vesa.hytonen@uta.fi](mailto:vesa.hytonen@uta.fi))

13 subdomains. Each subdomain contains 4 to 5 amphipathic helices folded into a compact helix bundle with a hydrophobic core. Talin rod subdomains have binding sites for other adhesion proteins, including vinculin, Rap1-GTP-interacting adapter molecule (RIAM), Deleted in liver cancer 1 (DLC1),  $\beta$ -integrins and actin, as reviewed by Calderwood *et al.*<sup>5</sup>. The most numerous binding sites are for vinculin, with a total of 11 binding sites located in 9 of the 13 rod subdomains. Many of these vinculin binding sites (VBS) are cryptic, which means that vinculin can only bind to them after the subdomain has partially unfolded. This unfolding event is thought to be initiated by mechanical force transmitted across the rod domain<sup>6,7</sup>. Different talin rod subdomains have been shown to unfold at different forces, ranging from 5–10 pN to 25–40 pN in *in vitro* experiments<sup>8–10</sup>. The gradual force-induced exposure of the talin VBSs creates a system where higher force causes more rod subdomains to unfold, exposing more VBSs. Vinculin accumulation is known to not only mechanically strengthen the adhesion, but also to initiate downstream signaling cascades. In addition, such multi-step unfolding of the talin rod domain has been suggested to create a force buffer that can smooth out sudden fluctuations in the cellular traction forces<sup>9</sup>.

Talin is among the first proteins involved in integrin-mediated adhesion formation<sup>11</sup>. Therefore, mechanotransduction by the force-induced unfolding of talin rod subdomains may have an important role in promoting either maturation or disassembly of nascent adhesions<sup>11,12</sup>. The R3 subdomain of talin has been found to be the first subdomain to open under mechanical load, unfolding in *in vitro* experiments already at a 5 pN pulling force<sup>8–10</sup>. This low mechanical stability of the R3 subdomain makes it especially suitable for acting as a mechanosensor during adhesion maturation, where low magnitude forces are transmitted through the talin rod domain. If the force-induced unfolding of the talin R3 subdomain is a key step in adhesion maturation, mechanically stabilizing or destabilizing mutations should affect cellular mechanosensing and mechanosignaling. In a previous study, mechanically stabilized talin R3 subdomain was found to affect fibroblast substrate rigidity sensing and YAP signaling, highlighting the importance of talin R3 subdomain in mechanosensing<sup>13,14</sup>. However, this experiment does not give any indication about whether also destabilization of talin R3 subdomain would result in altered mechanosignaling and changes in cell phenotype.

In this study, we present a series of talin point mutations that destabilize the talin rod R3 subdomain. Steered molecular dynamics simulations were used to confirm that these mutations decreased the mechanical stability of the R3 subdomain. Expression of these talin mutants in fibroblast cells enabled us to study the importance of this rod subdomain for talin recruitment into cell-matrix adhesions. Importantly, we show that even a single destabilizing mutation affected adhesion protein composition and adhesion dynamics. On a cellular level, talin destabilization decreased both the cell migration rate and traction force generation and affected integrin subtype usage and ECM sensing. This study demonstrates that a controlled decrease in the stability of talin rod domain affects several cellular functions and sheds light into the importance of talin stability as a key regulator of adhesion mechanosignaling.

## Results

**Stepwise mutagenesis destabilizes the talin R3 subdomain in steered molecular dynamics simulations and affects subdomain folding *in vitro*.** Talin-1 subdomain R3 is a four helix bundle located within the compact N-terminal end of the talin rod domain. It contains 2 vinculin binding sites in the helices 2 and 3 (Fig. 1b,c). Due to the presence of hydrophilic threonine residues in the hydrophobic core, the mechanical stability of the R3 subdomain helix bundle is relatively low<sup>8</sup>. With our mutagenesis design, we aimed to further destabilize the R3 subdomain by mutating conserved isoleucine and leucine residues within the hydrophobic core of the helix bundle to a small polar amino acid, serine. This addition of hydrophilic residues into the core of the helix bundle makes its tertiary structure thermodynamically less favorable, and thus facilitates its unfolding when the helix bundle is subjected to mechanical stretching. The multiple sequence alignment presented in Fig. 1c shows that the residues selected for mutagenesis are highly conserved over animal species. The side chains of the selected hydrophobic residues are oriented towards the core of the helix bundle (Fig. 1b). Furthermore, the residues targeted for mutagenesis are in a belt or ladder-like assembly through the hydrophobic core at sufficient distance from each other as well as from other polar residues in the core, so that stabilization of the mutated helix bundle through the organization of polar planes is unlikely. After the identification of the potential target residues for mutagenesis, a panel of mutants containing one to four single point mutations I805S, I812S, L890S and L897S in each construct was prepared (Fig. 1a).

The destabilized point mutations were investigated by using constant force steered molecular dynamics (SMD) simulations. The bundle behavior was assessed by analyzing the number of water molecules penetrating into the hydrophobic core of the R3 subdomain (Fig. 2). SMD simulations showed decreasing mechanical stability under mechanical load with the increasing number of single point mutations in the talin R3 bundle, as can be observed on the penetrating water count in Fig. 2g. The increase in the number of the penetrating water molecules reflects an increase in the total volume of the bundle due to the acting force and correlates with the number of destabilizing mutations. With the increased volume and area, also the number of water molecules that comply with the penetrated water selection criteria increases. The effect of the mutations on the R3 subdomains ability to withstand mechanical forces was also analyzed by observing the distance between the helix 1 (H1) and the helix 4 (H4) (Supplementary Figure S1). The H1-H4 displacement over time was followed on four vectors, drawn between the  $\alpha$ -carbons of residues Gln800 – Ala904, Thr804 – Ala900, Val808 – Gly896, and Ser815 – Gln888. During 10 ns simulations at 150 pN, WT and 1S mutant subdomains underwent only negligible changes in the range of approximately 0.2 nm. For the 2S mutant, we recognized increasing distance between Gln800 – Ala904 at the top of the bundle. At the same time, the distance between Ser815 – Gln888 at the bottom of the bundle was decreasing, pointing at closing the bottom of the bundle. Similar, yet more intensive, helix reorganization was observed for the 3S and 4S mutants especially during the last 2 ns of the pulling simulation. This suggests that these bundles are opening from the top, making H3 VBS more accessible for vinculin binding (Supplementary Figure S1).

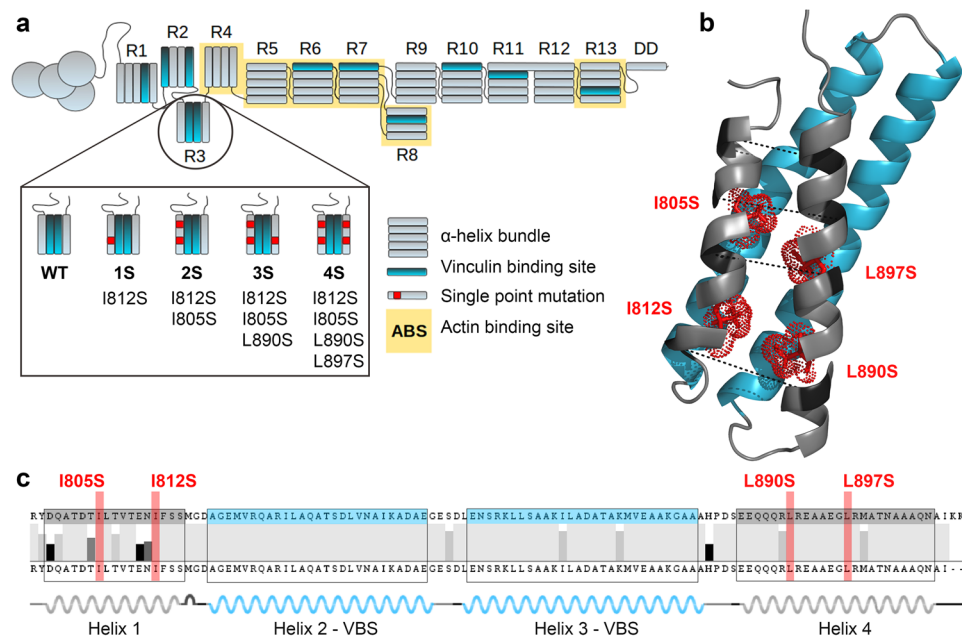


**Figure 1.** Talin-1 R3 domain destabilization by mutagenesis. **(a)** Schematic illustration of wild-type talin-1 and the locations of the mechanically destabilizing point mutations in the R3 subdomain in mutants 1S, 2S, 3S and 4S. **(b)** A cartoon model (PDB ID: 2L7A<sup>14</sup>) of mouse talin-1 R3 domain. The four mutated residues are shown as stick models colored in red and indicated with red labels. The pulling vectors in the SMD simulations are marked with a dashed black line and respective amino acids are indicated with dark coloring. The two vinculin binding helices in the R3 subdomain are colored in blue. **(c)** Talin-1 R3 domain helix boundaries and sequence conservation across 13 animal species (Human gi6739602, Mouse gi227116327, Rat gi189181726, Hamster gi344251776, Naked mole rat gi351707040, Threeshrew gi444729903, Bat gi432110771, Flying fox gi431902812, Cattle gi296484714, Turtle gi465952424, Quail gi667665823, Chicken gi45383127, Zebrafish gi57222259). The positions of the two VBS helices and four destabilizing point mutations are colored in blue and red, respectively.

To computationally investigate the stability of the mutated helix bundles in the absence of force, we compared the structural differences of wild-type R3 subdomain and the 4S mutant during subdomain refolding (Supplementary Figure S2). The refolding ability was measured on the Val808 – Gly896 vector located in the middle of the bundle. Although the 4S mutant showed increased Val808 – Gly896 distance during mechanical stretching, this distance returned to its original length within 7 ns of the relaxation simulation. This suggests that even the most heavily modified 4S mutant readily refolds to its equilibrated state and that the mechanically destabilizing mutations do not prevent refolding of the subdomain helix bundle.

In order to evaluate the effects of the mechanically destabilizing mutations on R3 subdomain thermal stability and secondary structure, we produced the corresponding His6-tagged talin fragments (amino acids 795 – 911) in *E. coli*. We observed robust protein expression and good solubility of the fragments. Because of surprisingly large differences in the electrophoretic mobility of the fragments in SDS-PAGE even in the presence of 8 M urea (Fig. 2h), we confirmed the molecular weights of the purified proteins by mass spectrometry. Size exclusion chromatography (SEC) was used to analyze solubility and size of the produced talin fragments. All studied fragments were found to be soluble and no protein aggregation was observed in SEC (Fig. 2i). However, 3S and 4S mutants showed faster penetration time, suggesting oligomeric structure. This was confirmed by inline right angle light scattering (RALS) analysis, where molecular weights for WT and 1S – 4S mutants were 12.7 kDa, 13.7 kDa, 14.2 kDa, 29.5 kDa and 27.6 kDa, respectively.

Circular dichroism (CD) spectroscopy was used to analyze folding and thermal stability of the purified talin fragments. In CD spectroscopy, wild-type talin R3 and 1S mutant showed closely matching spectra, while the 2S showed signs of decreased subdomain helicity. This decrease in the subdomain helicity was especially apparent for the 3S and 4S mutants. After deconvolution at 205–260 nm, the observed helical contents of WT, 1S, 2S, 3S and 4S were 79.7%, 77.4%, 51.2%, 25.8% and 26.4%, respectively (Fig. 2j). Similarly, in CD spectroscopy melting analysis (Fig. 2k) the 1S mutant was found to have a moderately decreased thermal stability ( $T_m$  52.6 °C) as compared to the wild-type fragment ( $T_m$  66.9 °C), while the 2S, 3S and 4S mutations resulted in a further decrease in  $T_m$  value (48.0 °C, 40.7 °C and 40.9 °C, respectively). These results suggest that at least in the conditions used during the analysis and in the absence of the surrounding talin domains, extensive mutagenesis of the hydrophobic core of the R3 helix bundle reduces the helical content and may expose hydrophobic patches, leading to dimerization in the case of 3S and 4S. Some indications of such behavior were also observed in MD simulations, where the mutated site was found to bend away from its original position, causing torsion of the helix.

Overall, the biochemical analyses indicate that 1S mutant resembles WT in all the characteristics while having decreased stability. The 3S and 4S mutants have severely affected folding and represent significantly destabilized

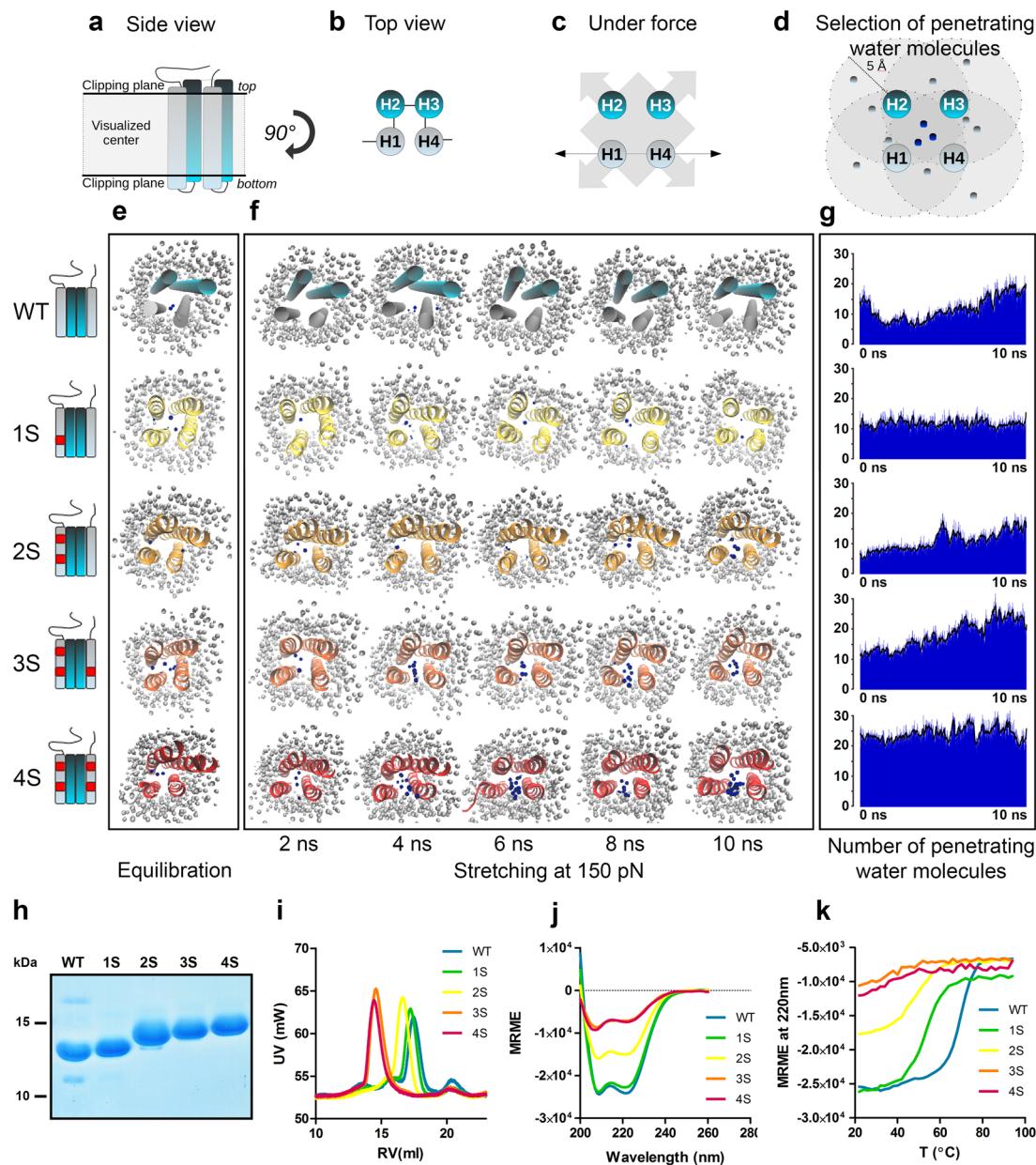


**Figure 2.** Simulated mechanical stretching and biochemical characteristics of destabilized mouse talin-1 fragments. Talin R3 subdomain stability during simulated mechanical stretching was analyzed by observing water penetration into the hydrophobic core of the subdomain. VBS in cyan color, point mutations in red, non-penetrating water in gray, penetrating water in blue. (a–d) Schematics of talin R3 subdomain helix positions and the criteria for selecting water molecules penetrated into the bundle core. The clippings planes used in visualizations in (e,f) are shown in (a). In (d), water molecules within 5 Å of each helix are marked in blue. (e) Snapshot images of the destabilized talin-1 R3 subdomains after a 20 ns equilibration without pulling force. The planes above and below the bundle ends are hidden to allow unobstructed view into the bundle core (schematics in (a)). Penetrating water molecules are colored in blue while water molecules outside the bundle are colored in gray. (f) Representative serial snapshot images of talin-1 R3 subdomain opening during a 10 ns simulation with a constant force of 150 pN. (g) The number of penetrating water molecules during a 10 ns pulling simulation as an average count of 5 experiments at each time point. Black lines represent sliding averages of 10 frames. Water molecules at the ends of the bundle are included in this total count, although they are hidden from the snapshot images in (e,f). (h) PageBlue staining for destabilized talin R3 subdomain fragments (amino acids 795–911) expressed in *E. coli*, affinity purified and separated by SDS-PAGE in the presence of 8 M urea. Apparent differences in fragment sizes result from differential SDS binding to purified talin forms. (i) Size exclusion chromatography analysis for the R3 subdomain fragments. RV = Retention volume (j) Circular dichroism spectroscopy scanning for the talin R3 fragments at wavelengths 200 nm–260 nm. MRME = Mean residue molar ellipticity. (k) Circular dichroism spectroscopy melting curves at 220 nm wavelength. Temperature was increased in 2 °C steps at a rate of 1 °C/min. Determined melting points for WT and 1S–4S mutants were 66.9 °C, 51.6 °C, 48.0 °C, 40.7 °C and 40.9 °C, respectively.

R3 subdomains. The 2S mutant appears an intermediate between 1S and 3S. Therefore, we were keen to evaluate how these mutants would affect cellular talin-mediated functions.

### Talin R3 subdomain destabilization induces talin accumulation into adhesions independently of the presence of talin R4 - R12 subdomains.

The destabilizing talin mutations were introduced into full-length talin expression constructs to study their effects on talin and vinculin recruitment into cell-matrix adhesions. Wild-type mouse embryonic fibroblast (MEF) cells were transfected with the talin constructs, fixed and immunostained for vinculin. Based on captured microscope images, fluorescence intensity ratios between adhesions and cytosolic areas were determined to minimize the bias caused by cell-to-cell variance in the expression levels of the talin proteins. Interestingly, even a single point mutation (1S mutant) in the R3 subdomain was enough to significantly increase this ratio, indicating increased talin partitioning into cell-matrix adhesions (Fig. 3c). Further mutagenesis increased the ratio up to three-fold (for the 4S construct) as compared to the wild-type talin construct. Similar increase in the intensity ratio was also observed for vinculin staining (Fig. 3d). However, the fold increase in this ratio for vinculin was smaller than that observed for talin, resulting in a decrease in the vinculin/talin ratio for the destabilized talin mutants (Fig. 3e). Also the maximal increase in vinculin intensity ratio was already achieved by introducing one destabilizing point mutation (1S mutant). Consequently, the highest vinculin/talin ratio was observed for wild type talin-1 and the ratio gradually decreased when additional point mutations were introduced into the construct. The observed decrease in the vinculin/talin ratio likely resulted from vinculin binding to the abnormally active VBS in talin R3, which activates downstream signaling cascades, whilst decreasing cellular traction forces generation. This, in turn, decreased the force applied on individual talin and results in a decrease in the number of activated VBSs (overall, there are 11 VBSs in talin rod and only two of them are within R3). Similar increase in talin accumulation and decrease in vinculin/talin ratio was also observed in *TLN1*<sup>-/-</sup>*TLN2*<sup>-/-</sup> cells, confirming that the results are not dependent on the presence of endogenous talin proteins (Supplementary Figure S3c,e). To confirm similar expression levels and the expression of intact talin protein for all talin constructs, lysates of *TLN1*<sup>-/-</sup>*TLN2*<sup>-/-</sup> cells expressing the studied talin proteins were analyzed by using Western blot with anti-mCherry antibody (Supplementary Figure S3b).

In a previous study, a cryptic actin binding site (ABS2) in talin-1 rod R4-R8 subdomains was proposed to be a key factor in controlling the incorporation of talin into adhesion structures<sup>15</sup>. To rule out the possibility that the increased accumulation of the destabilized talin constructs would result from altered regulation of talin autoinhibition or talin ABS2, we also studied the 4S mutations in the context of a truncated talin-1 mutant lacking subdomains R4 - R12. This centrally truncated talin-1 (Tal1  $\Delta$ R4-12) accumulated only very weakly into cell-matrix adhesions, resulting in a low adhesion/cytosol intensity ratio and poorly visible adhesions (Fig. 3f). However, introduction of the four destabilizing mutations (Tal1  $\Delta$ R4-12 4S) into this construct caused a similar increase in the adhesion/cytosol intensity ratio as was seen with the full length talin (Fig. 3f,g), indicating that other talin rod subdomains are not required for the enhanced cell-matrix adhesion recruitment caused by the destabilizing mutations. This suggests that the increase in talin-1 adhesion localization was indeed dependent on the unfolding of the talin-1 R3 subdomain and not as a result from disturbed autoinhibition of talin-1 ABS2<sup>15</sup>. In addition, because both Tal1  $\Delta$ R4-12 and Tal1  $\Delta$ R4-12 4S lack the R9 subdomain needed in the talin autoinhibitory interaction between the talin-1 head F3 domain and the rod R9 subdomain<sup>16,17</sup>, these results confirm that increased accumulation of destabilized full length talin is not caused by disrupted talin autoinhibition.

### Talin R3 subdomain destabilization affects traction force generation, talin and vinculin mobility in adhesions and the rate of cell migration.

Cell-matrix adhesions are important signaling hubs for the regulation of actomyosin contractility and cellular traction force generation. In turn, forces acting on the adhesion components are in part regulating adhesion dynamics. To study the effects of talin destabilization on cellular traction force generation, local traction forces were determined by using fluorescent 0.2  $\mu$ m beads embedded into polyacrylamide gel. Talin-1 in human osteosarcoma U2OS cells was ablated by CRISPR techniques as described by Qi *et al.*<sup>18</sup>. Talin-1 ablation resulted in a large decrease in the average cell area and in a complete loss of cellular traction forces (Fig. 4a-c). Re-expression of GFP-tagged wild-type talin-1 fully rescued cell spreading and largely rescued traction force generation. Re-expression of the destabilized talin proteins rescued cell spreading and traction force generation to a degree dependent on the mechanical stability of the expressed talin protein. Re-expression of the 1S construct fully rescued cell spreading and caused a small, statistically insignificant increase in cellular traction forces as compared to the cells expressing wild-type talin. It is important to notice that although the 1S mutant rescued the total traction force generation to the same level as wild-type talin, its increased accumulation into cell-matrix adhesions (Fig. 3c) most likely leads to a decrease in the forces applied to each individual talin molecule. Re-expression of 2S or 3S forms rescued both cell spreading and traction force generation to slightly lower levels than wild-type talin-1. Re-expression of the 4S form resulted in only a partial rescue of both cell spreading and traction force generation, indicating that drastic talin-1 R3 subdomain destabilization results in severe defects in cellular traction force generation and mechanosignaling.

Fluorescence recovery after photobleaching (FRAP) experiments were performed to analyze how the mechanically destabilizing mutations affect talin and vinculin turnover rates in cell-matrix adhesions. For talin and vinculin FRAP, *TLN1*<sup>-/-</sup>*TLN2*<sup>-/-</sup> cells were either transfected with Tal1-GFP or co-transfected with Tal1-mCherry and GFP-Vinculin, respectively, and imaged on a confocal microscope. Talin destabilization by 1S and 4S mutants increased the mobile fraction of talin localized to cell-matrix adhesions (mobile fractions of 0.33, 0.82 and 0.79 for WT, 1S and 4S, respectively), indicating increased mobility of the 1S and 4S mutants in cell-matrix adhesions (Fig. 4d). Co-expression of destabilized talin proteins also significantly increased the mobile fraction of GFP-vinculin, but the effect was not as large as it was for talin itself (mobile fractions of 0.59, 0.83 and 0.86 for WT, 1S and 4S, respectively) (Fig. 4e). Interestingly, co-expression of destabilized talin proteins also increased the fluorescence recovery half time of GFP-vinculin as compared to co-expression of wild type talin. This indicates

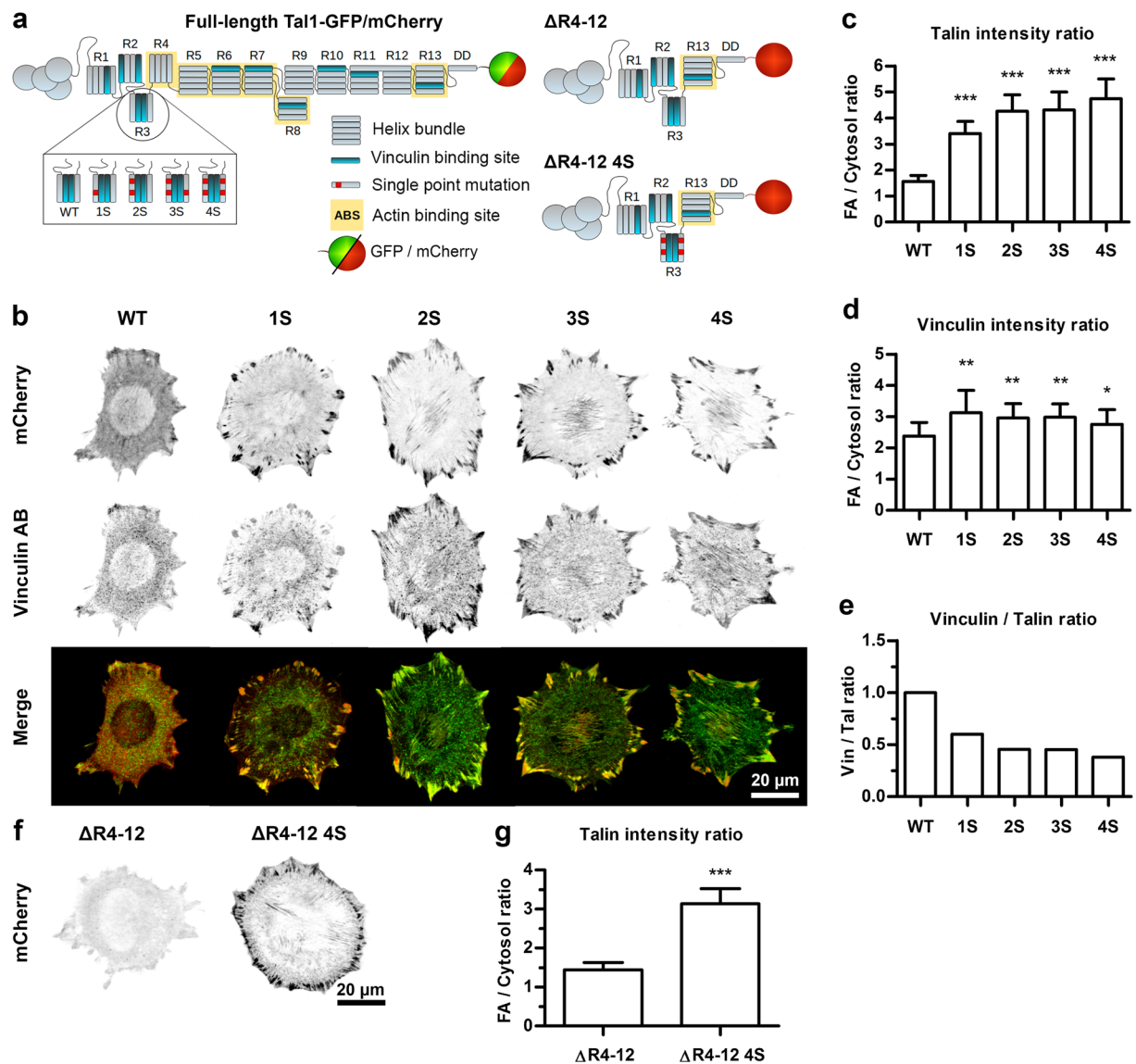


**Figure 3.** Talin-1 accumulation into cell-matrix adhesions in wild type MEF cells. **(a)** Schematic illustrations of full-length talin-1 constructs and truncated talin-1 constructs lacking rod subdomains R4-R12. The truncated talin  $\Delta R4-12$  construct does not contain any destabilizing mutations, while the  $\Delta R4-12$  4S construct contains all four point mutations presented in the Fig. 1a. **(b)** Representative images of wild type MEF cells expressing mCherry-tagged talin-1 proteins. In merged images, mCherry signal is shown in red and vinculin antibody staining as green. Colocalization of the two signals is indicated by yellow color. Scale bar is 20  $\mu\text{m}$ . **(c)** Mean ratios of mCherry signal intensities measured from adhesion sites and cytosolic areas in wild type MEF cells expressing mCherry-tagged talin-1 mutant proteins. Error bars represent SD.  $n = 15$  cells for each talin construct. The ratios measured for the talin-1 mutants were compared to mCherry-tagged wild type talin-1 by One-way ANOVA, \*\*\* $p < 0.0001$ . **(d)** Mean adhesion/cytosolic signal ratios for vinculin antibody staining of cells expressing mCherry-tagged talin-1 forms. Error bars represent SD.  $n = 22, 20, 15, 15$  and 17 cells for wild type talin-1 and 1S, 2S, 3S and 4S mutants, respectively. Comparison to cells expressing wild type talin-1 by one-way ANOVA. \*\* $p < 0.001$ , \* $p < 0.01$ . **(e)** Vinculin/talin-1 ratios for results in **(a,b)**. **(f)** Representative images of wild type MEF cells expressing truncated mCherry-tagged talin-1 mutant proteins. Scale bar is 20  $\mu\text{m}$ . **(g)** Mean ratios of mCherry signal intensities measured from adhesion sites and cytosolic areas in wild type MEF cells expressing truncated mCherry-tagged talin proteins. Error bars represent SD.  $n = 15$  cells for each construct. Statistical analysis by two-tailed t-test. \*\*\* $p < 0.0001$ .

that the exchange rate of GFP-vinculin was slower when it was co-expressed with destabilized talin proteins. This could be caused by slower refolding of the destabilized talin proteins, especially when under mechanical force.

To analyze the effects that talin destabilization has on the rate of cell migration,  $TLN1^{-/-}TLN2^{-/-}$  MEF cells were transfected with wild type and destabilized talin constructs and cultured for 12h on a fibronectin coated surface. Introduction of a single destabilizing mutation (1S mutant) into the talin-1 R3 domain did not significantly affect the observed rate of migration of talin-1 transfected  $TLN1^{-/-}TLN2^{-/-}$  MEF cells (Fig. 4f,g).

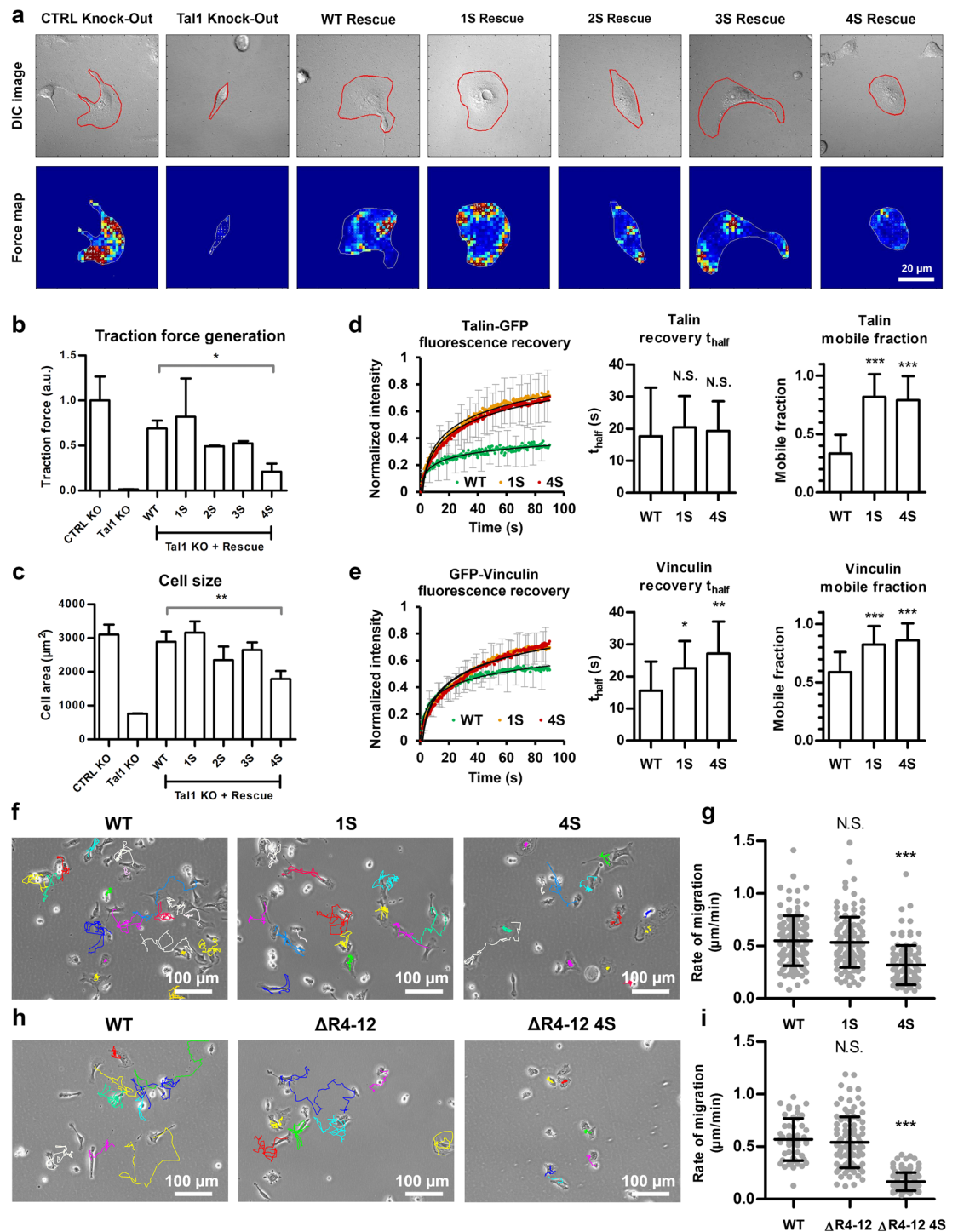


**Figure 4.** Talin destabilization decreased traction force generation and the rate of cell migration and increased talin and vinculin mobility in cell-matrix adhesions. **(a)** Representative traction force microscopy force maps and DIC images of talin-1 knock-out U2OS cells expressing talin-1 constructs. In the force maps, low local forces are illustrated by blue and green colors, while high local forces are illustrated by yellow and red colors. **(b)** Traction force analysis for talin-1 knock-out U2OS cells. Data are means  $\pm$  SD.  $n = 5, 3, 4, 5, 3, 3, 4$  for samples named in the graph legend from left to right. Comparison to cells expressing wild type talin-1 by one-way ANOVA and Tukey's test. \* $p < 0.05$ , Talin-1 WT vs. Talin-1 1S, 2S or 3S were not statistically significant. **(c)** Cell area analysis for talin-1 knock-out U2OS cells. Data are means  $\pm$  SD,  $n = 6, 3, 5, 4, 3, 3$  and 4 cells for samples named in the graph legend from left to right. Comparison to cells expressing wild type talin-1 by one-way ANOVA. \*\* $p < 0.001$ , Talin-1 WT vs. Talin-1 1S, 2S or 3S were not statistically significant. **(d)** Talin-GFP FRAP recovery curve, intensity recovery half time and mobile fraction for wild type talin and destabilized 1S and 4S mutants. Average of 24 cells for each construct from two fully independent experiments. Error bars represent SD. Comparison to cells expressing wild type talin by one-way ANOVA. \*\*\* $p < 0.0001$ . **(e)** GFP-vinculin FRAP recovery curve, intensity recovery half time and mobile fraction for cells expressing Talin-mCherry constructs.

Average of 29, 24 or 25 cells for WT, 1S and 4S, respectively, from two fully independent experiments. Error bars represent SD. Comparison to cells expressing wild type talin by one-way ANOVA.  $**p < 0.001$ ,  $*p < 0.01$ . (f,h) Representative 12-hour migration tracks for *TLN1*<sup>-/-</sup>*TLN2*<sup>-/-</sup> MEF cells expressing EGFP-tagged wild type talin-1 or full-length 1S and 4S talin mutants (f) or mCherry-tagged full-length talin and truncated talin forms (h). Scale bars are 100  $\mu\text{m}$  (g,i) Quantification of migration rates for cells expressing full-length or truncated talin-1 constructs. Horizontal lines indicate mean  $\pm$  SD. For each construct, the results were pooled from two fully independent experiments.  $n = 116, 122$  and  $111$  cells for wild type talin-1 and full length 1S and 4S talin mutants (g).  $n = 49, 98$  and  $105$  for wild type talin-1 and  $\Delta\text{R4-12}$  and  $\Delta\text{R4-12}$  4S mutants (i). Other samples were compared to cells expressing wild type talin-1 by one-way ANOVA and Tukey's test. N.S. = Difference not statistically significant,  $***p < 0.0001$ .

However, introduction of all four mutations (4S mutant) resulted in a significant decrease in the rate of migration, although it did not completely block migration. To analyze adhesion maturation and disassembly in these cells in detail, we used live-cell fluorescence imaging with cells expressing either GFP-tagged WT talin-1 or talin-1 4S mutant. Although talin-1 R3 subdomain destabilization caused a striking increase in its accumulation into cell-matrix adhesions, no other obvious differences in adhesion formation and disassembly were observed during a 120 min live cell imaging (Supplementary Movie S5). Surprisingly, deletion of the talin-1 rod R4 - R12 subdomains did not significantly affect the rate of cell migration (Fig. 4i). *TLN1*<sup>-/-</sup>*TLN2*<sup>-/-</sup> MEF cells expressing the truncated talin  $\Delta\text{R4-12}$  protein were still able to polarize and the rate of migration was comparable to that of cells expressing wild type talin-1. On the contrary, cells expressing the 4S-destabilized talin-1  $\Delta\text{R4-12}$  construct were able to spread, but their ability to migrate was fully blocked (Fig. 4i). Apart from small movement resulting from seemingly random detachment of lamellipodium on one side of the cell, cells expressing this construct were unable to migrate. This suggests that the correct mechanical stability of the R3 subdomain is indispensable for cell migration in the absence of rod subdomains 4-12, but not in the context of full length talin.

### Talin-1 R3 subdomain destabilization affects ECM sensing and talin colocalization with $\beta 3$ and $\beta 1$ integrin subtypes.

The structure of a cell-matrix adhesion is tightly linked to its function and it is constantly changing as a response to intracellular and extracellular signals. Changes in the structure and function of the intracellular adhesion complex are also reflected on the extracellular side of the plasma membrane, as demonstrated by the different integrins clustered in different adhesion subtypes<sup>19</sup>. To study the nature of cell-matrix adhesions induced by the destabilized mutants, wild type MEF cells expressing GFP-tagged wild type talin-1 or destabilized 1S or 4S mutants were cultured on coverslips micropatterned with fibronectin and vitronectin spatially separated from each other on a subcellular resolution, as described previously in Pinon *et al.*<sup>20</sup>. Imaging with superresolution microscopy (SIM) revealed that in the cells expressing wild type talin-1 adhesions were shorter and more punctuated, as compared to the long, streak-like adhesions seen in the cells expressing 1S and 4S mutants (Fig. 5). To minimize the bias caused by unspecific cytosolic fluorescence signal from the talin-1-GFP constructs, analysis of adhesion localization was limited to areas within a mask based on the paxillin antibody staining (Supplementary Figure S6). Adhesions associated with wild type talin-1 strongly favored vitronectin over fibronectin, with only 26% of adhesion area on fibronectin coated surfaces. Talin-1 destabilization caused a decrease in this preference, as indicated by 31% and 40% of adhesions on fibronectin coated areas for cells expressing the 1S and 4S mutants, respectively.

To study the interactions of integrin subtypes with the destabilized talin proteins, we coexpressed WT, 1S or 4S talins with GFP-tagged  $\beta 3$ -integrin on glass coverslips coated with fibronectin (Fig. 5e-l). This analysis revealed that the localization of the talin forms varied so that WT and 1S preferentially accumulated into the cell periphery (Fig. 5e,f), while 4S was mostly found in central adhesions within the cell body (Fig. 5g). The peripheral adhesions containing WT and 1S talins were found to be strongly associated with  $\beta 3$  integrin (Fig. 5e,f,h), while the central adhesions rich in 4S contained only negligible amounts of  $\beta 3$  integrin (Fig. 5g,h). We also studied the colocalization of talin forms with  $\beta 1$  integrin using 9EG7 antibody specific for activated  $\beta 1$ -integrin (Fig. 5i-k). Talin 4S mutant showed increased colocalization with  $\beta 1$ -integrin as compared to WT, indicating that the stability of talin rod domain can regulate the usage of  $\beta$ -integrin subtypes. These changes in the preference for different ECM proteins and the usage of different  $\beta$ -integrin subtypes suggest that talin-1 destabilization does not only affect adhesion dynamics, but also the protein composition of cell-matrix adhesions and adhesion segregation<sup>19</sup>.

## Discussion

Talin is a central adhesion scaffold protein and it is intensively involved in integrin-mediated processes. It contains confirmed or putative binding sites for at least ten other adhesion proteins, thus regulating their recruitment and activation. The mechanical properties of the talin rod domain have been proposed to be an important factor in the regulation of mechanosensing and mechanosignalling. The forces needed to unfold the talin rod subdomains *in vitro* cover a wide range, from 5–10 pN for talin R3 to 25–40 pN for R9<sup>9,10</sup>. The working hypothesis of this study was that the mechanical stabilities of the rod subdomains are optimized for cellular mechanotransduction and that the gradual unfolding of talin rod subdomain allows cells to measure small local changes in cellular forces at a high resolution. Despite of the vast amount of talin-focused research, mechanically altered talins have not been thoroughly characterized in previous studies. In particular, the effects of talin destabilization on the regulation of cellular processes are unknown.

Talin-1 R3 subdomain is in many ways unique among the talin-1 rod subdomains. It has binding sites for both vinculin and RIAM and its mechanical stability is the lowest of all rod subdomains<sup>8,13,14</sup>. Because of the low mechanical stability of the R3 subdomain, it may have a key role in the mechanotransduction of low magnitude forces during the maturation of nascent adhesions. If talin acts as a mechanosensor, any alteration to its

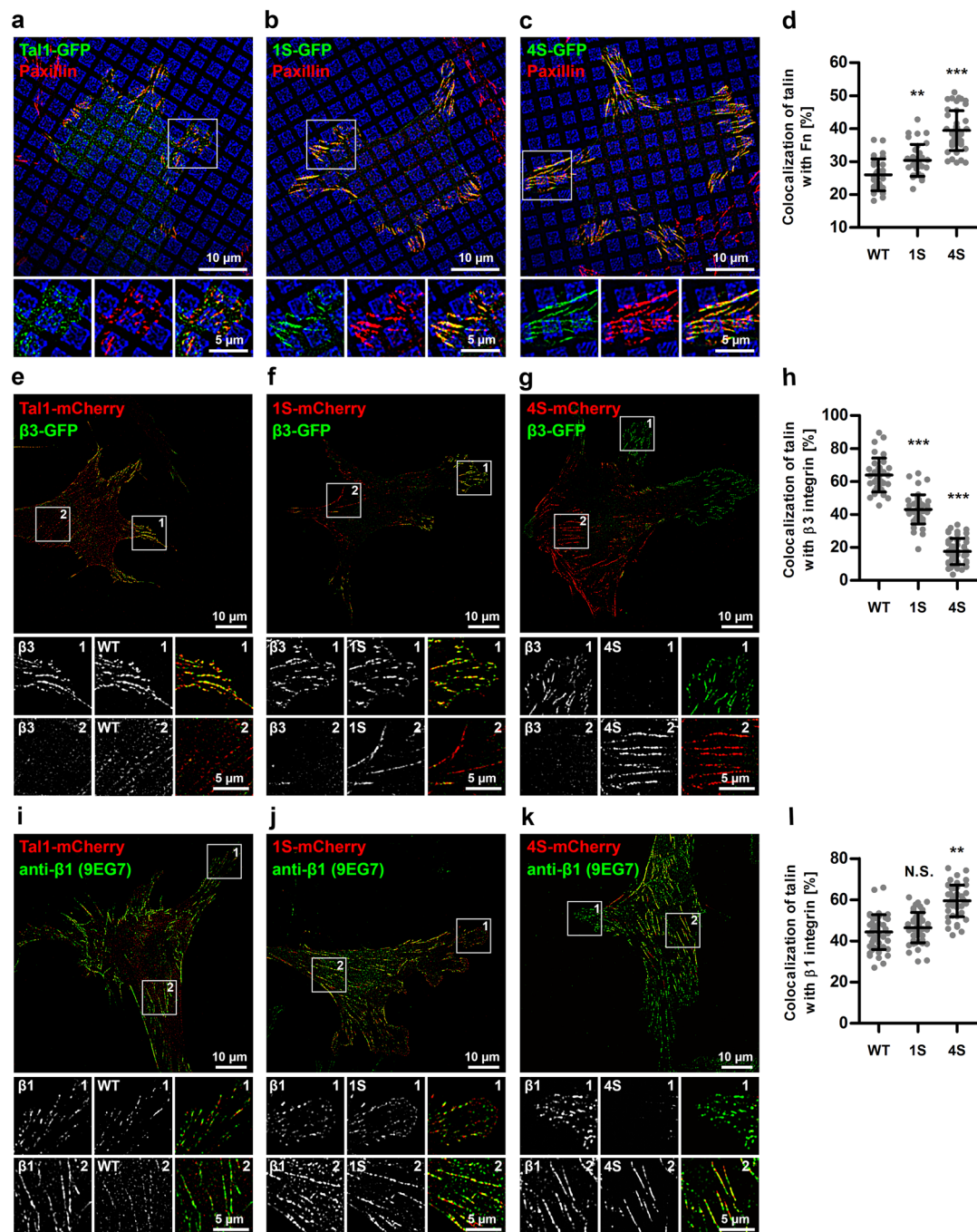


**Figure 5.** Analysis of talin recruitment to cell-matrix adhesions on Fn/Vn patterned substrates and talin colocalization with  $\beta 3$  and  $\beta 1$  integrin subtypes. (a–c) Representative SIM images of transfected wild type MEF cells cultured on micropatterned substrates with 56% of area coated with fibronectin (blue squares) and 44% of area coated with vitronectin (black background). Talin1-GFP fluorescence signal is shown as green and paxillin antibody staining used as a reference for cell-matrix adhesion localization is shown as red. (d) Quantification of talin recruitment to cell-matrix adhesions on Fn coated areas. Data were pooled from three fully independent experiments,  $n = 30, 34$  and  $43$  for cells expressing wild type talin-1, 1S mutant or 4S mutant, respectively. Mean  $\pm$  SD. Statistical analysis by one-way ANOVA and Tukey's test.  $**p < 0.001$ ,  $***p < 0.0001$ . (e–g) Representative SIM images of cells cotransfected with talin mutants and  $\beta 3$ -GFP and cultured on fibronectin-coated substrate. Notice how talin 4S mostly localized to central adhesions, while  $\beta 3$  integrin only localized to peripheral adhesions. (h) Quantification of talin colocalization with  $\beta 3$ -GFP.  $n = 36, 44$  and  $47$  cells for WT, 1S and 4S, respectively, pooled from three fully independent experiments. Mean  $\pm$  SD. Statistical analysis by one-way ANOVA and Tukey's test.  $***p < 0.0001$ . (i–k) Representative SIM images of cells transfected with talin mutants and immunostained with 9EG7 antibody for activated  $\beta 1$  integrin. (l) Quantification of talin colocalization with  $\beta 3$ -GFP.  $n = 46, 48$  and  $47$  cells for WT, 1S and 4S, respectively, pooled from three fully independent experiments. Mean  $\pm$  SD. Statistical analysis by one-way ANOVA and Tukey's test.  $**p < 0.001$ .

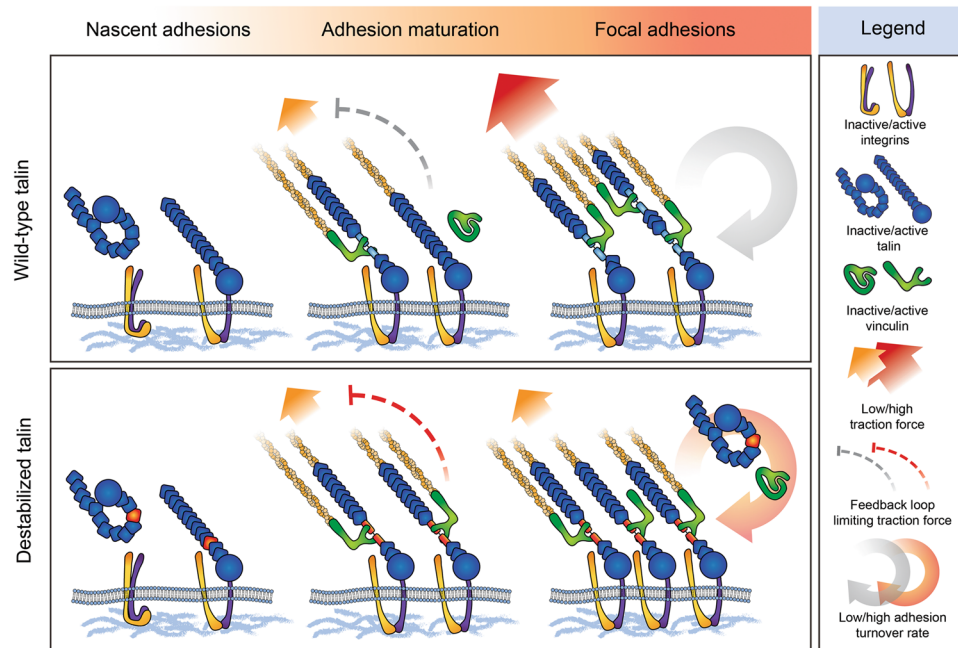


**Figure 6.** Model for decreased traction force generation and increased talin accumulation after talin rod domain destabilization. Talin is recruited into **nascent adhesions** in its autoinhibited conformation and in the absence of mechanical load. Other adhesion proteins participating in the recruitment of talin are omitted from the schematic representation for simplicity. During **adhesion maturation**, mechanical forces transmitted through the talin rod domain promote unfolding of the rod subdomains. Subdomain unfolding exposes cryptic VBSs and allows vinculin binding. Destabilized talin R3 subdomains unfold at lower force, facilitating subdomain unfolding and vinculin binding. Talin rod subdomain unfolding and vinculin binding initiate negative feedback loops that limit cellular traction force generation and adhesion growth. Decreased unfolding force of the destabilized talin rod R3 subdomain results in the activation of this negative feedback also in adhesions transmitting low magnitude forces, which decreases overall traction force generation. In mature **focal adhesions**, talin rod subdomains unfold at their characteristic threshold forces, creating a heterogeneous pool of talin molecules with rod subdomains unfolded to various degrees. Together with the decrease in cellular traction force generation, the intense accumulation of destabilized talin proteins into focal adhesions results in a large decrease in the force transmitted by an individual talin protein, which increases the mobility of talin proteins within focal adhesions. Decreased traction force generation also affects the unfolding of other talin rod domain bundles, which results in a decrease in the vinculin/talin ratio in these adhesions.

mechanical stability is likely to affect adhesion dynamics and cellular mechanosensing. Accordingly, in a previous study by Elosegui-Artola *et al.*, the expression of a mechanically stabilized talin R3 mutant called IVVI was shown to increase the threshold of the substrate rigidity needed for triggering cellular traction force generation and YAP signaling<sup>13</sup>. The likely reason for this increase in the threshold rigidity is that on softer substrates, the tensional forces are not high enough for force-induced unfolding of the stabilized R3 subdomain, which prevents vinculin recruitment to R3 subdomain and downstream signaling. In line with these findings, the destabilizing mutations described in the present study were found to make talin more sensitive for the mechanotransduction of low magnitude forces, as indicated by the observed decreases in both cell migration rate and traction force generation.

Although talin is recruited into nascent adhesions independently of vinculin or transmitted mechanical force, both mechanical stretching of the talin rod domain and recruitment of vinculin are needed for stabilizing talin into cell-matrix adhesions<sup>21, 22</sup>. Interestingly, we found that destabilization of the talin R3 subdomain strongly promoted talin accumulation into cell-matrix adhesions (Fig. 3c). Although slightly increased adhesion accumulation was also observed for vinculin, the vinculin/talin ratio was decreased in cells expressing the destabilized talin mutants. This decrease in vinculin/talin-ratio was accompanied by a decrease in the magnitude of cellular traction forces (Fig. 4b). This likely results from facilitated unfolding of the talin R3 subdomain, especially in adhesions transmitting low-magnitude forces. This leads to the exposure of cryptic VBSs in adhesions where the level of mechanical tensions would not normally be sufficient for talin subdomain unfolding (Fig. 6). Such talin unfolding and the resulting vinculin binding possibly trigger downstream signaling cascades that eventually downregulate cellular traction force generation. Decreased traction force generation, in turn, prevents further unfolding of talin rod subdomains and results in a decreased vinculin/talin ratio, as seen for the cells expressing destabilized talin mutants (Fig. 3e).

In the FRAP experiments, talin destabilization vastly increased the mobile fraction of talin localized into cell-matrix adhesions (Fig. 4d). Slightly surprisingly, this suggests that the large and protein-rich adhesions organized around mechanically destabilized talin proteins have a highly dynamic structure. Thus the majority of the

integrin-bound talin proteins are being constantly exchanged with the cytosolic pool of talin proteins. This finding is in line with the decreased traction force generation observed in this study and highlights the importance of mechanical force as a regulator of adhesion turnover<sup>21</sup>. Similarly to the increased mobile fraction observed for destabilized talin proteins, the mobile fraction of vinculin was increased after talin mutagenesis. However, at the same time we also observed increased FRAP half-recovery time for vinculin. This indicates that despite of the increased mobile fraction, vinculin shows slower initial fluorescence recovery after talin destabilization. This decrease in the vinculin turnover rate may be caused by decelerated dissociation of vinculin-talin complex due to slower refolding of talin rod subdomain after its release from integrin cytoplasmic domain. This is supported by the biochemical analysis of talin R3 mutants, where we found 3S and 4S being rather unstable and poorly folded as isolated domains when compared to WT, 1S and 2S (Fig. 2). Based on these findings, it seems clear that talin destabilization causes defects in cellular mechanosignaling and eventually lowers the force applied on an individual talin protein. This results in increased adhesion protein dynamics and affects the vinculin/talin ratio within cell-matrix adhesions (Fig. 6). The molecular feedback mechanism linking the talin-vinculin interaction to the regulation of applied mechanical load is currently unknown and it may involve several different proteins.

In addition to the increased talin mobile fraction and accumulation into cell-matrix adhesions, R3 destabilization also affected the size, shape and protein composition of cell-matrix adhesions. While wild type talin1-GFP localized mainly into short and roughly circular adhesions at the cell periphery, destabilized talin mutants localized into long, streak-like adhesions that were often found also in the central parts of the cell (Figs 3b and 5). To get a better understanding of the nature of the adhesions formed around the destabilized talin proteins, we analyzed the preference of modified talin proteins to accumulate on fibronectin or vitronectin coated areas. Interestingly, talin destabilization was found to strongly promote adhesion formation on fibronectin (Fig. 5d). In accordance with this finding, we also observed changes in the usage of different  $\beta$ -integrin subtypes after talin rod domain destabilization. These findings indicate that talin rod domain stability is indeed regulating the structure and function of cell-matrix adhesions at the levels of substrate sensing and integrin activation. However, the mechanism that links talin rod domain stability and differential activation of integrin subtypes remains to be found.

In the migration analysis, we observed decreased migration rates for cells expressing destabilized full-length talin-1. Together with the observed accumulation of destabilized talin proteins into cell-matrix adhesions, these results suggest that regulation of adhesion dynamics is controlled by the mechanical stability of talin. These findings are in line with a previous study by Carisey *et al.*, where mutations releasing the vinculin head-tail autoinhibition were shown to lock talin in cell-matrix adhesions, resulting in slower adhesion turnover and decreased cell polarization and migration<sup>21</sup>. In both cases, disturbances in the tight spatial and temporal control of talin-conformation regulated interactions negatively affected the ability of cells to polarize and migrate. It is possible that the defects in cell polarization and migration result from the failure of cells to probe local cellular tension because of the facilitated formation of the talin-vinculin interaction under low force. In this study, we found that neither talin-1 subdomain R3 destabilization nor deletion of the R4-R12 subdomains alone are sufficient to block cell migration. However, together they result in a completely static cell phenotype in talin-null cells (Fig. 4i). The impaired migration of these cells may result from the lack of cryptic and mechano-activatable vinculin binding sites in the talin-1 mutant that is both truncated and destabilized. It is possible that in the context of full-length talin, the defects in mechanosensing caused by the R3 subdomain destabilization can be partly compensated by the presence of other cryptic and mechano-activatable vinculin binding sites in the other rod subdomains. We propose that unfolding of mechanosensitive talin-1 rod subdomains results in local differences in the level of talin-initiated signaling in the cell. These local differences in signaling activity are a prerequisite for cell polarization and migration and the lack of them after both truncating and destabilizing talin rod domain would explain the severely impaired cell migration seen for the cells expressing this construct.

Talin R3 subdomain does not only contain two cryptic vinculin binding sites, but it also has a mutually exclusive binding site for a Rap1 effector protein RIAM. RIAM is thought to be an important regulator of talin recruitment to the plasma membrane and it is present mainly in nascent adhesions, while vinculin binding is needed for adhesion reinforcement and locking talin into mature focal adhesions<sup>23,24</sup>. Force-induced unfolding of the R3 subdomain likely acts as a switch releasing RIAM and allowing vinculin binding during adhesion maturation<sup>14</sup>. In the current study, we found that talin R3 subdomain destabilization increased talin and vinculin accumulation into cell-matrix adhesions, which likely indicates a decrease in the threshold force at which the transition from the RIAM-binding conformation to the vinculin-binding conformation occurs. This decrease in the threshold force facilitates the release of RIAM and simultaneously promotes vinculin binding. However, the mutations presented in this study are unlikely to directly affect the formation of the talin-RIAM complex, because they do not directly target the RIAM binding site in talin R3 helices H2 and H3. Moreover, RIAM binding to talin presumably occurs in the absence of mechanical load applied to talin<sup>14</sup>. To study this experimentally, we coexpressed talin mutants and RIAM-GFP and did not observe significant differences in RIAM localization between wild-type and destabilized talin proteins (Supplementary Figure S4). In addition to vinculin and RIAM binding, the R3 subdomain has been suggested to participate in the regulation of actin binding site 2 (ABS2), located in the talin rod subdomains R4 and R8<sup>15</sup>. Interestingly, Atherton *et al.* found that deletion of the R2 and R3 subdomains resulted in the formation of larger and more stable cell-matrix adhesions. Their experiments using talin mutants with reduced actin binding suggested that the R2-R3 region may have a role in the regulation of talin ABS2, which is located in the rod subdomains R4 and R8. Although the destabilizing mutations described in the present study could affect the regulation of ABS2 in an indirect way by promoting forced unfolding of the R3 subdomain, our experiments with the talin  $\Delta$ R4-12 4S mutant show that the increased talin accumulation into adhesions is independent of the presence of ABS2 (Fig. 3g). Therefore, it seems that the effects caused by talin R3 subdomain destabilization cannot be explained by the released autoinhibition of talin ABS2.

Our study highlights the importance of talin rod domain mechanical stability as a key factor in cellular mechanosensing. We demonstrate that the modulation of the mechanical stability of an individual talin rod subdomain affected a wide range of cellular processes dependent on mechanical signals and cellular mechanosensing. Our results suggest that talin acts as a mechanosensor together with vinculin and is responsible for controlling adhesion turnover, ECM sensing and consequently traction force generation and cell migration.

**Experimental procedures.** *Sequence analysis and mutation design.* Multiple sequence alignment (Clustal Omega<sup>25</sup>) and conservation analysis for talin-1 R3 domain was performed in order to identify candidates for mutation design (Fig. 1c). The alignment was visualized and analyzed with Jalview<sup>26</sup>. PyMOL, Molecular graphics system, version 1.4.1<sup>27</sup>. Was used for visualization, target residue identification and following mutagenesis of four talin-1 R3 residues.

*Molecular dynamics (MD) and steered molecular dynamics (SMD).* Gromacs version 4.6.7<sup>28</sup>. On Sisu supercomputer, CSC, Espoo, Finland was used for all MD and SMD simulations. All models were built with explicit TIP3P water model in 0.15 M KCl neutralized solution and placed into a 10 \* 10 \* 30 nm rectangular box. Each molecule was oriented in the water box so that the d3 vector (vector between V808 CA and G896 CA) was parallel to z-axis; i.e. the pulling direction was perpendicular to the H1-H4 orientation (Fig. 1, Supplementary Figure S1). The system was minimized with 100,000 steps and equilibrated for 10 ns before applying pulling force. Equilibration was performed with 2 fs step size at NTP conditions with v-rescale thermostat at 310 K for protein and solution applied separately and with the Berendsen barostat at 1 bar at isotropic setting. Simulations for domain stability assessment were performed at equilibration conditions for 20 ns. Simulations for domain refolding were performed at equilibration conditions for 20 ns starting from the structure coordinates after 10 ns pulling. Equilibration trajectory was recorded at 100 frames/ns for each analysis.

Pulling simulations were prepared to pull N-terminal helix H1 and C-terminal helix H4 apart in order to follow domain dissociation. Helices were pulled by 4 points in H4 at 150 pN constant force in the z-axis direction. In more detail, the alpha atoms of residues in helix 1 (H1; Q800, T804, V808, S815) were fixed, whilst alpha atoms of residues in helix 4 (H4; Q888, G896, A900 and A904) were pulled with constant force. The use of relatively high force is justified by the limitations in computing resources and based on previous studies suggesting predictive power for SMD simulations carried out using forces higher than observed in nature<sup>6,10</sup>. Pulling simulations were performed with 2 fs step size for 10 ns and recorded at 500 frames/ns. Berendsen thermostat at 310 K was applied for protein and solution separately while Berendsen barostat at 1 bar was used at semiisotropic setting (pressure control was applied in xy coordinates, while pulling was performed in z-axis direction). This setup was selected based on extensive optimization of the parameters (von Essen *et al.*, unpublished data). Equilibration was performed in one simulation experiment for each molecule. Stability and refolding simulations were simulated for wild type R3 subdomain and 4S mutant in one experiment. Finally, pulling simulations were repeated 5 times for each structure. All trajectories were analyzed with VMD<sup>29</sup> at 100 frames/ns.

**Protein expression and purification.** DNA fragments corresponding to the talin-1 residues 795 – 911 were subcloned into a modified pHis vector to create a construct with N-terminal His6-tag separated from the talin fragment by an 11 residue linker (SSSGPSASGTG). The expression of His6-tagged talin rod domain R3 protein in *Escherichia coli* BL21 Star cells (Invitrogen, USA) was induced by 1 mM IPTG for 5 h at 37 °C. Cell pellets were lysed by homogenization (Emulsiflex C3; Avestin, Inc., Germany) into pH 7.2 sodium phosphate buffer containing 1 M NaCl and 20 mM imidazole. After centrifugation, lysates were loaded into affinity column (HisTrap FF; GE Healthcare, UK) using a liquid chromatography system (Äkta purifier; GE Healthcare, UK). Proteins were eluted with a linear imidazole gradient 0–500 mM. Eluted fractions were run on SDS-PAGE gel. Samples purity were checked on the gels (>90%) and fractions containing proteins were dialyzed by stepwise decrease in imidazole concentration into 50 mM sodium phosphate buffer containing 150 mM NaCl pH 7.2. Dialyzed samples were again analyzed by SDS-PAGE and the concentrations detected by NanoDrop (Thermo Fisher Scientific, USA). Urea-PAGE gel was made in the same standard procedure as for SDS-PAGE gels, except 8 M urea was added. Samples were boiled in the sample buffer for 10 min at 100 °C. After cooling to room temperature, 8 M urea was added to the sample. Electrophoresis was performed at +4 °C, 100 V, for 2–3 hours. Protein concentration was determined by measuring A280 using NanoDrop. 1 mM EDTA and 1 mM DTT were added and protein samples were stored at +4 °C.

**Size exclusion chromatography.** Analysis was performed using a liquid chromatography instrument (CBM-20A, Shimadzu Corporation, Kyoto, Japan) equipped with autosampler (SIL-20A), UV-VIS (SPD-20A) and Malvern Zetasizer  $\mu$ V SLS/DLS detector (Malvern Instruments Ltd, Worcestershire, UK). Data were processed using Lab Solution Version 5.51 (Shimadzu Corporation) and OmniSec 4.7 (Malvern Instruments) softwares. A sample of the protein (200  $\mu$ g) was injected on a Superdex 200 10/300 GL column (GE Healthcare, Uppsala, Sweden) equilibrated with 50 mM NaH<sub>2</sub>PO<sub>4</sub>, 150 mM NaCl pH 7.2 buffer. Runs were performed with flow rate of 0.5 ml/min at 20 °C using a thermostated cabin. The molecular weight of the talin forms were determined using static light-scattering intensity (SLS) and the light scattering detector was calibrated using the monomeric peak of BSA.

**Talin fragment CD spectroscopy.** CD spectra were recorded on a Chirascan instrument (Applied Photophysics, UK). Spectra were recorded between 200 and 280 nm with sampling points every 1 nm. Three scans were recorded and baseline spectra were subtracted from each spectrum. Quartz cuvettes with a 0.1-cm path-length were used. Data was processed using Chirascan Pro-Data Viewer (Applied Photophysics, UK), CDNN<sup>30</sup>

written by Gerald Böhm (Martin-Luther Universität Halle-Wittenberg) and Microsoft Excel. The direct CD measurements ( $\theta$ ; mdeg) were converted into mean residue molar ellipticity ( $[\theta]_{MR}$ ) by Pro-Data Viewer. In thermal unfolding experiment a 2 °C step size at 1 °C/min ramp rate with  $\pm 0.2$  °C tolerance was used. The melting temperature was analyzed with Global3 (Applied Photophysics).

**Mass spectrometry.** The purified talin R3 fragments were analyzed by MALDI-TOF instrument (Ultraflex TOF/TOF, Bruker-Daltonics, Germany). A 10  $\mu$ l aliquot of the protein solution was concentrated using a Millipore  $\mu$ -C4 ZipTip pipette tip and mixed with a sinapic acid (Sigma Aldrich, USA) matrix. Single and double-charged peaks were detected without signs of significant impurities. The measured masses determined according to most intensive peaks were 14189.7, 14166.6, 14144.7, 14113.8 and 14088.2 (+1) and 7093.8, 7080.9, 7071.5, 7055.6 and 7041.8 (+2) for wild-type talin fragment and 1S, 2S, 3S and 4S mutants, respectively. The determined masses are reasonable when compared to the theoretical molecular weights calculated by ProtParam.

**Cell lines and cell culture methods.** The wild type MEF cell line was a kind gift from Dr. Wolfgang Ziegler and has been previously described by Xu & Baribault, 1998<sup>31</sup>. The *TLN1*<sup>-/-</sup>*TLN2*<sup>-/-</sup> MEF cell line has been previously described by Theodosiou *et al.*, 2016<sup>32</sup>. Both cell lines were maintained in high-glucose DMEM supplemented with 10% FBS and 1% GlutaMax (Thermo Fisher Scientific, USA). A 37 °C incubator with 5% CO<sub>2</sub> was used for culturing both cell lines.

**Expression constructs and transfection.** C-terminally EGFP- or mCherry-tagged full-length mouse talin-1 expression constructs were created by subcloning talin-1 (1-2541) and EGFP or mCherry DNA fragments into a modified pEGFP-C1 vector backbone (Clontech, USA). Destabilizing point mutations were created with overlapping mutagenesis primers and silent restriction sites in the talin sequence. Centrally truncated and C-terminally mCherry-tagged talin  $\Delta$ R4-12 and  $\Delta$ R4-12 4S constructs were created by subcloning mouse talin-1 fragments corresponding to amino acids 1–913 and 2296–2541 into a modified pEGFP-C1 based backbone. All DNA constructs were authenticated by sequencing.

Wild type and *TLN1*<sup>-/-</sup>*TLN2*<sup>-/-</sup> mouse embryonal fibroblast (MEF) cells were transfected with Neon transfection system (Thermo Fisher Scientific, USA). For all constructs, 5  $\mu$ g of plasmid DNA was used per 10<sup>6</sup> cells. The following electroporation parameters were used for wild type and talin deficient MEF cells: 1350 V, 30 ms, 1 pulse and 1400 v, 30 ms, 1 pulse, respectively.

**Immunostaining and imaging of fixed cells.** Zeiss high-performance 170  $\mu$ m thick coverslips were coated with 25  $\mu$ g/ml human fibronectin (Fn) for 1 hour at 37 °C and washed two times with PBS. Wild type MEF cells were transfected with talin constructs and allowed to recover for 24 h. The cells were trypsinized and plated at low confluency on Fn coated coverslips for 120 min, after which media was aspirated from the wells and the cells were fixed with 4% PFA in PBS (pH 7.4) for 15 min at RT. Fixed cells were washed two times with PBS and permeabilized with 0.2% Triton-X100 in PBS for 5 min at RT. Nonspecific antibody binding was blocked by incubating the samples in 5% FCS, 1% BSA and 0.05% Triton-X100 in PBS for 30 min at RT. Monoclonal anti-vinculin antibody (Clone hVIN-1, V9131, Sigma-Aldrich, USA) was diluted 1:400 in the blocking buffer and incubated on the coverslips for 1 h at RT. Coverslips were washed with PBS (3  $\times$  5 min) before incubation with AlexaFluor-488 conjugated anti-mouse secondary antibody (A21202, Life Technologies, USA) diluted 1:250 in the blocking buffer. Immunostained coverslips were washed with PBS (3  $\times$  10 min) and stored at +4 °C.

Fixed and immunostained samples were imaged with Nikon Eclipse Ti inverted microscope (Nikon Instruments, Japan) equipped with CFI Plan Apo VC 60x/1.40 Oil immersion objective (Nikon instruments, Japan), Yokogawa CSU10 spinning disk confocal unit (Yokogawa, Japan) and Andor NEO sCMOS camera (Andor Technology, UK). 488 nm and 651 nm DPSS lasers were used for exciting AlexaFluor-488 and mCherry fluorophores, respectively. The coverslips were mounted to the microscope stage with a detachable steel chamber and kept immersed in PBS during imaging. All imaging parameters were kept constant for all samples to allow quantitative image analysis.

**FRAP analysis for talin and vinculin.** For FRAP analysis of talin mutants, *TLN1*<sup>-/-</sup>*TLN2*<sup>-/-</sup> cells were transfected with C-terminally GFP-tagged talin constructs. For FRAP analysis of vinculin, cells were co-transfected with C-terminally mCherry-tagged talin constructs and N-terminally GFP-tagged full-length vinculin. Transfected cells were allowed to recover for 24 h and plated on fibronectin coated (25  $\mu$ g/ml) glass-bottom dishes 2 h before imaging. Samples were allowed to further equilibrate at the microscope stage for 30 min before imaging was started. Zeiss Cell Observer. Z1 microscope equipped with LSM780 confocal unit, 37 °C/5% CO<sub>2</sub> incubator and 63x/1.4 Oil immersion objective was used for imaging. Circular regions with a diameter of 2.6  $\mu$ m were photobleached with 488 nm argon laser operated at a high intensity. Only one region in each cell was selected to be bleached. Confocal microscope images were captured at 500 ms intervals for 5 s before photobleaching and for 90 s after photobleaching. Data was collected from fully independent experiments using the same bleaching and imaging parameters for all samples. Fluorescence recovery was analyzed by using equation  $F = [B(t)/B(t < 0)]/[Cell(t)/Cell(t < 0)]$ , where  $B(t < 0)$  and  $Cell(t < 0)$  are the average fluorescence intensities of the of bleached area and the entire cell, respectively, before bleaching and  $B(t)$  and  $Cell(t)$  intensities of the same regions at each time point after bleaching. The resulting F-values were further normalized to zero. EasyFRAP<sup>33</sup> FRAP analysis software was used to fit single exponential curves to each series individually to calculate mobile fraction and half-recovery times for each region.

**Traction force microscopy.** Traction force was measured as described previously by Qi *et al.*<sup>18</sup>. Briefly, glass-bottom dishes were silanized by 0.5% (3-Aminopropyl) triethoxysilane and activated by 0.5%

glutaraldehyde. A drop of gel solution containing acrylamide (6%), bis-acrylamide (0.75%), ammonium persulfate, TEMED, and FluoSpheres<sup>®</sup> carboxylate-modified beads (diameter 0.2 μm, 1:85 dilution by volume) was added to the dishes and covered by a coverslip. The coverslip was removed and the gels were activated with Sulfo-SANPAH under UVA exposure, followed by conjugation with fibronectin (200 μg/ml). Talin1-null US OS cells were transiently transfected with wild type talin-1 or destabilized talin mutants and plated on the gels for 12 h. Traction force was measured as described previously<sup>34</sup>, using a Nikon A1 confocal microscope in Lexington VA Medical Center, Kentucky.

**Migration analysis.** Polystyrene well plates were coated with 10 μg/ml fibronectin at 37 °C for 1 h and washed two times with PBS (pH 7.4). Transfected *TLN1*−/−*TLN2*−/− MEF cells were allowed to recover for 24 h, trypsinized and plated onto fibronectin coated well plates at a low confluency. Cells were allowed to attach for 1 h, followed by washing the cells with warm PBS (pH 7.4) to remove unbound (non-transfected) cells. The cells were cultured in fresh media for 30 min before imaging was started. Evos FL Auto (Life Technologies, USA) equipped with 37 °C and 5% CO<sub>2</sub> incubator was used for live cell imaging for 12 hours at 120 second intervals. The resulting image stacks were analyzed with ImageJ version 1.50e with MTrackJ plugin<sup>35,36</sup>.

**Microcontact printing of patterned substrates.** Stamps were incubated for 10 minutes with a fibronectin (Fn) solution consisting of 45 μg/ml inactive human Fn (thermal denaturation at 90°), 5 μg/ml active human Fn (Sigma Aldrich) and 1 μg/ml Alexa Fluor 647-labeled bovine Fn (protein-labeling kit; Life Technologies). Fn molecules adsorbed to the stamp were transferred to a glass coverslip for 10 minutes. Stamped structures were incubated with 5 μg/ml human Vn (Sigma Aldrich) for 1 h to coat protein-free regions. Micropatterned substrates were rinsed once with 1 × PBS before they were used for cell culture. Transiently transfected wild type MEF cells were seeded and cultured for 2 h on Fn/Vn substrates in serum-free DMEM. After 2 h of cultivation cells were fixed and immunostained using anti-paxillin primary antibody (BD Bioscience) and Cy3-conjugated secondary antibody (Dianova).

**Structured illumination microscopy (SIM) and talin-1 localization analysis.** SIM was performed at room temperature on a nonserial prototype microscope (ELYRA PS. 1; Carl Zeiss Microscopy) in superresolution SIM mode using a Plan Aplanachromat 63 × 1.40 NA oil objective (Carl Zeiss Microscopy). For each image, 15 raw images were processed and reconstructed to extract the superresolution information. Channels were aligned in x,y using predetermined shifts to correct for thermal drift or concussion.

SIM images of talin-1-GFP, paxillin label (Cy3) and labeled Fn (Alexa Fluor 647) were analyzed using Mander's overlap coefficient to determine colocalization of talin-1 with Fn patches. A paxillin mask was created to remove cytosolic fluorescence signal caused by talin expression and to minimize its bias on the quantification (see Supplementary Figure S6). Paxillin masking was done by extending the paxillin SIM signal using Gaussian Blur function in ImageJ and by thresholding the resulting image. This mask was used to calculate Mander's overlap coefficient with manual threshold to determine the degree of GFP fluorescence at sites of Alexa Fluor 647-labeled Fn. Data were obtained from three independent experiments (n = 30–40 cells per condition). For analyzing the colocalization of talin mutants and β3 and β1 integrin subtypes, masks based on widefield fluorescence images was used (see Supplementary Figure S6).

## References

- Schiller, H. B. & Fässler, R. Mechanosensitivity and compositional dynamics of cell–matrix adhesions. *EMBO Reports* **14**, 509–519 (2013).
- Hoffman, B. D., Grashoff, C. & Schwartz, M. Dynamic molecular processes mediate cellular mechanotransduction. *Nature* **475**, 316–323 (2011).
- Bate, N. *et al.* Talin contains a C-terminal calpain2 cleavage site important in focal adhesion dynamics. *PLoS One* **7**, e34461 (2012).
- Rees, D., Ades, S., Singer, S. & Hynes, R. Sequence and domain structure of talin. *Nature* **374**, 685–689 (1990).
- Calderwood, D. A., Campbell, I. D. & Critchley, D. R. Talins and kindlins: partners in integrin-mediated adhesion. *Nat. Rev. Mol. Cell Biol.* **14**, 503–17 (2013).
- Hytönen, V. P. & Vogel, V. How force might activate talin's vinculin binding sites: SMD reveals a structural mechanism. *PLoS Comput. Biol.* **4**, e24 (2008).
- del Rio, A. *et al.* Stretching single talin rod molecules activates vinculin binding. *Science* **323**, 638–641 (2009).
- Yao, M. *et al.* Mechanical activation of vinculin binding to talin locks talin in an unfolded conformation. *Sci. Rep.* **4**, 4610 (2014).
- Yao, M. *et al.* The mechanical response of talin. *Nat. Commun.* **7**, 11966 (2016).
- Haining, A. W. M., von Essen, M., Attwood, S. J., Hytönen, V. P. & del Rio Hernandez, A. All Subdomains of the Talin Rod Are Mechanically Vulnerable and May Contribute to Cellular Mechanosensing. *ACS Nano* **10**, 6648–6658 (2016).
- Wehrle-Haller, B. Assembly and disassembly of cell matrix adhesions. *Curr. Opin. Cell Biol.* **24**, 569–581 (2012).
- Jiang, G., Giannone, G., Critchley, D. R., Fukumoto, E. & Sheetz, M. P. Two-piconewton slip bond between fibronectin and the cytoskeleton depends on talin. *Nature* **424**, 334–337 (2003).
- Elosegui-Artola, A. *et al.* Mechanical regulation of a molecular clutch defines force transmission and transduction in response to matrix rigidity. *Nat. Cell Biol.* **18**, 540–548 (2016).
- Goult, B. T. *et al.* RIAM and vinculin binding to talin are mutually exclusive and regulate adhesion assembly and turnover. *J. Biol. Chem.* **288**, 8238–8249 (2013).
- Atherton, P. *et al.* Vinculin controls talin engagement with the actomyosin machinery. *Nat. Commun.* **6**, 10038 (2015).
- Goksoy, E. *et al.* Structural Basis for the Autoinhibition of Talin in Regulating Integrin Activation. *Mol. Cell* **31**, 124–133 (2008).
- Goult, B. T. *et al.* The structure of an interdomain complex that regulates Talin activity. *J. Biol. Chem.* **284**, 15097–15106 (2009).
- Qi, L. *et al.* Talin2-mediated traction force drives matrix degradation and cell invasion. *J. Cell Sci.* **129**, 3661–3674 (2016).
- Zamir, E. *et al.* Dynamics and segregation of cell–matrix adhesions in cultured fibroblasts. *Nat. Cell Biol.* **2**, 191–196 (2000).
- Pinon, P. *et al.* Talin-bound NPLY motif recruits integrin-signaling adapters to regulate cell spreading and mechanosensing. *J. Cell Biol.* **205**, 265–281 (2014).
- Carisey, A. *et al.* Vinculin regulates the recruitment and release of core focal adhesion proteins in a force-dependent manner. *Curr. Biol.* **23**, 271–281 (2013).

22. Missirlis, D. *et al.* Substrate engagement of integrins  $\alpha 5\beta 1$  and  $\alpha v\beta 3$  is necessary, but not sufficient, for high directional persistence in migration on fibronectin. *Sci. Rep.* **6**, 23258 (2016).
23. Humphries, J. D. *et al.* Vinculin controls focal adhesion formation by direct interactions with talin and actin. *J. Cell Biol.* **179**, 1043–1057 (2007).
24. Lee, H. S., Lim, C. J., Puzon-McLaughlin, W., Shattil, S. J. & Ginsberg, M. H. RIAM activates integrins by linking talin to Ras GTPase membrane-targeting sequences. *J. Biol. Chem.* **284**, 5119–5122 (2009).
25. Livingstone, C. D. & Barton, G. J. Protein sequence alignments: A strategy for the hierarchical analysis of residue conservation. *Bioinformatics* **9**, 745–756 (1993).
26. Waterhouse, A. M., Procter, J. B., Martin, D. M. A., Clamp, M. & Barton, G. J. Jalview Version 2-A multiple sequence alignment editor and analysis workbench. *Bioinformatics* **25**, 1189–1191 (2009).
27. DeLano, W. L. The PyMOL Molecular Graphics System. *Schrödinger LLC* Version 1., <http://www.pymol.org> (2002).
28. Hess, B., Kutzner, C., Van Der Spoel, D. & Lindahl, E. GRGMACS 4: Algorithms for highly efficient, load-balanced, and scalable molecular simulation. *J. Chem. Theory Comput.* **4**, 435–447 (2008).
29. Humphrey, W., Dalke, A. & Schulten, K. VMD: Visual molecular dynamics. *J. Mol. Graph.* **14**, 33–38 (1996).
30. Böhm, G. CDNN: CD spectra deconvolution software version 2.1 (1997).
31. Xu, W. & Baribault, H. Vinculin knockout results in heart and brain defects during embryonic development. *Development* **125**, 327–37 (1998).
32. Theodosiou, M. *et al.* Kindlin-2 cooperates with talin to activate integrins and induces cell spreading by directly binding paxillin. *Elife* **5**, e10130 (2016).
33. Rapsomaniki, M. A. *et al.* easyFRAP: an interactive, easy-to-use tool for qualitative and quantitative analysis of FRAP data. *Bioinformatics* **28**, 1800–1801 (2012).
34. Butler, J. P., Tolić-Nørrelykke, I. M., Fabry, B. & Fredberg, J. J. Traction fields, moments, and strain energy that cells exert on their surroundings. *Am. J. Physiol. Cell Physiol.* **282**, 595–605 (2002).
35. Schneider, C. a., Rasband, W. S. & Eliceiri, K. W. NIH Image to ImageJ: 25 years of image analysis. *Nat. Methods* **9**, 671–675 (2012).
36. Meijering, E., Dzyubachyk, O. & Smal, I. Methods for cell and particle tracking. *Methods Enzymol.* **504**, 183–200 (2012).

## Acknowledgements

Academy of Finland supported this research via grants 290506, 273192 and 136288 (for V.P.H.). American Cancer Society supported the work by Research Scholar Grant RSG-13-184-01-CSM (for C.H.). We thank University of Tampere for the financial support via TGPBB graduate school (for M. v. E). Finnish Cultural Foundation is acknowledged for the grant (for R.R.). Swiss Foundation for Research on Myopathies (B. W.-H.), the Swiss National Science Foundation (31003A-130742) (B. W.-H.) and the Ligue Genevoise contre le Cancer are acknowledged (B.W.-H.). We acknowledge CSC for the supercomputing resources and Biocenter Finland for the infrastructure support. The use of the facilities and expertise of the Biocenter Oulu core facility facility and Institute of Biotechnology Proteomics Unit, both members of Biocenter Finland, is gratefully acknowledged and Dr. Hongmin Tu is specially acknowledged for her contribution to CD analysis. Prof. Reinhard Fässler and Dr. Carsten Grashoff are acknowledged for the help with the *TLN1*<sup>-/-</sup>*TLN2*<sup>-/-</sup> cells. Prof. Jinhua Wu is acknowledged for providing us the RIAM-GFP expression construct. We thank Ulla Kiiskinen, Niklas Kähkönen and Merja Jokela for technical assistance.

## Author Contributions

R.R., M.v.E. and V.P.H. designed the research. R.R., M.v.E., M.S., L.Q., L.A. and C.K. performed the experiments. R.R., M.v.E., M.S., L.Q., C.K. and L.A. analyzed the data. T.O.I., B.W.H., M.B. and C.H. provided expert opinion, technical support and supervised the experimental work. R.R., M.v.E. and V.P.H. wrote the paper. All authors revised and accepted the final version.

## Additional Information

**Supplementary information** accompanies this paper at doi:[10.1038/s41598-017-03335-2](https://doi.org/10.1038/s41598-017-03335-2)

**Competing Interests:** The authors declare that they have no competing interests.

**Publisher's note:** Springer Nature remains neutral with regard to jurisdictional claims in published maps and institutional affiliations.



**Open Access** This article is licensed under a Creative Commons Attribution 4.0 International License, which permits use, sharing, adaptation, distribution and reproduction in any medium or format, as long as you give appropriate credit to the original author(s) and the source, provide a link to the Creative Commons license, and indicate if changes were made. The images or other third party material in this article are included in the article's Creative Commons license, unless indicated otherwise in a credit line to the material. If material is not included in the article's Creative Commons license and your intended use is not permitted by statutory regulation or exceeds the permitted use, you will need to obtain permission directly from the copyright holder. To view a copy of this license, visit <http://creativecommons.org/licenses/by/4.0/>.

© The Author(s) 2017

# Mechanical stability of talin rod controls cell migration and substrate sensing

Rolle Rahikainen <sup>1</sup>, Magdaléna von Essen <sup>†1</sup>, Markus Schaefer <sup>2</sup>, Lei Qi <sup>3</sup>, Latifeh Azizi <sup>1</sup>,  
Conor Kelly <sup>1</sup>, Teemu O. Ihalainen <sup>1</sup>, Bernhard Wehrle-Haller <sup>4</sup>, Martin Bastmeyer <sup>2</sup>, Cai Huang <sup>3</sup>,  
Vesa P. Hytönen <sup>1\*</sup>.

1) Faculty of Medicine and Life Sciences and BioMediTech, University of Tampere, Finland and Fimlab Laboratories, Tampere, Finland

2) Zoological Institute, Cell- and Neurobiology, Karlsruhe Institute of Technology (KIT), Institute of Functional Interfaces (IFG), Karlsruhe, Germany

3) Markey Cancer Center and Department of Molecular and Biomedical Pharmacology, University of Kentucky, Lexington, KY, USA

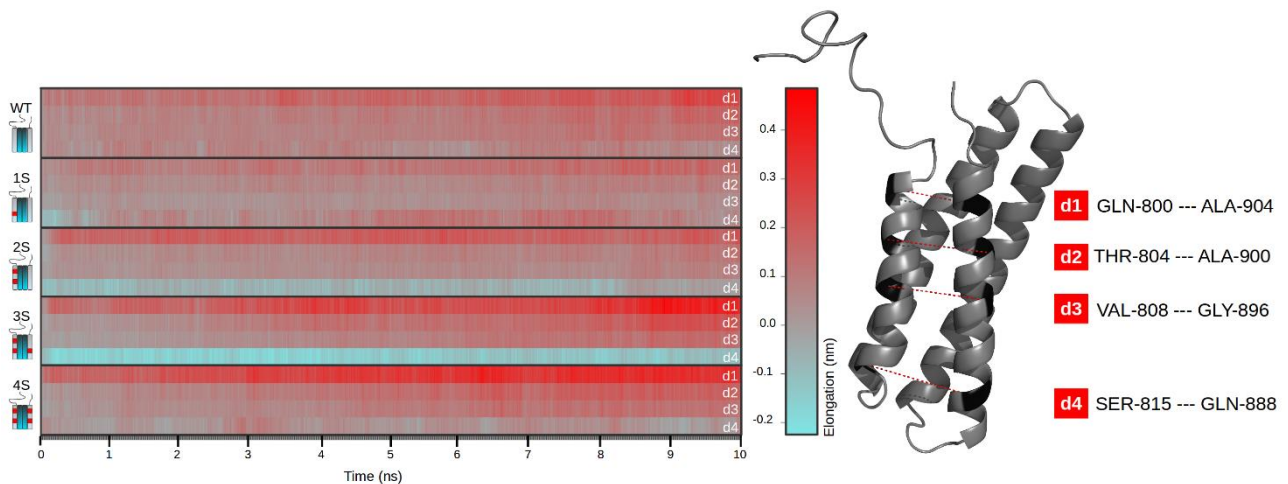
4) Department of Cell Physiology and Metabolism, University of Geneva, Switzerland

<sup>†</sup> Co-first author

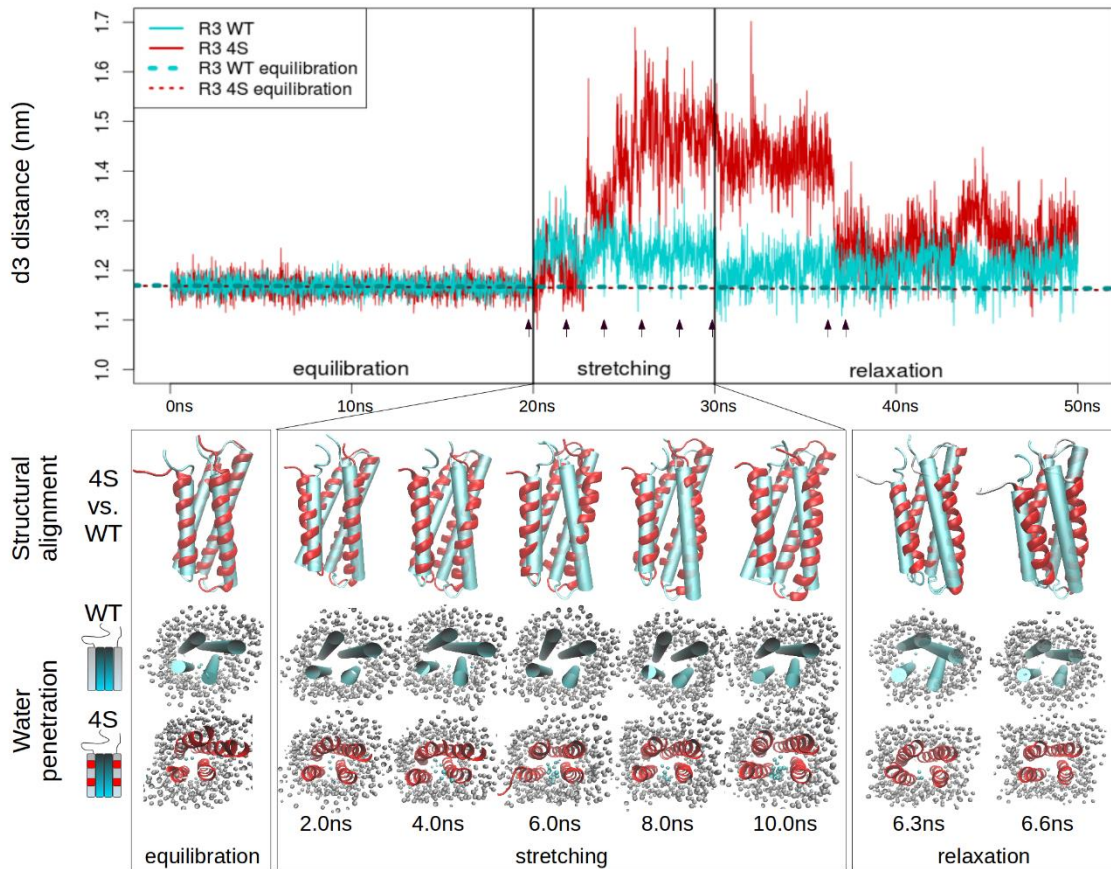
\* Corresponding author, email: vesa.hytonen@uta.fi

---

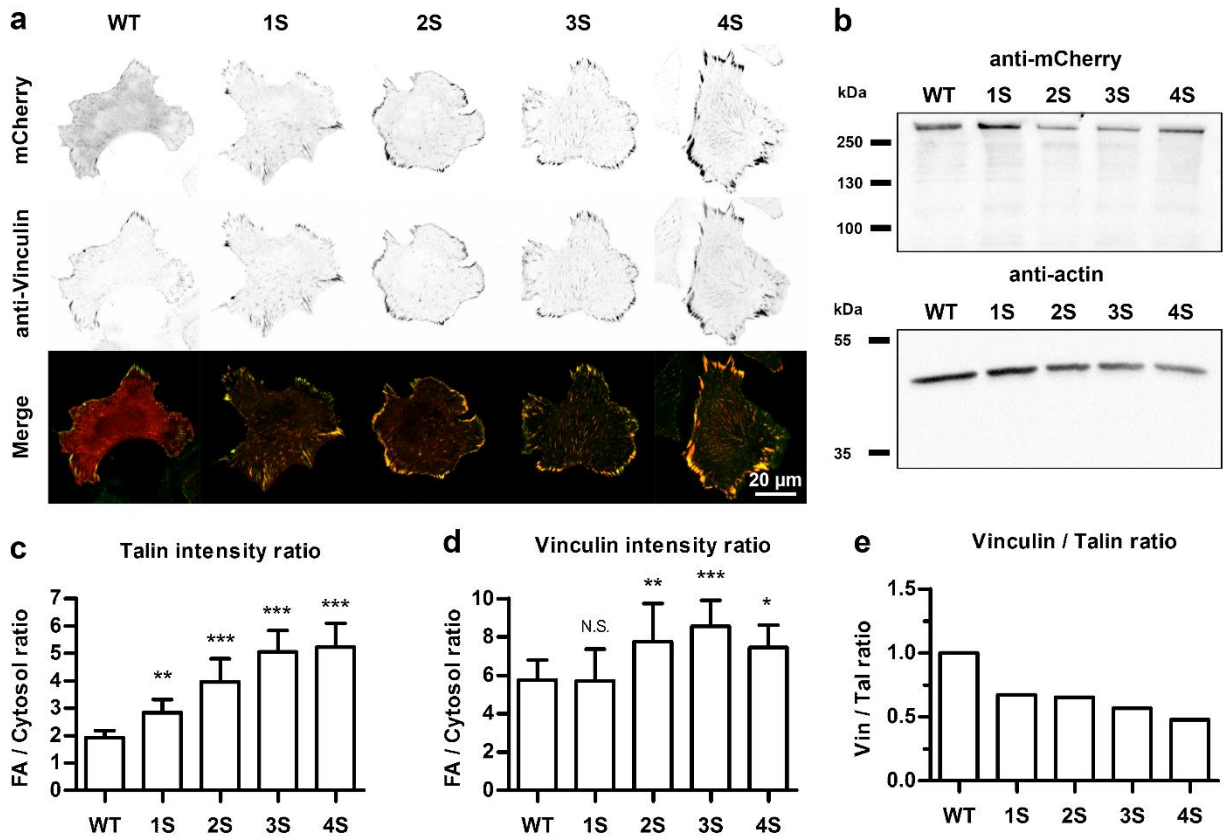
## Supplementary information



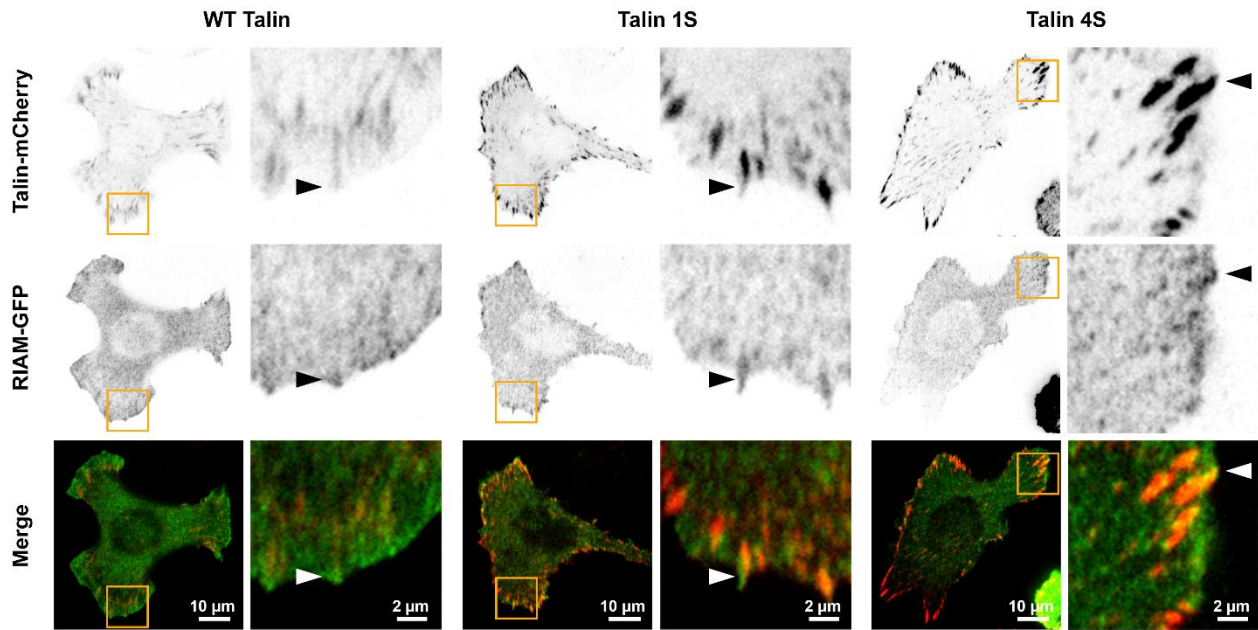
**Supplementary figure S1.** Talin R3 subdomain helix 1 (H1) to helix 4 (H4) distance during simulated stretching of the subdomain at 150 pN. H1 to H4 distance was analyzed at four vectors (d1 - d4), illustrated as dashed red lines on the structural model. In the graphical presentation of the d1 - d4 distances, decreased and increased distances are indicated with cyan and red colors, respectively.



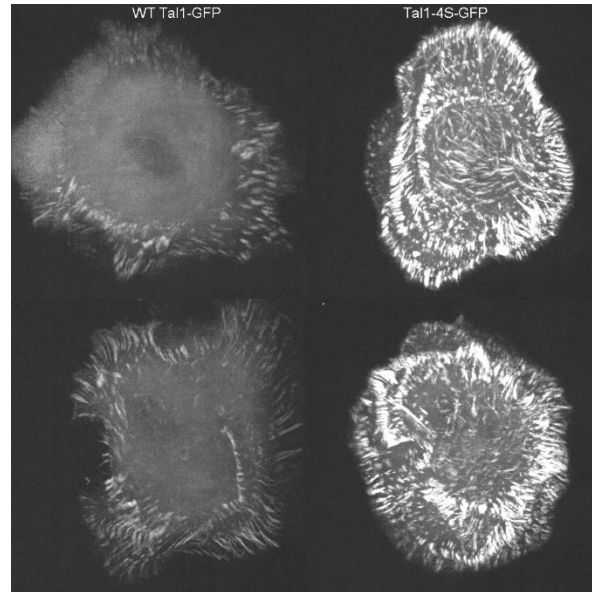
**Supplementary figure S2.** Domain refolding for wild type talin-1 R3 subdomain and destabilized 4S form. Starting from the structure coordinates after 10 ns pulling, simulations for domain refolding were performed at equilibration conditions for 20 ns. Top: The d3 (Val808-Gly896) distances for wild-type R3 subdomain (cyan solid line) and destabilized 4S form (red solid line) during equilibration, stretching and relaxation were plotted as a function of time. Cyan and red dashed lines indicate the average d3 distances during the equilibration step. Middle: Structural alignments for the wild-type R3 subdomain (cyan cylinder) and 4S mutant (red helices) during each step. Bottom: Water penetration into the R3 subdomain helix bundle core during stretching and relaxation. Note the exclusion of water from the core of the 4S form during the relaxation step.



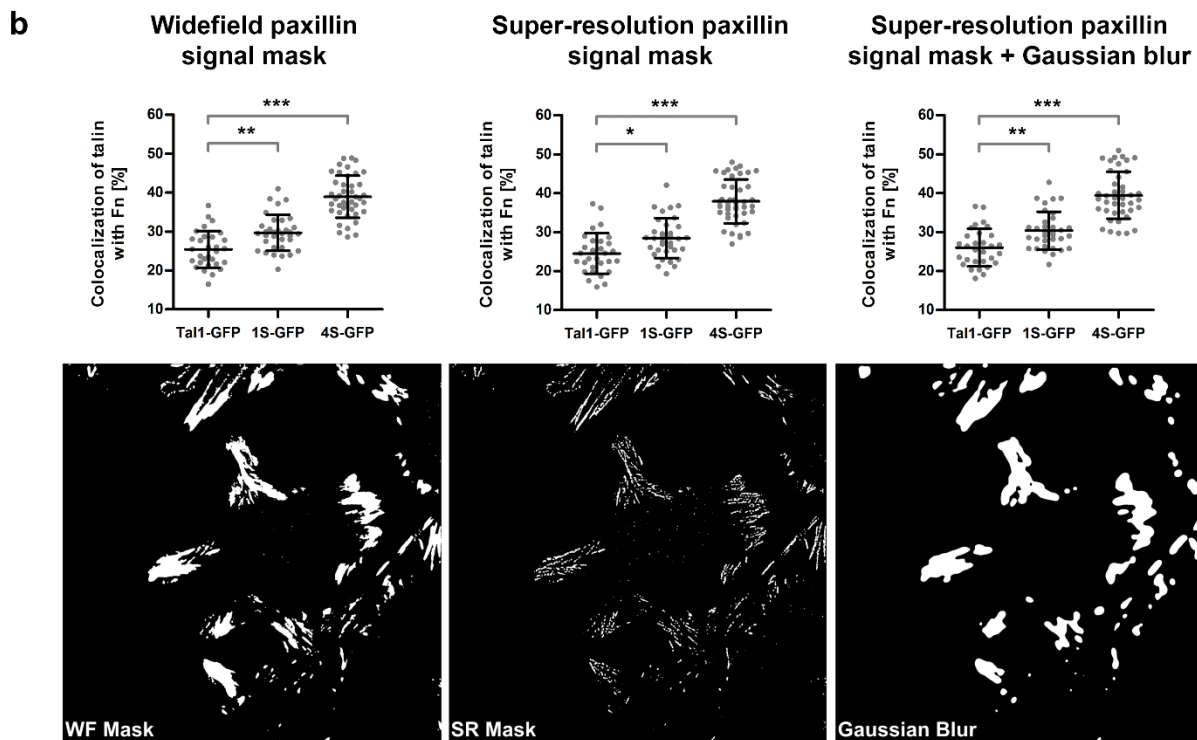
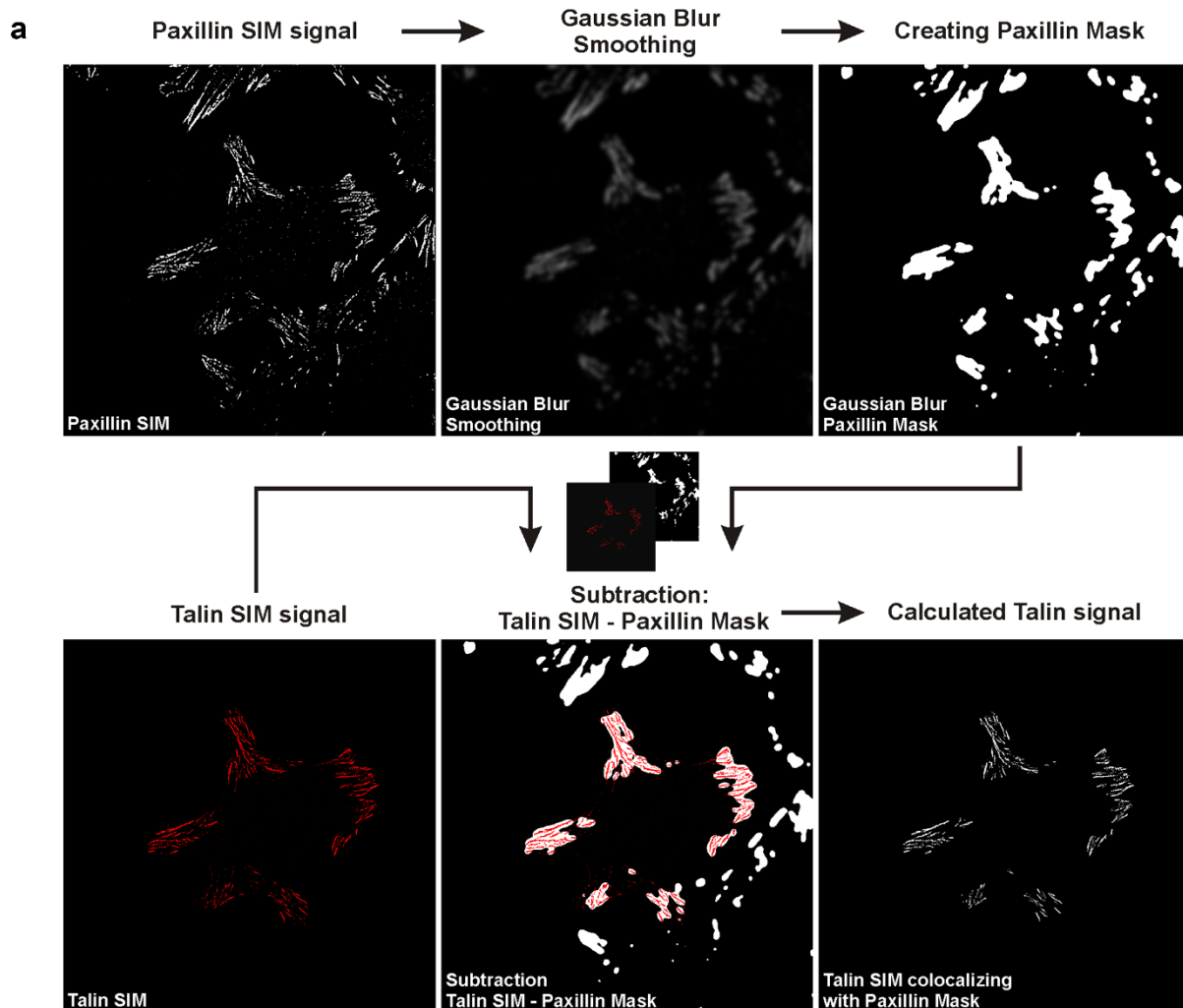
**Supplementary figure S3.** Talin-1 accumulation into focal adhesions in TLN1<sup>-/-</sup>TLN2<sup>-/-</sup> MEF cells. **(a)** Representative images of TLN1<sup>-/-</sup>TLN2<sup>-/-</sup> cells expressing mCherry-tagged talin-1 proteins. In merged images, mCherry signal is shown in red and vinculin antibody staining in green. Co-localization of the two signals is indicated by yellow color. Scale bar is 20 μm. **(b)** Western blot for concentration-normalized lysates of TLN1<sup>-/-</sup>TLN2<sup>-/-</sup> MEF cells expressing mCherry-tagged talin-1 proteins. Expressed talin proteins were detected by anti-mCherry antibody, while anti-actin antibody was used as a loading control. After normalization to actin intensity, the population level expression levels of destabilized 1S, 2S, 3S and 4S forms were 113%, 65%, 75% and 137% of the expression level of wild type talin. **(c)** Mean ratios of mCherry signal intensities measured from adhesion sites and cytosolic areas in cells expressing mCherry-tagged talin-1 mutant proteins. Error bars represent SD. n = 16 cells for each talin construct. **(d)** Mean adhesion/cytosolic signal ratios for vinculin antibody staining of cells expressing mCherry-tagged talin-1 forms. Error bars represent SD. n = 16 cells for each talin construct. In (c) and (d), The intensity ratios measured for the talin-1 mutants were compared to mCherry-tagged wild type talin-1 by One-way ANOVA and Tukey's test. \*\*\* = p < 0.0001 \*\* = p < 0.001, \* = p < 0.05. **(e)** Vinculin/talin ratios for the results in (c) and (d).



**Supplementary figure S4.** Localization of RIAM-GFP in cell expressing destabilized talin-1 proteins. *TLN1*<sup>-/-</sup>*-TLN2*<sup>-/-</sup> cells were co-transfected with RIAM-GFP and mCherry-tagged wild-type talin-1 or 1S or 4S destabilized talin constructs. Co-transfected cells were plated on fibronectin coated glass for 120 min before fixation. Representative confocal microscope images ( $n = 10$  for each talin construct) of the fixed cells are shown in the image panel. In the magnified views of lamellipodia, arrowheads indicate areas of nascent adhesion structures with high RIAM-GFP fluorescence signal and low talin-mCherry fluorescence signal. Co-expression of destabilized 1S or 4S mutants did not noticeably affect the localization of RIAM-GFP to the leading edge of advancing lamellipodia.



**Supplementary movie S5.** Live cell microscopy time-lapse video for *TNL1*<sup>-/-</sup>*TLN2*<sup>-/-</sup> cells expressing wild-type talin-1 or mechanically destabilized talin-1 4S form. Cells transfected with each construct were plated on fibronectin coated coverslips, allowed to attach for 15 min and imaged at 60 s intervals for 120 min. All imaging parameters were kept constant for all images to allow comparison of adhesion intensities.



**Supplementary figure S6.** Paxillin masking and localization analysis for cells expressing talin-1 constructs on Fn/Vn patterned substrates. Transiently transfected wild type MEF cells were cultured for 2h on micropatterned Fn/Vn substrates, PFA-fixed and immunostained for paxillin. Analysis of superresolution microscopy (SIM) images was performed using imageJ to determine the degree of GFP fluorescence at sites of Alexa Fluor 647-labeled Fn with Mander's overlap coefficient. **a)** A Paxillin mask was created in order to remove unspecific cytosolic fluorescence signals from the cytosolic fraction of talin-GFP and thus focusing the analysis on high density talin clusters. For paxillin masking, the paxillin SIM signal was extended via Gaussian blur smoothing to focus on true talin-1-positive adhesions without biasing analysis towards absolute talin-1 localization with paxillin. Finally, analysis of talin-1 localization with fibronectin coating was performed with Mander's overlap coefficient using manual threshold. **b)** Comparison of results from talin localization analysis using three different types of masks based on the paxillin signal. Talin-1 signal masking using paxillin widefield signal (left hand side), paxillin super-resolution signal (Middle) or Gaussian blur smoothed paxillin super-resolution signal (right hand side) all yielded closely matching results, suggesting that masking the talin-1 signal before the analysis caused only negligible bias to the results. Datapoints were pooled from three fully independent experiments, n = 30, 34 and 43 for cells expressing wild type talin-1-GFP, 1S-GFP or 4S-GFP mutant, respectively. Statistical analysis by one-way ANOVA and Tukey's test. \* =  $p < 0.05$ , \*\* =  $p < 0.001$ , \*\*\* =  $p < 0.0001$ .

## All Subdomains of the Talin Rod Are Mechanically Vulnerable and May Contribute To Cellular Mechanosensing

Alexander William M. Haining,<sup>†</sup> Magdaléna von Essen,<sup>‡,§</sup> Simon J. Attwood,<sup>†,#</sup> Vesa P. Hytönen,<sup>\*,‡,§</sup> and Armando del Río Hernández<sup>\*,†</sup>

<sup>†</sup>Cellular and Molecular Biomechanics Laboratory, Department of Bioengineering, Imperial College London, London SW7 2AZ, United Kingdom

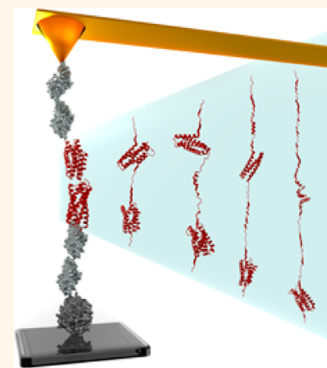
<sup>‡</sup>BioMediTech, University of Tampere, Biokatu 6, FI-33520 Tampere, Finland

<sup>§</sup>Fimlab Laboratories, Biokatu 4, FI-33520 Tampere, Finland

### Supporting Information

**ABSTRACT:** Although the relevance of mechanotransduction in cell signaling is currently appreciated, the mechanisms that drive this process remain largely unknown. Mechanical unfolding of proteins may trigger distinct downstream signals in cells, providing a mechanism for cellular mechanotransduction. Force-induced unfolding of talin, a prominent focal adhesion protein, has been demonstrated previously for a small portion of its rod domain. Here, using single-molecule atomic force microscopy (smAFM), we show that the entire talin rod can be unfolded by mechanical extension, over a physiological range of forces between 10 and 40 pN. We also demonstrate, through a combination of smAFM and steered molecular dynamics, that the different bundles within the talin rod exhibit a distinct hierarchy of mechanical stability. These results provide a mechanism by which different force conditions within the cell control a graduated unfolding of the talin rod. Mechanical unfolding of the rod subdomains, and the subsequent effect on talin's binding interactions, would allow for a finely tuned cellular response to internally or externally applied forces.

**KEYWORDS:** mechanotransduction, single-molecule force spectroscopy, steered molecular dynamics, protein mechanostability, mechanobiology



Research in recent years has demonstrated the relevance of a cell's ability to interpret the mechanical properties of its surroundings. This ability of a cell to convert mechanical signals into signaling cascades, *i.e.*, mechanotransduction, has been shown to drive a wide variety of cellular phenomena including cancer progression and stem cell differentiation.<sup>1,2</sup> Despite an appreciation of the importance of these mechanical signals, the mechanisms by which cells translate them remain unknown.

One of the focus areas for finding a mechanism of cellular mechanotransduction concerns the integrin-mediated adhesions. Integrins, as transmembrane proteins, provide a connection between the interior of the cell and the extracellular matrix (ECM) that surrounds it. As anchorage points for the cell, they orchestrate the bidirectional mechanical communication of the cell with the ECM. Integrins are important not just for stable cell–ECM adhesion but also for cellular force generation and motility. As well as providing this connection, integrins help to recruit a cluster of intracellular proteins. In this process, early adhesions (focal complexes) are matured to protein-rich plaques called focal adhesions. This

process is tightly regulated by mechanical signals: Contractile actomyosin cytoskeleton and adequate stiffness in the extracellular matrix are needed to drive the adhesion maturation process.<sup>3–5</sup> Furthermore, it is possible to control the size of the adhesion plaques by applying external force locally.<sup>6,7</sup> Thus, integrin-mediated adhesions have been a key area for investigations into cellular mechanotransduction. In particular, studies into the mechanosensitivity of these adhesions and how this might lead to cellular mechanotransduction have been centered on the focal adhesion protein talin.

Due to its unique and prominent position as a mechanical linkage between the ECM-bound integrins and the cellular cytoskeleton, talin has been hypothesized to be the crucial mechanosensitive molecule in focal adhesions.<sup>8</sup> Talin is essential for cellular spreading<sup>9,10</sup> and is responsible for early connections between integrin and actin cytoskeleton.<sup>11</sup>

**Received:** March 8, 2016

**Accepted:** July 5, 2016

**Published:** July 5, 2016

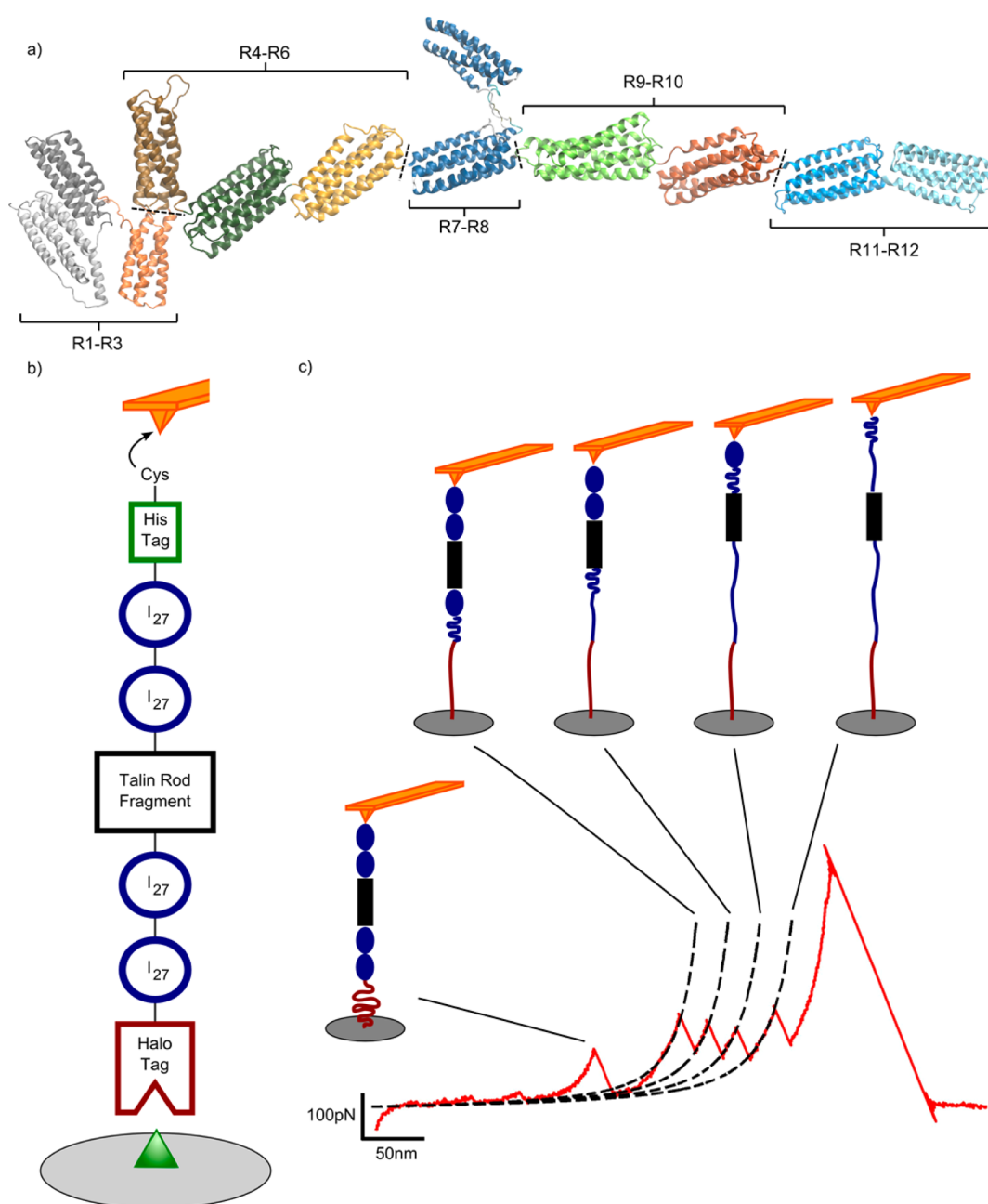


**Figure 1.** Talin rod polyprotein constructs for smAFM experiments. (a) Crystal structure of talin rod, showing the  $\alpha$ -helical bundles R1–R12. The rod was separated into different fragments as indicated for the AFM experiments. (b) Schematic of the polyprotein constructs containing: the talin fragment to be investigated; four flanking I<sub>27</sub> domains for fingerprinting; the HaloTag enzyme that binds to its associated ligand on the surfaces; a HisTag for protein purification; and a terminal cysteine for cantilever tip attachment. (c) Example of fingerprint used for identification. After the unfolding of the talin rod fragment, the first peak corresponds to the unfolding of the HaloTag enzyme. This is followed by the unfolding events for the four I<sub>27</sub> domains, creating the characteristic “sawtooth” pattern. The final peak represents the detachment of the polyprotein from either the surface or the cantilever. The dashed lines indicate a worm-like chain model fit applied to the I<sub>27</sub> unfolding events. (b, c) Not to scale.

Investigations into the mechanosensitivity of talin have so far been focused on talin’s interaction with vinculin, another focal adhesion protein. Our previous studies were the first to demonstrate this mechanosensitivity, both *in silico* and experimentally. We showed that force-induced stretching of the talin rod exposes new cryptic vinculin binding sites (VBS) and increases the vinculin recruitment to the talin rod.<sup>12,13</sup> Similar studies by others have supported and enhanced this concept.<sup>14,15</sup> All these studies, however, were focused around a small, N-terminal subregion of the rod, bundles R1–R3. The

compact nature of this region and the abundance of VBSs leads to the possibility that this region alone is responsible for talin’s mechanosensing, while the remainder of the rod, proposed to be linear in structure, is responsible for force propagation.<sup>16</sup> Up until now, however, the response of this linear region to force has never been investigated.

The mechanical load applied to cellular components may vary substantially depending on the cellular substructure and the cellular event. Thus, it is possible that a subpopulation of the proteins is under high load in certain situations, when

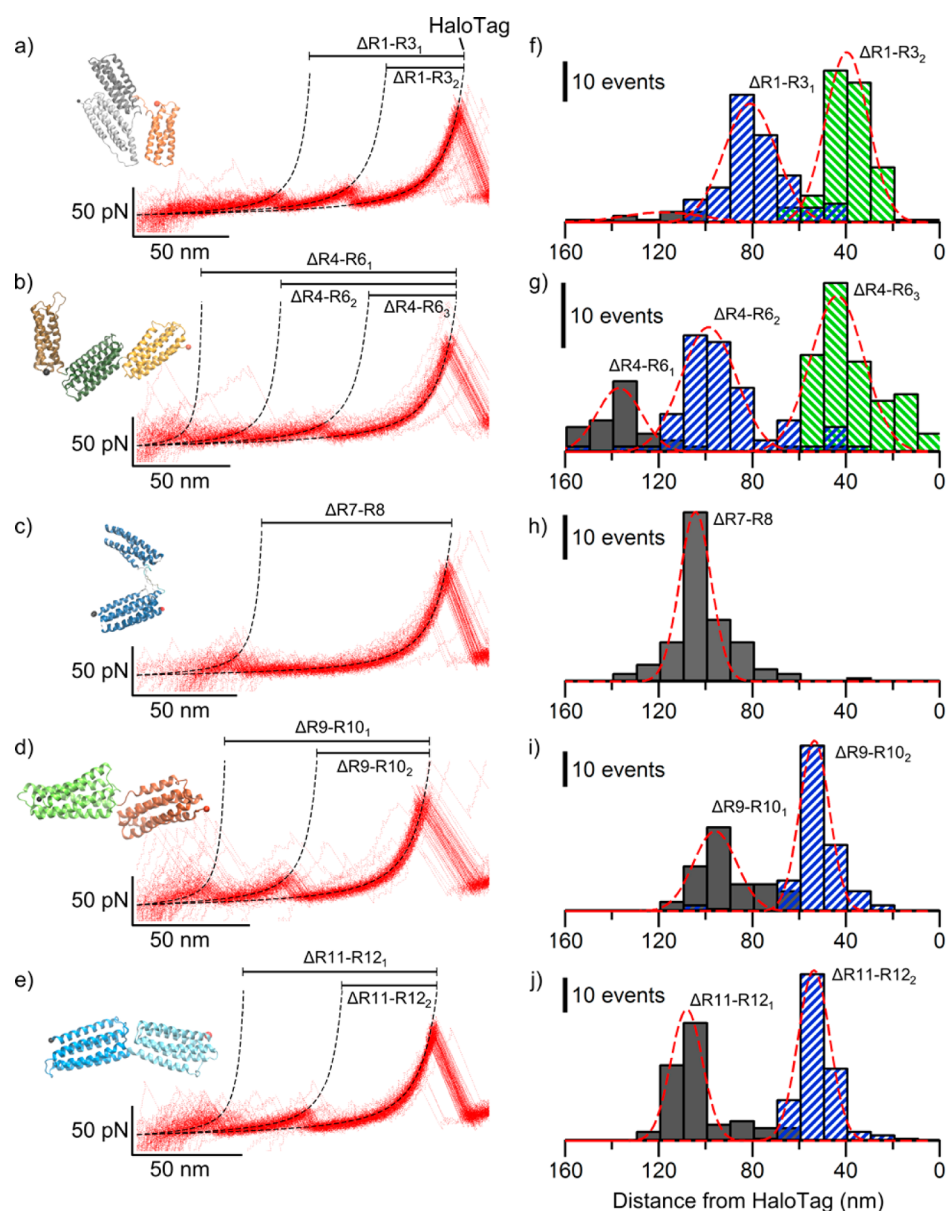


**Figure 2.** Unfolding pattern of talin rod fragments. (a–e) Aggregated force extension traces reveal the unfolding pattern of each fragment. The fingerprints of each trace were used for alignment, revealing the number of unfolding events and the extension associated with each. Inset: crystal structures for each fragment. Each event is fitted to the worm-like chain model (dashed lines). The method for measuring the extension of each event is also shown. (f–j) Histograms of the extensions associated with each unfolding events. The extension associated with each unfolding event was measured, using HaloTag as a reference point. The x-axes have been reversed so that the order of the unfolding peaks in the histogram matches the order of unfolding in the traces, *i.e.*, the furthest peak from HaloTag is the first to unfold. Red dashed lines show Gaussian fits applied to the histograms. Extension lengths are summarized in [Supporting Information Table S1](#). (a, f) R1–R3, number of traces analyzed,  $n = 101$ . (b, g) R4–R6,  $n = 76$ . (c, h) R7–R8,  $n = 82$ . (d, i) R9–R10,  $n = 91$ . (e, j) R11–R12,  $n = 103$ .

responsible for particular cellular functions. Experimental methods have emerged that allow measurement of these forces applied to intracellular proteins such as talin and vinculin.<sup>9,17</sup> The fact that talin is the most prominent candidate for consideration as a cellular mechanosensor means that the elucidation of the biomechanical properties of the full rod in response to force is indispensable to the understanding of its function. The presence of numerous relevant binding sites in the remainder of the rod (R4–R13), including six VBSs and binding sites for other proteins including RIAM, synemin and DLC1, means that the response of this region to force could have a profound effect on the modulation of talin's interactions.<sup>18–20</sup>

There are, however, difficulties associated with studying the full-length talin rod using single-molecule techniques. First, it is a large, amphipathic domain ( $\sim 2000$  aa) and as a result can be difficult to handle. Second, the length of the fully stretched talin rod domain is longer than the maximum travel distance ( $< 1 \mu\text{m}$ ) allowed by high-resolution single-molecule atomic force microscopy (smAFM) setups. Third, studies conducted on the complete rod would lose information about how the observed unfolding relates to individual bundle structures.

In this study, we circumvent these restrictions by separating the rod into smaller subdomains. These subdomains are then analyzed using a state of the art smAFM setup, combined with recent advances in single-molecule stretching techniques. The

subdomains are inserted into polyprotein constructs; these constructs contain flanking, fingerprinting molecules that allow for correct trace determination through a characteristic unfolding pattern (Figure 1).<sup>13</sup> The constructs also contain an N-terminal HaloTag enzyme that, when coupled to ligand-prepared surfaces, ensures that the talin subdomains are extended in the desired orientation.<sup>21</sup> This unique combination of smAFM techniques allows us to establish an outline of the unfolding pattern of the talin rod. We also used all-atom steered molecular dynamics (SMD) simulations on each of the individual bundles, to provide a profile for how this applied tension is rearranging these bundles at a structural level. These complementary data sets allow us to compare the relative stabilities of the bundles for the full rod and thus propose a sequence for how talin might unravel under force application *in vivo*.

## RESULTS

**Generation of Talin Rod Constructs.** The talin rod is comprised solely of  $\alpha$ -helical bundles, and the structures of these individual bundles have been resolved using structural biology methods. In this study, we utilized the current structural model of the full-length talin rod.<sup>1</sup> The talin rod consists of 62  $\alpha$ -helices, which then form into bundles (R1–R13), each containing four or five helices. The talin rod was first divided into five separate fragments in order to characterize their unfolding properties under force application by smAFM. The fragments were based on the best available knowledge of the organization of the bundles for the whole rod (Figure 1a): the boundaries between the fragments were placed similarly to those used to fragment the rod for the determination of the crystal structures.<sup>16</sup> In the case of two of the fragments, the boundaries were dictated by their structures: bundle R8 is inserted between the third and fourth helices of R7, and thus they were expressed together; and R11 and R12 share a common, elongated helix between them. The fragment R1–R3 has previously been analyzed and thus was included as a reference to those earlier works.<sup>2</sup> The remaining bundles, R4–R6 and R9–R10, were clustered into two fragments. R13 was excluded, as talin's primary actin binding site occurs in this bundle, and thus it is unlikely to be extended from its N and C termini. The details of the polyprotein expression plasmids are provided in Supporting Information Figure 1.

In order to improve the efficiency of data capture and analysis, these fragments were engineered into polyprotein constructs (Figure 1b). All constructs were produced in *E. coli* and purified to homogeneity according to previous protocols.<sup>13,22</sup> These constructs ensure that the talin fragments were extended in the correct orientation, *i.e.*, from their N and C termini. The use of an N-terminal HaloTag protein and C-terminal cysteine residue has been shown previously to provide specific, stable attachment of polyproteins to the Halo-ligand-functionalized smAFM surface and gold-coated cantilever tip, respectively.<sup>3</sup> The immunoglobulin domain, I<sub>27</sub>, from titin has been used to provide a molecular “fingerprint” to determine valid force extension traces.<sup>13,23</sup> Only traces which displayed the unfolding of the HaloTag and the characteristic “sawtooth” pattern of at least three I<sub>27</sub> domains were accepted for analysis (Figure 1c).

**Unfolding Pattern of Talin Rod Fragments.** The talin rod constructs were extended at a constant velocity (400 nm/s) in order to investigate how the individual fragments unfold. The molecular fingerprint, first used to filter for valid traces as

discussed above, was then used to match traces to one another by aligning the sawtooth patterns of the I<sub>27</sub> domains. These aggregated overlaid traces show that the talin rod fragments unfold in a consistent manner with defined unfolding events (Figure 2a–e). For each trace, these unfolding events were then fitted to a worm-like chain model, and the unfolding length of each event was measured, with the HaloTag peak as a reference point. Histograms of these unfolding lengths demonstrate the number of discrete unfolding events and the regular intervals at which they occur (Figure 2f–j).

For R4–R6, R9–R10, and R11–R12, the number of unfolding events is the same as the number of bundles in the fragment. This indicates that each bundle has a single dissociation event that allows it to unravel. The distances between the peaks of the histograms can be analyzed to determine the length of unfolding that occurs for each event. These lengths tend to be 10–30% shorter than the theoretical fully extended length of the amino acid chain for each bundle (Supporting Information Table S1).<sup>24</sup> This indicates that either the bundles partially unravel before their main dissociation event or that, after they dissociate, they still retain some of their  $\alpha$ -helical structure.

For R1–R3, a three bundle construct, only two events were usually observed, although in several traces the anticipated three events were discernible. This apparent difference is explained by previous work on this fragment that has shown that the R3 bundle unfolds at forces as low as 5 pN, which is below the resolution of this smAFM apparatus.<sup>15</sup> As with the other fragments, the length of unfolding is less than the theoretical maximum length of the amino acid chains (Supporting Information Table S1).

The R7–R8 fragment is different to the others both in structure and in the unfolding pattern that it generates. In all traces only a single unfolding event occurs, despite the presence of two bundles. Additionally the unfolding length of  $104 \pm 7$  nm is much greater than the potential unfolded length of either individual bundle (Supporting Information Table S1). This indicates that a single dissociation event results in both bundles unravelling. This notion is supported by the structural work on this fragment which demonstrated that the R8 bundle is much weaker than the R7 and stabilized by its insertion between the third and fourth helices of R7.<sup>5</sup> It can therefore be surmised that once the R7 bundle is ruptured and begins to unravel, the instability of the R8 bundle allows it to be unravelled without a second dissociation event.

### Talin Rod Bundles Dissociate over a Range of Forces.

As well as illuminating the pattern of fragment unfolding, the force extension data can be analyzed to determine the force associated with each unfolding event. These forces were combined into histograms that demonstrate the range of forces involved (Figure 3a–e). The unfolding of all talin rod fragments seems to occur over a range of forces between 10 and 40 pN. Within that range, individual unfolding events seem to occur at specific forces, indicating that different bundles may exhibit different levels of mechanical stability (Supporting Information Table S1). This indicates that talin may consist of mechanical elements with a range of mechanical stabilities, such as has been proposed previously for fibronectin.<sup>25</sup> We therefore performed further analyses to dissect the mechanical characteristics of the talin rod components.

**SMD and AFM Analysis Reveal Hierarchy of Bundle Stability.** Constant velocity end-to-end pulling simulations at 0.1 nm/ns and 2 nm/ns revealed that all tested talin rod

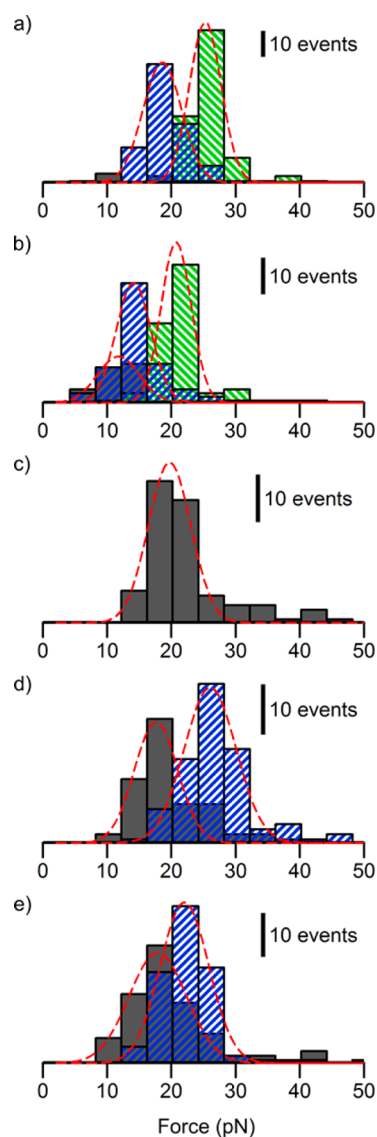


**Figure 3.** Unfolding force of talin rod fragments using smAFM. (a–e) Histograms of the unfolding force for each event. Gray bars represent the unfolding event closest to HaloTag. Blue bars, where applicable, show the next event further from HaloTag. Finally green bars show the first unfolding event, and furthest from HaloTag, for those traces exhibiting three events. Red dashed lines show Gaussian fits applied to the histograms. Forces are summarized in Supporting Information Table S1. (a) R1–R3. (b) R4–R6. (c) R7–R8. (d) R9–R10. (e) R11–R12.

domains unfold over a range of forces (Figure 4). The constant velocity simulations at 2 nm/ns allowed us to obtain a comprehensive picture of the unfolding pathway within 20 ns simulation. Three simulations were performed for each of the bundles to ensure the reproducibility of the traces obtained (Supporting Information Figure S3). Simulations at 0.1 nm/ns focused on the initial breaking of the domains over approximately 40 ns. This lower velocity pulling was used to test the method sensitivity and the impact of the velocity on the final force magnitude, rather than for a comparison of trajectories. Overall, similar patterns of unfolding force magnitude were observed for both tested velocities. The pulling rates used for these simulations were much greater than physiological, with the expectation that pulling at speeds closer

to those expected *in vivo* would result in dramatically lower forces, as revealed by the smAFM measurements.

Due to the character of the simulations, calculated unfolding forces from SMD are only relative and cannot be directly compared to the experimental unfolding forces. Despite the large differences in force magnitude, the unfolding trajectories illustrate very similar unfolding dynamics over the tested domains (Figure 5). Moreover, small differences in structural changes result in large changes in the calculated force magnitude. Hence, SMD unfolding force is used here only for pattern analysis and talin rod domain stability classification, but not for providing predictions for the absolute unfolding force. This is a similar approach to that presented in the work by Craig *et al.* concerning the stability of fibronectin Ig domains.<sup>25</sup> It is also good to keep in mind that the cellular processes may happen in the time frame of milliseconds to hours, not reachable by all-atom simulations.

Based on the relative force magnitude and unfolding trajectories, we have classified the tested talin  $\alpha$  helix bundles into three stability groups: weak, intermediate, and strong. The weak class contains the easily unfolding four-helix bundles R3 and R4. The R3 bundle contains a belt of polar residues in its hydrophobic core unique among the talin rod bundles. This polar pattern may cause R3 destabilization and unfolding under low mechanical load. Previous studies showed that replacement of the polar belt residues by hydrophobic amino acids increased the mechanical stability of R3.<sup>15,16</sup> Bundle R4 also unfolded gradually without noticeable resistance in SMD. In all three 2 nm/ns simulations, the helicity in H2 (Ala960 – Pro964) and H3 (Pro996 – Met1000) of R4 was greatly disturbed by twisting and bending. This effect was observed during pulling simulations, however the areas were not affected by the mechanical force directly. Interestingly, such proline occurrence is rather uncommon across other talin helices. Furthermore, both proline residues are highly conserved between species for both talin-1 and talin-2, as determined by multiple sequence alignment (Supporting Information Table S2). The weak class additionally contains two five-helix bundles, R6 and R10, which unfold under low force in SMD. Both R6 and R10 bundles have helix H1 considerably shorter compared to other bundle helices. This may contribute to the lower domain mechanostability. The short H1 was separated in both domains early in the simulation followed by gradual unfolding of H5 at the C terminal end. In both cases we have observed a 3-helix intermediate (H2–H4) stable between approximately 8 and 11 ns for R6 and approximately 9 and 12 ns for R10 (Figure 5). Whether this intermediate represents a functionally important state remains unclear.

The intermediate class contains domains R7, R11, and R12 with domain R7 fluctuating at the border of the soft and intermediate classes during the first 9 ns of 2 nm/ns simulation. All domains in this class consist of five-helix bundles where all the helices have similar lengths. In the R11 bundle, the highly conserved residue Met2121 in H5 (the long connecting helix between R11 and R12) was identified as a possible gatekeeper in all three simulations. Met2121 is located in the IBS2-A region<sup>26</sup> with its hydrophobic side-chain pointing toward the hydrophobic core of R11. It creates nonpolar contacts with H2 and H4 and possibly contributes to the stability of the bundle and thus maintains the IBS2-A. Similarly to unfolding trajectories of R6 and R10, we have observed possible 3-helix intermediates consisting of H2–H4 core also in R11 and R12 simulations (Figure 5).

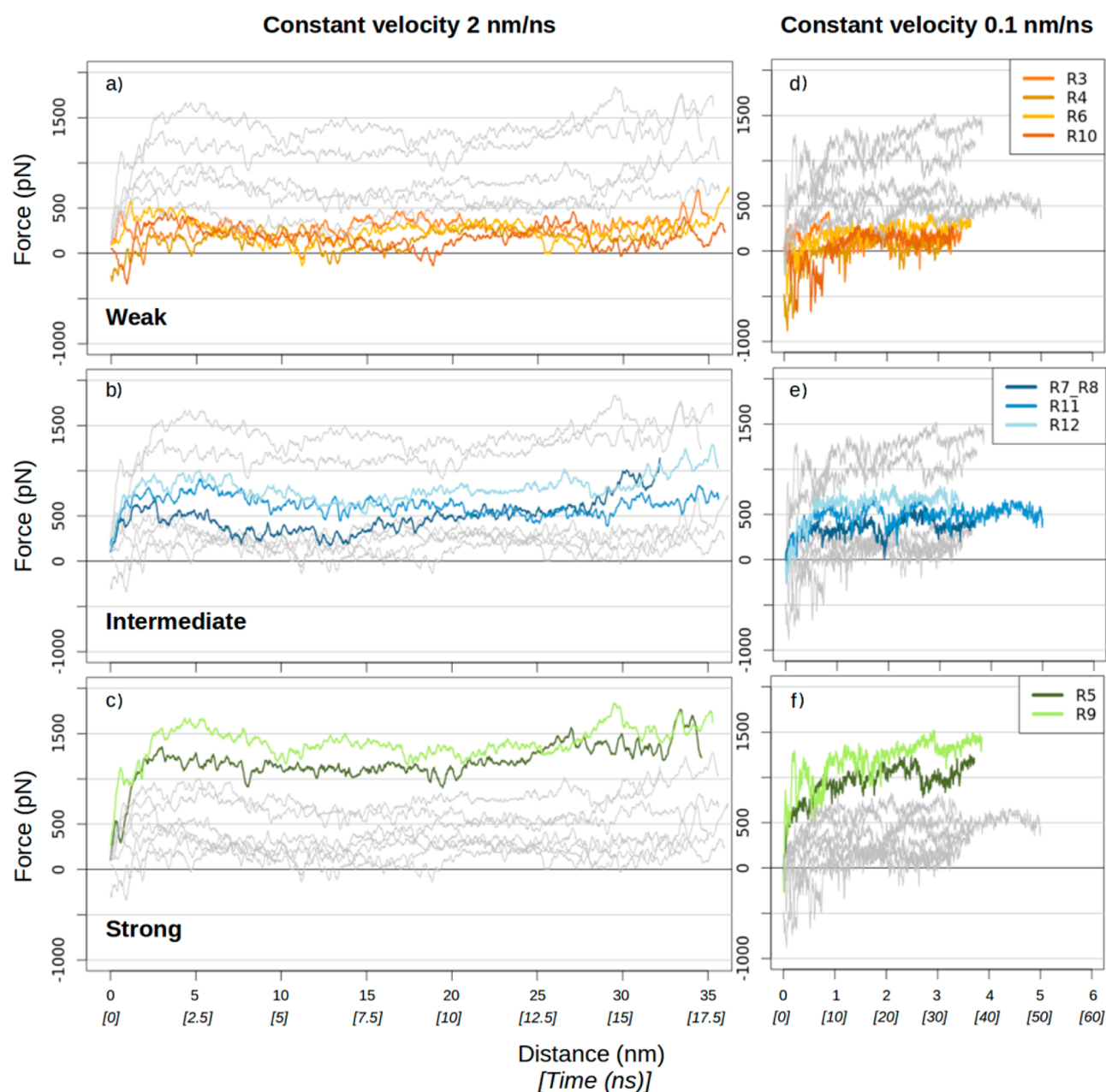


**Figure 4.** Unfolding force magnitude (pN) of talin rod domains in SMD. (a–c) Force against simulation time during constant velocity pulling at 2 nm/ns. (d–f) Force against simulation time during constant velocity pulling at 0.1 nm/ns. Gray lines visualize the force magnitude for all bundles. The tested rod domains show varying mechanical stability represented by different unfolding force magnitude. All rod domains are classified into three groups which are color highlighted in separate plots against the complete data set. (a, d) Weak class (orange) contains R3, R4, R6, and R10 bundles unfolding under maximum unfolding force 500pN; (b, e) intermediate class (blue) contains bundles R7, R11, and R12 unfolding between 500 and 1000pN; (c, f) strong class (green) with R5 and R9 bundles with unfolding force over 1000 pN. Similar classification was observed for both simulation settings at 0.1 nm/ns and 2 nm/ns velocity.

Finally, the strong group contains domains R5 and R9. Both of these two bundles are five-helix domains with similar helix lengths. Furthermore, in strong bundles, additional characteristic twisting of the helices around the bundle axis was observed in structural alignments when compared to the bundles of intermediate class. (Supporting Information Figure S2b). Greater displacement of helix ends at the bundle top and bottom was observed for R9 bundle, which also exhibits the greatest mechanical stability. On the other hand the smallest differences between the top and bottom helix positions can be seen for bundle R11 which is the softest of the presented bundles (R5, R9, R11, R12). Such specific twisting of the

bundle is likely to increase the contact areas between its helices and increase the unfolding force demand.

To further investigate the differences of the strong (R9) and intermediate (R11) bundles, we performed individual helix alignment against an ideal  $\alpha$ -helix. We observed that the helicity between the two bundles is affected. The average root-mean-square deviation (RMSD) of atomic positions of structural alignments was 1.810 Å for R9 and 1.599 Å for R11, suggesting that  $\alpha$ -helices of R9 bundles are more deformed compared to R11 helices. We identified two residues which may be important for the R9 bundle stability, namely Leu1668 in H1 and Met1803 in H5. These highly conserved residues create

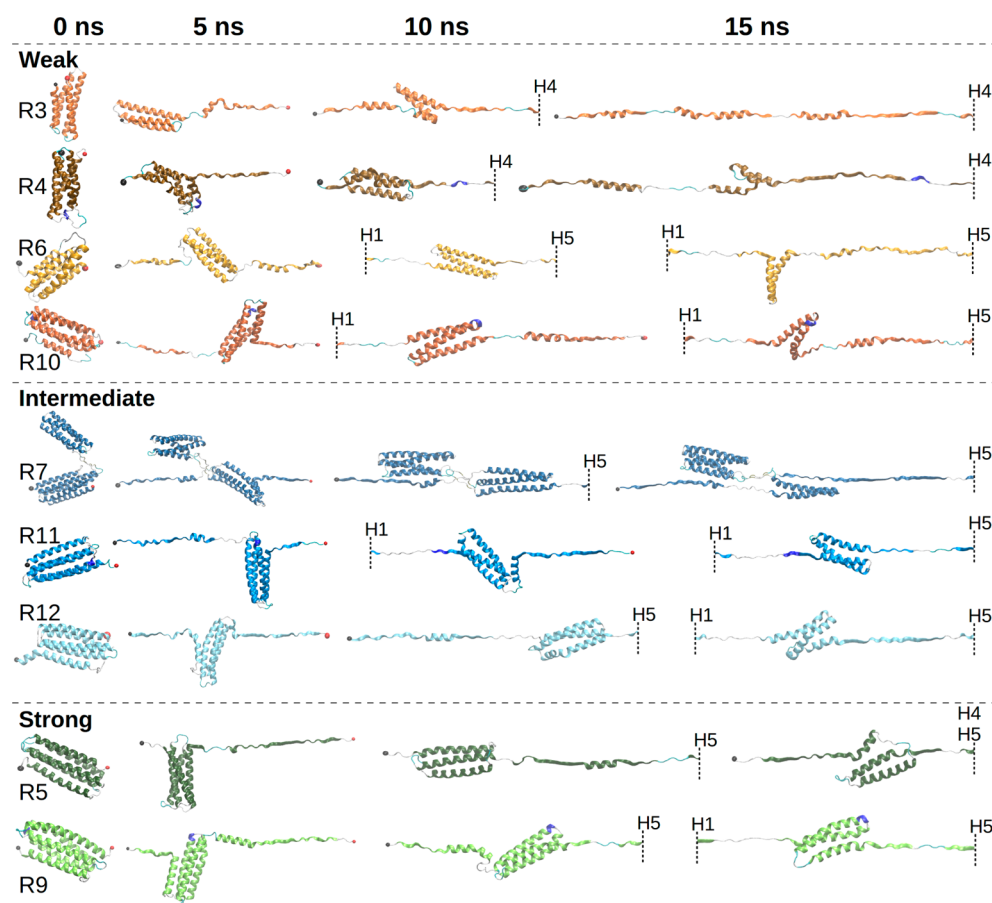


**Figure 5.** Representative structure snapshots of talin rod domains. Structure snaps were captured at 0, 5, 10, and 15 ns of the constant velocity pulling at 2 nm/ns. The three stability groups (weak, orange; intermediate, blue; strong, green) show mild yet distinct differences in the domain unfolding. Fully unfolded helices are cut away and presented by dashed line with a helix identifier.

large hydrophobic contacts with the core of R9. Furthermore, the Met1803 residue is located in close proximity to the R9–R8 interface as well as the interface between R9 and the talin head subdomain, F3, and may contribute to the stability of the autoinhibition conformation.<sup>27,28</sup>

The AFM force data support this proposed hierarchy of bundle stabilities. Based on the SMD classification, R4–R6 contain two bundles from the weak group, R4 and R6, and one strong bundle, R5. By AFM, we see two unfolding events occurring at a lower force (<20 pN) with one event at a higher force (>20 pN), well in agreement with the SMD (Figure 3b). In case of R9–R10, SMD proposes one weak bundle and one strong, and indeed, AFM demonstrates one lower force unfolding event and one with a higher force (Figure 3d). Finally, in the R11–R12 consisting of two bundles of intermediate strength according to SMD, both unfolding events seem to occur at a similar force regime (Figure 3e). Thus, there is excellent agreement between the mechanical stabilities derived from the bundle structures and those observed experimentally.

## DISCUSSION

The strong links between talin and a cell's mechanosensitivity have highlighted the need for a thorough understanding of its force response. Single-molecule studies focusing on the R1–R3 region of the rod have demonstrated the basic mechanisms of this mechanosensitivity. It has been shown that unfolding of this region can occur at forces as low as 5 pN and that this

unfolding leads to an increase in affinity for vinculin.<sup>13,15</sup> Despite the comparative lack of previous molecular investigations on the remainder of the rod, cellular studies have indicated that the regions R4–R12 may be actively involved in talin's mechanosensing. A study that measured the distance between talin's N- and C-termini showed that this length varied between 50 and 350 nm.<sup>29</sup> This increase in length would require the unfolding of more than just the R1–R3 region, as this region alone could only contribute up to 150 nm of added length. Additionally, super-resolution microscopy of focal adhesions has shown that vinculin binding occurs along the full rod, including R4–R13,<sup>30</sup> and this indicates that the cryptic VBSs of the full rod are being revealed through structural rearrangement. It is thus important to fully understand the mechanical hierarchy of the talin rod substructures in order to enable further studies to better understand the physiological and pathological role of talin.

Here we have shown that the bundles R4–R12 are vulnerable to mechanically induced structural rearrangement comparable to R1–R3. The application of force to these bundles results in characteristic unfolding events; these events are followed by extension that suggests substantial unfolding of the helical bundle structures. The unfolding of these additional bundles explains how the N–C terminal length varies in cells and also provides a mechanism by which the cryptic binding sites in these bundles become activated. Our data and techniques may be used in the future to design talin mutants of varying mechanical stability in order to evaluate the

contribution of talin-mediated mechanosensing in cellular differentiation or developmental biology processes.

In order to fully appreciate talin's role in cellular mechanotransduction, we have highlighted that force-induced structural rearrangement occurs in the whole rod domain. Crucially this occurs within a physiological force range. Recent advances in combined single-molecule cellular studies have revealed the forces acting on talin and other focal adhesion proteins. Single integrin molecules have been shown to experience forces up to 40 pN in magnitude. Additionally cells require this level of tension to be applied to integrins in early adhesion formation in order for the cells to adhere correctly.<sup>31,32</sup> When tension sensors were inserted into the talin molecule itself it was shown that the majority of talin molecules experience tension >7 pN with a proportion experiencing >10 pN.<sup>9</sup> In light of this cellular data, it is interesting that we see that all bundles in the rod unfold at forces in the 15–30 pN range, within the physiological range of forces applied to focal adhesions *in vivo*. Importantly, one may assume that the unfolding force predicted by AFM is the upper limit needed for the unfolding *in vitro*, as the retraction rate used, 400 nm/s, was higher than the accepted physiological actin retraction rate of 50–100 nm/s.<sup>33</sup> For comparison, Yao *et al.*, when using magnetic tweezers with a loading rate of 5 pN/s, found that the stronger bundles in R1–R3 unfolded at 12 pN and 20 pN, which compares to  $19 \pm 3$  pN and  $25 \pm 2$  pN for our data.<sup>15</sup> The loading or retraction rate affects the force of an unfolding event, with lower rates resulting in lower unfolding forces.<sup>34</sup> Given that our retraction rate is higher than physiological and the experiments of Yao *et al.* were conducted at the lower end or below physiological rates, it is likely that *in vivo* the unfolding forces of the talin bundles lie in the narrow range between our values.

Within this physiological range, a hierarchy of bundle stability can be observed as demonstrated by both the SMD simulations and smAFM unfolding. Stronger bundles unfold at consistently higher forces than the weaker bundles. This means that the full talin rod possesses a graduated response to force. Lower forces applied to the rod unfold only the weakest bundles, and as the force increases, first the intermediate and finally the strong bundles unfold, revealing or destroying appropriate binding sites in the unfolded domains (Figure 6).

The presence of cryptic VBSs along the rod and vinculin's importance in regulating focal adhesion pathways means that talin's graduated force response could result in a similarly graduated cellular response to force. Vinculin natively exists in an autoinhibited form where its head interacts with the tail domain. The binding of talin's VBSs with vinculin breaks this autoinhibition and thus releases the vinculin tail, which consequently interacts with actin and numerous other focal adhesion and cytoskeletal proteins.<sup>35</sup> Thus, increasing the force on talin could lead to greater unfolding of bundles, increased activation of vinculin, and therefore amplified vinculin-dependent downstream signaling.

This simple framework for mechanotransduction outlined above ignores the potential involvement of talin's additional binding partners. The bundles that we have investigated contain binding sites for numerous structural and signaling proteins including RIAM, synemin, and deleted in liver cancer 1 (DLC1). RIAM assists in targeting talin to plasma membranes, through its interaction with talin and Rap1.<sup>18</sup> DLC1 is a potent tumor suppressor protein whose action involves the down-regulation of RhoA activity and thus reduces the contractility of

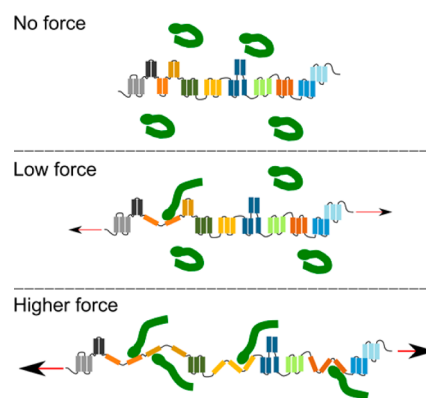


**Figure 6.** Cellular mechanotransduction as a result of graduated talin rod unfolding. Without force, the talin rod remains fully structured, and no VBSs are available. Under low-force regimes, only the very weakest bundle, R3, unfolds revealing its VBS. This activates one vinculin molecule, releasing it from its autoinhibited state. As the force applied to talin increases, more bundles are unfolded, revealing more VBSs and thus activating an increasing number of vinculin molecules. The helical bundles have been colored to reflect the mechanical hierarchy shown in Figure 4. This schematic represents a simplified version of vinculin-mediated talin mechanosensitivity. The process *in vivo* is likely to include additional binding partners and more complex modes of force application and unfolding.

cells.<sup>36</sup> The binding sites of these proteins overlap the locations of VBSs and thus are thought to compete for binding.<sup>16,20</sup> In the case of RIAM, it is expected that the bundled helical structure favors RIAM binding, whereas the disruption of the bundle leads to a greater affinity for vinculin. Thus, the influence of a range of physiological forces on talin's structure may modulate switching between favoring different binding partners to control cellular function. The binding to DLC1 and RIAM reduces contractility and increases the formation of lamellipodium,<sup>37,38</sup> whereas the presence of vinculin is a hallmark of more stable, mature adhesions. This process of mechanotransduction, through the exposure or disruption of binding sites, may be only one of the methods by which talin's behavior is controlled by force. Recent work in *Drosophila* development has shown the importance how two talin molecules are orientated with respect to each other when in its dimerized form.<sup>39</sup> Crucially, simulations have demonstrated that the orientation of the talin dimer, as dictated by its N-terminal dimerization domain, is controlled by the application of force.<sup>40</sup> Thus, the ability of talin to interpret forces and consequently direct cell behavior may be occurring on multiple levels of structure.

The current study communicates the role of  $\alpha$ -helical proteins in mechanosensing. It is worth noting that the vast majority of the previous studies focusing on mechanostability of the proteins are conducted using proteins mainly containing  $\beta$ -sheet secondary structures.  $\alpha$ -Helical proteins, however, may represent a highly important class of mechanosensing proteins.<sup>41,42</sup> Interestingly, twisting of the helical structures around the bundle axis, similar to our description for the R9 bundle, can be observed for other  $\alpha$ -helical proteins with an important role in mechanobiology. A broad variety of helical organization and degree of bundle twist can be detected over many mechanotransducers and structural proteins, such as spectrin,  $\alpha$ -actinin, or nuclear lamin. However, the role of such structural characteristics on the mechanostability is yet to be

fully determined. The unique properties of the  $\alpha$ -helices render some challenges in terms of the SMD. The helices stretch substantially upon unfolding, and the interactions between helices are dictated by entropy-mediated interactions, thus causing possible bias in the relevance of the absolute force determined. However, despite these limitations, we propose that SMD simulations are useful and reliable for the determination of relative mechanical stabilities, especially when used in conjunction with smAFM, a combination that has not been provided previously. It may be possible to further develop the SMD methodology to better serve the needs of  $\alpha$ -helical protein research, but this is out of the scope of the current study. It is also worth noting that although the separation of the rod into fragments facilitated the study of its biomechanical properties, it is possible that interactions between bundles in separate fragments may alter their stability and behavior under load. Future studies will be required to elucidate the complete picture of the unfolding of the full-length talin rod and precisely how this integrates with its role in mechanotransduction.

## CONCLUSIONS

The combination of SMD and AFM single-molecule experiments provide a valuable insight into the molecular behavior and biological mechanisms. In this study, it has revealed the range of forces over which the entire talin rod unfolds and the hierarchy of mechanical stability that the different bundles exhibit. While the contribution of these methods for biological predictions and clinical significance discovery is indisputable, it is a simplified representation of the complex biological system and does not take into account the other cellular components and the close proximity of the lipid bilayer. However, as compared to cellular experiments, the benefit is that we can exclude the contribution of other factors and thus enable better testing systems to be built using cell and animal models.

Based on the results of our study, we hypothesize that talin acts as a delicate force meter sensitive to a range of small mechanical forces. Such fine mechanosensing could control the affinity switch toward ligands triggering biochemical cascades that lead to strong surface adhesion or active spreading and locomotion. Given that the observed range of bundle stabilities depends on small structural differences, we also propose that changes in the mechanical stability of the talin rod bundles could be modulated by a small number of single-point mutations. These alterations may lead to misinterpretation of the mechanical impulse and an aberrant cellular response. Hypothetically, such false interpretation could lead into pathological changes in cell differentiation and tissue growth leading to disease development.<sup>43</sup> Work by others has shown that talin expression is vital for cell differentiation and embryogenesis.<sup>2,44</sup> The effect of mutations on talin mechanostability and cellular behavior, however, has yet to be demonstrated. In the light of this discussion, it is clear that understanding the principles and mechanisms of talin-mediated mechanotransduction may provide crucial insights into the biology in health and in disease.

## METHODS

**Generation of Polyprotein Constructs.** The talin fragment polyprotein constructs, including flanking I<sub>27</sub>, were synthesized and cloned in to pFN18a. The polyproteins were expressed in *E. coli* BL21-CodonPlus (DE3)-RILP competent cells, using the T7 promoter present in the plasmid. Protein expression was induced with IPTG

when the culture reached an OD<sub>600 nm</sub> of 0.6. Cells were lysed with lysozyme and sonication before being purified with Ni-NTA beads in a batch process. The eluted proteins were analyzed for purity with SDS-PAGE. Final concentration of protein used for experiments was 1–10  $\mu\text{g}/\text{mL}$ .

**Preparation of Ligand-Functionalized Surfaces.** Glass coverslips were functionalized with the chloroalkane ligand to HaloTag as previously described.<sup>21</sup> The glass coverslips were first cleaned using Helmanex III (1% in water), acetone, and ethanol washes. The surfaces were then prepped with O<sub>2</sub> plasma cleaning for 15 min. Surfaces were then silanized using (3-aminopropyl)trimethoxysilane, diluted to 1% in ethanol. Surfaces were then washed with ethanol and then dried with N<sub>2</sub>. These amine-functionalized surfaces were then incubated with 10 mM succinimidyl-[(*N*-maleimidopropionamido)-tetracosaeethylene glycol] ester (SMPEG24 – Thermo) diluted in 100 mM borax buffer (pH 8.5) for 1 h. The final step involved incubating the surfaces overnight with 10 mM HaloTag Thiol O4 ligand in the same buffer. The surfaces were quenched with 50 mM 2-mercaptoethanol in water.

**AFM Experiments and Analysis.** We used a commercial AFS-1 from Luigs & Neumann, GmbH, based on a device developed at the Fernandez Lab, Columbia University.<sup>22</sup> The cantilevers used were gold-coated OBL-10 levers from Bruker. The spring constants varied between 4 and 10 pN/nm as measured by equipartition theorem with the appropriate adjustments for cantilever geometry.<sup>45,46</sup> Around 20  $\mu\text{L}$  of protein solution was incubated on functionalized coverslips for 30 min prior to the experiments to allow for HaloTag binding. The cantilever was pressed into the surface with a force of  $\sim 300$  pN to bind the cantilever to the polyprotein. Force extension experiments were conducted at 400 nm/s retraction rate. Data analysis was carried out using Igor Pro (Wavemetrics), where the worm-like chain model was applied.

**SMD Simulation.** In SMD, all tested talin rod domains were analyzed for mechanical stability separately with the exception of R7. Bundle R7 was modeled together with inseparable R8 domain. The following structures from RCSB Protein Data Bank (RCSB PDB) were used for the models; R3 (id 2L7A residues 796–909), R4 (id 2LQG), R5 (id 2L7N), R6 (id 2L10), R7–R8 (id 2X0C), R9 (id 2KBB), R10 (id 2KVP), R11 (id 3DYJ residues 1975–2145), R12 (id 3DYJ residues 2131–2291). Anchors and extra sequence parts used for structure crystallization were removed from all analyzed models in PyMOL ver.1.4.1.

SMD simulations were performed using Gromacs ver 4.6.7 at the Sisu supercomputer, CSC, Finland.<sup>47,48</sup> For each model, the CHARMM27 force field and explicit TIP3P water model in 0.15 M KCL neutral solution were used. Pulling vector was set between C $\alpha$  of first and last residue of appropriate domain. Consequently each structure was oriented according to the pulling vector in *z* direction of the simulation box. Each model was minimized to 100,000 steps and equilibrated for 1 ns. The system equilibration was monitored by following the temperature, pressure, and density parameters over time. The structure equilibration was assessed by plotting the backbone RMSD value for each bundle subjected to pulling throughout the equilibration, *i.e.*, R8 was omitted from the analysis. For all bundles the RMSD reached plateau within 0.8 ns of 1 ns equilibration. All equilibration parameters were stabilized within 1 ns for all modeled structures. Simulations were performed with constant velocity pulling at 0.1 nm/ns ( $n = 1$ ) and 2 nm/ns ( $n = 3$ ). All simulations were run at NPT conditions with Berendsen thermostat and Berendsen barostat. Temperature control was set to 310 K, time constant to 0.1 ps, pressure control to 1.0 bar, and compressibility to  $4.5 \times 10^{-5}$  bar. Temperature and pressure controls were applied separately for protein and solution parts. Furthermore, equilibration was performed at isotropic conditions while pulling at semi-isotropic conditions where pressure control was turned off in the pulling direction (*z*-axis). The conditions used were validated by using extensive set of simulations. Spring constant was set to 1000 kJ/mol nm<sup>2</sup>.

Force of the spring was calculated according to  $F = k_{\text{spring}} (x_{\text{ideal } t} + x_0 - x_t)$ , where  $k$  is the spring constant,  $x_{\text{ideal } t}$  is the ideal elongation with velocity at time point,  $x_0$  is the pulling vector length at time = 0,

and  $x_t$  is the pulling vector length at time point. Resulting trajectories were analyzed with VMD ver 1.9.1 at 100 ps time window.<sup>49</sup> An average of 10 force values was presented to minimize fluctuation and eliminate noise caused by low time step (2 fs) and sampling (1000) setting for data collection and additional 5 window stride load setting in VMD analysis.

## ASSOCIATED CONTENT

### Supporting Information

The Supporting Information is available free of charge on the ACS Publications website at DOI: 10.1021/acsnano.6b01658.

A partial vector map for the polyprotein plasmids is included in Figure S1. Summaries of all smAFM unfolding lengths and forces are available in Table S1. A figure highlighting the extra twisting in certain bundles is provided in Figure S2. Further simulations for each of the bundles are included in Figure S3. The list of isoforms and species used for the multiple sequence alignment is detailed in Table S2 (PDF)

## AUTHOR INFORMATION

### Corresponding Authors

\*E-mail: [vesa.hytonen@uta.fi](mailto:vesa.hytonen@uta.fi)

\*E-mail: [a.del-rio-hernandez@imperial.ac.uk](mailto:a.del-rio-hernandez@imperial.ac.uk)

### Present Address

#Cambridge University Nanoscience Centre, University of Cambridge, CB3 0FF, Cambridge, United Kingdom

### Notes

The authors declare no competing financial interest.

## ACKNOWLEDGMENTS

This work was supported by the European Research Council (grant 282051 awarded to A.D.R.H.) and the Academy of Finland (grants 290506, 273192, 136288 awarded to V.P.H.). We acknowledge CSC, Center for Scientific Computing, Espoo, Finland for the supercomputing resources. We thank the University of Tampere for their financial support via TGPBB graduate school. We would like to acknowledge the contributions of J. Fernandez, A. Rivas-Pardo, I. Popa, and C. Badilla of the Fernandez Lab and R. Perez-Jimenez of the Nanobiomechanics Group and thank them for their insight and assistance with the smAFM and cloning experiments.

## REFERENCES

- (1) Paszek, M. J.; Zahir, N.; Johnson, K. R.; Lakins, J. N.; Rozenberg, G. I.; Gefen, A.; Reinhart-King, C. A.; Margulies, S. S.; Dembo, M.; Boettiger, D.; Hammer, D. A.; Weaver, V. M. Tensional Homeostasis and the Malignant Phenotype. *Cancer Cell* **2005**, *8*, 241–254.
- (2) Engler, A. J.; Sen, S.; Sweeney, H. L.; Discher, D. E. Matrix Elasticity Directs Stem Cell Lineage Specification. *Cell* **2006**, *126*, 677–689.
- (3) Choquet, D.; Felsenfeld, D. P.; Sheetz, M. P. Extracellular Matrix Rigidity Causes Strengthening of Integrin-Cytoskeleton Linkages. *Cell* **1997**, *88*, 39–48.
- (4) Balaban, N. Q.; Schwarz, U. S.; Riveline, D.; Goichberg, P.; Tzur, G.; Sabanay, I.; Mahalu, D.; Safran, S.; Bershadsky, A.; Addadi, L.; Geiger, B. Force and Focal Adhesion Assembly: A Close Relationship Studied Using Elastic Micropatterned Substrates. *Nat. Cell Biol.* **2001**, *3*, 466–472.
- (5) Han, S. J.; Bielawski, K. S.; Ting, L. H.; Rodriguez, M. L.; Sniadecki, N. J. Decoupling Substrate Stiffness, Spread Area, and Micropost Density: A Close Spatial Relationship between Traction Forces and Focal Adhesions. *Biophys. J.* **2012**, *103*, 640–648.
- (6) Riveline, D.; Zamir, E.; Balaban, N. Q.; Schwarz, U. S.; Ishizaki, T.; Narumiya, S.; Kam, Z.; Geiger, B.; Bershadsky, A. D. Focal Contacts as Mechanosensors: Externally Applied Local Mechanical Force Induces Growth of Focal Contacts by an Mdia1-Dependent and Rock-Independent Mechanism. *J. Cell Biol.* **2001**, *153*, 1175–1185.
- (7) Galbraith, C. G.; Yamada, K. M.; Sheetz, M. P. The Relationship between Force and Focal Complex Development. *J. Cell Biol.* **2002**, *159*, 695–705.
- (8) Kanchanawong, P.; Shtengel, G.; Pasapera, A. M.; Ramko, E. B.; Davidson, M. W.; Hess, H. F.; Waterman, C. M. Nanoscale Architecture of Integrin-Based Cell Adhesions. *Nature* **2010**, *468*, 580–U262.
- (9) Austen, K.; Ringer, P.; Mehlich, A.; Chrostek-Grashoff, A.; Kluger, C.; Klingner, C.; Sabass, B.; Zent, R.; Rief, M.; Grashoff, C. Extracellular Rigidity Sensing by Talin Isoform-Specific Mechanical Linkages. *Nat. Cell Biol.* **2015**, *17*, 1597–1606.
- (10) Theodosiou, M.; Widmaier, M.; Bottcher, R. T.; Rognoni, E.; Veelders, M.; Bharadwaj, M.; Lambacher, A.; Austen, K.; Muller, D. J.; Zent, R.; Fassler, R. Kindlin-2 Cooperates with Talin to Activate Integrins and Induces Cell Spreading by Directly Binding Paxillin. *eLife* **2016**, *5*, 24.
- (11) Jiang, G. Y.; Giannone, G.; Critchley, D. R.; Fukumoto, E.; Sheetz, M. P. Two-Piconewton Slip Bond between Fibronectin and the Cytoskeleton Depends on Talin. *Nature* **2003**, *424*, 334–337.
- (12) Hytonen, V. P.; Vogel, V. How Force Might Activate Talin's Vinculin Binding Sites: Smd Reveals a Structural Mechanism. *PLoS Comput. Biol.* **2008**, *4*, e24.
- (13) del Rio, A.; Perez-Jimenez, R.; Liu, R. C.; Roca-Cusachs, P.; Fernandez, J. M.; Sheetz, M. P. Stretching Single Talin Rod Molecules Activates Vinculin Binding. *Science* **2009**, *323*, 638–641.
- (14) Lee, S. E.; Kamm, R. D.; Mofrad, M. R. K. Force-Induced Activation of Talin and Its Possible Role in Focal Adhesion Mechanotransduction. *J. Biomech.* **2007**, *40*, 2096–2106.
- (15) Yao, M. X.; Goult, B. T.; Chen, H.; Cong, P. W.; Sheetz, M. P.; Yan, J. Mechanical Activation of Vinculin Binding to Talin Locks Talin in an Unfolded Conformation. *Sci. Rep.* **2014**, *4*, 4610 DOI: 10.1038/srep04610.
- (16) Goult, B. T.; Zacharchenko, T.; Bate, N.; Tsang, R.; Hey, F.; Gingras, A. R.; Elliott, P. R.; Roberts, G. C. K.; Ballestrin, C.; Critchley, D. R.; Barsukov, I. L. Riam and Vinculin Binding to Talin Are Mutually Exclusive and Regulate Adhesion Assembly and Turnover. *J. Biol. Chem.* **2013**, *288*, 8238–8249.
- (17) Grashoff, C.; Hoffman, B. D.; Brenner, M. D.; Zhou, R. B.; Parsons, M.; Yang, M. T.; McLean, M. A.; Sligar, S. G.; Chen, C. S.; Ha, T.; Schwartz, M. A. Measuring Mechanical Tension across Vinculin Reveals Regulation of Focal Adhesion Dynamics. *Nature* **2010**, *466*, 263–U143.
- (18) Lee, H. S.; Lim, C. J.; Puzon-McLaughlin, W.; Shattil, S. J.; Ginsberg, M. H. Riam Activates Integrins by Linking Talin to Ras Gtpase Membrane-Targeting Sequences. *J. Biol. Chem.* **2009**, *284*, 5119–5127.
- (19) Sun, N.; Critchley, D. R.; Paulin, D.; Li, Z. L.; Robson, R. M. Identification of a Repeated Domain within Mammalian Alpha-Synemin That Interacts Directly with Talin. *Exp. Cell Res.* **2008**, *314*, 1839–1849.
- (20) Li, G. R.; Du, X. L.; Vass, W. C.; Papageorge, A. G.; Lowy, D. R.; Qian, X. L. Full Activity of the Deleted in Liver Cancer 1 (Dlcl) Tumor Suppressor Depends on an Ld-Like Motif That Binds Talin and Focal Adhesion Kinase (Fak). *Proc. Natl. Acad. Sci. U. S. A.* **2011**, *108*, 17129–17134.
- (21) Popa, I.; Berkovich, R.; Alegre-Cebollada, J.; Badilla, C. L.; Rivas-Pardo, J. A.; Taniguchi, Y.; Kawakami, M.; Fernandez, J. M. Nanomechanics of Halotag Tethers. *J. Am. Chem. Soc.* **2013**, *135*, 12762–12771.
- (22) Popa, I.; Kosuri, P.; Alegre-Cebollada, J.; Garcia-Manyes, S.; Fernandez, J. M. Force Dependency of Biochemical Reactions Measured by Single-Molecule Force-Clamp Spectroscopy. *Nat. Protoc.* **2013**, *8*, 1261–1276.

- (23) Rivas-Pardo, J. A.; Alegre-Cebollada, J.; Ramirez-Sarmiento, C. A.; Fernandez, J. M.; Guixé, V. Identifying Sequential Substrate Binding at the Single-Molecule Level by Enzyme Mechanical Stabilization. *ACS Nano* **2015**, *9*, 3996–4005.
- (24) Ainaravapu, R. K.; Brujic, J.; Huang, H. H.; Wiita, A. P.; Lu, H.; Li, L. W.; Walther, K. A.; Carrion-Vazquez, M.; Li, H. B.; Fernandez, J. M. Contour Length and Refolding Rate of a Small Protein Controlled by Engineered Disulfide Bonds. *Biophys. J.* **2007**, *92*, 225–233.
- (25) Craig, D.; Gao, M.; Schulten, K.; Vogel, V. Tuning the Mechanical Stability of Fibronectin Type Iii Modules through Sequence Variations. *Structure* **2004**, *12*, 21–30.
- (26) Gingras, A. R.; Ziegler, W. H.; Bobkov, A. A.; Joyce, M. G.; Fasci, D.; Himmel, M.; Rothemund, S.; Ritter, A.; Grossmann, J. G.; Patel, B.; Bate, N.; Goult, B. T.; Emsley, J.; Barsukov, I. L.; Roberts, G. C. K.; Liddington, R. C.; Ginsberg, M. H.; Critchley, D. R. Structural Determinants of Integrin Binding to the Talin Rod. *J. Biol. Chem.* **2009**, *284*, 8866–8867.
- (27) Zhang, H.; Chang, Y.-C.; Huang, Q.; Brennan, M. L.; Wu, J. Structural and Functional Analysis of a Talin Triple-Domain Module Suggests an Alternative Talin Autoinhibitory Configuration. *Structure* **2016**, *24*, 721–729.
- (28) Goult, B. T.; Bate, N.; Anthis, N. J.; Wegener, K. L.; Gingras, A. R.; Patel, B.; Barsukov, I. L.; Campbell, I. D.; Roberts, G. C. K.; Critchley, D. R. The Structure of an Interdomain Complex That Regulates Talin Activity. *J. Biol. Chem.* **2009**, *284*, 15097–15106.
- (29) Margadant, F.; Chew, L. L.; Hu, X.; Yu, H.; Bate, N.; Zhang, X.; Sheetz, M. Mechanotransduction *in Vivo* by Repeated Talin Stretch-Relaxation Events Depends Upon Vinculin. *PLoS Biol.* **2011**, *9*, e1001223.
- (30) Liu, J. R.; Wang, Y. L.; Goh, W. I.; Goh, H.; Baird, M. A.; Ruehland, S.; Teo, S.; Bate, N.; Critchley, D. R.; Davidson, M. W.; Kanchanawong, P. Talin Determines the Nanoscale Architecture of Focal Adhesions. *Proc. Natl. Acad. Sci. U. S. A.* **2015**, *112*, E4864–E4873.
- (31) Wang, X. F.; Ha, T. Defining Single Molecular Forces Required to Activate Integrin and Notch Signaling. *Science* **2013**, *340*, 991–994.
- (32) Roein-Peikar, M.; Xu, Q.; Wang, X. F.; Ha, T. Ultrasensitivity of Cell Adhesion to the Presence of Mechanically Strong Ligands. *Phys. Rev. X* **2016**, *6*, 9.
- (33) Forscher, P.; Smith, S. J. Actions of Cytochalasins on the Organization of Actin-Filaments and Microtubules in a Neuronal Growth Cone. *J. Cell Biol.* **1988**, *107*, 1505–1516.
- (34) Merkel, R.; Nassoy, P.; Leung, A.; Ritchie, K.; Evans, E. Energy Landscapes of Receptor-Ligand Bonds Explored with Dynamic Force Spectroscopy. *Nature* **1999**, *397*, 50–53.
- (35) Carisey, A.; Tsang, R.; Greiner, A. M.; Nijenhuis, N.; Heath, N.; Nazgiewicz, A.; Kemkemer, R.; Derby, B.; Spatz, J.; Ballestrem, C. Vinculin Regulates the Recruitment and Release of Core Focal Adhesion Proteins in a Force-Dependent Manner. *Curr. Biol.* **2013**, *23*, 271–281.
- (36) Durkin, M. E.; Yuan, B. Z.; Zhou, X.; Zimonjic, D. B.; Lowy, D. R.; Thorgeirsson, S. S.; Popescu, N. C. Dlc-1: A Rho Gtpase-Activating Protein and Tumour Suppressor. *J. Cell. Mol. Med.* **2007**, *11*, 1185–1207.
- (37) Kim, T.; Vigil, D.; Der, C.; Juliano, R. Role of Dlc-1, a Tumor Suppressor Protein with Rhogap Activity, in Regulation of the Cytoskeleton and Cell Motility. *Cancer Metastasis Rev.* **2009**, *28*, 77–83.
- (38) Lee, H. S.; Anekal, P.; Lim, C. J.; Liu, C. C.; Ginsberg, M. H. Two Modes of Integrin Activation Form a Binary Molecular Switch in Adhesion Maturation. *Mol. Biol. Cell* **2013**, *24*, 1354–1362.
- (39) Klapholz, B.; Herbert, S. L.; Wellmann, J.; Johnson, R.; Parsons, M.; Brown, N. H. Alternative Mechanisms for Talin to Mediate Integrin Function. *Curr. Biol.* **2015**, *25*, 847–857.
- (40) Golji, J.; Mofrad, M. R. K. The Talin Dimer Structure Orientation Is Mechanically Regulated. *Biophys. J.* **2014**, *107*, 1802–1809.
- (41) Johnson, C. P.; Tang, H. Y.; Carag, C.; Speicher, D. W.; Discher, D. E. Forced Unfolding of Proteins within Cells. *Science* **2007**, *317*, 663–666.
- (42) Yonemura, S.; Wada, Y.; Watanabe, T.; Nagafuchi, A.; Shibata, M. Alpha-Catenin as a Tension Transducer That Induces Adherens Junction Development. *Nat. Cell Biol.* **2010**, *12*, 533–U35.
- (43) Haining, A. W. M.; Lieberthal, T. J.; del Río Hernández, A. Talin: A Mechanosensitive Molecule in Health and Disease. *FASEB J.* **2016**, *30*, 2073.
- (44) Monkley, S. J.; Kostourou, V.; Spence, L.; Petrich, B.; Coleman, S.; Ginsberg, M. H.; Pritchard, C. A.; Critchley, D. R. Endothelial cell talin1 is essential for embryonic angiogenesis. *Dev. Biol.* **2011**, *349*, 494–502.
- (45) Hutter, J. L.; Bechhoefer, J. Calibration of Atomic-Force Microscope Tips. *Rev. Sci. Instrum.* **1993**, *64*, 1868–1873.
- (46) Butt, H. J.; Jaschke, M. Calculation of Thermal Noise in Atomic-Force Microscopy. *Nanotechnology* **1995**, *6*, 1–7.
- (47) Berendsen, H. J. C.; Vanderspoel, D.; Vandrunen, R. Gromacs - a Message-Passing Parallel Molecular-Dynamics Implementation. *Comput. Phys. Commun.* **1995**, *91*, 43–56.
- (48) Lindahl, E.; Hess, B.; van der Spoel, D. Gromacs 3.0: A Package for Molecular Simulation and Trajectory Analysis. *J. Mol. Model* **2001**, *7*, 306–317.
- (49) Humphrey, W.; Dalke, A.; Schulten, K. Vmd: Visual Molecular Dynamics. *J. Mol. Graphics* **1996**, *14*, 33–38.

## Supporting Information

# All Subdomains of the Talin Rod Are Mechanically Vulnerable and May Contribute to Cellular Mechanosensing

Alexander William M. Haining<sup>†</sup>, Magdaléna von Essen<sup>‡</sup>, Simon J. Attwood<sup>†</sup>, Vesa P. Hytönen<sup>‡\*</sup>,  
Armando del Río Hernández<sup>†\*</sup>

<sup>†</sup> Cellular and Molecular Biomechanics Laboratory, Department of Bioengineering, Imperial College London, London SW7 2AZ, UK

<sup>‡</sup> BioMediTech, University of Tampere, Biokatu 6 and Fimlab Laboratories, Biokatu 4, FI-33520 Tampere, Finland

Corresponding authors:

Vesa Hytonen  
Protein Dynamics Group  
BioMediTech  
University of Tampere  
Tampere, Finland  
Telephone: +358401901517  
Email: vesa.hytonen@uta.fi

Armando del Río Hernández  
Cellular and Molecular Biomechanics Laboratory  
<http://biomechanicalregulation-lab.org/>  
Department of Bioengineering  
Imperial College London  
SW7 2AZ London  
telephone: +44(0) 20 7594 5187  
Mobile: +44(0)7407270946  
email: [a.del-rio-hernandez@imperial.ac.uk](mailto:a.del-rio-hernandez@imperial.ac.uk)

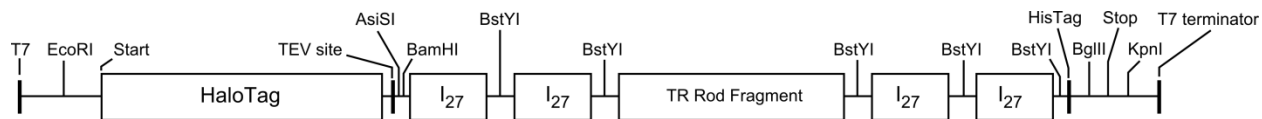


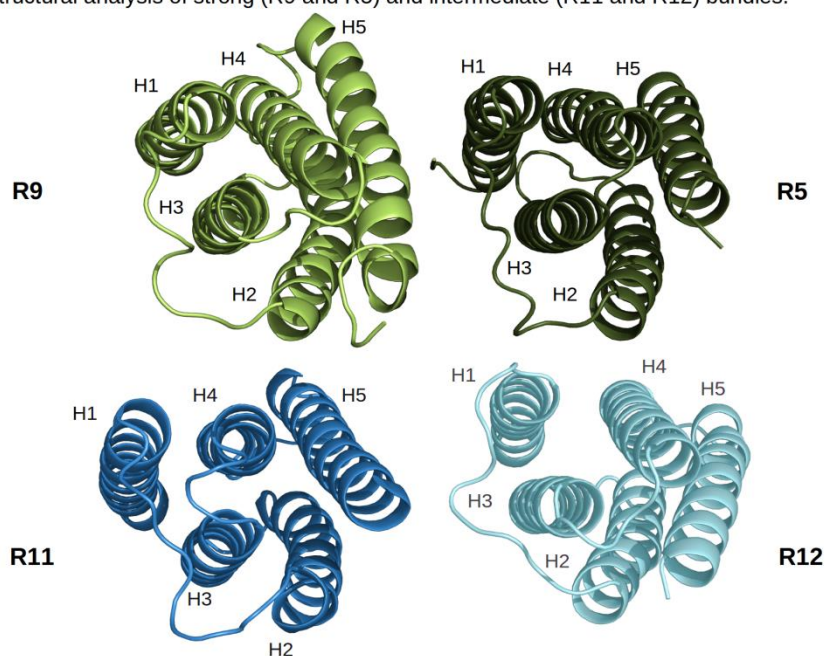
**Figure S1.** Partial vector map for polyprotein plasmids. The main features and restriction sites are shown for the T7-promoted coding region.

**Table S1. Summary of smAFM unfolding events**

		Force (pN)	Position (nm)	Position Delta (nm)	Theoretical Maximum Extension (nm)	Observed Relative Extension (%)	Number of Events
R1-R3	Peak 1	9 ± 1	118 ± 17	37 ± 28			11
	Peak 2	19 ± 3	81 ± 11	41 ± 20	161	71	90
	Peak 3	25 ± 2	40 ± 9	40 ± 9			100
R4-R6	Peak 1	11 ± 3	137 ± 10	38 ± 21			26
	Peak 2	14 ± 3	99 ± 12	55 ± 23	162	85	65
	Peak 3	21 ± 2	44 ± 11	44 ± 11			74
R7-R8	Peak 1	20 ± 3	104 ± 7	104 ± 7	115	90	82
R9-R10	Peak 1	17 ± 3	96 ± 9	42 ± 16	116	83	62
	Peak 2	26 ± 4	54 ± 6	54 ± 6			86
R11-R12	Peak 1	18 ± 4	108 ± 7	54 ± 14	121	89	78
	Peak 2	22 ± 4	54 ± 7	54 ± 7			88

Forces and positions are the mean ± standard deviation of the Gaussian fits shown in Figures 2 and 3. Positions are measured relative to HaloTag peak. Theoretical maximum extensions are calculated using the known number of amino acids and a fully-extended length of 0.4 nm per amino acid<sup>23</sup>.

a) Structural analysis of strong (R9 and R5) and intermediate (R11 and R12) bundles.



b) Helix positions at the top and bottom of strong (R9 and R5) and intermediate (R11 and R12) bundles

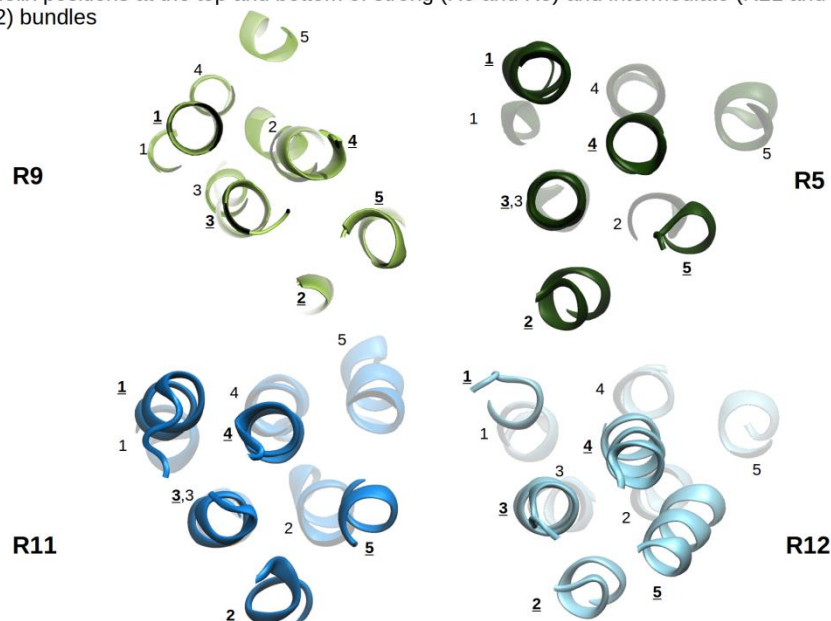


**Figure S2.** Structural analysis and bundle top-bottom helix projection. (a) Structural analysis of helix twisting around bundle axis: top view of complete bundles. R9 (*light green*), R5 (*dark green*), R11 (*dark blue*), R12 (*light blue*). Most twisted helices around the bundle axis were observed for R9 which also shows greatest mechanical stability over the tested bundles. Least twisting is presented for R11, the least stable of the four presented bundles. (b) Detail of helix positions in bundle: top view. At the top of bundle (*intensive colour and bold underlined font*) and at the bottom of the bundle (*fainted colour*). All bundles were manually oriented from top to bottom according to H3. VMD clipping planes were used to capture the helix positions at both bundle ends.

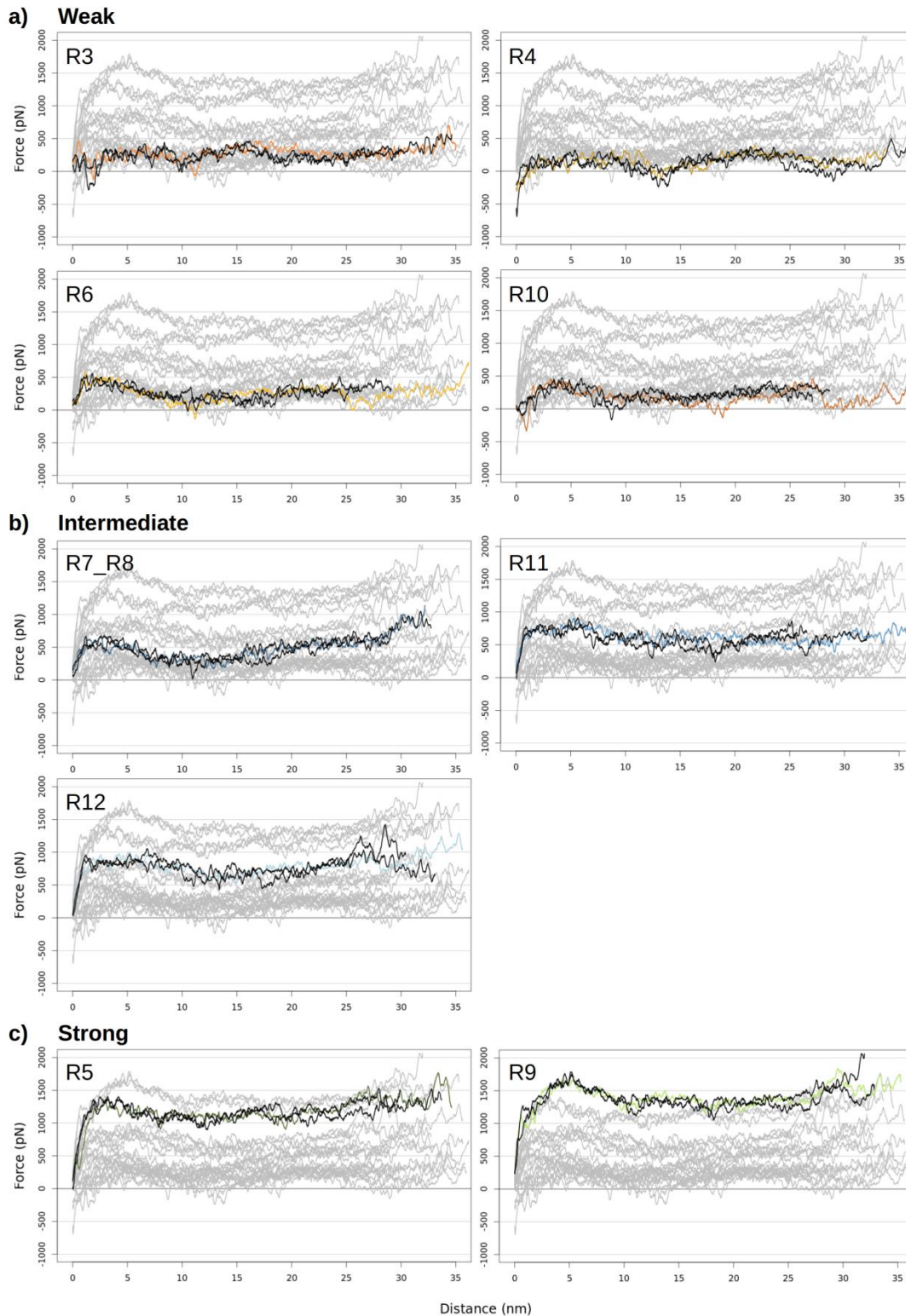


**Figure S3.** Unfolding force magnitude (pN) of talin rod domains in SMD. Force against simulation time during constant velocity pulling at 2 nm/ns in three repetitions. Grey lines visualize the force magnitude for the complete dataset. All repetitions are shown in black in separate plots for individual talin bundles. Colour highlighted is representative trajectory shown in main figure (Figure 4).

**Table S2. List proteins used for multiple sequence alignment (Clustal Omega)**

GI Number	Protein	Species
297684096	talin-1-like	Pongo abelii
397519475	talin-1	Pan paniscus
359320831	talin-1 isoform X1	Canis lupus familiaris
560923515	talin-1	Camelus ferus
27552808	Talin 1	Homo sapiens
351707040	Talin-1	Heterocephalus glaber
507549139	talin-1	Jaculus jaculus
558187984	PREDICTED: talin-1	Myotis lucifugus
194225464	talin-1 isoform X1	Equus caballus
329664158	talin-1	Bos taurus
402897016	talin-1	Papio anubis
640809509	talin-1	Tarsius syrichta
297270646	talin-1	Macaca mulatta
591299043	talin-1 isoform X2	Panthera tigris altaica
591299041	talin-1 isoform X1	Panthera tigris altaica
548477257	talin-1	Capra hircus
562827197	talin-1	Tupaia chinensis
227256	talin	
189181726	talin-1	Rattus norvegicus
354485771	talin-1 isoform X1	Cricetulus griseus
466017117	talin-1	Orcinus orca
594700180	talin-1	Balaenoptera acutorostrata scammoni
585662566	talin-1	Elephantulus edwardii
557331369	talin-1	Alligator sinensis
45383127	talin-1	Gallus gallus
57222259	talin-1	Danio rerio
632938640	talin-2	Callorhynchus milii
617453163	talin-2	Poecilia formosa
564242783	talin-2-like, partial	Alligator mississippiensis
363737914	talin-2 isoform X1	Gallus gallus
514782158	talin-2 isoform X3	Anas platyrhynchos
488558844	talin-2 isoform 1	Dasypus novemcinctus
529442107	talin-2	Falco peregrinus
465964156	Talin-2	Chelonia mydas
395502593	talin-2 isoform 1	Sarcophilus harrisii
591316418	talin-2 isoform X4	Panthera tigris altaica
586988808	talin-2 isoform X4	Felis catus
664727478	talin-2 isoform X2	Equus przewalskii
402874485	talin-2	Papio anubis

**Table S2. List proteins used for multiple sequence alignment (Clustal Omega)**

GI Number	Protein	Species
507557504	talin-2	Jaculus jaculus
21666571	talin 2	Homo sapiens
594114498	talin-2 isoform X1	Bubalus bubalis
119921718	talin-2 isoform X5	Bos taurus
560915691	talin-2	Camelus ferus
548483007	talin-2	Capra hircus
426233184	talin-2	Ovis aries
51261360	Tln2 protein	Mus musculus
602635180	talin-2	Python bivittatus
432104815	Talin-2	Myotis davidii
444730950	Talin-2	Tupaia chinensis
336391129	talin-2	Danio rerio

RESEARCH ARTICLE

# Mechanical unfolding reveals stable 3-helix intermediates in talin and $\alpha$ -catenin

Vasyl V. Mykuliak<sup>1</sup>, Alexander William M. Haining<sup>2</sup>, Magdaléna von Essen<sup>1</sup>, Armando del Río Hernández<sup>2\*</sup>, Vesa P. Hytönen<sup>1\*</sup>

**1** Faculty of Medicine and Life Sciences and BioMediTech, University of Tampere, Finland and Fimlab Laboratories, Tampere, Finland, **2** Cellular and Molecular Biomechanics Laboratory, Department of Bioengineering, Imperial College London, London, United Kingdom

These authors contributed equally to this work.

\* [a.del-rio-hernandez@imperial.ac.uk](mailto:a.del-rio-hernandez@imperial.ac.uk) (AdRH); [vesa.hytonen@uta.fi](mailto:vesa.hytonen@uta.fi) (VPH)



## Abstract

Mechanical stability is a key feature in the regulation of structural scaffolding proteins and their functions. Despite the abundance of  $\alpha$ -helical structures among the human proteome and their undisputed importance in health and disease, the fundamental principles of their behavior under mechanical load are poorly understood. Talin and  $\alpha$ -catenin are two key molecules in focal adhesions and adherens junctions, respectively. In this study, we used a combination of atomistic steered molecular dynamics (SMD) simulations, polyprotein engineering, and single-molecule atomic force microscopy (smAFM) to investigate unfolding of these proteins. SMD simulations revealed that talin rod  $\alpha$ -helix bundles as well as  $\alpha$ -catenin  $\alpha$ -helix domains unfold through stable 3-helix intermediates. While the 5-helix bundles were found to be mechanically stable, a second stable conformation corresponding to the 3-helix state was revealed. Mechanically weaker 4-helix bundles easily unfolded into a stable 3-helix conformation. The results of smAFM experiments were in agreement with the findings of the computational simulations. The disulfide clamp mutants, designed to protect the stable state, support the 3-helix intermediate model in both experimental and computational setups. As a result, multiple discrete unfolding intermediate states in the talin and  $\alpha$ -catenin unfolding pathway were discovered. Better understanding of the mechanical unfolding mechanism of  $\alpha$ -helix proteins is a key step towards comprehensive models describing the mechanoregulation of proteins.

## OPEN ACCESS

**Citation:** Mykuliak VV, Haining AWM, von Essen M, del Río Hernández A, Hytönen VP (2018) Mechanical unfolding reveals stable 3-helix intermediates in talin and  $\alpha$ -catenin. *PLoS Comput Biol* 14(4): e1006126. <https://doi.org/10.1371/journal.pcbi.1006126>

**Editor:** David van der Spoel, University of Uppsala, SWEDEN

**Received:** January 18, 2018

**Accepted:** April 6, 2018

**Published:** April 26, 2018

**Copyright:** © 2018 Mykuliak et al. This is an open access article distributed under the terms of the [Creative Commons Attribution License](https://creativecommons.org/licenses/by/4.0/), which permits unrestricted use, distribution, and reproduction in any medium, provided the original author and source are credited.

**Data Availability Statement:** All relevant data are within the paper and its Supporting Information files. The simulation data and parameter files can be downloaded via the following address: <https://etsin.avointiede.fi/dataset/urn-nbn-fi-csc-kata20180412134542867332>.

**Funding:** This work was supported by the Academy of Finland (<http://www.aka.fi/en>) grant no. 290506 to VPH. We thank European Research Council (ERC; <https://erc.europa.eu/>) grant 282051 Forceregulation. We acknowledge CSC – IT Center

## Author summary

In order to migrate and survive, most cells need to be attached to their environment. Cells anchor to the extracellular matrix via transmembrane integrin, connecting it to contractile the cytoskeleton. Similarly, cell-cell contacts are formed via transmembrane cadherin, which also connects to the contractile cytoskeleton through scaffolding proteins. Examples of such proteins include talin and  $\alpha$ -catenin, which connect integrin and cadherin respectively, to actin filaments of the cytoskeleton. Mechanical forces that are transmitted between the cell and its environment activate binding and regulate the functions of these

for Science, Finland (<https://www.csc.fi/>), for computational resources. We acknowledge EDUFI ([http://www.studyinfinland.fi/tuition\\_and\\_scholarships/cimo\\_scholarships/cimo\\_fellowships](http://www.studyinfinland.fi/tuition_and_scholarships/cimo_scholarships/cimo_fellowships)) (former CIMO) for Postdoctoral Fellowship for VVM. We thank the University of Tampere for their financial support via TGPBB graduate school ([www.uta.fi/med/en/MED\\_doctoral\\_programme.html](http://www.uta.fi/med/en/MED_doctoral_programme.html)). The funders had no role in study design, data collection and analysis, decision to publish, or preparation of the manuscript.

**Competing interests:** The authors have declared that no competing interests exist.

scaffolding proteins at cell-extracellular matrix and cell-cell contacts. Functions of talin and  $\alpha$ -catenin are tightly modulated by mechanical forces. The stretching of these proteins under mechanical load exposes buried binding sites for other partners, such as vinculin. We used steered molecular dynamics simulations and single-molecule atomic force microscopy to study how these proteins unfold under load. Our results suggest that  $\alpha$ -helical talin and  $\alpha$ -catenin unfold through stable 3-helix intermediates. These intermediates represent biologically active states, which may allow recruitment of other binding partners.

## Introduction

Protein activity can be modulated by mechanical cues in addition to chemical stimuli and ligand binding. Mechanical forces can induce conformational changes in the protein structure, that leads to either a switch between the functional states of the protein, or allows for multiple functions[1,2].

$\alpha$ -helix folds are highly abundant among the structural proteins located at the cell-cell and cell-ECM contacts [3–5], among the essential muscle costamere complexes[6], as well as among the structures interconnecting the cytoskeleton[7,8] and cellular organelles[9]. Despite the numerous studies on mechanotransduction and the mechanosensitivity of proteins, the mechanisms associated with forced protein unfolding and mechanosignaling are not well understood especially where  $\alpha$ -helical proteins are concerned. One reason for such a lack of understanding might be that  $\alpha$ -helices are, in general, mechanically weaker compared to  $\beta$ -strand folds[10] and are therefore challenging to study experimentally. The low mechanical stability of  $\alpha$ -helical proteins requires sophisticated experimental methods capable of force measurement in the range of piconewtons[11].

Among the  $\alpha$ -helical structural proteins, several distinct folds have been identified. Talin-like proteins contain 5- and 4-helix bundles[12]. Proteins of the catenin family contain a 4-helix conformation with long  $\alpha$ -helices interconnecting two bundles[13]. Both of these multi-helical protein folds respond to mechanical load by a dissociation of the bundles leading to mechanoregulatory function. The spectrin fold is formed of a 3-helix conformation with a long  $\alpha$ -helix connecting the neighboring domains, forming a rigid rod of interacting 3-helix bundles. The spectrin-like conformation accounts for structural reinforcement in the cellular scaffolds[3,4,7]. Finally, single long  $\alpha$ -helices and coils can also be found among structural  $\alpha$ -helical proteins (PDB id 5KHT).

Focal adhesions and adherens junctions are fundamental mechanosensitive structures through which cells communicate with the extracellular matrix and with their adjacent cells, respectively. The processes of focal adhesion formation and maturation are regulated by mechanical signals[14,15]. Similar to the role of focal adhesions in the cell-ECM connection, adherens junctions are essential for cell-cell contacts. Adherens junctions are associated with the cadherin super-family of transmembrane proteins, which are connected through catenin-rich protein complexes to the actin cytoskeleton. The cadherins bind to the cytoplasmic protein  $\beta$ -catenin, which in turn binds to the filamentous F-actin binding adaptor protein,  $\alpha$ -catenin[16,17].

Talin is a large focal adhesion protein that contains an N-terminal head domain, which is responsible for integrin binding. The larger talin rod domain consists of amphipathic  $\alpha$ -helices arranged into 13 four or five-helix bundles (R1–R13) and a single helix dimerization domain (DD) at the C-terminal end (Fig 1A). Talin provides a link between the ECM, via the talin head-integrin interaction, and the cytoskeleton through the binding of actin filaments at actin

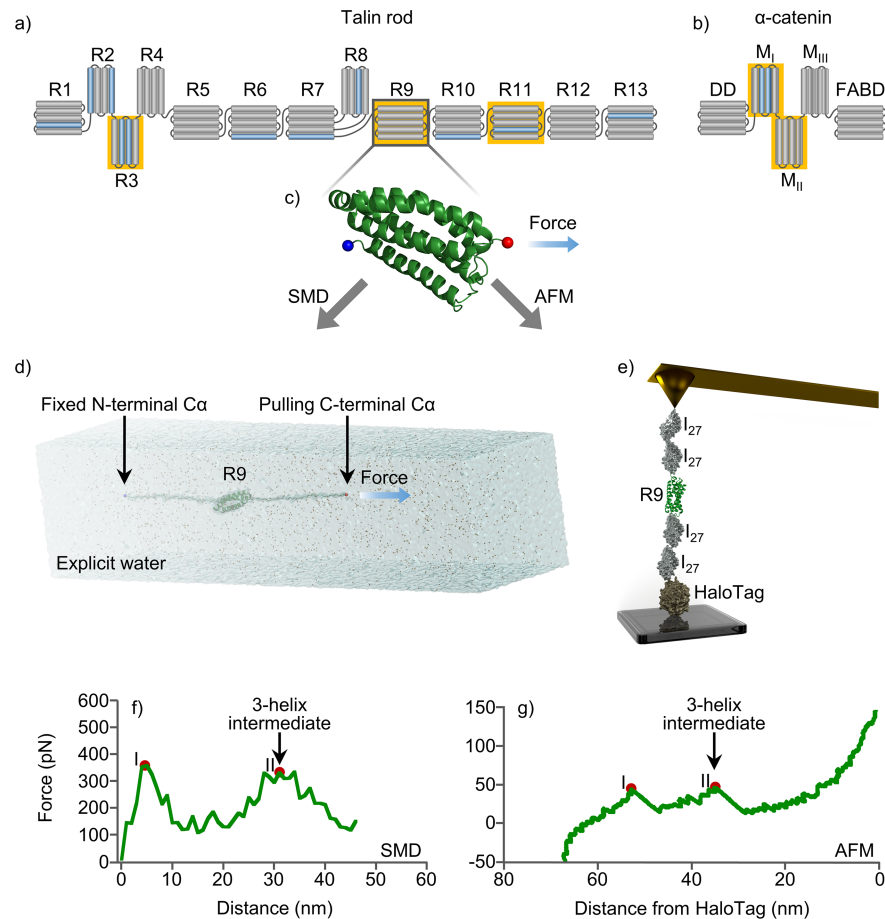


**Fig 1.  $\alpha$ -helix bundle mechanical stability.** (a) Schematic representation of talin rod bundles and (b)  $\alpha$ -catenin domains. Vinculin binding sites colored in blue. (c) Cartoon illustration of R9, where C $\alpha$  of N-terminal residue colored in blue and C $\alpha$  of C-terminal residue is red. (d) SMD water box and (e) smAFM setup, that were used for end-to-end stretching of studied proteins. Unfolding force profiles of talin rod R9 in (f) SMD and (g) smAFM experiments, where after collapsing of 5-helix bundle (peak I) the stable 3-helix intermediate was found (peak II).  $\alpha$ -helix bundles used in unfolding experiments highlighted with yellow.

<https://doi.org/10.1371/journal.pcbi.1006126.g001>

binding sites located in the rod domain. Furthermore, the talin rod comprises up to 11 buried vinculin binding sites (VBSs), distributed along its structure. These binding sites are exposed by partial or complete unfolding of different bundles [18,19] as a result of mechanical stretching. In this way mechanical load regulates talin function by exposing the buried binding sites for certain binding partners such as vinculin [20], while simultaneously, epitopes for other binding partners become inactivated. An example of such epitope inactivation would be the talin binding partner RIAM which binds only to folded talin domains [21]. Thus, conformational changes of talin under mechanical load regulate the recruitment and activation of talin-interacting proteins. Interestingly, talin dimerization is also regulated by mechanical force [22]. This property highlights talin as a key player in the transmission and sensing of mechanical signals between the extracellular matrix and cell cytoskeleton. These mechanical signals are central for a variety of cellular functions including spreading, migration, invasion and substrate sensing [23–25].

Similar to talin,  $\alpha$ -catenin recruits vinculin, providing the mechanical connection between cell-cell adhesions and the cytoskeleton.  $\alpha$ -catenin contains 5  $\alpha$ -helix domains: the

dimerization domain (DD) functioning as  $\beta$ -catenin binding domain, three modulation domains I, II and III ( $M_I$ ,  $M_{II}$  and  $M_{III}$ ), and an F-actin binding domain (FABD) (Fig 1B). Vinculin binds the  $M_I$  domain of  $\alpha$ -catenin while the two adjacent domains ( $M_{II}$  and  $M_{III}$ ) inhibit vinculin binding to  $M_I$ . It has been demonstrated that vinculin is recruited in a force-dependent manner to the cadherin/catenin complex upon force-dependent unfolding of  $\alpha$ -catenin. This process resembles the binding of vinculin to the talin rod domain upon tension-dependent unfolding. This tension-dependent unfolding is thought to be central in cell-cell adhesion mechanosensing[9,26,27].

It has been previously hypothesized that the force-dependent unfolding of the vinculin binding domains of the talin rod and the  $\alpha$ -catenin domains includes stable intermediate conformations[28–30]. However, this has never been previously studied in detail in computational simulation or in experimental setup suitable for analysis of single-molecule unfolding events.  $\alpha$ -helical proteins are associated with key physiological and pathological processes in mechanobiology[31–33]. A number of diverse diseases from heart[34] and muscle[35], diseases of bone, vascular and nervous system, or skin[36] have been associated with mechanobiology. Hence, better understanding of their unfolding characteristics will open the possibility of answering a plethora of questions in biology and medicine. In this study, we investigate the molecular mechanisms of the unfolding of two  $\alpha$ -helical proteins, talin and  $\alpha$ -catenin, on an atomistic level by a combination of steered molecular dynamics (SMD) simulations and single-molecule atomic force microscopy (smAFM).

This study elaborates in closer detail on observations made during our previous work described in Haining et al. [28]. Previously, we have concentrated on the mechanical sensitivity of the talin rod subdomains during the initial domain breaking. We have reported that the talin subdomains are similar, however not identical in their ability to withstand mechanical load. All the tested talin subdomains unfolded in AFM setup over a range of mechanical forces between 10 and 40 pN. During the SMD simulations we repeatedly observed a possible unfolding intermediate in the unfolding trajectories which we intended to investigate further. Therefore, in the light of our previous findings, we have now selected two talin subdomains on either end of the mechanical sensitivity scale for the current study; weak R3 and strong R9. Talin R9 is an exceptional subdomain responsible for talin autoinhibition while it does not contain VBS. For that reason, we have also included subdomain R11 to investigate the unfolding intermediate in the terms of VBS activation.

## Results

In order to probe the existence of stable intermediates in the unfolding trajectory of  $\alpha$ -helical mechanosensitive domains, we have selected two mechanoregulatory proteins, talin and  $\alpha$ -catenin (Fig 1). We have selected the mechanically stronger talin 5-helix bundles R9 and R11, and the mechanically weaker 4-helix bundles of talin R3 and  $\alpha$ -catenin modulation domains I to II ( $M_I$ - $M_{II}$ ).

### Constant velocity pulling simulations reveal that talin rod bundles unfold through stable 3-helix intermediates

We subjected two talin rod 5-helix bundles, R9 and R11, to end-to-end SMD stretching with constant velocity pulling simulation at 2 nm/ns. Previously, talin 5-helix bundles were more mechanically stable in our SMD simulations compared to 4-helix bundles. According to our previous study[28], R9 was one of the strongest rod bundles. Overall, unfolding of R9 and R11 showed two force peaks (Fig 2A), which correspond to breaking of the 5-helix bundle and 3-helix intermediate. This unfolding intermediate consists of core helices (H2–H4) after the

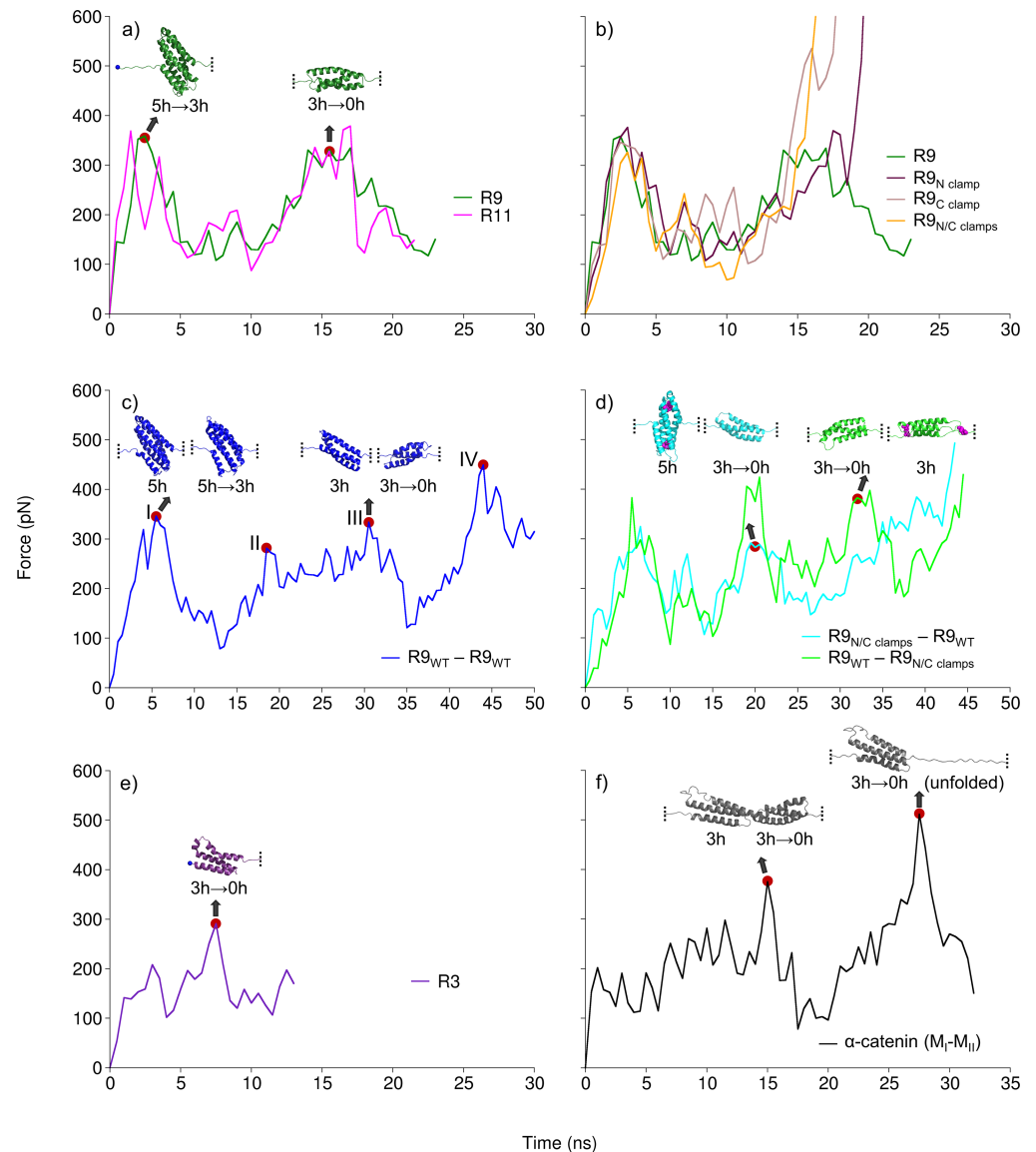


**Fig 2. Unfolding force profiles of the studied protein constructs in constant velocity SMD.** (a) Unfolding forces for 5-helix talin rod R9 and R11 have similar profiles and show two peaks, which correspond to breaking of 5-helix and 3-helix state respectively. (b) R9 constructs with disulphide clamps have similar force profiles to wild-type R9, but unfolding of 3-helix state was blocked. Tandem constructs for (c & d) R9 and (f)  $\alpha$ -catenin ( $M_I$ - $M_{II}$ ) were unfolded through 3-helix state for both monomers simultaneously. (c) R9 (wt)-R9 (wt) tandem showed four peaks, corresponding to breaking of the 5h & 5h $\rightarrow$ 3h (peak I), 5h $\rightarrow$ 3h & 3h (peak II), 3h & 3h $\rightarrow$ 0h (peak III), and 3h $\rightarrow$ 0h (peak IV) respectively. (d) Tandems with the clamped 3-helix state in one monomer showed three peaks, lacking the peak for unfolding of the clamped 3-helix state. (e) Unfolding force for 4-helix R3 bundle has one peak that corresponds to collapsing of 3-helix state. (f) 4-helix  $\alpha$ -catenin showed one peak for breaking the 3-helix state in each domain. Cysteine residues in (d) R9 tandems, that form disulphide clamps shown as magenta spheres. Structure snapshots correspond to force peaks highlighted with red dots.

<https://doi.org/10.1371/journal.pcbi.1006126.g002>

dissociation of H1 and H5. For R9 the maximum unfolding forces detected in constant velocity pulling simulation at 2 nm/ns were  $348 \pm 24$  pN and  $349 \pm 39$  pN (average force  $\pm$  standard deviation). Unfolding peak forces for R11 were very similar to those for R9 (Fig 2A). Representative snapshots of the unfolding trajectories are shown in Fig 3, indicating changing of the bundle conformation during unfolding.

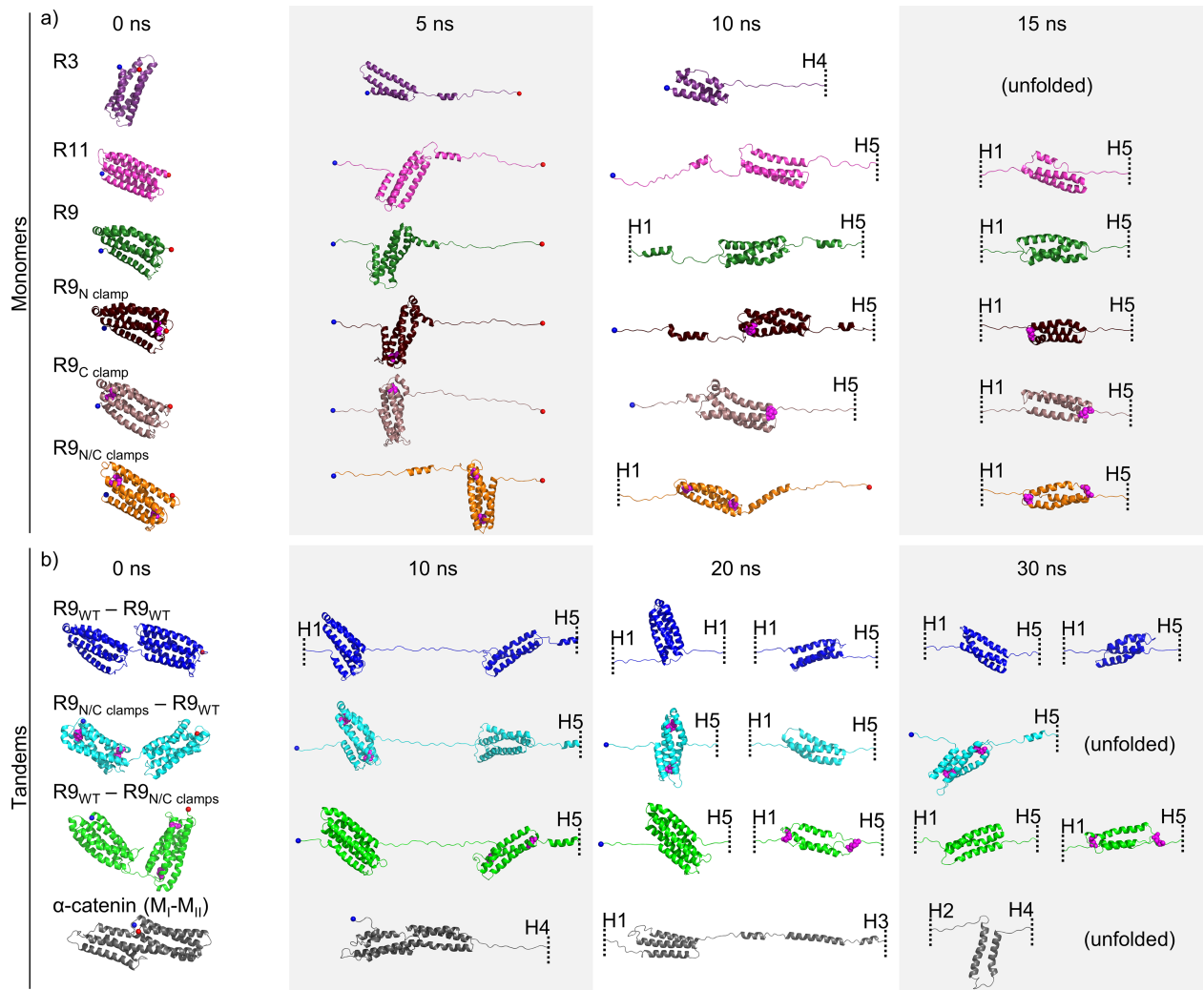


**Fig 3. Representative structure snapshots from SMD.** Talin rod domain bundles and  $\alpha$ -catenin ( $M_I$ - $M_{II}$ ) in constant velocity SMD simulations. Structures were taken (a) at 0, 5, 10 and 15 ns for monomers, and (b) at 0, 10, 20 and 30 ns for tandem constructs. Cysteine residues forming the disulphide clamps shown as magenta spheres. Unfolded structures are cut away and presented by dashed line with a helix identifier.

<https://doi.org/10.1371/journal.pcbi.1006126.g003>

To confirm the unfolding intermediate, we designed point mutations in the R9 bundle forming disulfide bonds (clamps) in order to block the unfolding of the 3-helix core. These clamped R9 mutants were subjected to end-to-end pulling in simulation and experimental setup. We prepared three constructs including L1698C and A1748C cysteine mutations that protect 3-helix core from N-terminus (N clamp), A1720C and A1779C mutations that prevent unfolding of the 3-helix core from C-terminus (C clamp), and R9 construct with both N- and C-terminal disulfide clamps (N/C clamps) (S1 Fig). All R9 clamp mutants showed very similar unfolding of 5-helix state compared to the wild-type R9 (Fig 2B). The unfolding of the 3-helix state was effectively blocked in the R9 equipped with N/C clamps, while the constructs with only one disulfide clamp allowed unfolding of either H2 (R9 with C clamp) or H4 (R9 with N clamp) of the 3-helix core, but did not compromise the stability of the 3-helix intermediate (Fig 2B).

In additional experiments, we investigated talin R3 bundle and  $\alpha$ -catenin modulation domains I to II ( $M_I$ - $M_{II}$ ), which are all 4-helix bundles. Talin R3 was easily unfolded to the 3-helix state by the separation of H4. The 3-helix intermediate (H1-H3) was more stable

compared to the 4-helix bundle, the unfolding peak force for breaking the R3 3-helix state was  $276 \pm 20$  pN (Fig 2E). Similarly,  $\alpha$ -catenin was unfolded to 3-helix conformation by dissociation of H4 (four out of five simulations) in  $M_{II}$  and H1 in  $M_I$  (all five simulations). Further unfolding showed two force peaks for breaking the 3-helix state in  $M_{II}$  (at  $349 \pm 33$  pN) and  $M_I$  (at  $461 \pm 68$  pN) (Fig 2F). Collectively these data suggest that both 4- and 5-helix bundles unfold through stable 3-helix intermediate state. Furthermore, 5-helix bundles withstand mechanical load better than 4-helix domains, which are easily unfolded to the 3-helix state.

Described constant velocity SMD simulations of individual talin rod bundles and  $\alpha$ -catenin were run five times each. Unfolding force profiles showed that our results are well reproducible (S2 Fig) and allowed us to calculate average peak force and a standard deviation (S1 Table).

### Talin tandem domain experiments confirm the existence of 3-helix intermediates

To assess the effects of force penetration on the unfolding mechanisms in SMD simulations, we studied the unfolding mechanisms and the existence of the stable intermediates in linear protein chain consisting of two talin R9 monomers resembling the natural biological assembly of talin. We designed tandem construct possessing exactly the same mechanical stability, i.e. two talin R9 domains (R9<sub>WT</sub>-R9<sub>WT</sub> tandem). Furthermore, we analyzed the R9 tandems with disulfide clamps, protecting the 3-helix core from unfolding, in either first or second monomer, with respect to the fixed N-terminal and pulled C-terminal end. Thus, we prepared two tandem constructs with clamps, R9<sub>N/C clamps</sub>-R9<sub>WT</sub> and R9<sub>WT</sub>-R9<sub>N/C clamps</sub>, respectively. For R9<sub>WT</sub>-R9<sub>WT</sub> tandem, unfolding force showed four peaks, corresponding to the breaking of 5-helix states first, followed by dissociation of the 3-helix states in both  $\alpha$ -helix bundles (Fig 2C). Because the pulling was applied to C $\alpha$  atom of C-terminal residue, the second R9 in the tandem was closest to the point of pulling and unfolded to 3-helix state first. Both monomers of the R9<sub>WT</sub>-R9<sub>WT</sub> tandem unfolded to the 3-helix intermediate within approx. 30 ns of the SMD simulation with 2 nm/ns pulling velocity, and unfolded at approx. 50 ns. Both tandems containing one clamped monomer showed three unfolding force peaks (Fig 2D) lacking the peak corresponding to the breaking of the disulfide-clamped 3-helix structure. Indeed, the force penetration did affect the two different tandems with clamps resulting in different unfolding trajectories. For R9<sub>WT</sub>-R9<sub>N/C clamps</sub> tandem, both monomers had 3-helix conformations at  $\sim 30$  ns, while for R9<sub>N/C clamps</sub>-R9<sub>WT</sub>, closest to the point of pulling monomer (R9<sub>WT</sub>) unfolded completely before R9<sub>N/C clamps</sub> molecule unfolded to 3-helix state (Fig 2D, Fig 3).

The investigation of the unfolding of a tandem provided us with a tool of studying the unfolding principles of multiple domains. Furthermore, the use of disulfide clamps in the tandem construct protecting the stable state provided us with a comparison force trace and additional proof of an intermediate unfolding conformation in both mechanosensitive proteins. Altogether, these findings indicate that the unfolding force required for the unfolding of the 3-helix intermediate state is similar to that needed for the unfolding of 5-helix state.

### smAFM analysis of $\alpha$ -helical bundles confirms unfolding through intermediate states consistent with 3-helix pattern shown by SMD

We utilized smAFM to characterize the unfolding patterns of R9 and R11 constructs and captured the 3-helix intermediate (Fig 4). Similarly to the SMD, we detected two unfolding events for each of the bundles, implying that unfolding occurs through a mechanically stable intermediate. Overall the bundle stability was higher in the case of R9 than R11, consistent with our previous results[28]. The distance between the two unfolding events is 20–25 nm, which is consistent with the collapse from 5 helices to 3 helices. Likewise, the distance from the second

unfolding event to the HaloTag ruler of 25–35 nm is consistent with the subsequent collapse of the 3-helix intermediate. As such the smAFM data supports the picture derived from the SMD analysis: 5-helix bundles collapse via a stable 3-helix intermediate.

We also tested the R9 tandem construct to examine if the 3-helix intermediate could be detectable within a model of a polyprotein (Fig 5A–5D). We detected 4 unfolding events, consistent with a pattern of two bundles unfolding via a stable intermediate. The distances between the first and second event (~20 nm), second and third (~30 nm), third and fourth (~20 nm) and fourth and HaloTag (~30 nm) imply that, contrary to the SMD results, one  $\alpha$ -helix bundle collapsed completely through a 3-helix intermediate before the second  $\alpha$ -helix domain started unfolding. However, it is difficult to be certain, given the error margin of the peak locations and the likely stochastic nature of the unfolding process. When the 3-helix disulfide clamp was introduced into one of the tandem R9 domains, we saw a reduction in the number of unfolding events from 4 to 3 (Fig 5E–5H). This, along with the reduction of the overall unfolding length from 105 nm to 85 nm, demonstrates that the disulfide clamping was able to protect the 3-helix intermediate of the R9 from mechanical unfolding.

The forced unfolding of  $\alpha$ -catenin modulation domains I to II ( $M_I$ – $M_{II}$ ) by AFM produced a pattern consistent with the SMD simulation (Fig 5I–5L). We detected two unfolding events with a maximum unfolding length of ~50 nm which implies that there is no unfolding event with respect to the reduction of both 4-helix bundles into 3-helix states. This is in agreement with herein presented SMD data and with our previous work reporting on the lower mechanical stability of the 4-helix bundles[28]. The two events observed with unfolding lengths of ~25 nm correspond to the mechanical unfolding of 3-helix intermediate states.

### Constant force SMD confirms the existence of 3-helix intermediates in talin rod R3 and R9

For the comparison of the 3-helix state mechanical stability we selected two mechanically diverse talin rod bundles, i.e. the mechanically weaker R3 and the mechanically stronger R9

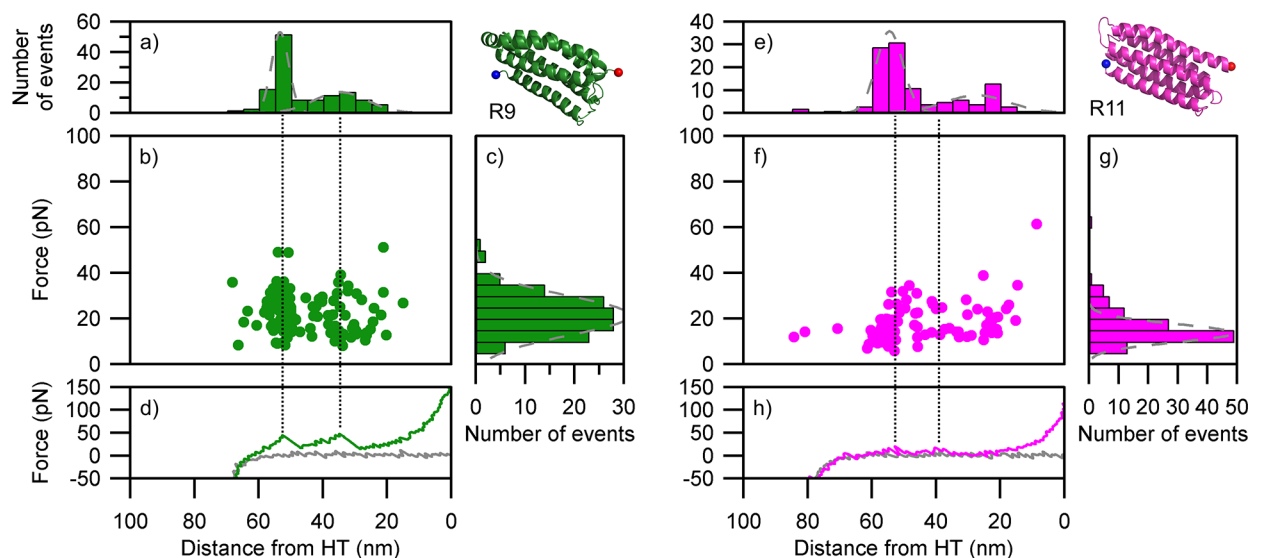


**Fig 4. Unfolding patterns of the  $\alpha$ -helix monomers as determined by smAFM.** (a–d) R9 (87 traces). (e–h) R11 (79 traces). (a & e) length histogram indicating the distance from unfolding event to HaloTag standard; (b & f) scatter plot showing force vs position for all unfolding events; (c & g) histogram the force associated with unfolding events; (d & h) representative force extension retraction curve (green & magenta line) showing how the unfolding events relate to scatter plot and length histogram (black dotted line), gray line represents approach curve for AFM tip. Gray dotted lines on (c & g) histograms represent Gaussian fits.

<https://doi.org/10.1371/journal.pcbi.1006126.g004>

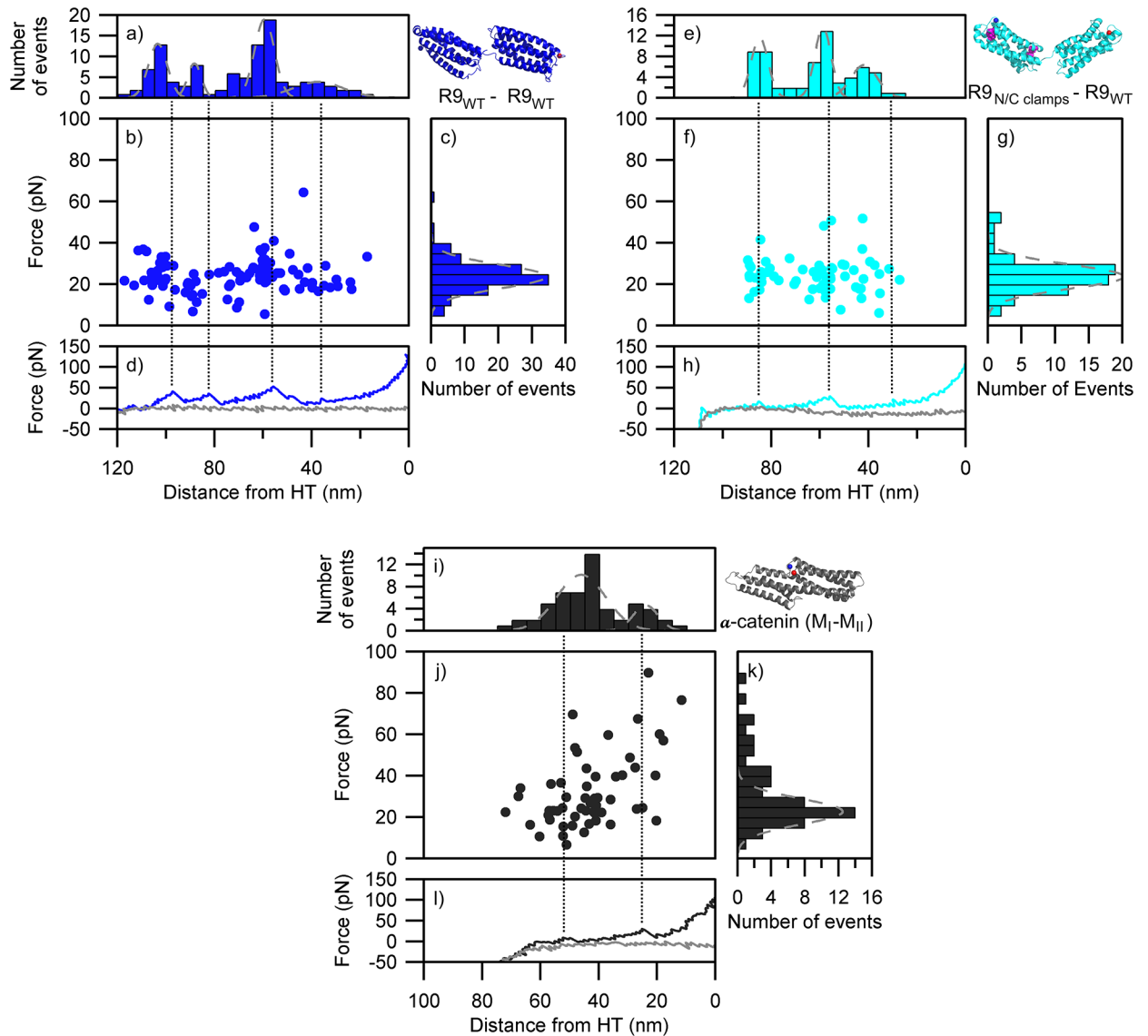


**Fig 5. Unfolding patterns of tandem  $\alpha$ -helical bundles as determined by smAFM.** (a-d) Talin R9 (wt)-R9 (wt) (47 traces). (e-h) R9 (N/C-clamps)-R9 (wt) (34 traces). (i-l)  $\alpha$ -catenin (M<sub>I</sub>-M<sub>II</sub>) (40 traces). (a, e & i) length histogram indicating the distance from unfolding event to HaloTag standard; (b, f & j) scatter plot showing force vs position for all unfolding events; histogram the force associated with unfolding events; (d, h & l) representative force extension retraction curve (blue, cyan & black line) showing how the unfolding events relate to scatter plot and length histogram (black dotted line), gray line represents approach curve for AFM tip. Gray dotted lines on (c, g & k) histograms represent Gaussian fits.

<https://doi.org/10.1371/journal.pcbi.1006126.g005>

for more detailed analysis. Although constant velocity SMD simulations are an excellent tool comparing the results with AFM analysis, they are less sensitive for the assessment of intermediate states as compared to constant force simulations. Therefore, we subjected the R3 and R9 bundles to constant force pulling simulations where, after screening of suitable force regime, constant force ranging from 160 pN to 200 pN for R3, and from 200 pN to 300 pN for R9 (Fig 6) was used. In constant force SMD, 4-helix R3 was weak even at 160 pN and rapidly unfolded to 3-helix state (within  $\sim 3$  ns). After the separation of H4, H3 was slowly sliding relative to H1 and H2 (from  $\sim 3$  ns to  $\sim 23$  ns). The 3-helix intermediate did not unfold at 160 pN in 40 ns time window (Fig 6A), however, it unfolded completely (at  $\sim 72$  ns) in extended 160 pN simulation (S3A Fig). R3 was extended also with constant force at 170 pN, 180 pN and 200 pN.

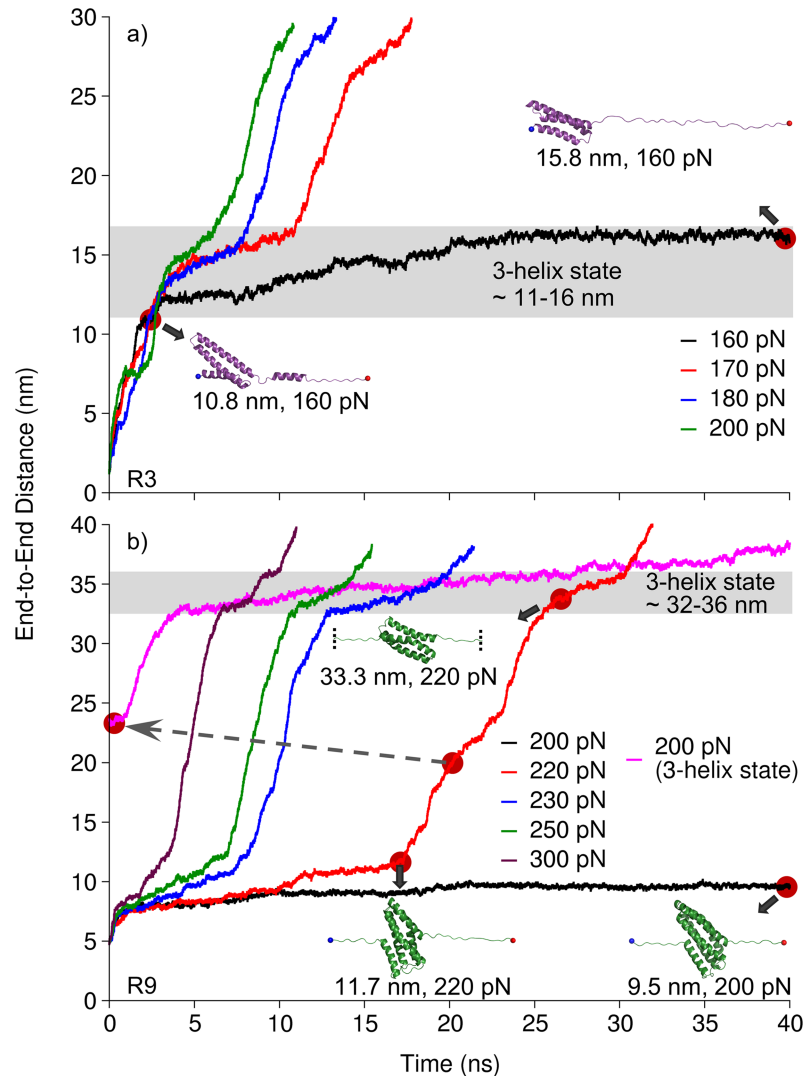


**Fig 6. Stability of the intermediate states.** Talin rod (a) R3 and (b) R9 over time in constant force SMD using constant force pulling at different force regimes. R9 is a strong 5-helix bundle, while stable 3-helix intermediates were observed in both R3 and R9 (gray shading). The pink trace in panel (b) corresponds to end-to-end distance measured under 200 pN applied force, where 220 pN simulation was used as a starting structure after passing the 5h to 3h transition (dashed gray arrow).

<https://doi.org/10.1371/journal.pcbi.1006126.g006>

Although it was completely unfolded after  $\sim 18$  ns,  $\sim 13$  ns and  $\sim 11$  ns respectively, the stable 3-helix intermediate was observed in all trajectories (Fig 6). For strong R9 bundle, we first applied constant force of 200 pN and observed only partial uncoiling of terminal helices (H1 and H5) within 40 ns time window (Fig 6B), yet the 5-helix state remained intact. However, R9 unfolded to the 3-helix state (at  $\sim 86$  ns) in extended 200 pN simulation (S3B Fig). The application of constant force of 220 pN or higher resulted in gradual unfolding of the bundle. During the unfolding, we recognized two stable states (5-helix and 3-helix states). In order to compare mechanical stability of 5- and 3-helix states, we used the disrupted 5-helix state of R9 and subjected it to stretching with constant force of 200 pN. Although 3-helix intermediate was relatively stable, it slowly unfolded over time under 200 pN while 5-helix bundle resisted the unfolding under the same force magnitude.

These results suggest that 3-helix state in R9 is a stable conformation. However, it is weaker as compared to the 5-helix state of R9. In more detail, the 3-helix state can be unfolded under lower force load once the 5-helix state of the R9 bundle is broken. On the other hand, the 3-helix intermediate state in R3 is the most stable conformation of the R3 bundle.

## Discussion

Numerous studies concerning  $\alpha$ -helical mechanosensitive proteins have provided information on mechanically regulated switches between diverse binding partners and their associated functions. Perhaps one of the best known examples of this mechanoregulated protein-protein interaction is the tandem talin-vinculin, where mechanical stress applied to talin rod exposes binding sites for vinculin[37,38].

Our observation of SMD trajectories for talin multidomain constructs, described in our previous work[28], revealed a possible stable 3-helix intermediate during the forced domain unfolding. Because of the complexity of the SMD and smAFM data we obtained during the multidomain construct unfolding, we were not able to identify previously the 3-helix intermediate among the force traces directly. However, simultaneous domain unfolding was recognized for bundles of similar mechanostability in smAFM[28].

In this study, we investigated the detailed unfolding mechanisms of  $\alpha$ -helical talin rod bundles and  $\alpha$ -catenin  $M_I$ - $M_{II}$  domains to probe the presence of any intermediate or partial unfolded states. Our results show that the two studied proteins unfold through a stable 3-helix intermediate. Constant velocity pulling used in SMD and smAFM revealed, that the unfolding force profiles for the 5-helix rod bundles R9 and R11 have two peaks, which correspond to the breaking of the 5- and 3-helix states (Fig 2A). The talin 4-helix bundle R3 and  $\alpha$ -catenin bundles  $M_I$ - $M_{II}$  also unfolded through stable 3-helix intermediates (Fig 2E and 2F). In addition, this 3-helix state was recognized as the most mechanically stable conformation for the 4-helix domains (Fig 6A).

Other studies have also provided indirect evidence of unfolding intermediates in alpha helical proteins. Investigations of the talin R3 subdomain have revealed a possible 3-helix intermediate capable of rapid or instant activation for vinculin binding. Specifically, the deletion of helix 4 of rod subdomain R3 ( $\Delta$ R3H4) leads to super-active R3 localizing efficiently in cell-ECM contacts (S6 Fig). Rahikainen et al., 2017[23] showed that one or two destabilizing mutations in R3 H1 were sufficient to facilitate bundle unfolding, increasing the activation of vinculin binding and resulting in a strong cellular phenotype. The phenotype of the further destabilized state modified with four mutations was comparable to the super-active R3 potentially indicating a 3-helix intermediate. Further evidence of a 3-helix state in R3 domain is found in a recent study by Baxter et al. [39]. A 3-helix open state has been recognized after the dissociation of H1 from the R3 bundle under high pressure conditions. Similar effects were observed even for the talin R1 bundle, where the deletion of H5 resulted in the exposure of the VBS located in H4 and an active conformation of R1[40]. The authors also suggest that the deletion of H5, resulting in a 4-helix partial bundle, causes a destabilization of the R1 domain leading to partial unfolding. This observation is in line with our results; we showed that the 4-helix fold is a fragile conformation which does not require excessive mechanical force to unfold to a stable 3-helix state (Fig 2E). Finally, even previous computational studies suggested that only partial unfolding of talin subdomains described by minimal protein extension is sufficient for VBS activation. In more detail, R1 VBS was activated through torsional conformational change of the hydrophobic core orientation within R1 subdomain during an extension of less than 2 Å [41].

Inspection of the molecular characteristics of 5- (4- in R3) and 3-helix states did not reveal any dominant differences between these assemblies in terms of interactions or packing. The

hydrophobic interactions appear to be the main factor in maintaining both these states, as shown in S4 Fig. In the previous study[28], we proposed two conserved residues that are important for maintaining R9 5-helix bundle stability, namely Leu1668 in H1 and Met1803 in H5. Further studies including experimental investigation of subdomains carrying mutations targeting the 3-helix core fragment would be needed to evaluate the contributions of individual residues for the mechanical stability of the 3-helix intermediate state.

Further unfolding of the 3-helix intermediate was observed in our experimental and simulation setup. Whether the complete unfolding of an  $\alpha$ -helical domain takes place *in vivo*, or whether the 3-helix state is the final unfolding conformation remains unclear. Hints of both of these options can be found in the literature. As discussed earlier[40], S6 Fig, the deletion of terminal helix in R1 and R3 is sufficient for VBS activation and vinculin recruitment. Thus, we speculate that the 3-helix state is capable of vinculin binding. Vinculin binding to unfolded talin or  $\alpha$ -catenin domains inhibits domain refolding under low mechanical load[20,27,42]. Simultaneously, vinculin binding to the 3-helix state bundle may protect it from complete unfolding[43]. Studies by Margadant et al.[43] show that the maximal length of talin is approx. 400 nm in living cells. This also supports the notion of partial unfolding even in the absence of vinculin. Interestingly, recently published work by Ringer et al.[11] revealed a force gradient across the talin rod domain. In the presence of vinculin, greater force was measured at the N-terminal end than at the C terminal end resulting in the bundle unfolding and activation for vinculin binding. As vinculin binds to activated talin and to actin, the force acting on the talin rod is divided and reduced towards the C-terminal end. We speculate that the reduced force might be insufficient to unfold the stable 5-helix subdomains located at the C-terminal end of the talin rod. However, here we showed that the intermediate resulting from 4-helix unfolding was mechanically weaker compared to the intermediate of a 5-helix bundle. Thus, the complete unfolding of 4-helix bundles at the N-terminal end of the talin rod may be possible. Based on the work by Yao et al., we may assume that complete yet reversible unfolding of R3 domain takes place under low force load. It was shown that under 4.8 pN of constant force load exerted on the full length talin, R3 occupies two distinct conformations with elongation of approx. 19 nm. However, which states these in fact are remains unclear [44]. We may hypothesize that only the end-to-end attachment to the pulling device and initial elongation under low force load is sufficient to collapse R3 into an activated 3-helix state. Such immediate conformational change would not necessarily result into an observable difference in the total end-to-end elongation compared to the R3 conformation in solution (S5 Fig) [41]. Similar elongation of approx. 19 nm between the 3-helix intermediate and the completely unfolded state was shown in our SMD results (Fig 6A). Here we also see that the 3-helix intermediate remained stable even though the end-to-end distance increased by 5 nm. This distance increase was caused by the uncoiling of H4.

Based on our observations of the talin unfolding mechanisms, we propose a model of multi-domain  $\alpha$ -helical protein unfolding under mechanical load, shown in Fig 7. In the absence of mechanical force,  $\alpha$ -helical bundles remain in a folded conformation, capable of binding their ligands such as RIAM (R2, R3, R8 and R11) and DLC1 (R8) in the case of talin[45]. At low mechanical load, soft  $\alpha$ -helix bundles, namely 4-helix domains, unfold to stable 3-helix intermediates. Since the activation of vinculin binding sites (VBSs) requires the unfolding of talin bundles[14], the formation of 3-helix states suggests that VBSs located at the terminal helices become available for vinculin. At the same time, the partial unfolding of the bundles leads to a disturbance of the binding sites for other binding partners located on the bundle surface, which abrogates their interaction[21]. With increasing force, additional bundles collapse to a 3-helix conformation switching from the mechanoregulatory role to a structural reinforcement role, similar to that of spectrin. In other words, it is possible that talin reacts to a range of small

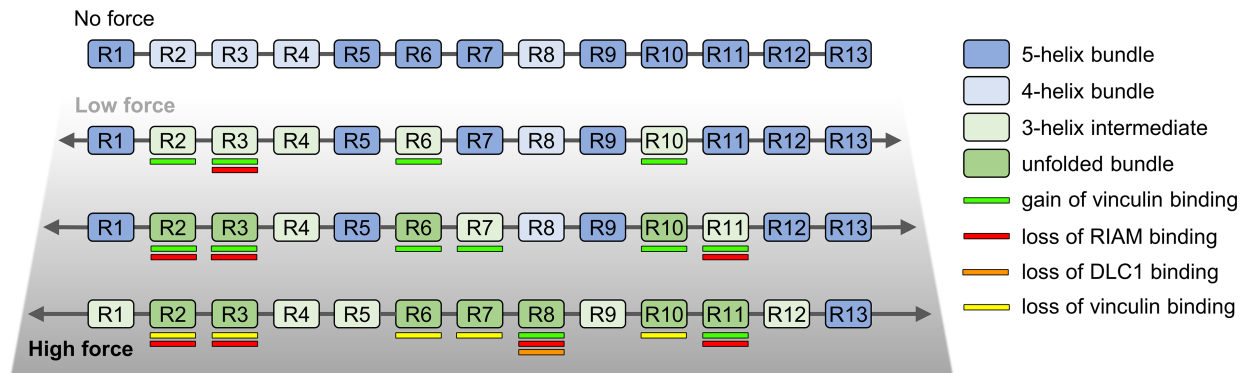


**Fig 7. Schematic representation of talin rod unfolding through stable 3-helix intermediates.** Without force, the talin rod subdomains remain intact and no VBSs are exposed. Under low load weak 4-helix bundles unfold to stable 3-helix intermediates. As the force increases, some of the 5-helix bundles unfold, forming the 3-helix intermediates along talin rod structure. Force-regulated unfolding of the talin rod changes affinity to different binding partners. RIAM and DLC1 are known to bind folded bundles, while recruitment of vinculin requires partial or complete unfolding of rod domains. VBSs that are located at terminal helices of the R2, R6, R7, and R10 bundles become available after unfolding to the 3-helix state (panel “Low force”).

<https://doi.org/10.1371/journal.pcbi.1006126.g007>

mechanical forces by the dissociation of certain bundles leading to a change in binding to other proteins. Such mechanoregulation would take place until the bundles reach a stable 3-helix spectrin-like conformation. At this point, the talin protein would assume a structural reinforcement role. Finally, at a high force, completely unfolded bundles would lose the ability to support ligand binding as well as structural function[20]. Such a model enables rich mechanosignaling through talin. A recent study by the Barsukov group has proposed the talin protein as being a hub for several different binding partners[45] where the proposed 3-helix intermediate state could be an essential component of binding regulation. Moreover, it has been recently shown, that the mechanical load across talin is not homogeneous, providing further variation in the regulation of talin functions[11]. Since the talin rod experiences a force gradient, once vinculin is bound, the local stress may become modulated and insufficient to unfold the 3-helix state. The 3-helix state may thus represent abundant talin rod subdomain conformation in living cells[11,43]. Experimental work is essential to confirm and refine these models.

While the activation of talin binding sites by mechanical force has been long studied, the detailed mechanism of the forced unfolding has not been previously discussed. The existence of a stable 3-helix intermediate may offer yet another level in the mechanoregulation process and in the cell’s response to mechanical stimuli. The existence of the unfolding intermediate also adds additional complexity to the assessment of the impact of mutations in the case of diseases.  $\alpha$ -catenin truncating mutations have been detected in patients with hereditary gastric cancer[46] possibly increasing the disease susceptibility. Furthermore,  $\alpha$ -catenin mutations have been directly associated with macular dystrophy[47]. The understanding of molecular mechanisms would shed light on the disease development and guide new treatment solutions. We may also speculate that the existence of a 3-helix intermediate, whether undergoing full unfolding or not, may provide an additional structural support. It is also possible that the 3-helix state functions as a molecular bumper reducing the impact of functional mutations present in the mechanosensitive protein. In other words, with additional level of mechanoregulation, the mutation effect on the cells behavior may be defused with only moderate effect on the cells fitness. Such a theory may be of importance in the case of talin which has been presented as a vital protein in cell and tissue biology. Yet, despite its important roles, only one

mutation has been recognized as disease causing, in the talin-2 isoform located outside of the mechanosensitive region[48].

We show that  $\alpha$ -helical proteins unfold via stable 3-helix intermediate states, representing biologically active states. smAFM and disulphide clamp mutations were used to confirm the models obtained with SMD. Our results suggest that talin is a central scaffolding hub in focal adhesions with multiple discrete unfolding states, acting as a sophisticated mechanosensor and an important regulatory switch. We further propose that the mechanical stability of  $\alpha$ -helical domains as well as the mechanical stability of their unfolding intermediates should be considered when studying mechanoregulation models of  $\alpha$ -helical proteins.

## Materials and methods

### SMD simulations

The following structures from RCSB Protein Data Bank were used as the protein models for the individual talin rod subdomains: R3 (id 2L7A residues 796 to 909), R9 (id 2KBB) and R11 (id 3dYJ residues 1975 to 2140). Talin R9 tandems were constructed using PyMOL, by creating a peptide bond between the last residue of the first R9 monomer and the first residue of the second R9 monomer.  $\alpha$ -catenin including  $M_I$  and  $M_{II}$  domains (id 4IGG residues 275 to 506) was used in our simulations. The point mutations introducing cysteine residues into the talin rod subdomains in order to form the disulphide bonds (clamps) preventing the unfolding of 3-helix state, were designed and mutated using PyMOL.

MD and SMD simulations were performed using Gromacs ver 2016.1[49,50] at the Sisu supercomputer, CSC, Finland. The CHARMM27 force field[51] and explicit TIP3P water model[52] in 0.15 M KCl solution were used and the total charge of the system was adjusted by  $K^+$  and  $Cl^-$  ions. The energy minimization of the system was performed in 10 000 steps using the steepest descent algorithm. The system was equilibrated in three phases using harmonic position restraints on all heavy atoms of the protein. The first phase of the equilibration was performed with NVT ensemble for 100 ps using the Berendsen weak coupling algorithm[53] to control the temperature of the system at 100 K. Integration time step of 2 fs was used in all the simulations. Following the NVT, the system was linearly heated from 100 to 310 K over 1 ns using an NPT ensemble at 1 atm of pressure. During this process, the Berendsen algorithm was used to control both temperature and pressure. For the final phase of equilibration and for all subsequent simulations, an NPT ensemble was maintained at 310 K using the V-rescale algorithm[54], and 1 atm as implemented in Gromacs 2016.1. The temperature coupling was applied separately for the protein and the solution parts. Each system was equilibrated up to 30 ns, with subsequent monitoring of the root mean square deviations (RMSD) of  $C\alpha$  atoms, considering the first approx. 5 ns as relaxation step. Hence, snapshots at 5 ns were used as starting structures for SMD simulations. Pulling vector was set between  $C\alpha$  of the first and the last residue of the appropriate domain. The movement of  $C\alpha$  of N-terminal residue was restrained with harmonic potential, while  $C\alpha$  of C-terminal residue was subjected to the constant velocity or constant force pulling. The pressure control was turned off for the pulling dimension (z-axes) in all SMD simulations as described in our previous work[28]. The constant velocity pulling SMD simulations were performed at 2 nm / ns with the spring constant set to 1000 kJ/mol  $nm^2$ . In the constant force pulling SMD simulations, different force regimes were applied, 160 pN, 170 pN, 180 pN and 200 pN for R3 and 200 pN, 220 pN, 230 pN, 250 pN and 300 pN for R9. The system size in SMD was 227 thousand atoms for R3, about 800 thousand atoms for R9, R11 and  $\alpha$ -catenin  $M_I$ - $M_{II}$ , and about 1.2 million atoms for R9 tandems. Detailed composition of the systems used SMD simulations shown in S2 Table.

## Generation of polyprotein constructs

The constructs and experimental procedure for the smAFM were similar to those described before[28]. The talin fragment polyprotein constructs, including flanking I27, were synthesized and cloned in to pFN18a. The polyproteins were expressed in *E. coli* BL21-CodonPlus (DE3)-RILP competent cells, using the T7 promoter present in the plasmid. Protein expression was induced with IPTG when the culture reached an OD600 nm of 0.6. Cells were lysed by applying 0.2 mg/ml lysozyme for 30 minutes at 25°C, followed by sonication with an Sonifier cell disruptor model SLPe (Branson Ultrasonics Corporation, USA) and clarification of the lysate using centrifugation. The clarified lysate was subjected to Ni-NTA affinity chromatography beads in a batch process. The proteins eluted with imidazole were analyzed for purity with SDS-PAGE and used at a final concentration between 1–10  $\mu$ g/mL.

## Preparation of ligand-functionalized surfaces

Glass coverslips were functionalized with the chloroalkane ligand to HaloTag as previously described[28]. The glass coverslips were first cleaned using Helmanex III (1% in water), acetone, and ethanol washes. The surfaces were then prepped with O<sub>2</sub> plasma cleaning for 15 min. Surfaces were then silanized using (3-aminopropyl)trimethoxysilane, diluted to 1% in ethanol. Surfaces were then washed with ethanol and then dried with N<sub>2</sub>. These amine-functionalized surfaces were then incubated with 10 mM succinimidyl-[(N-maleimidopropionamido)tetraco-saethylene glycol] ester (SMPEG24 –Thermo) diluted in 100 mM borax buffer (pH 8.5) for 1 h. The final step involved incubating the surfaces overnight with 10 mM HaloTag Thiol O4 ligand in the same buffer. The surfaces were quenched with 50 mM 2-mercaptoethanol in water.

## AFM experiments and analysis

We used a commercial AFS-1 from Luigs & Neumann, GmbH, based on a device developed at the Fernandez Lab, Columbia University[55]. The cantilevers used were gold-coated OBL-10 levers from Bruker. The spring constants varied between 4 and 10 pN/nm as measured by equipartition theorem with the appropriate adjustments for cantilever geometry[56,57]. Around 20  $\mu$ L of protein solution was incubated on functionalized coverslips for 30 min prior to the experiments to allow for HaloTag binding. The cantilever was pressed into the surface with a force of  $\sim$  300 pN to bind the cantilever to the polyprotein. Force extension experiments were conducted at 400 nm/s retraction rate. Data analysis was carried out using Igor Pro (Wavemetrics). Unfolding peaks were identified by adjustable smoothing with a moving box average and then by searching for local maxima. The force of the peaks along with their unadjusted distance from the HaloTag benchmark was measured.

## Supporting information

**S1 Fig. Design of disulphide clamps in R9.** L1698C and A1748C cysteine mutations prevent unfolding of the 3-helix core from N-terminus (N clamp), while A1720C and A1779C mutations protect the 3-helix core from C-terminus (C clamp).  
(TIF)

**S2 Fig. Statistical analysis of constant velocity SMD.** Five parallel simulations were performed for (a) R9, (b) R11, (c) R3 and (d)  $\alpha$ -catenin. Unfolding force profiles show that proposed mechanism of unfolding is reproducible.  
(TIF)

**S3 Fig. Constant force SMD simulations in 100 ns time range.** (a) R3 at constant force of 160 pN completely unfolded during  $\sim 72$  ns, and (b) R9 unfolded to 3-helix state at 200 pN during  $\sim 86$  ns.

(TIF)

**S4 Fig. Comparison between the folded and 3-helix intermediate state.** Packing of hydrophobic residues in R3, R9 and R11 in (a, b & c) folded bundle (upper panel) and in (d, e & f) the 3-helix state (lower panel). The 3-helix structure snapshots were captured from constant velocity SMD simulations at 7 ns (R3) and 14 ns (R9 & R11). Side chains of hydrophobic residues are shown as orange sticks.

(TIF)

**S5 Fig. Analysis of R3 domain unfolding and corresponding end-to-end distance.** The end-to-end distance of the folded bundle was measured in PyMol 1.7.x. The end-to-end distance of the collapsed R3 domain is hypothetical. It is based on the observation of the steered molecular dynamics under mechanical load. The length of intact helices was measured in PyMol 1.7.x. The final length of the unfolded state summed all measures of folded helices and contour lengths of the interconnecting linkers. The end-to-end distance of the theoretical unfolded R3 corresponds to the calculated contour length. 4 Å average length per residue was used in the theoretical length calculation (Ainavarapu et al. 2007).

(TIF)

**S6 Fig. Deletion of helix from talin rod subdomain R3 leads to enhanced accumulation to adhesion sites.** Various mCherry-tagged talin forms were overexpressed in Talin-1<sup>-/-</sup> mouse embryonal fibroblast cells [58]. Paxillin was used as a marker for the cellular adhesions. Wild type talin-1 and truncated ( $\Delta$ R4-12) talin were found to co-localize with paxillin to similar extent. In contrast, talin  $\Delta$ R4-12 4S containing destabilizing mutations in the R3 subdomain [23] and as well as talin  $\Delta$ R4-12  $\Delta$ R3H4 having deletion of the last helix of R3 subdomain showed enhanced accumulation into paxillin-rich adhesion structures.

(TIF)

**S1 Table. Unfolding peak force in constant velocity SMD.**

(DOCX)

**S2 Table. Composition of the systems used in SMD simulations.**

(DOCX)

## Acknowledgments

We thank Rolle Rahikainen (University of Tampere) for the help with [S6 Fig](#).

## Author Contributions

**Conceptualization:** Magdaléna von Essen, Armando del Río Hernández, Vesa P. Hytönen.

**Data curation:** Vasyl V. Mykuliak, Alexander William M. Haining.

**Formal analysis:** Alexander William M. Haining.

**Funding acquisition:** Armando del Río Hernández, Vesa P. Hytönen.

**Investigation:** Vasyl V. Mykuliak, Alexander William M. Haining, Magdaléna von Essen.

**Methodology:** Alexander William M. Haining.

**Project administration:** Armando del Río Hernández, Vesa P. Hytönen.

**Resources:** Armando del Río Hernández, Vesa P. Hytönen.

**Supervision:** Armando del Río Hernández, Vesa P. Hytönen.

**Validation:** Armando del Río Hernández, Vesa P. Hytönen.

**Visualization:** Vasyl V. Mykuliak, Alexander William M. Haining, Magdalena von Essen.

**Writing – original draft:** Vasyl V. Mykuliak, Alexander William M. Haining, Magdalena von Essen.

**Writing – review & editing:** Armando del Río Hernández, Vesa P. Hytönen.

## References

1. Seifert C, Grater F. Protein mechanics: how force regulates molecular function. *BiochimBiophysActa*. 2013; 1830: 4762–4768. <https://doi.org/10.1016/j.bbagen.2013.06.005> PMID: 23791949
2. Hu X, Margadant FM, Yao M, Sheetz MP. Molecular stretching modulates mechanosensing pathways. *Protein Sci*. 2017; 26: 1337–1351. <https://doi.org/10.1002/pro.3188> PMID: 28474792
3. Ipsaro JJ, Harper SL, Messick TE, Marmorstein R, Mondragon A, Speicher DW. Crystal structure and functional interpretation of the erythrocyte spectrin tetramerization domain complex. *Blood*. 2010; 115: 4843–4852. <https://doi.org/10.1182/blood-2010-01-261396> PMID: 20197550
4. Muthu M, Richardson KA, Sutherland-Smith AJ. The crystal structures of dystrophin and utrophin spectrin repeats: implications for domain boundaries. *PLoS One*. 2012; 7: e40066. <https://doi.org/10.1371/journal.pone.0040066> PMID: 22911693
5. Choi H-J, Weis WI. Crystal structure of a rigid four-spectrin-repeat fragment of the human desmoplakin-plakin domain. *J Mol Biol*. 2011; 409: 800–812. <https://doi.org/10.1016/j.jmb.2011.04.046> PMID: 21536047
6. Rao ST, Satyshur KA, Greaser ML, Sundaralingam M. X-ray structures of Mn, Cd and Tb metal complexes of troponin C. *Acta Crystallogr D Biol Crystallogr*. 1996; 52: 916–922. <https://doi.org/10.1107/S0907444996006166> PMID: 15299599
7. Ylanne J, Scheffzek K, Young P, Saraste M. Crystal structure of the alpha-actinin rod reveals an extensive torsional twist. *Structure*. 2001; 9: 597–604. PMID: 11470434
8. Strelkov S V, Herrmann H, Geisler N, Wedig T, Zimbelmann R, Aebi U, et al. Conserved segments 1A and 2B of the intermediate filament dimer: their atomic structures and role in filament assembly. *EMBO J*. 2002; 21: 1255–1266. <https://doi.org/10.1093/emboj/21.6.1255> PMID: 11889032
9. Kobiela A, Fuchs E. Alpha-catenin: at the junction of intercellular adhesion and actin dynamics. *Nat Rev Mol Cell Biol*. 2004; 5: 614–625. <https://doi.org/10.1038/nrm1433> PMID: 15366705
10. Carrion-Vazquez M, Oberhauser AF, Fisher TE, Marszalek PE, Li H, Fernandez JM. Mechanical design of proteins studied by single-molecule force spectroscopy and protein engineering. *Prog Biophys Mol Biol*. 2000; 74: 63–91.
11. Ringer P, Weis A, Cost A-L, Freikamp A, Sabass B, Mehlich A, et al. Multiplexing molecular tension sensors reveals piconewton force gradient across talin-1. *Nat Methods*. 2017; 14: 1090–1096. <https://doi.org/10.1038/nmeth.4431> PMID: 28945706
12. Roberts GCK, Critchley DR. Structural and biophysical properties of the integrin-associated cytoskeletal protein talin. *Biophys Rev*. 2009; 1: 61–69. <https://doi.org/10.1007/s12551-009-0009-4> PMID: 19655048
13. Rangarajan ES, Izzard T. Dimer asymmetry defines alpha-catenin interactions. *Nat Struct Mol Biol*. 2013; 20: 188–193. <https://doi.org/10.1038/nsmb.2479> PMID: 23292143
14. Hytönen VP, Wehrle-Haller B. Mechanosensing in cell–matrix adhesions—Converting tension into chemical signals. *Exp Cell Res*. 2016; 343: 35–41. <https://doi.org/10.1016/j.yexcr.2015.10.027> PMID: 26518118
15. Campbell ID, Humphries MJ. Integrin structure, activation, and interactions. *Cold Spring Harb Perspect Biol*. 2011; 3. <https://doi.org/10.1101/cshperspect.a004994> PMID: 21421922
16. Dorland YL, Huvneers S. Cell-cell junctional mechanotransduction in endothelial remodeling. *Cell Mol Life Sci*. 2017; 74: 279–292. <https://doi.org/10.1007/s00018-016-2325-8> PMID: 27506620

17. Mui KL, Chen CS, Assoian RK. The mechanical regulation of integrin-cadherin crosstalk organizes cells, signaling and forces. *J Cell Sci.* 2016; 129: 1093–1100. <https://doi.org/10.1242/jcs.183699> PMID: [26919980](https://pubmed.ncbi.nlm.nih.gov/26919980/)
18. Gingras AR, Ziegler WH, Frank R, Barsukov IL, Roberts GCK, Critchley DR, et al. Mapping and consensus sequence identification for multiple vinculin binding sites within the talin rod. *J Biol Chem.* 2005; 280: 37217–37224. <https://doi.org/10.1074/jbc.M508060200> PMID: [16135522](https://pubmed.ncbi.nlm.nih.gov/16135522/)
19. Calderwood DA, Campbell ID, Critchley DR. Talins and kindlins: partners in integrin-mediated adhesion. *Nat Rev Mol Cell Biol.* 2013; 14: 503–517. <https://doi.org/10.1038/nrm3624> PMID: [23860236](https://pubmed.ncbi.nlm.nih.gov/23860236/)
20. Yao M, Goult BT, Chen H, Cong P, Sheetz MP, Yan J. Mechanical activation of vinculin binding to talin locks talin in an unfolded conformation. *Sci Rep.* 2014; 4: 4610. <https://doi.org/10.1038/srep04610> PMID: [24714394](https://pubmed.ncbi.nlm.nih.gov/24714394/)
21. Goult BT, Zacharchenko T, Bate N, Tsang R, Hey F, Gingras AR, et al. RIAM and vinculin binding to talin are mutually exclusive and regulate adhesion assembly and turnover. *J Biol Chem.* 2013; 288: 8238–8249. <https://doi.org/10.1074/jbc.M112.438119> PMID: [23389036](https://pubmed.ncbi.nlm.nih.gov/23389036/)
22. Golji J, Mofrad MRK. The talin dimer structure orientation is mechanically regulated. *Biophys J.* 2014; 107: 1802–1809. <https://doi.org/10.1016/j.bpj.2014.08.038> PMID: [25418161](https://pubmed.ncbi.nlm.nih.gov/25418161/)
23. Rahikainen R, von Essen M, Schaefer M, Qi L, Azizi L, Kelly C, et al. Mechanical stability of talin rod controls cell migration and substrate sensing. *Sci Rep.* 2017; 7: 3571. <https://doi.org/10.1038/s41598-017-03335-2> PMID: [28620171](https://pubmed.ncbi.nlm.nih.gov/28620171/)
24. Yang J, Zhu L, Zhang H, Hirbawi J, Fukuda K, Dwivedi P, et al. Conformational activation of talin by RIAM triggers integrin-mediated cell adhesion. *Nat Commun.* 2014; 5: 5880. <https://doi.org/10.1038/ncomms6880> PMID: [25520155](https://pubmed.ncbi.nlm.nih.gov/25520155/)
25. Klann JE, Remedios KA, Kim SH, Metz PJ, Lopez J, Mack LA, et al. Talin Plays a Critical Role in the Maintenance of the Regulatory T Cell Pool. *J Immunol.* 2017; 198: 4639–4651. <https://doi.org/10.4049/jimmunol.1601165> PMID: [28515282](https://pubmed.ncbi.nlm.nih.gov/28515282/)
26. Ladoux B, Nelson WJ, Yan J, Mège RM. The mechanotransduction machinery at work at adherens junctions. *Integr Biol Quant Biosci from nano to macro.* 2015; 7: 1109–1119. <https://doi.org/10.1039/c5ib00070j> PMID: [25968913](https://pubmed.ncbi.nlm.nih.gov/25968913/)
27. Yao M, Qiu W, Liu R, Efremov AK, Cong P, Seddiki R, et al. Force-dependent conformational switch of  $\alpha$ -catenin controls vinculin binding. *Nat Commun.* 2014; 5: 4525. <https://doi.org/10.1038/ncomms5525> PMID: [25077739](https://pubmed.ncbi.nlm.nih.gov/25077739/)
28. Haining AWM, von Essen M, Attwood SJ, Hytönen VP, Del Río Hernández A. All Subdomains of the Talin Rod Are Mechanically Vulnerable and May Contribute To Cellular Mechanosensing. *ACS Nano.* 2016; 10: 6648–6658. <https://doi.org/10.1021/acsnano.6b01658> PMID: [27380548](https://pubmed.ncbi.nlm.nih.gov/27380548/)
29. Maki K, Nakao N, Adachi T. Nano-mechanical characterization of tension-sensitive helix bundles in talin rod. *Biochem Biophys Res Commun.* 2017; 484: 372–377. <https://doi.org/10.1016/j.bbrc.2017.01.127> PMID: [28131835](https://pubmed.ncbi.nlm.nih.gov/28131835/)
30. Maki K, Han S-W, Hirano Y, Yonemura S, Hakoshima T, Adachi T. Mechano-adaptive sensory mechanism of alpha-catenin under tension. *Sci Rep.* 2016; 6: 24878. <https://doi.org/10.1038/srep24878> PMID: [27109499](https://pubmed.ncbi.nlm.nih.gov/27109499/)
31. Towbin JA. Inherited cardiomyopathies. *Circ J.* 2014; 78: 2347–2356. PMID: [25186923](https://pubmed.ncbi.nlm.nih.gov/25186923/)
32. Johnson CP, Gaetani M, Ortiz V, Bhasin N, Harper S, Gallagher PG, et al. Pathogenic proline mutation in the linker between spectrin repeats: disease caused by spectrin unfolding. *Blood.* 2007; 109: 3538–3543. <https://doi.org/10.1182/blood-2006-07-038588> PMID: [17192394](https://pubmed.ncbi.nlm.nih.gov/17192394/)
33. Chiu C, Bagnall RD, Ingles J, Yeates L, Kennerson M, Donald JA, et al. Mutations in alpha-actinin-2 cause hypertrophic cardiomyopathy: a genome-wide analysis. *J Am Coll Cardiol.* 2010; 55: 1127–1135. <https://doi.org/10.1016/j.jacc.2009.11.016> PMID: [20022194](https://pubmed.ncbi.nlm.nih.gov/20022194/)
34. Theis JL, Bos JM, Bartleson VB, Will ML, Binder J, Vatta M, et al. Echocardiographic-determined septal morphology in Z-disc hypertrophic cardiomyopathy. *Biochem Biophys Res Commun.* 2006; 351: 896–902. <https://doi.org/10.1016/j.bbrc.2006.10.119> PMID: [17097056](https://pubmed.ncbi.nlm.nih.gov/17097056/)
35. Nowak KJ, Wattanasirichaigoon D, Goebel HH, Wilce M, Pelin K, Donner K, et al. Mutations in the skeletal muscle alpha-actin gene in patients with actin myopathy and nemaline myopathy. *Nat Genet.* 1999; 23: 208–212. <https://doi.org/10.1038/13837> PMID: [10508519](https://pubmed.ncbi.nlm.nih.gov/10508519/)
36. Pulkkinen L, Rouan F, Bruckner-Tuderman L, Wallerstein R, Garzon M, Brown T, et al. Novel ITGB4 mutations in lethal and nonlethal variants of epidermolysis bullosa with pyloric atresia: missense versus nonsense. *Am J Hum Genet.* 1998; 63: 1376–1387. <https://doi.org/10.1086/302116> PMID: [9792864](https://pubmed.ncbi.nlm.nih.gov/9792864/)
37. Hytönen VP, Vogel V. How Force Might Activate Talin's Vinculin Binding Sites: SMD Reveals a Structural Mechanism. *PLoS Comput Biol.* 2008; 4: e24. <https://doi.org/10.1371/journal.pcbi.0040024> PMID: [18282082](https://pubmed.ncbi.nlm.nih.gov/18282082/)

38. del Rio A, Perez-Jimenez R, Liu R, Roca-Cusachs P, Fernandez JM, Sheetz MP. Stretching Single Talin Rod Molecules Activates Vinculin Binding. *Science*. 2009; 323: 638–641. <https://doi.org/10.1126/science.1162912> PMID: 19179532
39. Baxter NJ, Zacharchenko T, Barsukov IL, Williamson MP. Pressure-Dependent Chemical Shifts in the R3 Domain of Talin Show that It Is Thermodynamically Poised for Binding to Either Vinculin or RIAM. *Struct*. 2017; <https://doi.org/10.1016/j.str.2017.10.008> PMID: 29153504
40. Papagrigoriou E, Gingras AR, Barsukov IL, Bate N, Fillingham IJ, Patel B, et al. Activation of a vinculin-binding site in the talin rod involves rearrangement of a five-helix bundle. *EMBO J*. 2004; 23: 2942–2951. <https://doi.org/10.1038/sj.emboj.7600285> PMID: 15272303
41. Lee SE, Kamm RD, Mofrad MRK. Force-induced activation of talin and its possible role in focal adhesion mechanotransduction. *J Biomech*. 2007; 40: 2096–2106. <https://doi.org/10.1016/j.jbiomech.2007.04.006> PMID: 17544431
42. Ciobanasu C, Faivre B, Le Clairche C. Actomyosin-dependent formation of the mechanosensitive talin-vinculin complex reinforces actin anchoring. *Nat Commun*. 2014; 5: 3095. <https://doi.org/10.1038/ncomms4095> PMID: 24452080
43. Margadant F, Chew LL, Hu X, Yu H, Bate N, Zhang X, et al. Mechanotransduction In Vivo by Repeated Talin Stretch-Relaxation Events Depends upon Vinculin. Brugge JS, editor. *PLoS Biol*. 2011; 9: e1001223. <https://doi.org/10.1371/journal.pbio.1001223> PMID: 22205879
44. Yao M, Goult BT, Klapholz B, Hu X, Toseland CP, Guo Y, et al. The mechanical response of talin. *Nat Commun*. 2016; 7: 11966. <https://doi.org/10.1038/ncomms11966> PMID: 27384267
45. Zacharchenko T, Qian X, Goult BT, Jethwa D, Almeida TB, Ballestrem C, et al. LD Motif Recognition by Talin: Structure of the Talin-DLC1 Complex. *Structure*. 2016; 24: 1130–1141. <https://doi.org/10.1016/j.str.2016.04.016> PMID: 27265849
46. Majewski IJ, Kluijft I, Cats A, Scerri TS, de Jong D, Kluijn RJC, et al. An alpha-E-catenin (CTNNA1) mutation in hereditary diffuse gastric cancer. *J Pathol*. 2013; 229: 621–629. <https://doi.org/10.1002/path.4152> PMID: 23208944
47. Saksens NTM, Krebs MP, Schoenmaker-Koller FE, Hicks W, Yu M, Shi L, et al. Mutations in CTNNA1 cause butterfly-shaped pigment dystrophy and perturbed retinal pigment epithelium integrity. *Nat Genet*. 2016; 48: 144–151. <https://doi.org/10.1038/ng.3474> PMID: 26691986
48. Deng H, Deng S, Xu H, Deng H-X, Chen Y, Yuan L, et al. Exome Sequencing of a Pedigree Reveals S339L Mutation in the TLN2 Gene as a Cause of Fifth Finger Camptodactyly. *PLoS One*. 2016; 11: e0155180. <https://doi.org/10.1371/journal.pone.0155180> PMID: 27223613
49. Van Der Spoel D, Lindahl E, Hess B, Groenhof G, Mark AE, Berendsen HJC. GROMACS: fast, flexible, and free. *J Comput Chem*. 2005; 26: 1701–1718. <https://doi.org/10.1002/jcc.20291> PMID: 16211538
50. Berendsen HJC, van der Spoel D, van Drunen R. GROMACS: A message-passing parallel molecular dynamics implementation. *Comput Phys Commun*. 1995; 91: 43–56. [https://doi.org/10.1016/0010-4655\(95\)00042-E](https://doi.org/10.1016/0010-4655(95)00042-E)
51. MacKerell A, Bashford D, Bellott M, Dunbrack R, Evanseck J, Field M, et al. All-Atom Empirical Potential for Molecular Modeling and Dynamics Studies of Proteins. *J Phys Chem B*. 1998; 102: 3586–3616. <https://doi.org/10.1021/jp973084f> PMID: 24889800
52. Jorgensen WL, Madura JD. Quantum and statistical mechanical studies of liquids. 25. Solvation and conformation of methanol in water. *J Am Chem Soc*. 1983; 105: 1407–1413. <https://doi.org/10.1021/ja00344a001>
53. Berendsen H, Postma J, van Gunsteren W, DiNola A, Haak J. Molecular dynamics with coupling to an external bath. *J Chem Phys*. 1984; 81: 3684–3690. <https://doi.org/10.1063/1.448118>
54. Bussi G, Donadio D, Parrinello M. Canonical sampling through velocity rescaling. *J Chem Phys*. 2007; 126: 14101. <https://doi.org/10.1063/1.2408420> PMID: 17212484
55. Popa I, Kosuri P, Alegre-Cebollada J, Garcia-Manyes S, Fernandez JM. Force dependency of biochemical reactions measured by single-molecule force-clamp spectroscopy. *Nat Protoc*. 2013; 8: 1261–1276. <https://doi.org/10.1038/nprot.2013.056> PMID: 23744288
56. Hutter JL, Bechhoefer J. Calibration of atomic-force microscope tips. *Rev Sci Instrum*. 1993; 64: 1868–1873. <https://doi.org/10.1063/1.1143970>
57. Butt H-J, Jaschke M. Calculation of thermal noise in atomic force microscopy. *Nanotechnology*. 1995; 6: 1–7. <https://doi.org/10.1088/0957-4484/6/1/001>
58. Zhang X, Jiang G, Cai Y, Monkley SJ, Critchley DR, Sheetz MP. Talin depletion reveals independence of initial cell spreading from integrin activation and traction. *Nat Cell Biol*. 2008; 10: 1062–1068. <https://doi.org/10.1038/ncb1765> PMID: 19160486

## Supporting Information

### Mechanical unfolding reveals stable 3-helix intermediates in talin and $\alpha$ -catenin

Vasyl V. Mykuliak 1  , Alexander William M. Haining 2  , Magdaléna von Essen 1  , Armando del Río Hernández 2 \* , Vesa P. Hytönen 1 \*

1 Faculty of Medicine and Life Sciences and BioMediTech, University of Tampere, Finland and Fimlab Laboratories, Tampere, Finland,

2 Cellular and Molecular Biomechanics Laboratory, Department of Bioengineering, Imperial College London, London, United Kingdom

Corresponding authors:

Vesa Hytönen

Protein Dynamics Group

BioMediTech

University of Tampere

Tampere, Finland

Telephone: +358401901517

Email: [vesa.hytonen@uta.fi](mailto:vesa.hytonen@uta.fi)

Armando del Río Hernández

Cellular and Molecular Biomechanics Laboratory

<http://biomechanicalregulation-lab.org/>

Department of Bioengineering

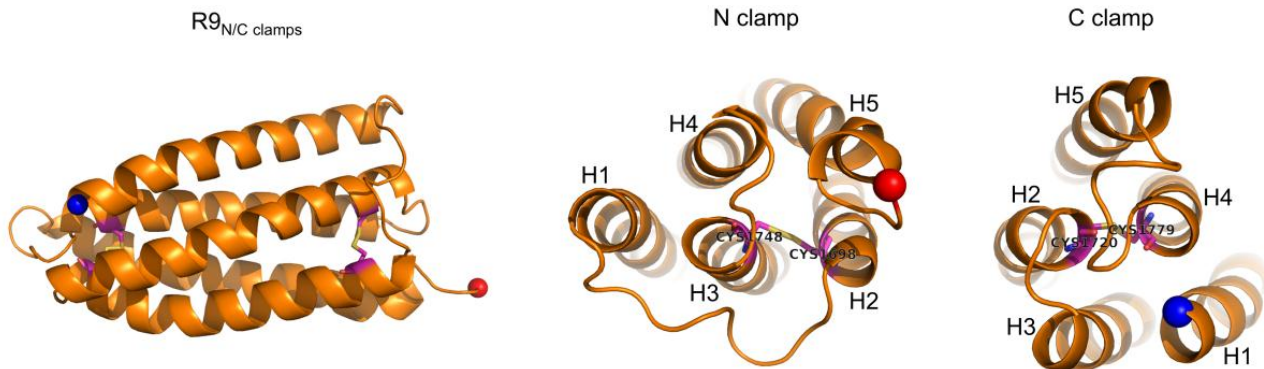
Imperial College London

SW7 2AZ London

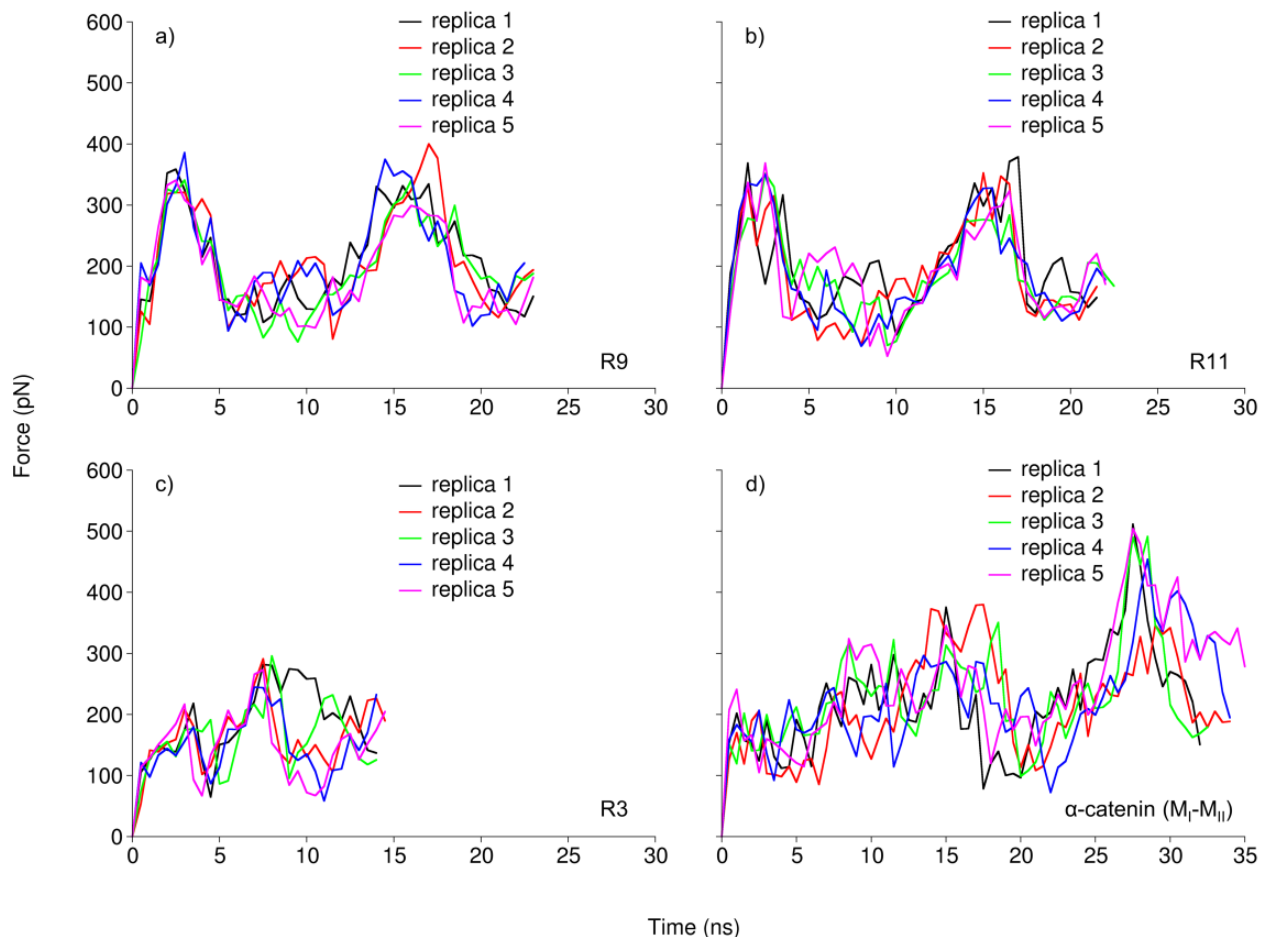
telephone: +44(0) 20 7594 5187

Mobile: +44(0)7407270946

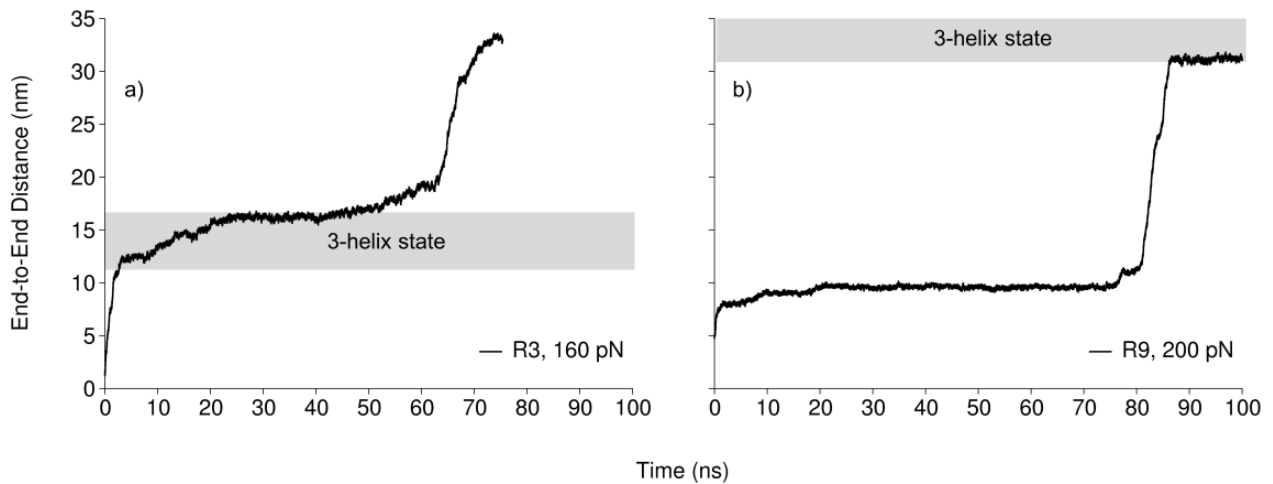
email: [a.del-rio-hernandez@imperial.ac.uk](mailto:a.del-rio-hernandez@imperial.ac.uk)



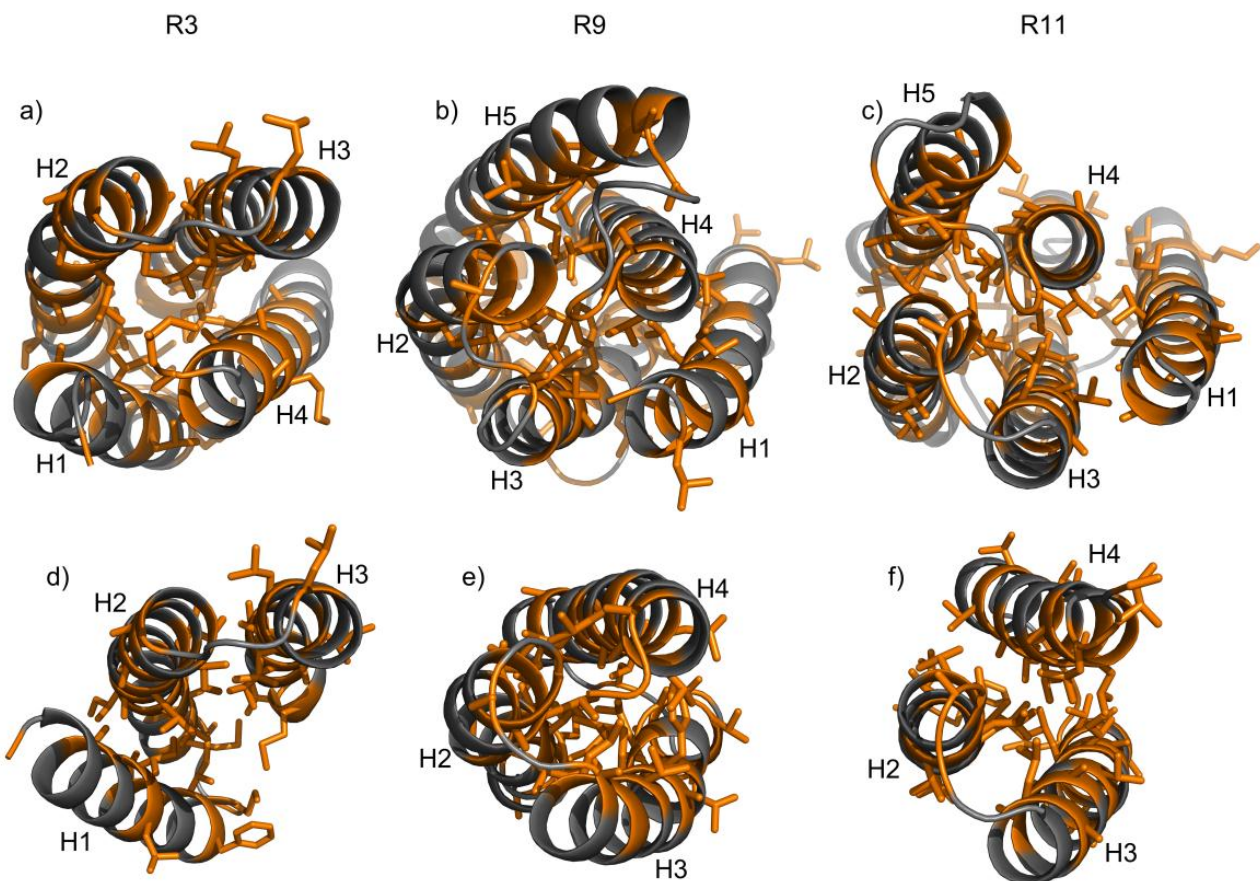
**S1 Fig. Design of disulphide clamps in R9.** L1698C and A1748C cysteine mutations prevent unfolding of the 3-helix core from N-terminus (N clamp), while A1720C and A1779C mutations protect the 3-helix core from C-terminus (C clamp).



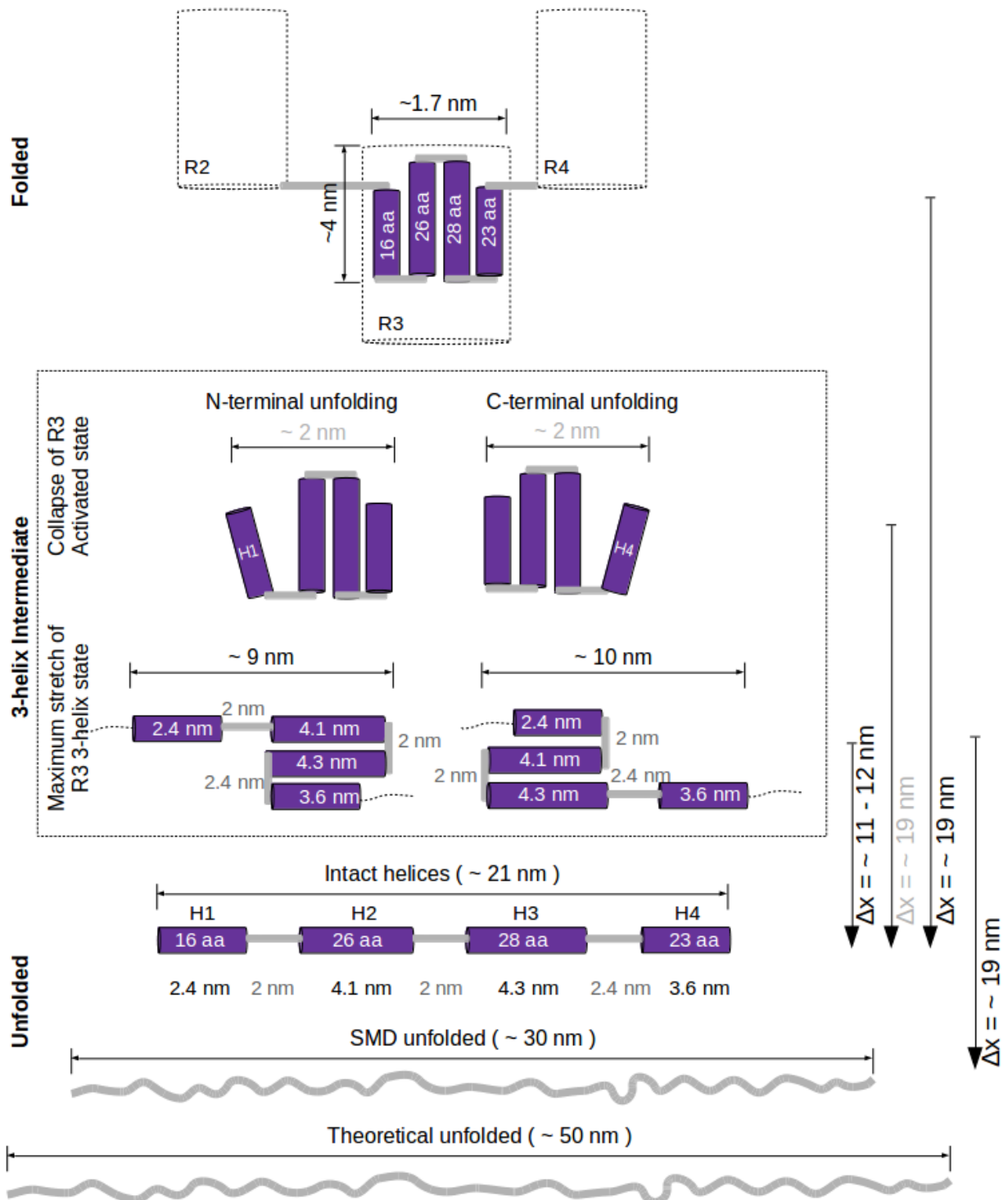
**S2 Fig. Statistical analysis of constant velocity SMD.** Five parallel simulations were performed for (a) R9, (b) R11, (c) R3 and (d)  $\alpha$ -catenin. Unfolding force profiles show that proposed mechanism of unfolding is reproducible.



**S3 Fig. Constant force SMD simulations in 100 ns time range.** (a) R3 at constant force of 160 pN completely unfolded during  $\sim 72$  ns, and (b) R9 unfolded to 3-helix state at 200 pN during  $\sim 86$  ns.

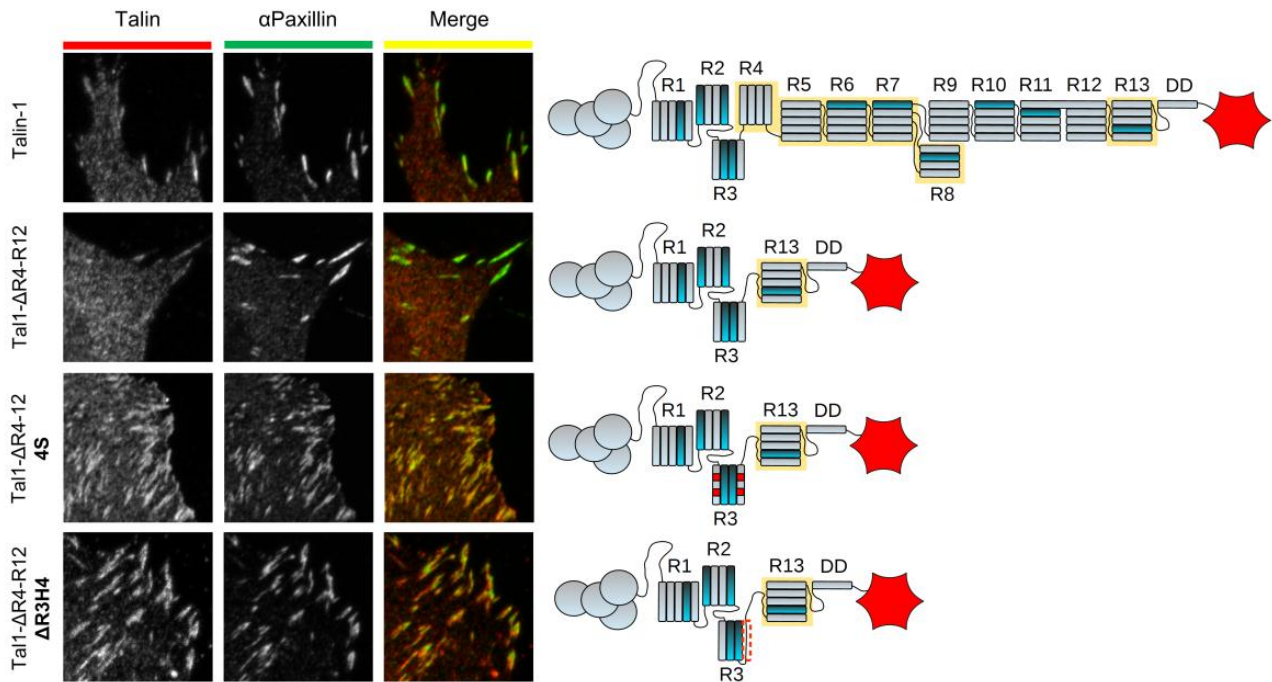


**S4 Fig. Comparison between the folded and 3-helix intermediate state.** Packing of hydrophobic residues in R3, R9 and R11 in (a, b & c) folded bundle (upper panel) and in (d, e & f) the 3-helix state (lower panel). The 3-helix structure snapshots were captured from constant velocity SMD simulations at 7 ns (R3) and 14 ns (R9 & R11). Side chains of hydrophobic residues are shown as orange sticks.



**S5 Fig. Analysis of R3 domain unfolding and corresponding end-to-end distance.**

The end-to-end distance of the folded bundle was measured in PyMol 1.7.x. The end-to-end distance of the collapsed R3 domain is hypothetical. It is based on the observation of the steered molecular dynamics under mechanical load. The length of intact helices was measured in PyMol 1.7.x. The final length of the unfolded state summed all measures of folded helices and contour lengths of the interconnecting linkers. The end-to-end distance of the theoretical unfolded R3 corresponds to the calculated contour length. 4 Å average length per residue was used in the theoretical length calculation (Ainavarapu et al. 2007).



**S6 Fig. Deletion of helix from talin rod subdomain R3 leads to enhanced accumulation to adhesion sites.** Various mCherry-tagged talin forms were overexpressed in Talin-1  $-/-$  mouse embryonal fibroblast cells [58]. Paxillin was used as a marker for the cellular adhesions. Wild type talin-1 and truncated ( $\Delta$ R4-12) talin were found to co-localize with paxillin to similar extent. In contrast, talin  $\Delta$ R4-12 4S containing destabilizing mutations in the R3 subdomain [23] and as well as talin  $\Delta$ R4-12  $\Delta$ R3H4 having deletion of the last helix of R3 subdomain showed enhanced accumulation into paxillin-rich adhesion structures.

**S1 Table. Unfolding peak force in constant velocity SMD**

Protein construct	Conformational state	Unfolding peak force (pN)					Average $\pm$ standard deviation
		Replica 1	Replica 2	Replica 3	Replica 4	Replica 5	
R3	3h $\rightarrow$ 0h	281	291	295	244	272	276 $\pm$ 20
R9	5h $\rightarrow$ 3h	358	320	340	385	340	348 $\pm$ 24
R9	3h $\rightarrow$ 0h	331	400	340	374	299	349 $\pm$ 39
R11	5h $\rightarrow$ 3h	368	329	351	349	368	353 $\pm$ 16
R11	3h $\rightarrow$ 0h	378	352	283	327	322	332 $\pm$ 35
$\alpha$ -catenin	3h $\rightarrow$ 0h (M <sub>I</sub> )	511	345	491	454	504	461 $\pm$ 68
$\alpha$ -catenin	3h $\rightarrow$ 0h (M <sub>II</sub> )	375	379	350	296	345	349 $\pm$ 33

**S2 Table. Composition of the systems used in SMD simulations**

Protein construct	Residues	Number of protein residues (atoms)	Number of water molecules	Number of ions		Total number of atoms
				K <sup>+</sup>	Cl <sup>-</sup>	
R3	Gly796-Ile909	114 (1672)	75 236	214	208	227 802
R9	Gly1657-Gly1825	169 (2469)	281 331	792	780	848 034
R11	Thr1975-Thr2140	166 (2429)	272 147	758	754	820 382
$\alpha$ -catenin (M <sub>I</sub> -M <sub>II</sub> )	Gly275-Thr506	232 (3655)	237 484	665	659	717 431